The effect of photon dose calculation algorithms on the clinical outcome of radiotherapy as assessed by radiobiological models

Thesis submitted in accordance with the requirements of the
University of Liverpool
for the degree of Doctor in Philosophy by

Mekala Chandrasekaran

September 2012

I dedicate this thesis to my beloved

Amma, Appa, Kanch and Anand

who mean the world to me!

Abstract

The accuracy of dose calculation algorithms used for radiotherapy treatment planning can play a significant role in the clinical outcome of radiotherapy treatment regimens. Heterogeneities in human anatomy such as lung, air cavities, bone, soft tissue and fat present challenges to the dose calculation algorithms as they are prone to disrupt the charged-particle equilibrium. Monte Carlo (MC) based dose calculation algorithms are proven to be superior to all the current analytical algorithms owing to their ability to account for all the physical interactions that are involved in radiation transport. Numerous publications have examined the differences in physical doses calculated by analytical algorithms when compared to MC in dealing with heterogeneities. However, before this work the clinical significance of these differences in physical dose has never been investigated in detail.

An EGSnrc, BEAMnrc and DOSXYZnrc based MC dose calculation engine was set up in a parallel computing environment to simulate three-dimensional conformal radiotherapy (3DCRT) and intensity modulated radiation therapy (IMRT). A Varian 2100 C/D accelerator head was modeled and validated to match measurements of open and dynamic wedged fields in a homogeneous water phantom which was found to be in good agreement with measurements within 2%/2mm and 3%/3mm respectively. In addition, MC calculated doses in a heterogeneous lung phantom were compared to radiochromic film measurements. Overall, there was good agreement between the two, although large differences were found in some cases. This dose calculation system was used to perform MC simulations on computed tomography (CT) images.

The clinical impact of the differences in absolute doses calculated by various photon dose calculation algorithms for two clinical tumour sites was investigated.

The tumour control probability (TCP) and normal tissue complication probability (NTCP) were estimated using well established bio-mathematical radiobiological models. This work includes the analysis of 7 convolution (i.e. pencil-beam) and convolution-superposition (CS) based photon dose algorithms available in commercial treatment planning systems (TPSs) as well as MC, in treatment plans of non-small cell lung carcinoma (NSCLC) and nasopharyngeal carcinoma (NPC). In both NSCLC and NPC, the convolution algorithms overestimate the dose to the tumour and hence overestimate the TCP to up to 45%. Some of the CS algorithms were comparable to MC though others exhibit significant differences. In NSCLC, the absolute differences in the NTCP values with radiation pneumonitis and rib fracture as end points were not as large as the differences found in the TCPs. On the other hand, in NPC, the overestimation of probability of occurrence of xerostomia by some TPS algorithms may be preventing dose escalation.

Parameters for the TCP model were derived by fitting the TCP predictions to published outcome for four widely varying dose-fractionation regimens for a patient cohort undergoing radical radiotherapy treatment for NSCLC. The derived parameter sets strongly depend on the accuracy of the dose calculation algorithm involved. Parameters derived based on dose-distribution data sets obtained using one particular dose calculation algorithm may not hold good when evaluating treatment plans calculated with a different algorithm. In this sub-study, the influence of dose calculation algorithms on TCP model parameters was evaluated. Significant differences were found in TCPs when calculated with inconsistent parameters. Hence, the choice of dose calculation algorithm is crucial and although some algorithms generally perform close to MC in handling inhomogeneities, it is necessary to understand how the underlying differences affect the predicted clinical outcome.

Acknowledgments

I would like to extend my heartfelt thanks to my supervisors, Prof Alan Nahum and Dr Colin Baker for their valuable guidance, support and encouragement through out my project and for shaping me into a researcher.

I am extremely grateful to Dr Vanessa Panettieri for introducing me to Monte Carlo simulations and for extending helping hand whenever I encountered problems and to Dr Ian Smith of the Computing Services at University of Liverpool for his extensive support to set up the Monte Carlo dose calculation engine on a parallel computing environment.

I thank Dr Antoniu Popescu, Dr Tony Teke and Julio Lobo for sharing their python routines which were used at various stages of Monte Carlo dose calculation and for helping to set up the Monte Carlo system. I would like to thank Dr Emiliano Spezi and Dr Patrick Downes for sharing their Enhanced Dynamic Wedge Monte Carlo component module and other python routines. I would like to thank Mr Peter Pryce for making the balsa inserts for the lung phantom.

I extend my since thanks to The Clatterbridge Cancer Research Trust for funding my PhD project.

My time here in the Wirral wouldn't have been as enjoyable without my dear friends - Alison Scott, Aisyah Yusof Azuddin, Claire Margreth, Eva Rutkowska, Jothy Basu, Julien Uzan, Juan Pardo Montero, Katherine Kneebone, Lynda Appleton, Mary Anthonypillai, Przemek Rutkowski, and Steven Riley. Thanks a lot for keeping my spirit up with espresso shots, wonderful continental cuisine, interesting conversations, walking and weekend activities.

I would also like to thank everyone in the Department of Physics, Clatterbridge Cancer Centre especially Andrew Riley, Andrzej Kacperek, Antony Carver, Francis Harris, Helen Mayles, John Thornton, Julie Kirk, Kathy Sztanko, Linda Mor-

timer, Martin Green, Martyn Gilmore, Philip Mayles, Richard Clements, Simon Meara, Simon Temple, and Sue Nixon. I thank everyone in the clinical trials of Research and Development, Clatterbridge Cancer Centre for making the last few years memorable.

I would like to thank my university mates, friends and colleagues in Mumbai for their constant support online and offline.

I would like to thank my future in-laws for being open, understanding and supporting.

I would like to thank all my cousins, aunts and uncles for their affection.

I thank my grand father for his whole-hearted affection.

I take this opportunity to thank my fiancé for all his love, frienship, patience and for always being there for me. His love mean the world to me.

Above all, I extend my gratitude and love to my parents, sister and brother for motivating me all the way through. It would have been impossible for me to finish my dissertation without their valuable support. I would like to thank them for everything they have given up and for always being there for me in every possible way.

Contents

List of Figures

List of Tables

Chapter 1

Introduction and Project Outline

Radiation therapy is one of the three main modalities used in the treatment of cancer, the others being surgery and chemotherapy. It is used both in curative and palliative management of cancer, often in combination with surgery and or chemotherapy. Ionizing radiation like photons, electrons and protons are used to 'kill' malignant or cancerous cells. The aim of radiation therapy is to deliver a precisely known dose of radiation to a defined tumour volume with as minimal damage as possible to the surrounding healthy tissue, resulting in the eradication of the tumour and hence a high quality of life for the individual post therapy.

The external radiotherapy era began with use of ortho voltage x-ray machines and then moved towards Co-60 external beam therapy. More advanced treatment units such as linear accelerators were introduced in the 50s with the capability of delivering radiotherapy with megavoltage photons and electrons without the use of a physical radioactive source [1]. The development of imaging modalities such as computed tomography (CT), magnetic resonance imaging (MRI), and functional imaging such as functional MRI, single photon emission computed tomography (SPECT), and positron emission tomography (PET) has paved the way to find the precise location of the tumour at various stages of radiotherapy process; prior to treatment, treatment planning and for image guidance [2–6]. This ability to localise the tumour with high accuracy reduces the gross tumour volume (GTV) and clinical target volume (CTV) that define the tumour or malignant growth that is visible on an imaging scan and the microscopic extension of the tumour [7]. It is necessary to eradicate all the clonogenic cells in the GTV

and CTV volumes. By delivering a tailored dose to the tumour by conforming the fields, it has become possible to escalate the doses with minimal damage to the normal tissues. Recent technological advances in external beam radiotherapy such as intensity-modulated radiation therapy (IMRT), image-guided radiation therapy (IGRT) with the use of cone beam CT and ultrasound, stereotactic radiosurgery and radiation therapy (SRS/SRT), and intensity-modulated arc therapy (IMAT) have enabled us to deliver radiation with high precision and hence has improved the therapeutic gain which is defined as the ratio of probability of tumour control to that of the normal tissue complication.

1.1 Background

Radiotherapy involves a chain of complex processes which are executed step by step. It is essential to maintain the accuracy of each and every step involved in order to ensure the quality of the treatment. There are uncertainties associated with each step, ranging from machine-specific uncertainties to patient-specific uncertainties; these uncertainties have been studied by various research groups [8–14]. Ahnesjö and Asparadakis [15] have reported percentage uncertainties pertaining to various steps of radiotherapy process, beginning from absolute dose calibration to patient set-up and delivery, with respect to what was achievable at the time of publication (1999) and in the future. The uncertainty due to dose calculation which directly depends upon the type of algorithm employed is one of the major contributors to the over all uncertainty that is practically achievable in radiotherapy. The uncertainties associated with radiotherapy process as reported by Ahnesjö and Asparadakis are given in table 1.1. Dose calculation accuracy was estimated to be between 1% and 5% during the time when the report was published and 0.5% to 4% in the future. The ranges of dose accuracies depend upon the technique used; smaller uncertainty values correspond to less sophisticated conventional treatments delivered with open square or rectangular fields and the larger uncertainties correspond to more complex techniques such as dynamic wedged treatments, IMRT, and IMAT. Van Dyk *et al.* [13] have reported dose accuracy criteria required for homogeneous calculation, inhomogeneity cor-

rection, and different regions with combination of high and low doses with high and low dose gradients.

Table 1.1: Uncertainties associated with each step of radiotherapy process, Ahnesjö and Asparadakis, 1999

Radiotherapy process	Present technique $100 \times \Delta D(1\sigma)$	Future Development $100 \times \Delta D(1\sigma)$
Absorbed dose at the calibration point	2.0	1.0
Additional uncertainty for other points	1.1	0.5
Monitor stability	1.0	0.5
Beam flatness	1.5	0.8
Patient data uncertainties	1.5	1.0
Beam and patient set-up	2.5	1.6
Overall excluding dose calculation	4.1	2.4
Dose calculation	1.0 2.0 3.0 4.0 5.0	0.5 1.0 2.0 3.0 4.0
Resulting overall uncertainty	4.2 4.6 5.1 5.7 6.5	2.4 2.6 3.1 3.8 4.7

The dose-effect relationship exhibits a sigmoidal behaviour which has been studied extensively over the years [16–22]. A typical sigmoidal curve plot representing the probability of tumour control and probability of normal tissue complication is shown in figure 1.1 in which the change in TCP and NTCP expressed as percentage as a function of delivered dose is depicted. The clinical outcome following a radiotherapy treatment course can be determined by using bio-mathematical models of tumour control probability (TCP) and normal tissue complication probability (NTCP) [17, 22–28]. These models can be empirical which are based on clinical observations, or mechanistic in nature that takes into account the details of cell kill mechanism and tissue architecture [29, 30]. Some models are quasi-mechanistic in nature which are partially empirical and partially mechanistic: eg. Marsen TCP model developed [27, 31, 32]. These models have parameters that characterise the sigmoidal curve which are specific to the type of the tumour, and to the organ at risk (OARs) for which the complication probability is to be determined. Such parameters have been derived and reported in the literature for various tumours and OARs [33–42]. The slope of the sigmoidal curve varies

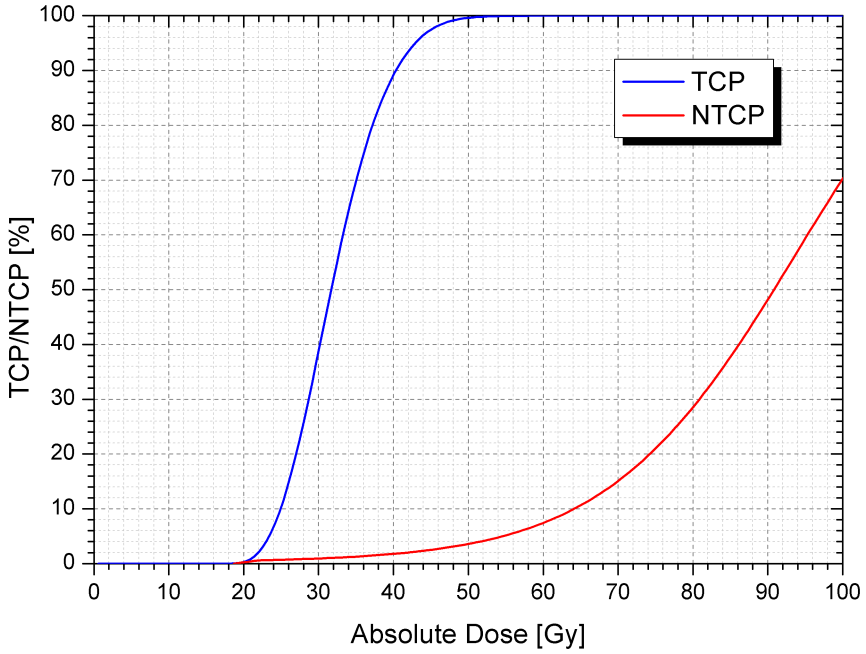

Figure 1.1: TCP and NTCP curves plotted against absolute dose in Gy. Both the dose-response curves exhibit a sigmoidal relationship with the absolute dose. It is essential to keep these curves as much apart as possible to increase the therapeutic ratio.

depending upon the type of the tumour and normal tissue under investigation as they differ significantly in the way they respond to radiation [8, 43–47].

Some normal tissues are early responding, and some are late responding, and in addition the tumour response varies from patient to patient. The TCP and NTCP model parameters are derived based on clinical outcome data; the probability of tumour control for various tumour types and normal tissue complications to various OARs in a cohort of patients irradiated with different dose fractionation regimens are evaluated for the end-points in question. These end-points could be disease-free or local-progression-free survival following the treatment for assessing the tumour response in case of TCP models [27, 48], and radiation induced pneumonitis in lung, rectal bleeding or incontinence, rib fracture, oesophagitis, xerostomia in case of NTCP models. Recently, qualitative analyses of normal tissue effects in the clinic (QUANTEC) publications have reported on radiation response, dose-volume effects, tolerances, NTCP models and parameters corresponding to various OARs and endpoints [49–64]. It has been reported by Orton *et al.* [65] that a change of 5% in dose may result in a 10% to 20% difference in

probability of tumour control at a TCP of 50% and 20%-30% change in probabilities of normal tissue complication [65]. Dutreix *et al.* [9] have shown that a difference in dose of 7% is clinically detectable.

Computerised treatment planning systems (TPS), with various dose calculation algorithms, are used to calculate the dose delivered to patients undergoing radiotherapy. The accuracy of dose calculation algorithms plays a significant role in generating reliable dose distributions so as to deliver the planned or intended dose. The human body comprises of heterogeneities such as lung, air cavities, bone, soft tissue, muscle and fat which have varying physical and electron densities. The heterogeneities that are radiologically different from that of water can result in disruption of charged-particle equilibrium when a patient is irradiated [15,66–68]. This is a consequence of differences in electron ranges in different medium. The electron ranges are longer in a medium of lower density than that of higher density as a result of which the number of charged-particles and their energy entering and leaving a unit spherical volume is not the same. This effect is predominant at the interfaces between media of low and high density. The charged-particle equilibrium is restored if the volume is sufficiently large. The differences in calculated dose distribution increases with increase in photon energy, decrease in the density of the medium involved and the field size [69–71]. A discussion of the necessity of using tissue inhomogeneity corrections in megavoltage photon beam dose calculation is given by Papanikolaou *et al.* [68].

Historically, before the advent of computerised TPSs, for Co-60 units treatment time required to deliver a dose to a particular point of interest was merely calculated manually by using basic measured beam quantities such as percentage depth dose (PDD), tissue air ratio (TAR), and tissue maximum ratio (TMR). Later on, patient body contour of the central slice with the tumour delineated and standard isodose charts were used to calculate 2D dose distribution on a single slice which was ideally located at the centre of the tumour. When more than one treatment field was used the dose distribution in the central slice was calculated by overlapping isodose charts for each field and tracing the resulting dose distribution based on the overlapping isodose lines. There was no possibility to account for the inhomogeneities in the human body due to lack of patient-specific

anatomical information or to perform three-dimensional (3D) dose calculation.

Tsien [72] proposed the application of computers in radiotherapy treatment planning in the mid 50s. The depth dose data of several sets of field sizes were recorded on punched cards which were inserted in a computer to perform the dose calculation. Later, in the mid 60s Bentley developed an interactive digital computerised system for radiotherapy treatment planning [73]. With the advent of CT scanners that have the capability to produce 3D images of patient anatomy in the form of a number of slices of the region of interest (ROI), 3D treatment planning for radiotherapy came into being.

Originally, measurement based algorithms were used in treatment planning; these algorithms simply consisted of basic beam data in terms of central-axis depth doses and off-axis ratios at various depths. These measurement-based algorithms were subsequently replaced by more accurate analytical algorithms. Convolution-based algorithms such as pencil -beam convolution were conceived in the 90s [74–78]. The PBC algorithm has been extensively used in the past owing to its faster calculation speed. It accounts for tissue heterogeneities using various methods which are Batho power law (BPL), modified Batho (MB), and equivalent tissue-air ratio (ETAR), equivalent path length (EPL) correction. These heterogeneity correction methods account for the differences in the medium and their densities along the fan line of the pencil beam but do not consider varying tissue densities in the lateral direction of the beam. This results in incorrect modelling of electron transport as a result of which doses are significantly different when compared to measurements in sites such as lung and in head and neck (HN) tumours involving air or nasal cavities [79, 80]. Figure 1.2 shows CT images with varying heterogeneities in lung and HN.

Other analytical algorithms include convolution-superposition algorithms such as collapsed cone convolution (CCC) and analytical anisotropic algorithm (AAA) that are far more accurate than simple pencil beam algorithms due their ability to approximately model electron transport [81–84]. Dose calculation based on Monte Carlo simulations is potentially more accurate than the analytical dose calculation algorithms due to its proven superiority and accuracy in computing dose distributions as it models the actual physics of energy deposition by ra-

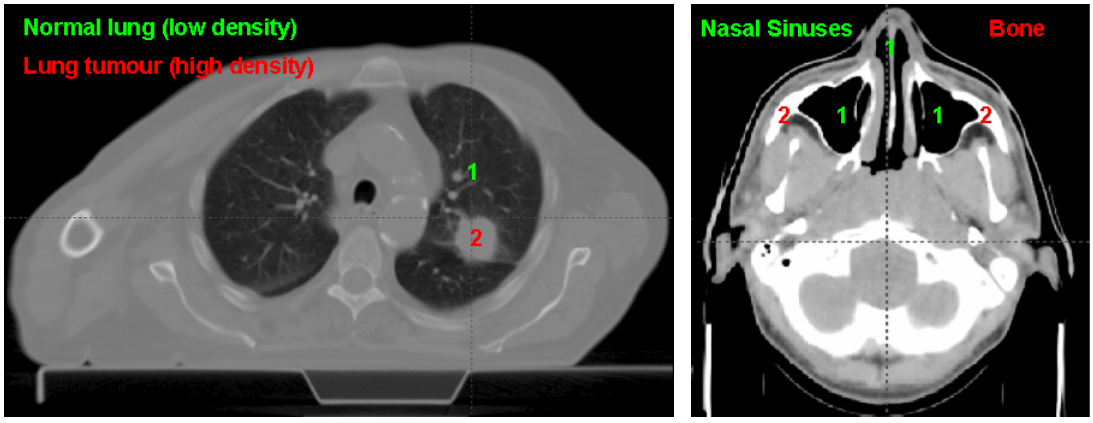

(a) (b)

Figure 1.2: Heterogeneities in (a) Thorax (b) HN in the form of low density lung, nasal sinuses and bone.

diation in tissues. The rationale for using MC dose-calculation algorithms for clinical planning include improved accuracy for inhomogeneities, particularly for lung, airways and sinuses, bone, tissue interfaces and very small fields including those used in intensity modulated radiation therapy (IMRT) treatments that also exhibit lateral electron disequilibrium effects. The physics of convolution, convolution-superposition and MC dose calculation algorithms is described in detail in chapter 2.

1.2 Aims

Numerous publications describe the differences between the dose calculation algorithms which are available in commercial TPSs and MC systems in terms of physical doses [69, 70, 85–90]. In particular, the influence of dose calculation algrorithms on the accuracy of the calculated dose distribution in lung has been studied extensively and in bone to a lesser extent. The effects on the differences in dose distribution in sites like nasopharyngeal tumours are not well described. Evaluation of a radiotherapy regimen solely in terms of physical dose may not be sufficient as this does not provide any information on the biological effect or the clinical outcome of the treatment. Some authors have reported the use of other physical metrics such as gamma index and relative normalised total dose (rNTD) [91, 92].

A radiobiological evaluation of the clinical outcome of radiotherapy plans done with various photon dose calculation algorithms is crucial in order to understand the significance of the reported differences in physical doses on the predicted probabilities of tumour control and complications caused to normal tissues. A reasonably small difference in the physical dose may result in larger differences in the estimated clinical outcome attributing to the steep slopes of the dose-response curves. The rationale for using radiobiolgical models is owing to their ability to effectively summarise the dose distribution in both tumour and normal tissue in terms of biological outcome. These models enable us to understand the effect of cold or hot spots in tumour and OARs respectively and also to evaluate the best of rival treatment plans.

To our knowledge, to date, the number of studies performed in order to estimate the clinical outcome of these absolute dose differences is small. Hence, the objective of the study we present here is to investigate the clinical impact of the differences in absolute 3D radiation dose distributions for target volumes and critical organs for patients undergoing curative radiotherapy for thoracic and head and neck tumours, in particular non small-cell lung carcinoma (NSCLC) and nasopharyngeal carcinoma (NPC), respectively, as these two sites involve heterogeneities; the former has a unit density tumour surrounded by low density normal or healthy lung and the latter has air cavities, nasal sinuses and bone. Evaluation in terms of bio-mathematical models of TCP and NTCP will be applied and the resulting differences in TCP and NTCP values are reported.

TCPs with tumour control as the end-point in both NSCLC and NPC and NTCPs with radiation-induced pneumonitis of lung in 3DCRT for conventional and hypo-fractionated treatments are evaluated. In addition the probability of rib fracture in case of hypo-fractionated SABR treatment is also assessed. The TCPs and NTCPs are calculated based on dose distributions derived using commercially available TPS dose calculation algorithms that are presently used in the clinic such as PBC with MB and ETAR heterogeneity corrections, and anisotropic analytical algorithm (AAA) of Eclipse, the PBC with EPL heterogeneity correction and CCC of Oncentra, and the adaptive convolution (AC) and CCC of Pinnacle. All of these algorithms are compared against MC.

MC dose computation system is one of the major tools of this work. The EGSnrc based MC dose calculation engine with the capability of simulating 3D conformal, wedged, IMRT, IMAT treatments has been set up on a parallel computing facility. BEAMnrc and DOSXYZnrc modules of the EGSnrc MC system will be used to model the accelerator head and to perform MC simulations in phantom and patient geometry. The MC accelerator model has been validated against measurements in a homogeneous water phantom by comparing central axis depth doses and beam profiles. Also, absolute dose calibration of the virtual MC accelerator was performed based on the method proposed by Popescu *et al.* [93]. In addition to the validation of the accelerator model in a homogeneous water phantom, gafchromic film measurements were done on a heterogeneous lung phantom in order to verify the performance of our MC model in dealing with inhomogeneities.

Bio-mathematical TCP models use parameters that are derived based on clinical observation. The clinical outcome following a radiotherapy regimen is generally evaluated for a particular end-point of interest such as local tumour control. The parameters that are obtained by fitting the models to data sets may depend on the accuracy of the dose calculation algorithm used. In this study, we calculate Marsden TCP model parameters for NSCLC using data sets that are derived from dose distributions calculated with convolution, convolution-superposition and MC algorithms. These parameters are obtained by fitting them to published tumour control probabilities of four different radiotherapy regimes.

1.3 Thesis outline

In this section a brief outline of the chapters of this thesis is given. Chapter 2 gives a comprehensive overview of photon dose calculation algorithms ranging from convolution, convolution-superposition to MC investigated in this project and different ways in which these photon dose calculation algorithms account for heterogeneities in the patient anatomy.

In chapter 3, a detailed description of the mechanism of cell kill following radiotherapy and the rationale for using radiobiological models to predict prob-

abilities of tumour control and normal tissue complication in order to evaluate the clinical outcome of treatment plans is given. The bio-mathematical models of TCP and NTCP that are used in this project are also elaborated.

This project involves extensive back-ground work to perform MC dose calculation on patient CT data sets for radiation therapy techniques such as conventional, conformal, intensity modulated radiation therapy. MC dose computation is a complex process which includes individual transport of photons and the charged-particles that are generated as a result of photon interactions through the accelerator head and in the geometry of the patient. The steps involved in modelling the accelerator head, MC dose computation in phantom or patient geometry and validation of the MC accelerator beam model against measurements in a homogeneous water phantom and MC dose calculation in a heterogeneous wooden lung phantom compared against gafchromic film measurements are explained in detail in chapters 4 and 5.

Chapter 6 elaborates the influence of photon dose calculation algorithms on the clinical outcome of lung radiation therapy. This study includes the comparison of dosimetrical differences and the clinical outcome of treatments done with various photon dose calculation algorithms in a virtual lung phantom and NSCLC patients in terms of TCPs and NTCPs with local control of the tumour and radiation pneumonitis of normal uninvolved lung, rib fracture as end points respectively. Two different radiation therapy fractionation schemes - 55 Gy in 20 fractions (3DCRT) and 55 Gy in 5 fractions (SABR) are studied and reported. In chatper 7, another tumour site, NPC which is commonly treated using IMRT technique is studied to quantify the differences in predicted local control and normal tissue complication with xerostomia as the end point.

In chapter 8, the influence of photon dose calculation algorithms on the TCP model parameters for NSCLC is explained in detail. Parameters of Marsden TCP model are derived by fitting the DVHs derived from treatment plans calculated with convolution, convolution-superposition and MC algorithms to clinically observed outcome data for three fractionation regimens published in literature and our own clinical experience. The main conclusions derived from this work and suggestions of possible work to be done in the future are given in chapters 9 and

10 respectively.

Chapter 2

Photon Dose Calculation Algorithms

This chapter presents a comprehensive overview of the physics of photon dose calculation algorithms investigated in this study. Seven algorithms of three commercially available TPSs and the basic principles MC based dose calculation algorithm are described which are used for the work done in chapters 6,7 and 8. An additional eighth TPS algorithm is used in the study explained in chapter 8. All of the TPS algorithms investigated in this work are kernel based dose calculations algorithms were proposed in the mid 80s by Chiu and Mohan [94]. Ahnesjö *et al.* [75] conceived a similar kernel based pencil beam convolution algorithm for 3D treatment planning in the early 90s. An energy deposition kernel, also known as a point spread function is the energy deposition by secondary particles around a primary photon interaction site of monoenergetic beam of photons in an infinite homogeneous medium of unit density. The kernels can originate from a point source (photon interaction at a given point) or a pencil beam which are respectively known as point kernel and pencil beam kernel. These kernels have four main components: primary dose, phantom or patient scatter, head scatter and charged-particle contamination and can be obtained either by deconvolving narrow beam distributions or by using MC simulation.

The MC derived photon energy deposition kernels in a homogeneous medium are used as the source for convolution algorithms such as pencil beam convolution algorithms and also for other superior analytical algorithms like CS algorithms

such as collapsed cone convolution and analytical anisotropic algorithm [75, 81–84]. The principles and methods of dose calculation of the convoltion, CS and MC algorithms are given in the following sections.

2.1 Pencil beam convolution algorithm

The PBC algorithm of Eclipse v.10.0[1] involves two main processes in photon dose calculation: beam reconstruction in which calculation is performed in a homogeneous water phantom, patient modelling where correction is done for the irregularities in the patient geometry and tissue inhomogeneities. The photon beam is split into finite pencil beams of dimensions 0.25×0.25 cm^2 perpendicular to the incident beam direction. Then the energy deposited by these beamlets in a homogeneous water medium is calculated by convolution process in five depths. The final dose distribution is obtained by interpolating the doses in the rest of the points. All the beam modifying/shaping devices are accounted for at this stage including jaws, wedges, and MLCs. The pencil beam kernel is derived from measured data as explained by Storchi *et al.* [76–78] which is based on the Milan and Bentley model [95]. The dose is finally corrected for the curvature in the geometry and inhomogeneities using one of the methods given in section 2.1.2. The PBC algorithm of Oncentra v.4.0[2] TPS, uses precalculated pencil beam kernels that are generated by MC simulations. The primary, phantom scatter, head scatter and contaminant charged-particle contributions are accounted for in the total dose distribution.

In addition to the PBC algorithms of Eclipse and Oncentra, the finite-size pencil beam algorithm of Pinnacle TPS (TPB_{Pin}) which is used in the IMRT optimisation process. This algorithm uses precalculated set of mono-energetic pencil beam kernels calculated in a homogeneous water phantom. The spectral variations of the photon beam used is accounted for to form a poly-energetic kernel. It accounts for heterogeneities only in the primary beam direction and ignores its influence on secondary scatter. This algorithm was used only in the NPC study described in chapter 8 as this option is available only for IMRT plans.

[1] Varian medical systems, Palo Alto, USA.
[2] Nucletron, Veenendaal, The Netherlands.

2.1.1 General considerations and dose calculation

The energy deposited is defined by a pencil-beam convolution kernel, K_{PB} that represents the energy distribution released from a pencil beam which is normalised to the fluence at the entry point on the patient surface. The dose deposited at a point P is calculated using a 2D convolution integral given in equation 2.1.

$$\mathrm{D(x,y,z)} = \int\int \frac{\mu}{\rho}\Psi_E(x',y')K_{PB}(x-x',y-y',z)dx'dy' \tag{2.1}$$

Here, Ψ_E*(x',y')* is the energy fluence at the entrance in $\mathrm{J/m^2}$, μ/ρ is the mass attenuation coefficient in $\mathrm{m^2Kg^{-1}}$, K_{PB}*(x-x',y-y',z)* is the kernel calculated at point *P(x,y,z)* for a pencil beam interacting at a point *P'(x',y')* as shown in figure 2.1. The term $\mu/\rho\Psi_E$*(x',y')* represents the total energy released per unit mass (TERMA) in $\mathrm{JKg^{-1}}$ or Gy.

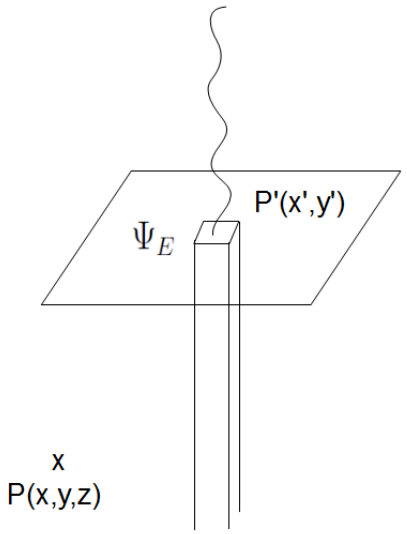

Figure 2.1: A pencil beamlet impinging on the surface of a patient at a point *P'(x',y')* with an energy fluence Ψ_E*(x',y')* at that point. *P(x,y,z)* represents the point of dose calculation.

2.1.2 Inhomogeneity correction methods

The Eclipse TPS employs three inhomogeneity correction methods namely generalised Batho power law (BPL), modified batho power law (MB) and equivalent tissue air ratio (ETAR). In this work, the modified Batho which is an improvement over the generalised BPL and ETAR correction methods are used which are

explained in this section. In case of these two inhomogeneity correction methods dose is calculated in a water-equivalent material and multiplied by the inhomogeneity correction factors defined [96]. On the other hand, the Oncentra TPS has the PBC algorithm which is based on the work done by Ahnesjö *et al.* [75] uses the equivalent path length (EPL) inhomogeneity correction method [97].

Modified Batho (MB)

The inhomogeneity correction factor (ICF) supplied by Batho [98] in the form of a power law function of tissue air ratio (TAR) of the two mediums involved taking into account the thickness and density of both the mediums involved is expressed in equation 2.2.

$$\text{ICF} = \frac{TAR(d_1, W_d)^{\rho_1 - \rho_2}}{TAR(d_2, W_d)^{1-\rho_2}} \tag{2.2}$$

Here, d_1 and d_2 corresponds to the depth within the medium 1 in which dose is to be calculated and distance to the overlying material or medium 2 respectively ρ_1 and ρ_2 are relative electron density of the two mediums and W_d is the field width. El-Hatib and Battista [99] conceived an improved BPL correction formula in which they used tissue maximum ratio (TMR) unlike the original BPL method which uses TAR.

Later, Webb *et al.* [100] proposed a model based on Batho model [98] and Young and Gaylord [101] to account for heterogeneities in patient body. Earlier, effective or radiological depth methods were used in which the radiological depth was calculated by using the physical thickness and density of the materials along the path of the radiation beam. As the name suggests, MB is a modified version of the equation 2.2 proposed by Batho. This was done by Webb and Fox so as to enable CT based inhomogeneity correction and the new correction factor based on TAR/TMR is given in equation 2.3.

$$\text{ICF} = \prod_{m=1}^{m=N} TAR(X_m)^{(\rho_m - \rho_{m-1})/\rho_0} (\mu_{en}/\rho)_N / (\mu_{en}/\rho)_W \tag{2.3}$$

Here, N is the number of layers of different densities above the point of calculation, m is the layer number, x_m is the distance from point of interest to the

surface of the m^{th} layer, ρ_m and ρ_0 are the electron densities of the m^{th} layer and that of water, μ_{en}/ρ is the mass energy absorption coefficient of the material in layer *N*. Thomas [102] has proposed a formula in which the TAR or TMR is calculated by scaling the depth in accordance to the heterogeneous medium.

Equivalent tissue air ratio (ETAR)

Sontag *et al.* [103, 104] conceived a different method to correct for the inhomogeneities in the patient anatomy. This method is based on the density scaling theorem which states that the TAR in a field of radius r at depth d in a uniform medium of density ρ relative to water is to the TAR in a unit density medium for a field size ρr and depth ρd. In other words, the depth and the radius are scaled according to the relative electron density of the heterogeneous medium. The ICF based on the ETAR principle is given in equation 2.4.

$$\text{ICF} = \frac{TAR(\rho d, \rho r)}{TAR(d, r)} \tag{2.4}$$

Equivalent path length (EPL)

The EPL inhomogeneity correction algorithm uses a one-dimensional convolution method which takes into account the heterogeneities along the fan lines of the beam. It does not account for inhomogeneities that are present across or lateral to the beam direction. It rescales the depth of the inhomogeneity by accounting for the density of the medium involved. The heterogeneity correction factor is applied on the primary photon beam kernel and not on the scattered photon kernel. This model calculates the change in the primary energy fluence at the depth of dose calculation due to the presence of heterogeneity [15]. The equivalent path length is calculated as a density averaged depth at the point of calculation at a physical depth z and is given by equation 2.5.

$$\text{z}' = \frac{1}{\rho_w} \int_0^z \rho(z'')dz'' \tag{2.5}$$

Here ρ_w is the density of water and $\rho(z")$ is the density at local depth $z"$

which is calculated from CT images and the dose is corrected by replacing the calculated equivalent path length *z'*.

2.2 Analytical anisotropic algorithm

The AAA of the Eclipse TPS (AAA_{Ecl}) was proposed by Ulmer *et al.* [83] in 2003. It is a 3D convolution/superposition algorithm based on a triple Gaussian convolution model which was preceded by the triple pencil beam model developed in the mid 90s [105, 106]. The primary photons, the scattered extra-focal photons and the electrons are modeled independently. An overview of AAA dose calculation algorithm in heterogeneous media and its validation is reported by Tillikainen *et al.* [107, 108] and Van Esch *et al.* [109] have done an elaborate study on validation of AAA dose calculation algorithm against measurements in homogeneous and heterogeneous cases. This section on AAA_{Ecl} is largely drawn from Tillikainen *et al.* [107, 108] which gives an excellent overview of this model, Van Esch *et al.* [109] and Eclipse algorithms reference guide [96].

The primary photons are modeled using MC simulations and the lateral transport of electrons is represented with six exponential curves [84, 96]. In this multiple source model, the broad clinical photon beam is divided into finite beamlets β, as shown in figure 2.2, where the intensities of the photons and electrons are different.

2.2.1 Primary source

A point source at the level of the target is the primary photon source. The incident electron beam hits the target which results in the production of bremsstrahlung photons. Photons which do not undergo any interactions in the accelerator head until they reach the patient geometry are the primary photons. The primary photon beam spectrum is generated using BEAMnrc MC system [110]. A combination of mean energy radial curve and radial intensity profile are used to account for the beam hardening due to the flattening filter and variation of the photon fluence respectively. Optimisation of these two curves yield correct depth dose curves and beam profiles.

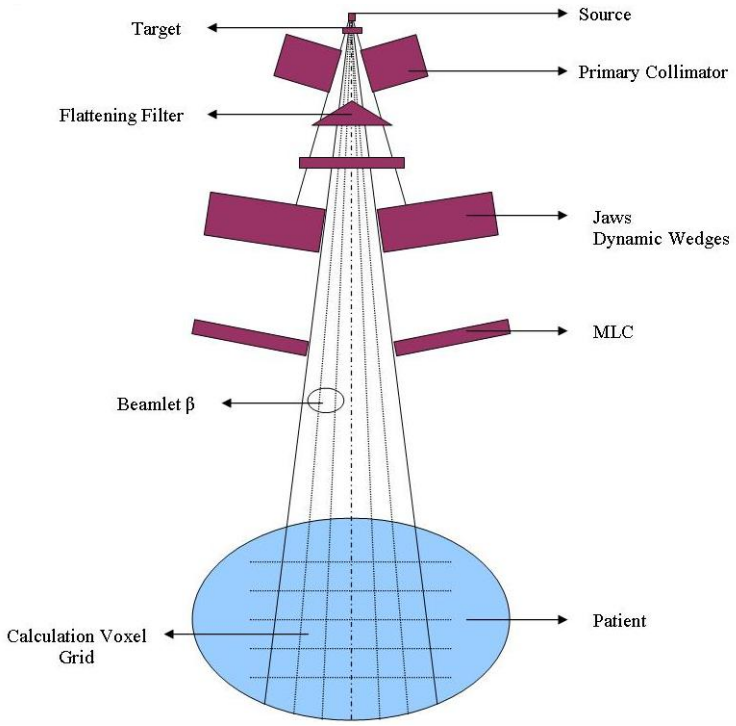

Figure 2.2: Treatment Unit Components modelled by AAA

2.2.2 Extra-focal Source

Secondary photons are generated in the components of the accelerator head which includes the flattening filter, the primary collimator and the secondary jaws. The extra-focal source with a finite width is defined just below the flattening filter and it produces a broader beam than the primary source as it is closer to the machine isocentre. The mean energy and the relative intensity of the extra-focal photon source are derived by convolving the primary fluence and a Gaussian with a width proportional to the finite source.

2.2.3 Electron contamination

Compton interactions in the head of the accelerator and the outside air between the treatment machine head and the patient surface results in the electron contamination. It also accounts for the photon contamination due to electron interactions. It is a finite source located at the plane of the target and is represented as a linear combination of two Gaussians convolved with the primary energy fluence. It is modelled with six exponential functions.

2.2.4 Volumetric dose calculation

The clinical broad beam in divided into small beamlets β and the patient geometry is divided into 3D dose calculation voxels of desirable dimensions to achieve reasonable resolution. Patient CT images are imported and the mean electron density ρ is derived according to the CT machine specific electron density Hounsfield unit calibration curve. The dose calculation grid is divergent and is aligned with the divergence of the photon beam.

Calculation of dose deposited by primary and secondary sources

An energy deposition density function $I_\beta(z,\rho)$ models the attenuation of the photon beam and a scatter kernel $K_\beta(x,y,z)$ defines the lateral photon energy scatter. Each beamlet β is defined individually by the functions I_β and K_β. Both the primary and secondary photons are calculated in a similar method with their respective spectra, position and size of focal spot. The convolution is performed in terms of energy and the energy to dose conversion is done by scaled-water approximation.

The energy distribution from a beamlet β in the homogeneous medium is calculated by the convolving the photon fluence by the energy deposition density function and the scatter kernel.

$$\mathrm{E}_{\mathrm{ph},\beta}(\tilde{\mathrm{X}},\tilde{\mathrm{Y}},\tilde{\mathrm{Z}}) = \Phi_\beta \times I_\beta(z,\rho) \times K_\beta(X,Y,Z) \tag{2.6}$$

Here $(\tilde{X},\tilde{Y},\tilde{Z})$ represents the patient coordinate system and (x,y,z) denotes the beamlet coordinate system. Φ_β is the uniform photon fluence over the cross-section of the beamlet β. $I_\beta(z,\rho)$, the energy deposition function represents the area integral of the energy deposited over the spherical surface of the pencil beam at depth z.

$$\mathrm{I}_\beta(\mathrm{z}) = \int\int h_\beta(t,v,z)dtdv \tag{2.7}$$

where h_β is the poly-energetic pencil beam kernel derived from MC simulations.

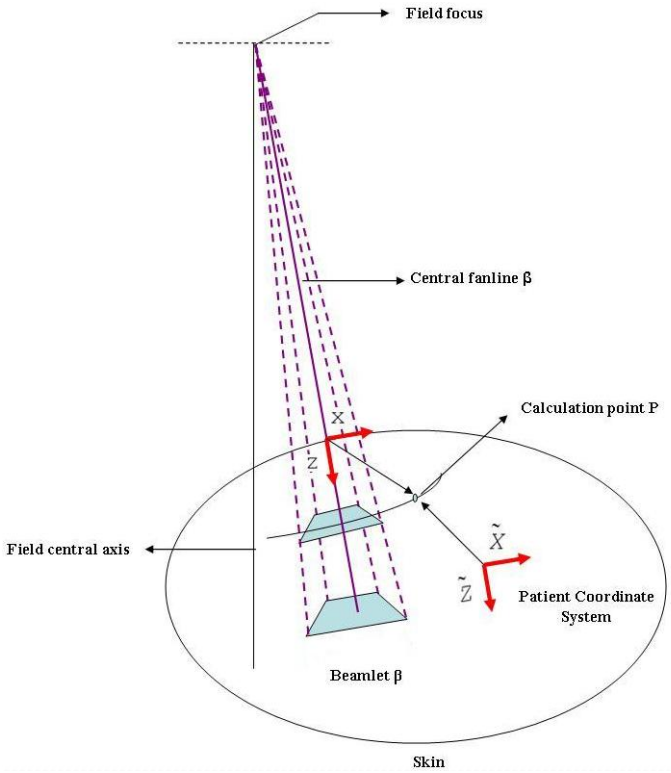

Figure 2.3: Coordinates in Patient Coordinate System and Beamlet Coordinate System on X-Z Plane

2.2.5 Inhomogeneity correction

The inhomogeneities present in the patient model are accounted for by separating them into depth directed and lateral components. The depth directed component accounts for the variation in densities along the axis of the beam whereas the lateral component considers the differences in densities in the direction perpendicular to that of the beam axis or in the radial direction. The heterogeneities in the tissues is accounted by the energy deposition function $I_\beta(z,\rho)$ by radiological scaling which is done by equation 2.8.

$$\mathrm{I}_\beta(\mathrm{z},\rho) = I_\beta(z') \tag{2.8}$$

where the radiological depth is defined in equation 2.9.

$$\mathrm{z}' = \int_0^z \frac{\rho(0,0,t)}{\rho_{water}} dt \tag{2.9}$$

The depth directed component $I_\beta\ (p_z)$ accounts for the total energy deposited by

the pencil beam in a layer, p_z in the phantom as given in equation 2.10.

$$\mathrm{I}_\beta(\mathrm{p_z}) = \Phi_\beta \int\int h_\beta(x, y, p_z) dx dy \tag{2.10}$$

in which the photon fluence or the number of incident photons Φ_β is assumed to be uniform through out the cross section of the beamlet β. On the other hand, the lateral component $k_\beta(\theta,\lambda,p_z)$ is characterised by a weighted sum of six radial exponential functions given in equation 2.11.

$$\mathrm{k}_\beta(\theta, \lambda, \mathrm{p_z}) = \sum_{i=1}^{6} c_i \frac{1}{\mu_i} e^{-\mu_i \lambda} \tag{2.11}$$

2.3 Collapsed cone convolution algorithm

The collapsed cone convolution algorithm (CCC) is a CS algorithm which uses the point spread kernels calculated using EGS code [111]. This algorithm was developed by two different groups at the same time. The CCC of the Pinnacle v.9.0[3] TPS (CCC_{Pin}) was developed by the research group in Madison [112], Wisconsin whereas the CCC of Oncentra TPS (CCC_{Onc}) was developed by Ahnesjö, Stockholm [81]. Another faster version of a CS algorithm in Pinnacle known as AC_{Pin} is also investigated in this work which changes the resolution of the dose calculation grid adaptively according to the curvature of TERMA [112]. The principle behind both the CCC algorithms are very similar although there are certain differences in the implementation of the algorithms which are given in section 2.3.1.

Both the CCC algorithms use precalculated monoenergetic photon energy deposition kernels calculated in a homogeneous water medium for photon energies of therapeutic relevance and applies a kernel scaling to account for inhomogeneities in the patient anatomy. The dose distribution of a polyenergetic photon beam is calculated by accounting for each of the monoenergetic component energy of the spectrum separately. Another way of obtaining the dose distribution of a polyenergetic photon beam would be to convolve a polyenergetic kernel with the corresponding polyenergetic TERMA. Both CCC_{Pin} and CCC_{Onc} have been

[3]Philips Healthcare, Andover, MA, USA.

studied extensively by various research groups [82, 113–116].

2.3.1 General principles of the model

This is a point kernel photon energy dose deposition model that uses convolution-superposition principle in order to calculate the dose distribution in a medium. This is done by convolving the TERMA with a spatially invariant kernel of a monoenergetic photon beam three dimensionally. The convolution kernel of a monoenergetic beam is spatially invariant as the energy of the primary beam remains constant throughout the phantom whereas the kernel of a polyenergetic beam is spatially variant owing to its nature of beam hardening with depth.

The generic equation to calculate dose delivered by a monoenergetic beam in a voxel of a homogeneous phantom is given by equation 2.12.

$$\mathrm{D(x,y,z)} = \int\int\int \frac{\mu}{\rho}\Psi(x',y',z')K(x-x',y-y',z-z')dV' \tag{2.12}$$

Here, *D(x,y,z)* is the dose deposited in a voxel, μ/ρ is the mass attenuation coefficient in $\mathrm{m^2Kg^{-1}}$, Ψ *(x',y',z')* is the energy fluence at the point *P'* in $\mathrm{J/m^2}$ and *K(x-x', y-y', z-z')* is the photon energy deposition point kernel which is derived using MC calculations. The energy deposition kernel represents the fraction of energy deposited at point P from the charged particles that are produced due to interaction of primary photons at point *P'*. The TERMA is calculated by multiplying the mass energy absorption coefficient with the energy fluence.

The physics concepts of CCC_{Pin} and CCC_{Onc} are very similar but they differ in certain aspects. The TERMA is calculated as a single component by CCC_{Pin} whereas in case of CCC_{Onc} it is separated as primary and scatter components. The CCC algorithm represents the point spread function or the point photon energy deposition kernel in the form of set of cones extending from a point which deposits energy in the medium by collapsing it along a line in a phantom or patient medium. Ahnesjö *et al.* [81] have represented these cones in the form of a lattice structure which covers $3\times3\times3$ $\mathrm{cm^3}$ calculation voxels with 26 discrete cone directions. The polyenergetic kernels are calculated as weighted sum of the monoenergetic kernels with respect to the composition of the photon energy spectrum.

2.3.2 Energy fluence and TERMA

The point spread function or the point photon energy deposition kernel is calculated using EGS MC code as explained by Ahnesjö *et al.* [117] and Mackie *et al.* [111]. They have suggested using an analytical function to derive the precalculated kernels which is given in equation 2.13.

$$\mathrm{K(r)} = \frac{A_\theta e^{-a_\theta} + B_\theta e^{-b_\theta}}{r^2} \tag{2.13}$$

Monoenergetic photons are forced to interact at the voxel present in the origin of a homogeneous phantom. The primary and scatter kernels are calculated either as two separate components or together. The kernels are calculated for all the energy components of the spectrum and a weighted sum of all the kernels is done to get the polyenergetic dose deposition kernel.

The energy fluence, sum of the energies of the photons entering a unit volume is uniform within the field aperture and falls along the edges with a minimal value outside the field. The primary energy fluence entering a patient body is comprised of the bremsstrahlung photons from the tungsten target and extrafocal radiation arising from the flattening filter, collimators and the accelerator head. Ahnesjö *et al.* [74] have shown that energy fluence can essentially be calculated practically in three steps. The first step is to reconstruct a dose matrix in Cartesian coordinates from beam profile measurements and the next step is to obtain the energy deposition kernel for the same coordinates and then the final step is to deconvolve both to get the energy fluence.

The TERMA component is calculated by multiplying the energy fluence with the mass energy absorption coefficient corresponding to the energy component of the spectrum and the interacting medium. The beam divergence is an important factor that has to be accounted for by tilting the point photon energy deposition kernels with respect to the distance from the source and the angle of divergence.

2.3.3 Kernel scaling to account for inhomogeneities

The final step is to account for inhomogeneities in the phantom or patient anatomy in which the dose calculation is done. The TERMA and the energy deposition

kernels are calculated for a homogeneous water phantom of unit density. Both the TERMA and the energy deposition kernel have to be rescaled to correct for inhomogeneities that are present. The rescaling is done in all directions by applying the inverse of the density. The energy deposition kernels that are calculated in a homogeneous water phantom are spatially invariant but when there are inhomogeneities in the phantom, the energy deposition kernels are not spatially invariant anymore. In order to account for the inhomogeneities, in addition to convolution, superposition principle is used. The accuracy of the CCC algorithm depends if density scaling is done for both TERMA and the kernel, TERMA or kernel, and none of the two [118].

2.4 Monte Carlo algorithm

MC dose calculation plays a major role in radiotherapy treatment planning [119]. Analytical dose calculation algorithms such as convolution and CS algorithms that are routinely being used in the clinic are based on MC derived photon energy deposition kernels or point spread functions. Out of these two classes of algorithms, CS algorithms are proven to be far more accurate than simple convolution based algorithms. Although they perform well in certain situations (eg. lung) they still have shortcomings in dealing with heterogeneities like nasal sinuses and bone [80, 120]. Full MC dose computation is proven to be superior than any other analytical dose calculation algorithm due to its ability to transport radiation through matter by accounting for all the physical interactions that take place. It requires enormous computational power and long computing hours have held back the usage of MC for routine treatment planning as it transports all the particles. A detailed description of setting up a MC code for external beam radiotherapy dose computation in explained in detail in chapter 4. In this section, a comprehensive overview of the basic physics of MC radiation transport is given in detail.

2.4.1 Steps involved in MC transport

The MC simulation is stochastic in nature and randomly chooses the type of interaction which is a function of photon energy and the interaction coefficient of the medium. Number of steps are involved in MC radiation transport which are listed below. A comprehensive overview of steps involved in MC photon transport is given by Raeside [121, 122]. The photons undergo one of the four major interactions namely Raleigh scattering, photo electric effect, Compton scattering and pair or triplet production.

1. The energy and direction of the incident photon is chosen.

2. The distance to interaction, x is determined and the photon is transported to this point of interaction. The distance to interaction is chosen randomly by solving the probability density function equation 2.14. Here, μ is the attenuation coefficient in cm^2g^{-1} and r is a uniformly distributed random number between 0 and 1.

$$\mathrm{x} = -\frac{1}{\mu} log_e(1-r) \tag{2.14}$$

3. The type of interaction that takes places at the point of interaction is determined by generating a second random number. The interaction could be Raleigh scattering, photoelectric effect, Compton scattering or pair production depending upon the incident photon energy.

4. The direction, kinetic energy of the particles that are produced due to the photon interaction with the medium are determined by sampling from the cross-sectional coefficients of these interactions in the medium of interest. The Compton cross-section is defined by Klein-Nishina [123].

5. The photon is transported in the same way until it leaves the geometry of interest or when its kinetic energy falls below a preset cut off energy.

6. The charged-particles eg. electrons that are produced in step 3 and 4 are transported until they leave the geometry or when their kinetic energy falls below a preset cut off energy. Other particles such as bremsstrahlung photons, auger electrons are also transported.

7. The energy deposition in the medium is scored in voxels or region of interest.

8. The steps 1-7 are repeated for many number of incident photons.

Electrons undergo interactions either with the atomic nuclei or atomic orbital electrons. These interactions may involve collision or scattering which may be either elastic or inelastic in nature. As the electrons are charged-particles which have a negative charge, they undergo numerous interactions before they lose all their kinetic energy. They undergo multiple scattering with the atomic nuclei or atomic orbital electrons in the form of elastic and inelastic collisions. The type of electron interaction depends upon the radius of the atom from the centre of the nucleus to the outer orbital and the distance of the electron trajectory from the centre of the nucleus. When the former is greater than the latter, the electron undergoes a soft collision where there is no energy loss, if both are fairly equal the electron undergoes a hard collision with the orbital electron where there is energy loss and scattering, when the latter is larger than the former, the electron is close to the vicinity of the field of the nucleus which results in bremsstrahlung or "braking" radiation.

The electron interactions are far more difficult to track than the photon interactions as the number of interactions an electron undergoes is far higher than a photon. Berger [124] conceived a technique known as condensed history method (CHM) or electron transport. The electrons although they undergo multiple interactions, the number of interactions that result in considerable energy loss and scattering is feeble. Therefore, these events that do not cause dramatic differences are combined together as cumulative events. The energy loss is calculated by means of continuous slowing down approximation (CSDA) method by accounting for the stopping power of the electrons [125, 126].

2.4.2 A MC photon transport code written in MATLAB

An inhouse MC photon transport code called Clatterbridge Monte Carlo code (CMCC) was written in MATLAB v.7.6.0 R2008a (MathWorks, Natick, MA, USA) in order to understand the underlying physics of MC radiation transport. Only photons were transported in a semi infinite water phantom and the charged

particles that were produced as a result of photon interactions were considered to deposit their energy at the site of interaction. The charged particle transport was not modelled due to the complexity involved and to avoid long computational time. The results of the CMCC are presented in this section. A number of quantities were calculated using this code.

Figure 2.4 shows the relative importance of various photon interactions in water as a function of photon energy in MeV. The average fraction of energy transferred to the recoil electrons in Compton effect is shown in figure 2.5.

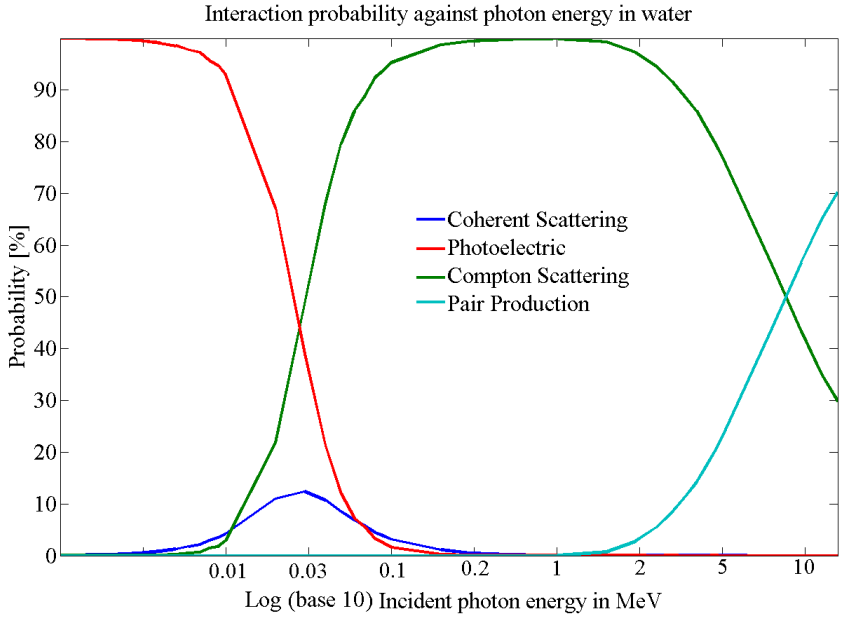

Figure 2.4: Variation of interaction probability of Raleigh scattering, photoelectric effect, Compton scattering and pair production with photon energy in water (photon energy expressed as logbase10 along the x-axis and percentage probability of each type of interaction

The probability of photons with kinetic energy less than 30 keV are higher and then probability falls for energies between 30 keV and 100 keV after which the probability of Compton interaction starts to increase. Also, figure 2.6 shows the average number of interaction a photon undergoes in a homogeneous water medium until it is totally absorbed. It is evident from the figure that the number of interactions a photon undergoes increases with increasing photon energy and it reaches its maximum very close to the photon energy when pair production kicks off and thereby it starts falling.

The percentage depth kerma curve of photons of energy 1 MeV and 10 MeV

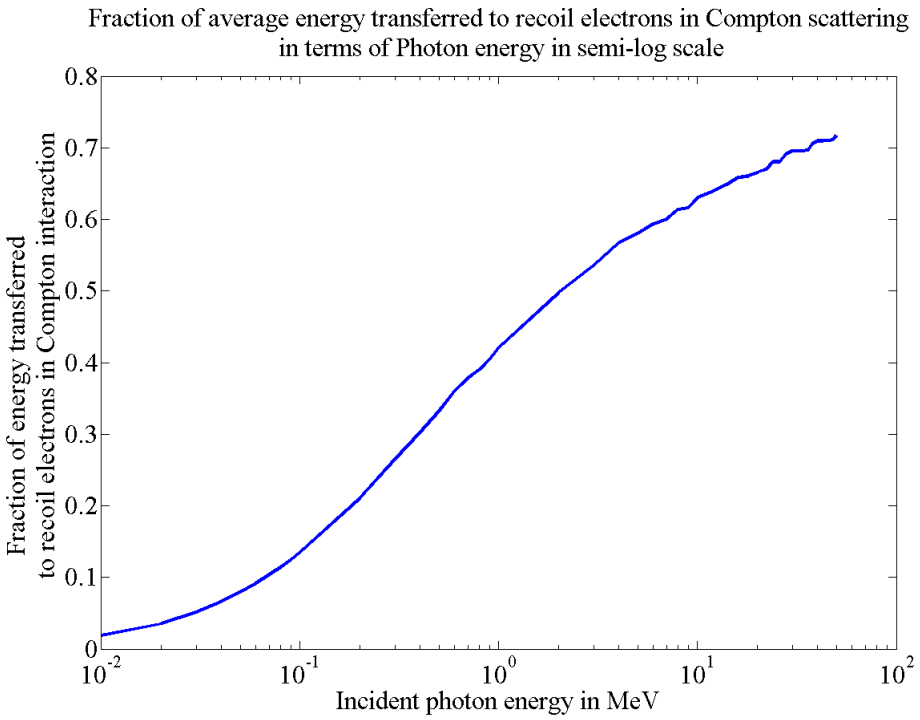

Figure 2.5: Fraction of average energy transferred to recoil electrons in Compton scattering in terms of Photon energy in semi-log scale

which was obtained by CMCC and PENELOPE without transporting the charged-particles in a homogeneous water phantom. 10^5 photon histories were used in both the cases and the percentage depth kerma curves of 1 MeV and 10 MeV photons are shown in figures 2.7 and 2.8 respectively.

2.4.3 Sources, phantoms and their geometries

Monoenergetic electron, photon sources and bremsstrahlung photon spectra of linear accelerators, and Co-60 external radiotherapy source can be modelled using MC for plane parallel beams and point diverging beams. The phantoms are defined as homogeneous or heterogeneous volumes of one or more materials and also in the form of materials and material densities derived from DICOM CT data sets in order to do dose calculation in patient anatomy. The interaction cross-section data of the materials defined in the phantom and the energy of the incident particles are the two main factors which decide on the distance to interaction, type of interaction, angle and energies of the scattered and newly generated particles. Figures 2.9 and 2.10 show the uniform planar distribution

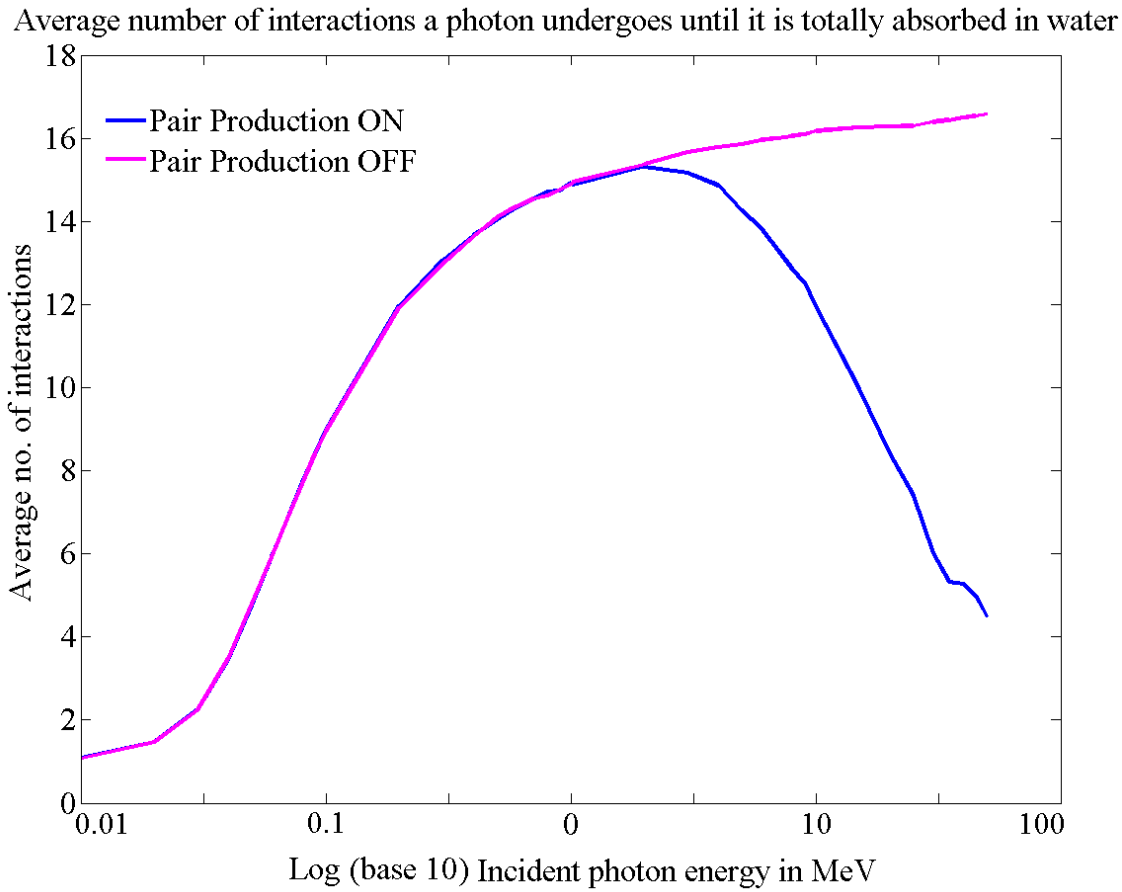

Figure 2.6: Average number of interaction a photon undergoes until it is totally absorbed in water with pair production ON and OFF

of photons in a circular field of radius 5 cm and a square field of side 10 cm simulated by the CMCC respectively.

2.4.4 Statistical uncertainties

MC based dose computation, owing to its stochastic nature is always associated with statistical uncertainties. Various steps or physical processes involved in MC radiation transport are randomly chosen by generating a random number which falls between intervals calculated based on the interaction cross-sections for a particular photon energy in a certain material. Histories of billions of photons or electrons are required in order to keep the statistical uncertainty associated with energy deposition within acceptable tolerances. Figure 2.11 shows the influence of statistical uncertainties on dose calculation of 6 MV photon beam of square field of

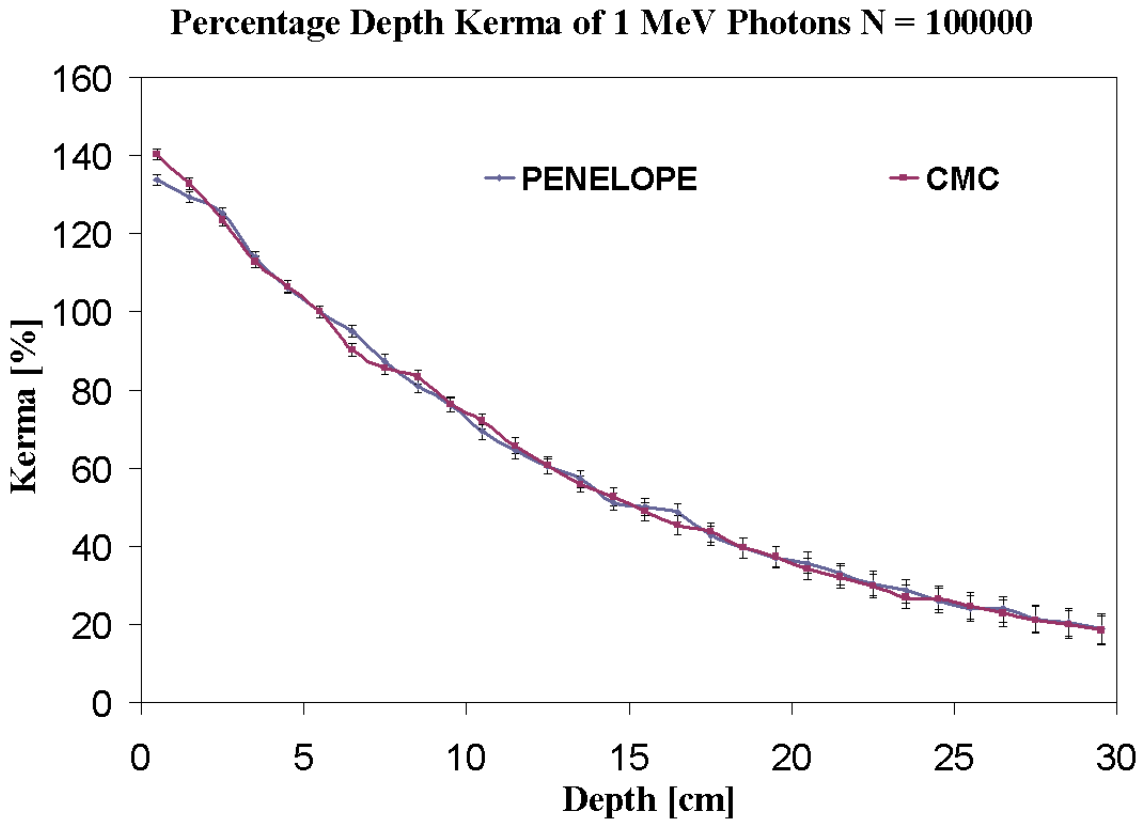

Figure 2.7: Percentage depth kerma curve of 1 MeV photons N=100000 normalised at 5 cm depth.

side 10 cm in a water phantom. The depth kerma curved calculated with CMCC and PENELOPE with 10^5 photon histories have large statistical fluctuations whereas when the same simulation was repeated with 1 billion histories using PENELOPE, it resulted in a smoother percentage depth curve with statistical uncertainties within 1%.

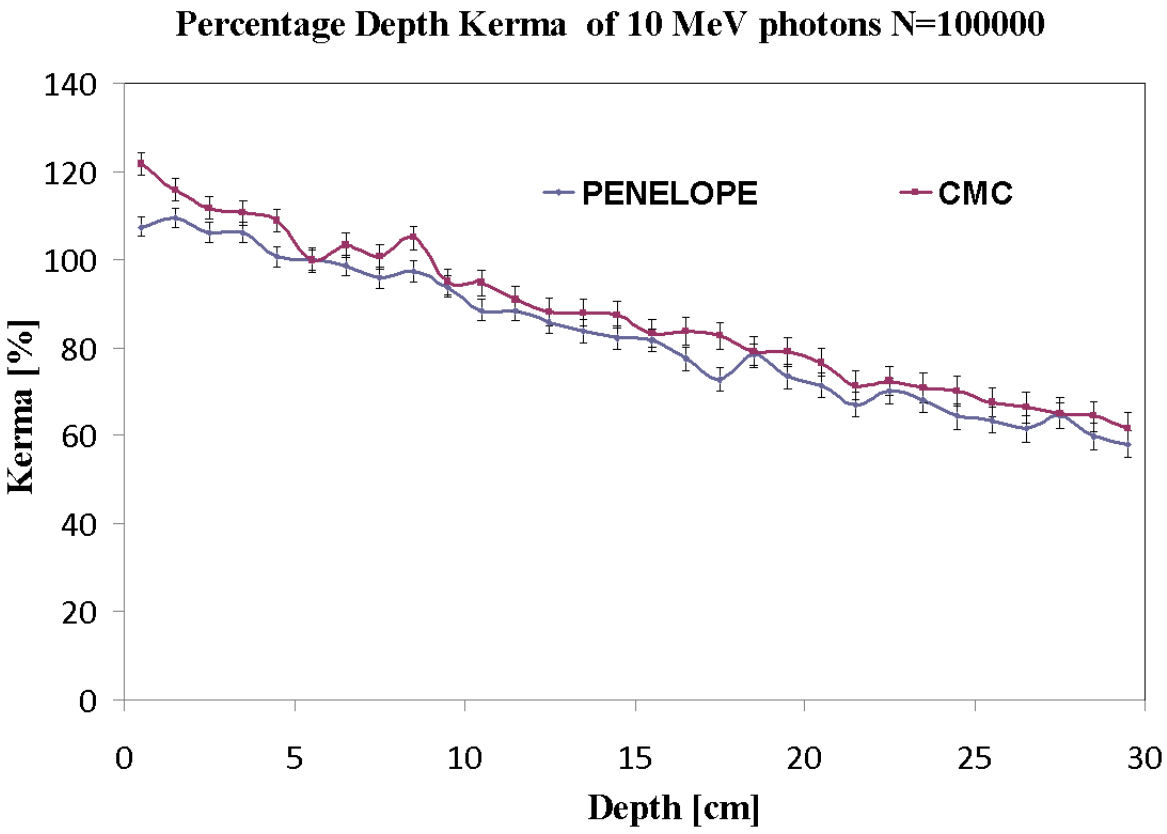

Figure 2.8: Percentage depth kerma curve of 10 MeV photons N=100000 normalised at 5 cm depth.

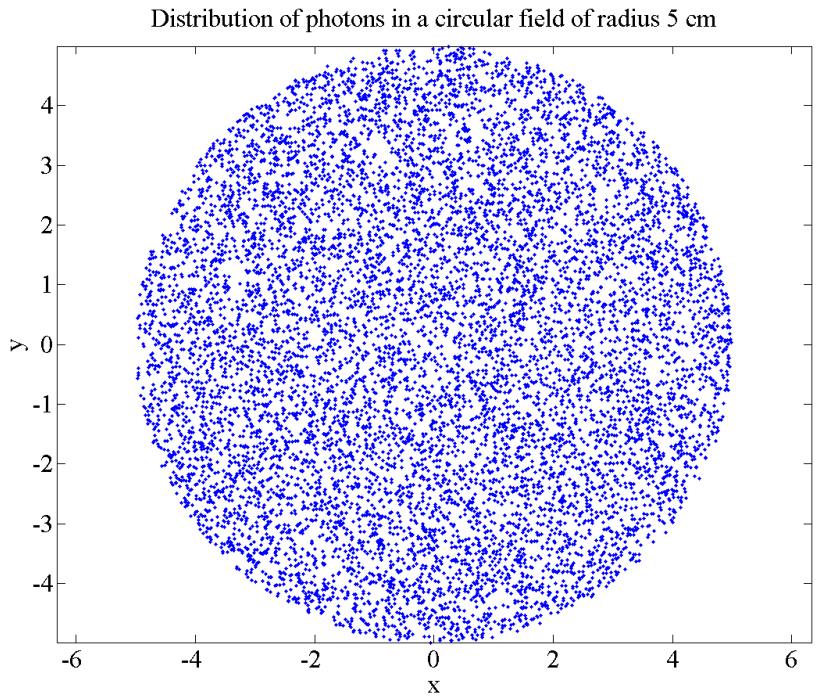

Figure 2.9: Distribution of photons in a circular field of radius 5 cm

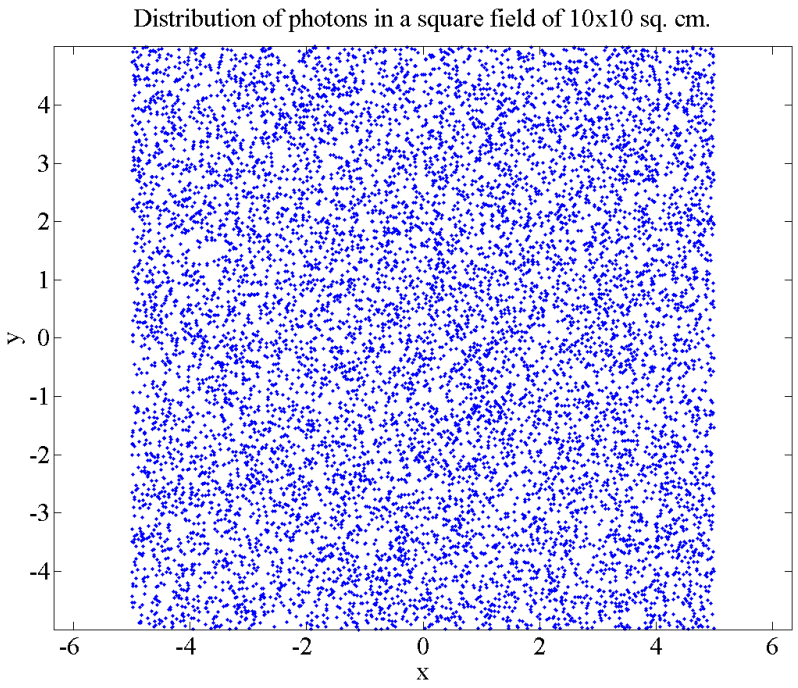

Figure 2.10: Distribution of photons in a square field of side 10 cm

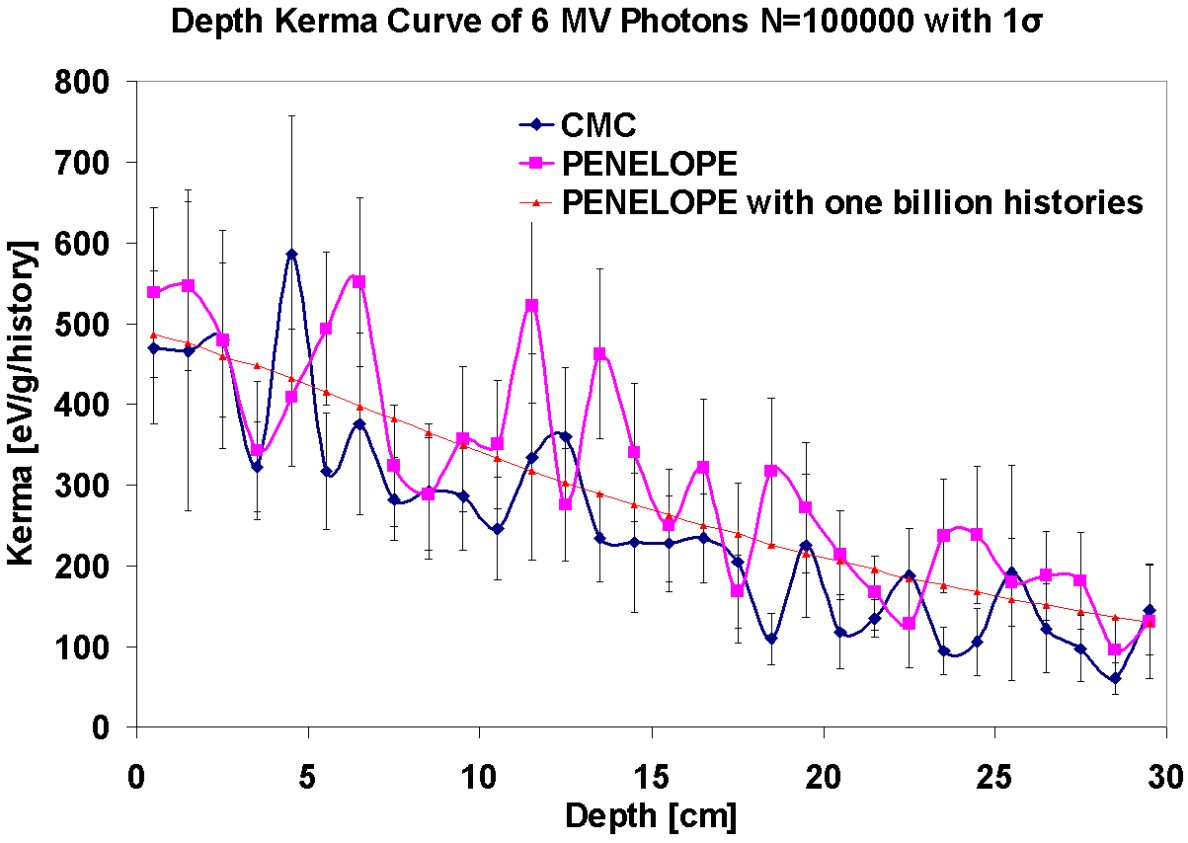

Figure 2.11: Depth kerma curve of 6 MV photons N=100000

Chapter 3

Radiobiological models of Tumour Control Probability and Normal Tissue Complication Probability

Our knowledge base on the effect of damage caused by ionizing radiation on cells have widened enormously over the past few decades. Many aspects on the basis of radiation damage such as the nature of damage caused, cell repair mechanisms, temporal dependence, and sensitivity of cell cycle have been studied extensively. These studies enabled the scientific community to build bio-mathematical models of cell kill which are used to predict the probability of local control with the addition of empirical aspects of normal tissue complication. These models can now be used for evaluation as well as for designing treatment modalities. This chapter presents an overview of the bio-chemical and mathematical concepts which form the core of these models, how they work and their limitations.

3.1 Mechanism of cell kill

The mechanism of cell damage by ionising radiation is a complex process which can be broken down into two main components: direct and indirect damage. Indirect damages are those that are caused by radiolysis of water (which constitutes

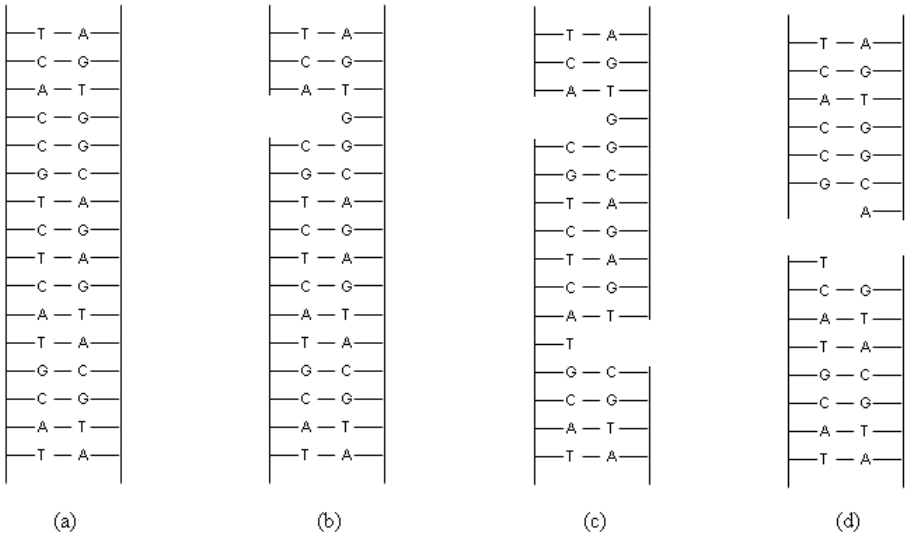

Figure 3.1: DNA structure and strand breaks (a) normal DNA with sugar and phosphate back bone and sequence of AT-GC base pairs (b) single strand break (c) two single strand breaks far apart (d) double strand break. The single strand breaks are easily repairable unlike double strand breaks. The double strand breaks mostly result in a lethal damage (reproduced from Hall, 2000).

about 80% of the weight content of cells) leading to the production of highly unstable free radicals such as reactive oxygen species and charged particles. The resulting molecules in turn will interact chemically and oxidise the cell membrane, proteins, enzymes and deoxyribonucleic acid (DNA). Ionising radiation can also directly interact with cell components by breaking chemical bonds by means of transferring kinetic energy of charged-particles. In case of both direct and indirect interactions that lead to cell kill, the damage caused to a DNA molecule is the most critical aspect owing to its crucial role in the development and functioning of living species.

DNA has a complex double helical structure which consists of a sugar and phosphate back bone with two different base pairs which are arranged in a specific sequence. Damages can be caused in the form of single strand breaks (SSBs) or double strand breaks (DSBs) as shown in figure 3.1 [127]. The SBSs are easier to repair whereas the DSBs have a more complex repair mechanism and are prone to mis-repair which in turn could result in mutation. All damages that are caused to a cell by ionising radiation are not lethal.

Three types of damages are caused to cells: lethal, sublethal and potentially

lethal damage in decreasing order of severity. The lethal damages is deterministic or non-stochastic in nature whereas the sublethal and potentially lethal damage is stochastic or random. Lethal damage is irreparable or irreversible and results in immediate death of the cell. Sublethal damage might become lethal when it is in proximity to yet another sublethal damage, but singly they have the capability to repair themselves. Potentially lethal damages are those which can be repaired under certain conditions such as the cell cycle phase they were in when the damage was caused or if they were left longer to recover before inducing additional damage. They would potentially result in a lethal event if not repaired.

3.2 Rationale for using radiobiological models

Radiation results in cell killing, both tumour and normal cells are killed following radiotherapy. The objective of radiotherapy as mentioned earlier is to kill just the tumour cells and spare any normal cells around the tumour in the beam path. Radiotherapy dose delivery is measured in terms of absorbed dose which is a physical quantity which does not give direct information about the probability of controlling the disease. The radiobiological models enable us to understand the outcome of a radiotherapy treatment by predicting the biological response. It has been proven that the dose-response curve exhibits a sigmoidal relationship as shown in figure 3.2 and in order to have a high therapeutic gain it is necessary to maximise the TCP while minimising the NTCP [16–22]. It is not possible to generalise the outcome of radiotherapy as the behavioural response of different cells are different. Some cells are inherently radiosensitive whereas others are not, there is also evidence of variation in inter patient radiosensitivity. In addition all the cells in a tumour do not respond the same way, other factors like hypoxia play a major role in tumour control. The mechanism of cell kill and hence the accurate prediction of the probability of controlling a tumour and complication to normal tissues is highly complex in nature.

Radiobiological models are bio-mathematical models that are used to predict the outcome of radiotherapy. Some models are empirical whereas others are mechanistic, the difference and advantages of each of these models are explained

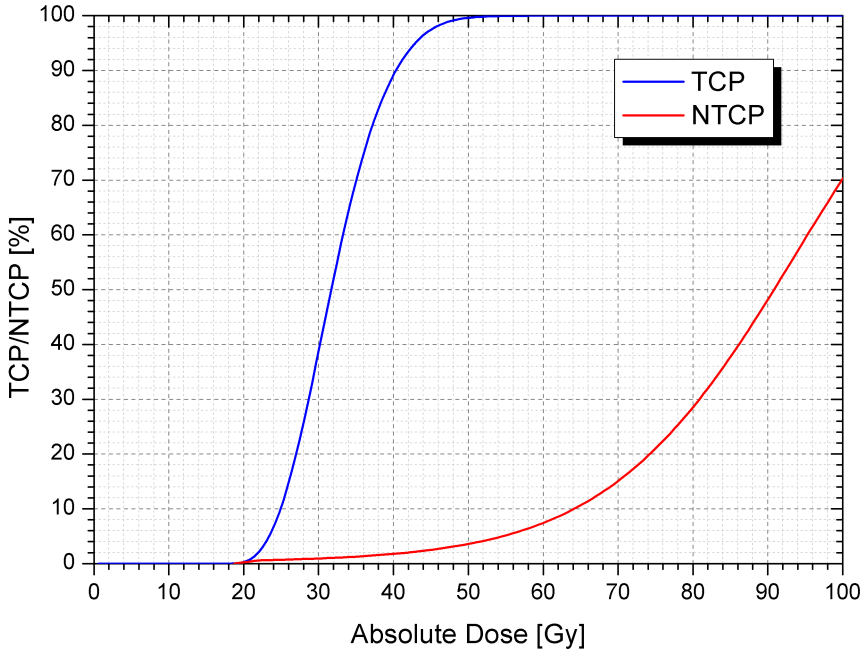

Figure 3.2: TCP and NTCP curves plotted against absolute dose in Gy. Both the dose-response curves exhibit a sigmoidal relationship with the absolute dose. To obtain a large therapeutic ratio it is essential to keep these curves far apart.

in section 3.3.

3.3 Empirical and mechanistic models

Radiobiological models are used to predict the clinical outcome following a radiotherapy regimen. This involves assessing the probabilities of controlling the tumour and complications caused to normal tissues. Various empirical and mechanistic models are used for TCP and NTCP modelling. The empirical models use experimental or clinically observed data whereas mechanistic models take into account the underlying physical and bio-chemical processes involved in inducing radiation damage. Also, the empirical models contain parameters that have no or little relation to relevant mechanisms, e.g. slope of a TCP curve. On the other hand, a mechanistic model may enable one to predict the way the slope changes for a constant fraction size or fraction number. The empirical models have the advantage of possibility to use them readily whereas the mechanistic models are more complex and their development in still in infancy.

Nominal standard dose (NSD) proposed by Ellis [128] is an example of an em-

pirical model which establishes a power law relationship between dose, time and number of fractions to predict a biological effect. Linear-quadratic (LQ) model is partly a mechanistic model which is used to calculate the surviving fraction (SF) of cells following irradiation. LQ model has a mechanistic interpretation as it incorporates lethal and sub-lethal events caused by dose D.

Although mechanistic models are preferred over empirical models to predict the clinical outcome due to their insight in actually modelling the radiation induced damage, the complexity of these models have held them back from routine use in practical applications. Some models are quasi-mechanistic, for example the Marsden model [27, 31, 32] is partly mechanistic and partly empirical as it calculates the surviving fraction of cells based on the LQ model whereas the model parameters are derived from clinical observations.

3.4 Dose volume histograms

DVHs which provide information about the dose volume relationship of tumour and other OARs and are often used in evaluating treatment plans. Two types of DVHs namely differential and cumulative DVHs are used; the former is a graphical representation of summed volume elements of a particular organ of interest that receives dose within a certain dose range against equal dose intervals. The latter represents the volume, usually expressed as a percentage of the total organ volume, receiving a dose greater than or equal to a specified dose. The differential and cumulative DVHs as shown in figures 3.3(a) and 3.3(b) can be plotted either in absolute or relative units of dose and volume, depending upon the purpose of evaluation. The best plan out of rival treatment plans is chosen by comparing DVHs; generally cumulative DVHs are used in the clinic. The DVHs specify the percentage prescribed dose received by percentage volume of tumour and OARs. Treatment plans are generally approved when the tumour and OARs receive an acceptable dose with reference to the tolerance limits specific to the protocols followed in the clinic.

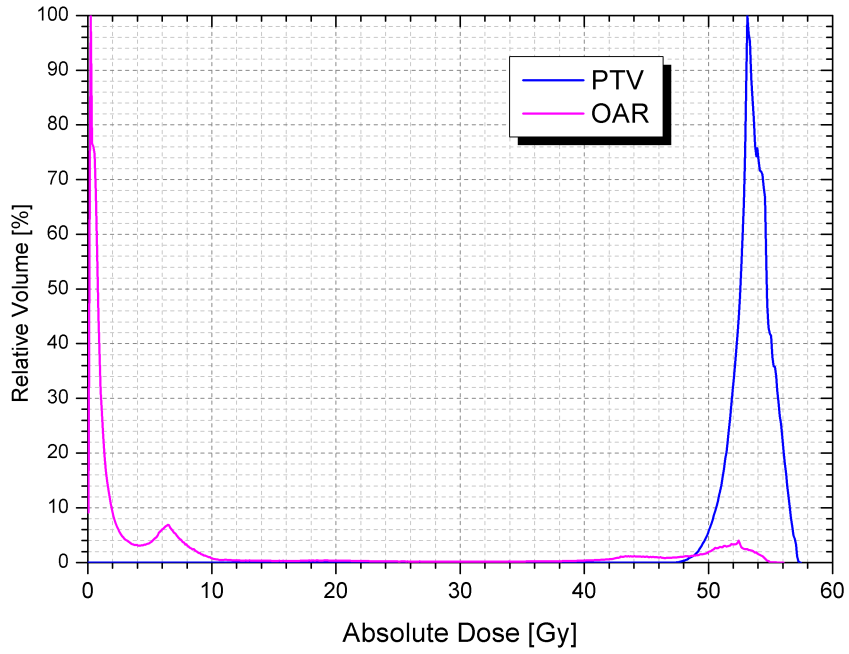

(a)

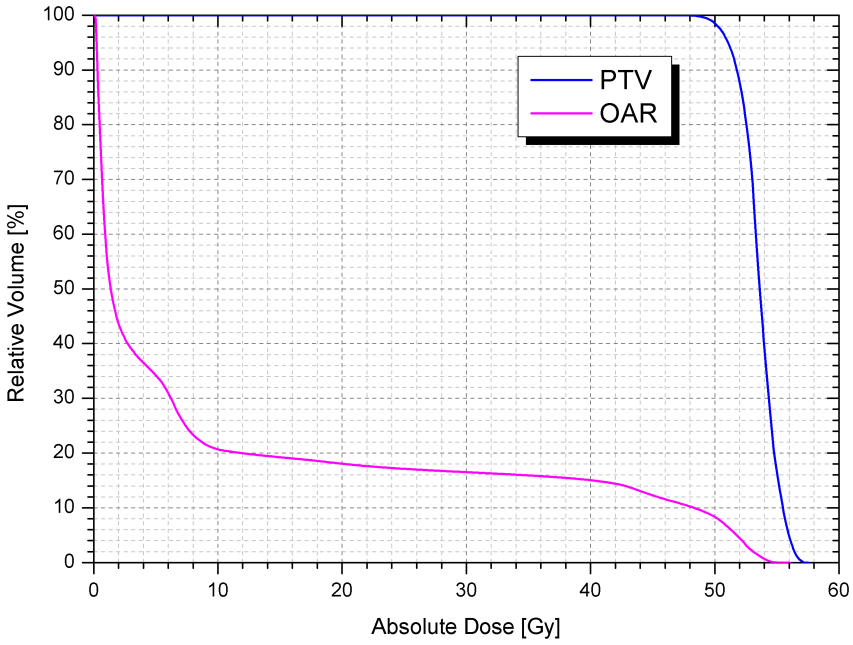

(b)

Figure 3.3: (a) Differential (b) Cumulative DVHs of PTV and OAR expressed in terms of absolute dose and relative volume.

3.5 Tumour Control Probability (TCP)

3.5.1 Marsden TCP model

The Marsden TCP model developed by Nahum-Tait [31], Webb and Nahum [27] and Nahum and Sanchez-Nieto [32] is a quasi-mechanistic model based on LQ model of cell killing and Poisson statistics. In this model, the surviving fraction of cells after radiotherapy is expressed as a function of dose, characterised by two parameters α and β which are related to the initial slope and curvature of the cell survival curve. The surviving fraction of cells after uniform irradiation with dose D is given by equation 3.1.

$$\mathrm{SF} = \frac{N_s}{N_0} = exp(-\alpha D - \beta D^2) \tag{3.1}$$

The parameters α and β are proportional to the dose and square of the dose respectively and hence the name linear-quadratic model [129]. The number of cells surviving after irradiation of all the fractions is calculated by the formula given in equation 3.2.

$$\mathrm{N_s} = N_0 exp\bigg[- \alpha D \bigg(1 + \frac{\beta}{\alpha} d \bigg) \bigg] \tag{3.2}$$

where N_s is the number of cells that survive after irradiation, N_0 is the initial number of clonogenic cells, α is the cell radiosensitivity, $D{=}nd$ in which n is the number of fractions, D is the total dose, d is the dose per fraction.

The Marsden model employs Poisson statistics given in equation 3.3 is used to calculate TCP. The Poisson equation gives the probability P of occurrence of exactly Y events when the mean number of events is N.

$$\mathrm{P(N, y)} = \frac{e^{-N} N^y}{y!} \tag{3.3}$$

$$\mathrm{TCP} = \frac{1}{\sigma_\alpha \sqrt{2\pi}} \int_0^\infty \bigg(\prod_i exp\bigg[\rho_{cl} V_i exp\bigg\{ - \alpha D_i \bigg(1 + \frac{\beta}{\alpha} d_i \bigg) \bigg\} \bigg] \bigg) exp[-(\alpha - \bar{\alpha})^2 / 2\sigma^2] d\alpha \tag{3.4}$$

In equation 3.4, i is the number of dose bins in the DVH, D_i is the total dose in bin i in Gy, d is the dose per fraction in Gy, α and β are the clonogenic

radiosensitivities in the LQ expression, $\bar{\alpha}$ is the mean of the radiosensitivity within the patient population, σ_α is the distribution of radiosensitivity over the patient population, ρ_{cl} is the clonogenic cell density in clonogens/cm^3. Another term $\gamma(T\text{-}T_k)$ is sometimes included in the square brackets of equation 3.4 to account for proliferation or repopulation of the tumour cells over the treatment period; this is valid only when $T > T_k$. Here, $\gamma = ln\ 2/T_d$, T_d is the average doubling time, T is the overall treatment time, T_k is the time at which proliferation or repopulation starts. V_i is the volume of the GTV corresponding to the dose bin d_i in the GTV, D_i of the ith dose voxel and is derived from the dDVHs of the GTVs.

3.5.2 Marsden TCP model parameters

NSCLC with tumour local control as the end point

The parameters for the Marsden TCP model were derived by Nahum *et al.* [130] by fitting data sets to clinically observed tumour control data for four radiotherapy regimens. The Marsden TCP model is characterised by six main parameters (see equation 3.4) out of which the mean radiosensitivity $\bar{\alpha}$ and distribution of radiosensitivity over a population of patients σ_α, delay before repopulation T_k, doubling time T_d were obtained by fitting. The clonogenic cell density ρ_{cl} and α/β ratio were kept constant. These parameters were derived by fitting to the Marsden quasi-mechanistic LQ and population based model using DVH data sets to clinical outcome data of the control and trial arms of the study done on continuous hyper accelerated radiation therapy (CHART) by Mount Vernon Cancer Centre published by Saunders *et al.* [131], our own clinical experience at Clatterbridge Cancer Centre and UMCC data of the work published by Martel *et al.* [37]. The clinically observed tumour control probabilities reported in these studies were 12%, 18%, 35% and 43% respectively. The parameters and their values used in this study are shown in table 3.1.

NSCLC SABR with tumour local control as the end point

SABR treatments are known for their high local control. Timmerman *et al.* [132]

have reported clinically observed TCPs (with an end point of 3 year primary tumour control) as high as 97.6% in patients with early stage medically inoperable non-small cell tumours measuring less than 5 cm diameter treated with hypofractionated doses of 18 Gy in 3 fractions. However, the validity of the LQ model is in doubt when large doses per fraction are delivered. It is suggested that LQ model fails at larger dose per fraction and the cell survival curve tends to straighten out at daily doses larger than 7 Gy exhibiting a linear-quadratic-linear (LQL) relationship. Guerrero and Li [133] proposed a method to extend the LQ model for large fraction doses such as those delivered in SABR treatments. Carlone *et al.* [134] suggested a way to derive the Guerrero and Li LQL model mechanistically. Alternatively, Fowler [135] has suggested an α/β value of 20 Gy instead of 10 Gy for NSCLC tumours.

In our study, we derived a separate TCP parameter set for NSCLC SABR treatments in order to address the issue of validity of the LQ model in large dose per fractions. We propose to use a lower $\bar{\alpha}$ value instead of using a higher α/β ratio (greater than 20 Gy). In order to do this, $\bar{\alpha}$ and σ_α values were lowered by keeping the same $\bar{\alpha}$ to σ_α ratio of NSCLC TCP parameter sets derived by Nahum *et al.* until the TCP value calculated using a SABR DVH dropped to around 90% from the highest 100%. The rest of the Marsden TCP model parameters were kept the same as the original. The new $\bar{\alpha}$ to σ_α values are 0.14 Gy^{-1} and 0.017 Gy^{-1} respectively which are used to estimate the TCPs of SABR NSCLC patient plans as reported in chapter 6.

NPC with tumour local control as the end point

The Marsden model parameter set for NPC derived by Selvaraj *et al.* [136] is used to predict the TCPs reported in chapter 7. The mean radiosensitivity, $\bar{\alpha}$ and variation in the radiosensitivity in a patient population, σ_α were obtained by adjusting these two parameters iteratively to match the γ_{50} value of 2.8 reported by Steel [137] for NPC. The $\bar{\alpha}$ and σ_α values hence derived for NPC are 0.3 Gy^{-1} and 0.048 Gy^{-1} respectively.

Table 3.1: Marsden TCP model parameters for NSCLC 3DCRT, NSCLC SABR and NPC with local control as the end point.

TCP parameters	NSCLC 3DCRT	NSCLC SABR	NPC IMRT
$\bar{\alpha}$ [Gy^{-1}]	0.307	0.140	0.300
σ_α [Gy^{-1}]	0.037	0.017	0.048
ρ_{cl} [clonogens/cm^3]	10^7	10^7	10^7
α/β [Gy]	10	10	10
T_k [days]	20.9	21.0	21.0
T_d [days]	3.7	3.0	3.0

3.5.3 Effect of model parameters on the TCP curve

As explained in section 3.5.1, the Marsden TCP model is a four parameter model, the parameters being mean value of the intrinsic radiosensitivity over a patient population $\bar{\alpha}$, statistical uncertainty on the intrinsic radiosensitivity over a patient population σ_α, time at which repopulation kicks in T_k, and tumour doubling time T_d. The shape and slope of the predicted TCP curve depends upon the derived model parameters. A higher $\bar{\alpha}$ value indicates that the patient population responds to a lower dose or in other words, the TCP curve shifts towards the left hand side on the plot where absolute total dose along is specified along the x-axis and probability of local control along the y-axis. The σ_α value governs the slope of the curve, the lower the value the steeper is the TCP curve. The effect of varying $\bar{\alpha}$ for a given σ_α and vice-versa on the TCP curve by keeping the other parameters constant is shown in figures 3.4(a) and 3.4(b).

3.6 Normal Tissue Complication Probability (NTCP)

3.6.1 Serial and parallel architecture of organs

Organs are classified into serial and parallel organs depending upon either their structural or functional basis as explained by Withers *et al.* [138]. The fundamental functional reserve of an organ is defined by functional subunits (FSUs). The damage caused by irradiating an organ depends upon its architecture in addition

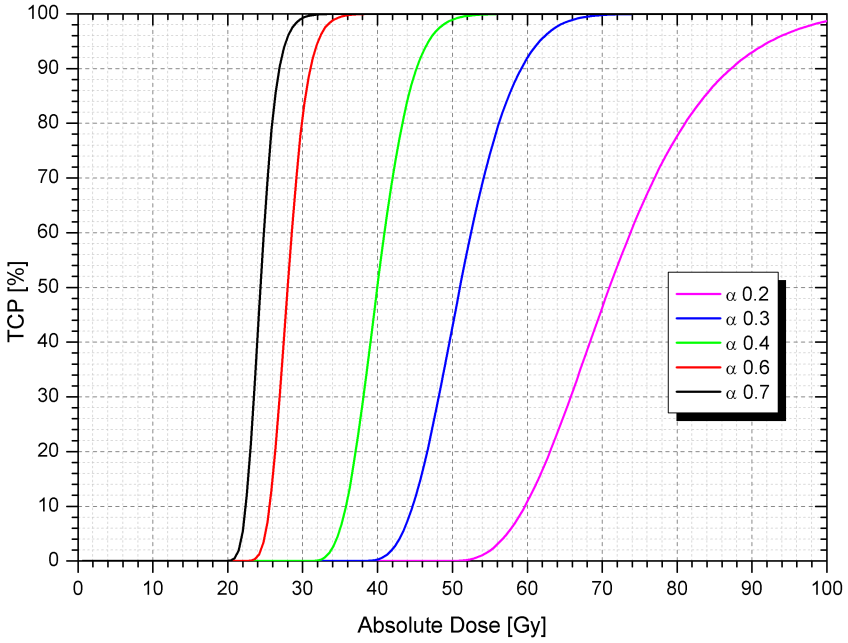

(a)

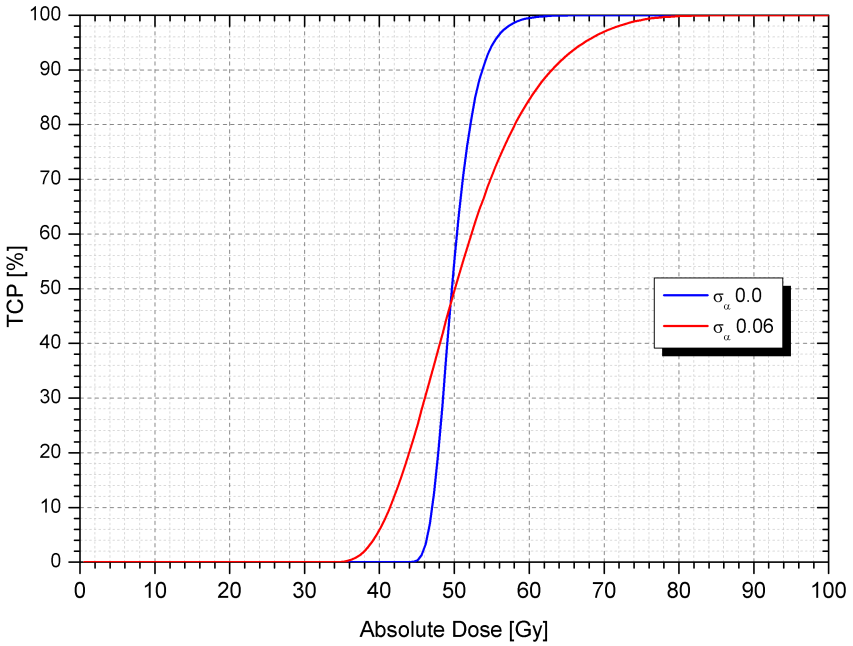

(b)

Figure 3.4: Effect of varying (a) mean radiosensitivity, $\bar{\alpha}$ (b) variation in radiosensitivity over a patient population, σ_α on the TCP curve by keeping the other parameters constant.

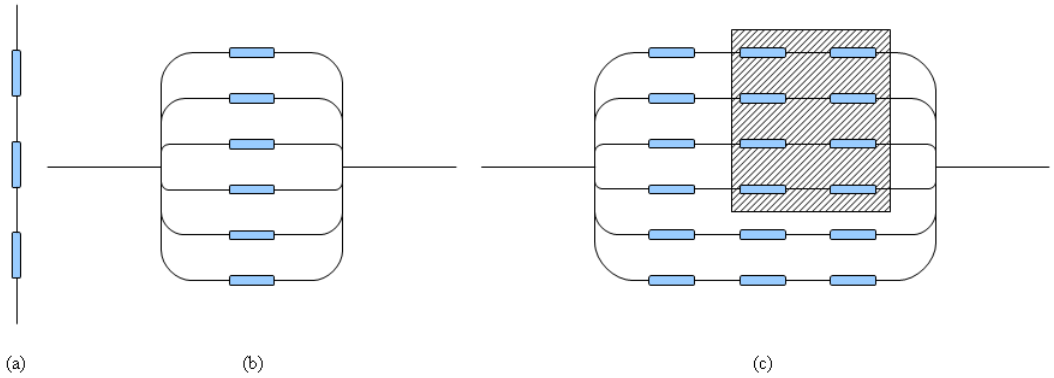

Figure 3.5: Organ architecture models (a) serial (b) parallel (c) serial-parallel (reproduced from Källman, 1992).

to other factors. A serial organ has its FSUs organised like a chain and loss of one of these FSUs can result in dysfunction of the organ. On the other hand, the FSUs of a parallel organ are independent of each other and a damage caused to one of its FSUs will not result in total organ failure.

The functional reserve of an organ following radiotherapy is preserved or damaged depending upon the dose delivered and the behavioural response of an organ based on its architecture. Spinal cord is an example of a serial organ, the tolerance of which is determined by the maximum dose whereas lung is a parallel organ and the toxicity caused is usually a function of mean dose. Some organs have partly serial and partly parallel architecture like the nephrons of the kidney. Figure 3.5 shows the serial, parallel, serial-parallel organisational architecture of organs [26].

3.6.2 Lyman-Kutcher-Burman (LKB) Model

The LKB model proposed by Lyman *et al.* [139] employs an error function given by equation 3.5 to represent the sigmoidal behaviour of dose-reponse following irradiation of a partial volume of an organ.

$$\mathrm{NTCP} = \frac{1}{\sqrt{2\pi}} \int_{-\infty}^{t} e^{-t^2/2} dt \tag{3.5}$$

The probability of causing a complication to the organ of interest is a function of both dose and volume. The LKB model is a four parameter model and is given by the formulas expressed in equations 3.5 to 3.7.

$$\mathrm{t} = \frac{D - TD_{50}(V/V_{ref})}{mTD_{50}(V/V_{ref})} \tag{3.6}$$

$$\mathrm{TD}_{50}(1) = TD_{50}(V/V_{ref})(V/V_{ref})^{n} \tag{3.7}$$

Here $TD_{50}(1)$ is the dose to the whole organ which would result in a complication in 50% of the patient population, V_{ref}, is the reference volume which is usually the whole organ volume, m, a parameter representing the steepness or the slope of the dose-response curve, n represents the volume effect parameter; a power law relationship is assumed between the tolerance doses for uniform whole and partial organ irradiation, D is the reference dose. A low n value indicates the serial behaviour of an organ whereas a higher n value corresponds to organs that have parallel architecture. For example, lung which is a parallel organ has a n value close to 1.

The above equations are valid for uniform irradiation of an organ. In order to account for inhomogeneous dose distribution in treatment plans it is essential to reduce the DVHs into single dose and define the reference volume of the organ receiving this dose. In our study, we use the effective volume method proposed by Kutcher and Burman. The DVH of the organ of interest is converted into an effective volume V_{eff} which is the volume of the organ as a whole or less than the total volume that receives the maximum dose D_{max}. The effective dose D_{eff} and volume V_{eff} are derived by equations 3.8 and 3.9 respectively.

$$\mathrm{V}_{\mathrm{eff}} = \sum_{i=1}^{k} \Delta V_i (D_i/D_{max})^{1/n} \tag{3.8}$$

$$\mathrm{D}_{\mathrm{eff}} = \sum_{i} \left[{D_i}^{1/n} \frac{V_i}{V_T} \right]^{n} \tag{3.9}$$

Here, D_i is the dose in each bin, V_i is volume in each bin, D_{max} is the maximum dose received by the organ of interest, V_T is the whole organ volume, n is the volume effect parameter.

3.6.3 Logistic Model

The NTCP of ribs with rib fracture as the end point was calculated for the SABR patient plan as the tumour was adjacent to one of the ribs. NTCP of the ribs were calculated using the logistic model and the parameters suggested by Petterson *et al.* [140]. In this study, the authors have evaluated the risk of rib fracture in terms of two models, one based on cut-off volume and the other based on cut-off dose. Results show that the cut-off volume model resulted in a better fit than the cut-off dose model. The NTCP of rib is calculated by logistic-model which is given in equation 3.10.

$$\mathrm{NTCP(D_V)} = \frac{1}{1 + e^{4\gamma_{50,V}\frac{\left(\frac{D_{50,V}}{3}+\frac{\alpha}{\beta}\right)}{\left(\frac{2D_{50,V}}{n}+\frac{\alpha}{\beta}\right)}\left[1-\frac{D_V}{D_{50,V}}\frac{\left(\frac{D_V}{n}+\frac{\alpha}{\beta}\right)}{\left(\frac{D_{50,V}}{n}+\frac{\alpha}{\beta}\right)}\right]}} \tag{3.10}$$

Here, D_V is the cut-off volume descriptor which is the maximum dose received by the high dose volume, D_{50} is the dose at which there is 50% risk of complication, γ_{50} is the normalised dose-response gradient and n is the number of fractions.

3.6.4 NTCP parameters for LKB model and logistic model

End point: radiation pneumonitis

The parameters to calculate NTCPs for lung were taken from De Jaeger *et al.* [40] which are shown in the table 3.2.

Table 3.2: LKB model NTCP parameters for lung with radiation pneumonitis as the end point.

NTCP parameters	Values
TD_{50}	29.2 Gy
m	0.45
n	1

End point: rib fracture

Petterson *et al.* [140] derived the parameters D_{50} = 49.8 Gy and γ_{50} = 2.05 to

calculate the probability of rib fractures for the dose received by 2 cm^3 cut-off volume.

Table 3.3: Logistic model NTCP parameters for ribs with rib fracture as the end point.

NTCP parameters	Values
D_{50}	49.8 Gy
γ_{50}	2.05

End point: xerostomia

Xerostomia is a common toxicity following radiotherapy of head and neck tumours which is caused by irradiation of salivary glands such as parotids, submandibular and sublingual glands. Deasy *et al.* [53] have given a detailed report on the radiotherapy dose-volume effects on the salivary glands. NTCPs with xerostomia as an end point has been evaluated and reported for NPC IMRT in the study explained in chapter 8. The parameter sets given in table 3.4 derived by Semenenko *et al.* [141] for LKB model is used to calculate the NTCPs of parotids.

Table 3.4: LKB model NTCP parameters for parotids with xerostomia as the end point.

NTCP parameters	Values
TD_{50}	31.4 Gy
m	0.54
n	1

3.7 Influence of dose calculation uncertainty on the predicted TCP and NTCP

MC dose calculation is always associated with statistical uncertainties as it is a stochastic or random process unlike analytical dose calculation algorithms. It is therefore essential to minimise these uncertainties in order to predict accurate doses. The magnitude of the statistical uncertainties can affect the accuracy of

dose distribution and hence accuracy of DVHs and quantities including TCPs and NTCPs which are derived from the DVHs. Several researchers have studied the influence of statistical uncertainties on MC dose calculation [142–146]. Keall *et al.* [143] have suggested that a standard deviation 1σ of less than 2% on the maximum dose is sufficient. The MC statistical uncertainties depend upon the number of initial electron histories simulated, the greater the number of histories, the smaller is the statistical uncertainty. σ is inversely proportional to the square root of the number of histories. Buffa *et al.* [142] have shown that the DVHs have a broadening effect with increase in the statistical uncertainty resulting from either decrease in voxel dimensions or number of histories. This in turn results in a systematic underestimation of the predicted TCP values. Jiang *et al.* [145] have shown that the low doses of target DVHs are under estimated and high doses are over estimated by increasing statistical uncertainty. The DVHs of the normal structures or critical organs and hence their NTCPs are insignificant.

In this study the standard deviation (1σ) on the dose maximum of all the patient plans were less than 0.6% which is well within the recommended tolerance limits specified by the above mentioned publications. The total statistical uncertainty resulting from individual contributions of statistical uncertainties of all the fields of a treatment plan were calculated by taking square root of the quadratic sum of each component.

Chapter 4

Setting up an EGS-BEAM-DOSXYZnrc based Monte Carlo dose calculation engine

4.1 Introduction

One of the essential tools for this project is a Monte Carlo system with the capability of performing dose calculations both in phantom and patient geometry. Setting up an MC dose calculation system is a complex process which starts with modelling of an accelerator head with all its components to match measured beam data in a water phantom. The modelled virtual linac is then used to perform dose calculation in CT based patient geometry. This chapter describes the various steps involved in the MC dose calculation process done with the EGSnrc, BEAMnrc, DOSXYZnrc open source MC radiation transport system developed by the National Research Council (NRC), Canada [147].

As the validation of the beam model is the basis for the accuracy of the whole dose calculation system it was crucial to do the modelling with sufficient accuracy to achieve good agreement within the recommended tolerance limits over the range of field sizes the treatment machine can deliver.

4.1.1 Choice of MC code

Numerous MC codes have been developed in the past, some of which are general purpose MC codes and some specific to simulation of radiation therapy beams. The first code ETRAN/ITS, electron and gamma transport with secondary radiationby MC was written by Halbleib *et al.* [148] in the late 80s at the National Bureau of Standards, Washington. It was written in FORTRAN IV and ran on UNIVAC, IBM computers. Martin Berger, a world renowned physicist was involved in the development of this code [149]. EGS4, electron gamma shower originated at the National Research Council, Canada which was followed by the introduction of BEAMnrc/DOSXYZnrc [110, 150–154]. Another general purpose MC N-Particle transport code MCNP was conceived by the group at Los Alamos National laboratory [155].

GEANT4, a general purpose MC code for radiation transport through matter was developed by the research group at CERN [156]. PENELOPE was developed by Joseph Sempau and Frances Salvat of University of Barcelona [157]. In the recent years, with the availability of sophisticated computing resources, MC based treatment planning has been introduced for routine clinical use e.g. voxel based MC algorithms VMC, XVMC (incorporated in MONACO[1] TPS), VMC++ were developed by Iwan Kawrakow and Mathias Fippel [158,159]. The Brainlab iPlan[2] version has the capability of calculating doses with MC algorithm. Additionally, some of the TPSs such as Eclipse and Oncentra have electron MC dose engines.

It was essential to choose an MC code which is flexible to incorporate various components of the accelerator and ability to perform wide variety of techniques ranging from conformal, dynamic wedge treatments, IMRT, and rotational IMRT. We chose to use the EGSnrc based MC package with BEAMnrc to model the accelerator and DOSXYZnrc for MC dose computation in phantom and patient geometries as this code has been used and studied extensively by various research groups across the world.

[1]Elekta, Stockholm, Sweden.
[2]Brainlab AG, Feldkirchen, Germany.

4.1.2 EGSnrc

The Electron Gamma Shower (EGSnrc) system [152] is a general purpose package for the Monte Carlo simulation of coupled electron-photon transport of particles with energies from 1 keV up to 10 GeV in an arbitrary geometry. This is an extended and improved version of the EGS4 package originally developed by Nelson, Hirayama and Rogers [151].

4.1.3 BEAMnrc

BEAMnrc [110, 153] is a Monte Carlo simulation system for modelling radiotherapy sources which is based on the EGSnrc code system. BEAMnrc is the current version of BEAM which can work under various operating systems such as Linux, Unix, and Windows. It is a module in the EGSnrc package which enables to model the accelerator head. The BEAMnrc is the most commonly used code for accelerator head modelling and around 800 publications have cited the BEAM paper which was published by Rogers *et al.* [110].

4.1.4 DOSXYZnrc

DOSXYZnrc [154] is a special purpose code which is used to simulate radiation transport in phantom and patient geometry in Cartesian coordinate system.

4.2 Work Flow

4.2.1 Modelling of the accelerator head

The head of a Varian 2100 CD accelerator[3] was defined according to the manufacturer specifications. The accelerator head consists of component modules (CMs) along the z direction in the descending order of target, primary collimator, vacuum window, ionisation chamber, mirror, dynamic jaws, jaws, Multi Leaf Collimator (MLC) were modelled using the CMs of BEAMnrc package namely SLABS, CONS3R, CONESTAK, FLATFILT, CHAMBER, MIRROR, EDW, JAWS, DYNVMLC respectively. Each part of the accelerator unit was

[3]Varian Medical Systems, Palo Alto, CA, USA.

considered as a single CM which takes up a horizontal slab portion of the accelerator. Every CM has a front surface and back surface and the accelerator was built with many such blocks. The gaps between the CMs were automatically filled with air by the main BEAMnrc routine, which is consistent with the case of the real accelerator. The surrounding medium outside the accelerator head up to phantom or patient geometry was defined as air in all cases. The model of the entire accelerator head from the target to the MLCs is shown in figure 4.1.

4.2.2 BEAM and DOSXYZ sources

Two main sources are available to model an accelerator head - full BEAM simulation and simulation using phase-space files (PSFs). The former is a compact way of characterising the distribution of particles whereas the latter stores the information of the particles generated, their kinetic energy, charge, the CM from where each particle originated. The MC model used in this work employs a full BEAM simulation starting from the electron source which results in bremsstrahlung photons after impinging on the tungsten target to the patient geometry through all the CMs of the accelerator head. The reason for choosing full BEAM simulation over PSFs is to avoid - storing large amount of data which requires enormous disk space, recreation of the particle data files for each field geometry and delay in accessing large PSFs via a networked computing environment [160–162].

The BEAMnrc source, *isource 9* of DOSXYZnrc was used for simulating conventional, conformal and IMRT treatments in both phantom and patient geometry. Both of the sources use the particles sampled from a BEAM simulation which runs concurrently along with DOSXYZ simulation. In order to run a concurrent simulation using either of the two above mentioned sources, the DOSXYZ input file along with a BEAM input file which has the information of the components of the accelerator head and the initial electron parameters and *pegs4* data file which contains the necessary cross section data are provided. The BEAM accelerator code is compiled as a shared library in dynamic link library (*.dll) or shared object (*.so) file format for windows and LINUX/UNIX machines respectively.

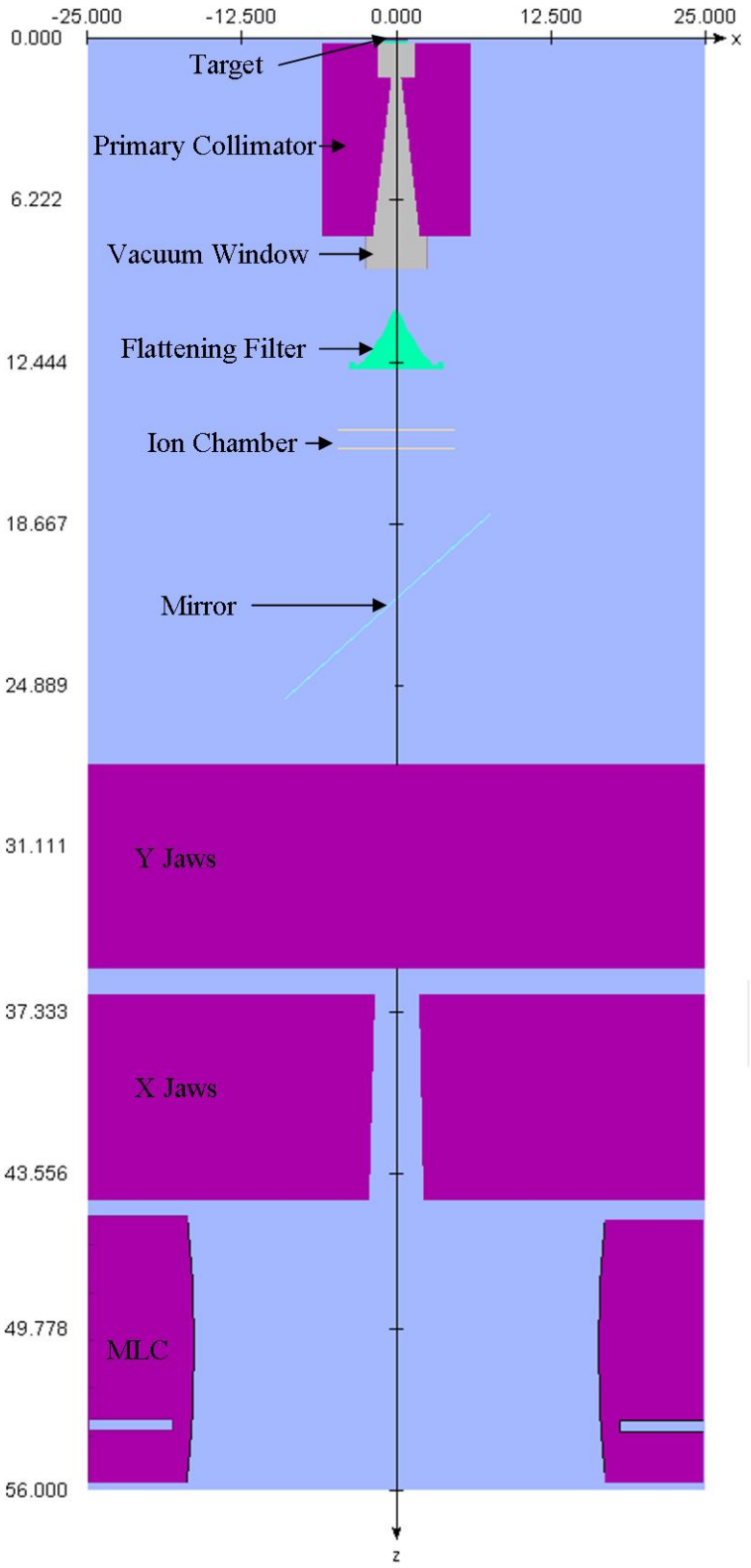

Figure 4.1: MC model of Varian 2100 CD accelerator head with its CMs starting from tungsten target, primary collimator, vacuum window, flattening filter, monitor ionisation chamber, mirror, X and Y jaws and MLCs in the same order one below the other. The volume around the CMs and outside the accelerator head is automatically filled with air which is shown by the blue region.

4.2.3 Variance reduction techniques

Directional bremsstrahlung splitting

The directional bremsstrahlung splitting (DBS) technique was conceptualized as a part of the variance reduction techniques in BEAMnrc [153]. This involves splitting each bremsstrahlung event into NBRSPL photons, where NBRSPL is the splitting number specified by the user. Then, the weight of each photon is reduced to W_e/NBRSPL where W_e is the weight of the parent electron. The direction and energy of resulting bremmstrahlung photons are randomly chosen from relevant distribution while the energy of the initial electron is decreased by energy of just one photon (as if only one photon was produced per bremsstrahlung event).

The DBS algorithm loops through the split photons and determines whether they are aimed at the field of interest in which case the photon is kept. The field size (FS) of the treatment field being simulated is input along with the SSD at which the field size is defined. If the photons fall outside the treatment field, Russian Roulette (RR) is played on the photon, where a random number is generated and compared to the survival threshold of 1/NBRSPL. If the random number is below this value the photon is kept and its weight is increased by NBRSPL; these photons aimed away from the field that survive RR are considered "fat" and have same weight (unity). Thus, the efficiency of the calculations is increased as tracking of photons that fall outside the region of interest is avoided. These photons that fall inside the defined treatment field are called low-weight photons and those which fall outside the treatment field are called fat or heavy-weight photons. This concept is extended to other type of interactions like, annihilation, Compton scattering, pair production, and photo electric effect and so on to reduce the variance and to increase the efficiency of the calculations. The DBS is superior to the predecessors of the splitting techniques called uniform bremsstrahlung splitting (UBS) and selective bremsstrahlung splitting (SBS). UBS used a constant splitting number between 20 and 100 whereas SBS used variable splitting number between 200 and 1000. In case of DBS, a splitting number of 1000 is recommended by Kawrakow *et al.* [163] for a 6 MV which means each bremsstrahlung event is

split into 1000 photons each with a weight of 1/1000.

The DBS can be used with and without electron splitting out of which the former increases the statistics of the electrons which is crucial at the bottom of the accelerator head as these contaminant electrons have relatively high probability to reach the patient plane. Two planes, perpendicular to the beam axis known as RR and splitting plane are defined. The DBS option is ON above the Russian roulette (RR) plane in order to increase the efficiency of calculation whereas in the region below this plane the RR is turned OFF hence increasing the number of transported electrons. The option to use DBS with electron splitting involves the definition of three regions, the upper region where the DBS is carried out resulting in many low-weight photons, less fat photons and lesser low-weight electrons. The middle region which is defined 2 mm as recommended by Kawrakow *et al.* [163]. This is specified above the splitting plane and has both fat and non-fat electrons. The bottom region which is defined at the bottom of the flattening filter has many non-fat electrons and no fat electrons. In our study we used a DBS field width 10 cm wider than the longest side of the treatment field and a splitting number of 1000 as the simulations were performed with electron splitting. These simulations were done with *isource 9* of DOSXYZnrc, which employ full BEAM simulations where both DOSXYZ and BEAM simulations are run concurrently from the target to the phantom or patient geometry with the definition of air medium in the space between the accelerator head and the phantom or patient geometry. It has been shown by Kawrakow *et al.* [161] that both the approaches of running a BEAM simulation first to create phase-space files which are then used as a source to do the DOSXYZ simulation and running both BEAM and DOSXYZ simulations concurrently are equally efficient when appropriate variance reduction techniques are used despite the fact that there is time loss with the second method as it repeats the simulation through the common fixed components of the accelerator every time.

4.2.4 BEAM and DOSXYZ input parameters

The default EGS parameters in BEAMnrc and DOSXYZnrc were used for all the simulations except the boundary crossing algorithm (BCA) was EXACT instead

of PRESTA I as previous studies by Walters *et al.* [164] have shown that the default PRESTA I algorithm tends to overestimate the dose to up to 2.5% in photon beams. The over prediction is higher with high energy photons and at the regions where there is no charge particle equilibrium. The photon and electron cutoff energies were AP=PCUT=10 keV and AE=ECUT=700 keV respectively where the electron cut off energy is including the rest mass energy of the electrons, 511 keV which means the histories of the electrons with kinetic energy less than 189 keV were terminated and their energy was deposited on the spot. Here AP and AE are the thresholds for production of secondary bremsstrahlung photons and knock-on electrons whereas PCUT and ECUT are the global cut off energies of photons and electrons respectively. It is recommended that the PCUT and ECUT values are greater than or equal to AP and AE.

In DOSXYZ, for the simulations involving the validation of the accelerator where a homogeneous cubical water phantom was used the HOWFARLESS option was turned ON in order to neglect the voxel boundaries due to the uniformity in the phantom material [165]. This increases the efficiency of the calculations by a factor of 2.5 to 3.5 when used along with a more accurate BCA algorithm like EXACT as it considers only the outer boundaries of the defined homogeneous phantom [153]. This parameter was turned OFF in all the patient calculations where it is crucial to account of voxel boundaries while transporting the photons and other charged particles due to variable voxel densities. The electron step length parameter (SMAX) and ESTEPE, the parameter that defines the maximum fractional energy loss per step length were set to $1e^{10}$ cm and 0.25 respectively (default values corresponding to EXACT BCA). ESAVE was set as 2 MeV which defines the maximum energy expressed in MeV at which the electron range rejection calculations are done. This parameter ensures that the high energy electrons which are capable of producing a bremsstrahlung interaction are not rejected.

The cross section data of various interactions for different materials defined in the MC phantom were derived from *pegs4* data. All the simulations were done using *700icru pegs4* data as the electron cut off energy ECUT was set to 700 keV.

4.2.5 Input files for full BEAM simulation

The full BEAM MC simulation requires a BEAM input file which has the technical specifications of the accelerator head and DOSXYZ input file along with the MC phantom, BEAM library file to launch the simulations in parallel, *pegs4* data file which contains the interaction cross section data for all the materials. The accelerator component specifications were included in the BEAM input file according to the information given by the manufacturer. The input of all the CMs above the jaws starting from the tungsten target to the mirror remained the same in all the cases. The settings of the jaws and multi leaf collimators (MLCs) varied for each simulation depending upon the field size and MLC aperture. In case of wedge simulations one of the Y jaws swept across the field to produce the wedge profile as explained in section 4.2.7. There was a slight modification in the wedge input files which included a line specifying the wedge angle, orientation and energy of the photon beam. Segmented treatment table (STT) (see section 4.2.7) corresponding to the specified wedge angle was generated from the golden STT (see section 4.2.7).

The MLCs were completely retracted while simulating the open fields for the validation of the accelerator head. The field size was defined only with the X and Y jaws in case of open fields. The input files were created using the BEAM and DOSXYZ graphical user interfaces (GUIs) directly for both open and wedge field simulations.

Python routines written by Tony Teke[4] and Patrick Downes[5] were used in order to generate the BEAM and DOSXYZ input files from the DICOM RT (RP)[6] plan file *.dcm exported from the Eclipse TPS. Before creating the input files the *.dcm was exported to DICOM MANAGER, an in-house anonymiser to remove all patient identification tags. After the plan file was anonymised it was exported to a local computer where the python routines were used to extract the jaw position, MLC position for the BEAM input file. The DOSXYZ input file was also created. The BEAM and DOSXYZ input files contain two random number seeds RNG1 and RNG2 each of which has its own random number sequence.

[4]Physics and Astronomy, University of Columbia, Vancover, Canada.
[5]School of Computer Science, Cardiff University, Cardiff, UK.
[6]The RP file consists of geometric and dosimetric data related to a treatment plan in DICOM format.

The next step was to create parallel input files, in our study the simulations were run in parallel in the University of Liverpool giga bit cluster (*ulgbc*) and condor pool of University of Liverpool (UoL). The simulations were launched using the DOSXYZ GUI with the options optimisation ON, long, batch, and were run in parallel with the run parallel option specifying the number of parallel jobs, *N_parallel*. For the simulations launched in the condor, the BEAM and DOSXYZ input files along with the MC phantom file, *pegs4* data file, BEAM library file, and a submission file which specifies the location of all of the input files was also created. DOSXYZ parallel input files were created in which the total number of histories were split into *N/N_parallel* in each of the input file. The first random number seed remained the same in all the parallel input files whereas the second random number seed was incremented by 1.

4.2.6 Modelling of the Varian 120 millennium MLC

The Millennium 120 MLC of the Varian 2100 CD accelerator was modelled using DYNVMLC[7] CM of BEAMnrc which was coded by Heath *et al.* [110, 166]. The Millennium 120 MLC contains 60 leaves on each of the bank with 80 inner and 40 outer leaves that project 0.5 cm and 1.0 cm at the isocentre with a height of 6.5 cm and 6.7 cm respectively.

The outer leaves are called as full leaves whereas the inner leaves that are arranged alternatively with thick end towards the target and thick end towards the isocentre are known as target and isocentre leaves respectively. Like many other types of MLCs, Varian Millennium 120 MLCs have complex intricate structures such as tongue and groove, and rounded leaf ends as a result of which there is leakage between the adjacent leaves and abutting leaves even when they are completely closed. There is a thin air gap between the adjacent leaves for smooth sliding movement of the leaves which presents as a source of leakage. It is essential to model the MLCs effectively so as to estimate both inter and intra leaf leakage between and through the leaves respectively. The electron transport through the MLCs is very crucial as in the Varian accelerators the MLCs are tertiary structures which are mounted below the Y and X jaws and are closer to the patient

[7]DYNVMLC CM is specifically designed to model Varian Millennium 120 MLC.

because of which they are one of the main sources of electron contamination. A schematic diagram of the cross sectional view of Varian Millennium 120 MLCs is shown in figure 4.2.

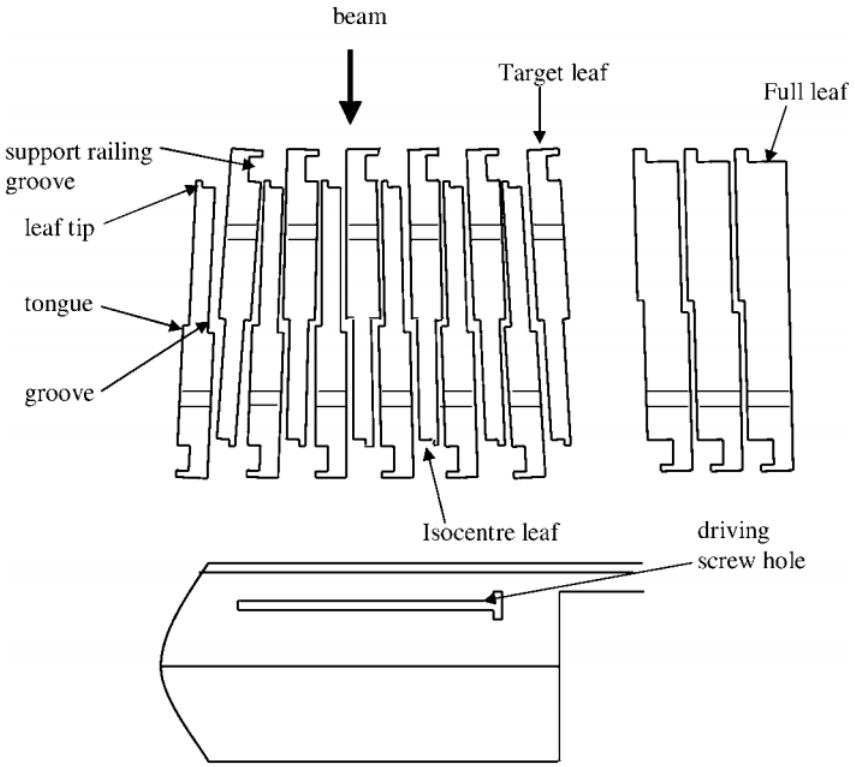

Figure 4.2: A schematic diagram representing the cross-sectional and side view of full, isocentre, target leaves of a Varian Millennium 120 MLC showing its toungue, groove, leaf tip and driving screw hole (Figure reproduced from Heath *et al.* (Heath, 2003).

The VARMLC[8] CM module was modified by Heath *et al.* [110, 166] and the new module was named as DYNVMLC. It is capable of simulating static, step and shoot, and dynamic deliveries. The static mode is used to simulate conformal treatments whereas the step and shoot and dynamic modes simulate static and dynamic or sliding window IMRTs respectively. For simulating IMRT plans, the MLC leaf sequence file is separately input along with the main BEAM input file which contains the number of segments and the fraction of MUs received by each segment. In our study, we simulated only 3D conformal plans with static or single aperture MLC fields for all the plans used in the lung study and step and shoot IMRT in case of treatment of NPC, the dynamic option was not used.

[8]VARMLC CM is designed to model focusing multi-leaf collimators with rounded or straight leaf ends.

4.2.7 Modelling of the enhanced dynamic wedges

The Varian 2100 CD machine has the capability of delivering dynamic wedge fields using enhanced dynamic wedge (EDW)[9] which produce wedge profiles by sweeping the jaws across the treatment field during the delivery as explained in the Varian EDW implementation guide [167]. One of the two Y jaws remain stationary and the other jaw moves across the field. There are two possible orientations IN and OUT where the Y1 and Y2 jaw moves respectively. Both the jaw speed and dose rate are varied with time during the jaw movement. EDW can produce wedge profiles for seven wedge angles 10°, 15°, 20°, 25°, 30°, 45°, 60° for Y jaw setting form -20 cm to 10 cm at the isocentre. To generate the wedge profiles corresponding to the different wedge angles, part of the MUs are delivered by an open static field and the rest with the jaw motion. Irrespective of the wedge orientation, there is a gap of 0.5 cm between the jaws at the end of the jaw movement.

Verhaegen *et al.* [168, 169] has suggested two methods to model the dynamic wedges the first one being position probability sampling (PPS) in which particles are sampled as a cumulative probability density function (CPDF)[10] of fluence with respect to the jaw position and the second one being static component simulation (SCS) in which the treatment field is split into multiple segments analogous step and shoot technique. According to their results both these methods are robust and yield similar results except for the fact that the former has the advantage over the latter as the entire dynamic wedge field is calculated as one simulation. In this study, the CM EDW developed by Patrick Downes[11] based on the technique suggested by Verhaegen *et al.* [168,169] has been employed to model the dynamic wedges.

In this method uniformly distributed random numbers are created for each simulated history which is tied to the jaw position and the CPDF of fluence or MUs. The CPDF of 60° wedge angle which is dependant on the beam quality known as the golden STT is provided by the manufacturer that gives the dose versus jaw position relationship. 'The normalised CPDF of MUs as a function of

[9] Varian Medical Systems, Palo Alto, CA, USA.

[10] CPDF is the probability of a variable to have a value less than or equal to x.

[11] School of Computer Science, Cardiff University, Cardiff, UK.

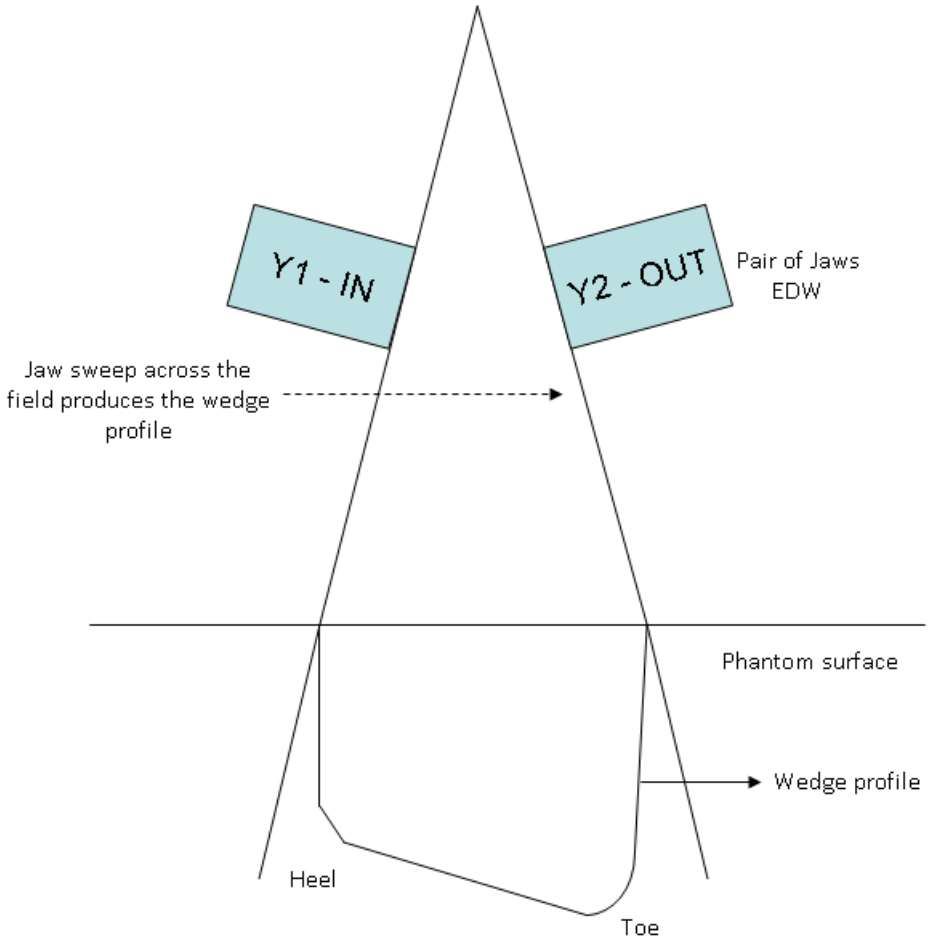

Figure 4.3: Mechanism of producing wedge profiles by an enhanced dynamic wedge. One of the Y jaws sweeps across the field when the beam in ON in order to generate wedge profiles. It has the capability of generating intensity modulated beams with wedge angles 10°, 15°, 20°, 25°, 30°, 45°, 60°. This is done by delivering the total MUs partly as open fields and partly with the Y jaw sweep.

jaw position for 7 wedge angles is shown in figure 4.4. The MUs corresponding to the open field and the wedge field delivery is calculated by equations 4.1 to 4.3 [167].

$$\mathrm{W}_{0^\circ} = \frac{(tan60^\circ - tan\theta)}{tan60^\circ} \tag{4.1}$$

$$\mathrm{W}_{60^\circ} = \frac{tan\theta}{tan60^\circ} \tag{4.2}$$

The number of MUs delivered as open and wedge fields normalised to the total MUs as a function of wedge angle is shown in figure 4.5.

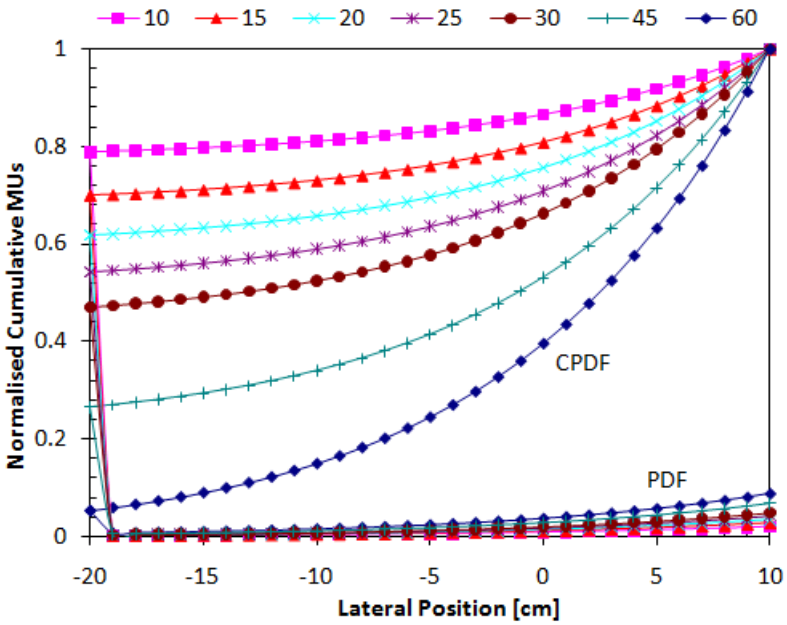

Figure 4.4: Normalised cumulative probability density function of MUs as a function of jaw position

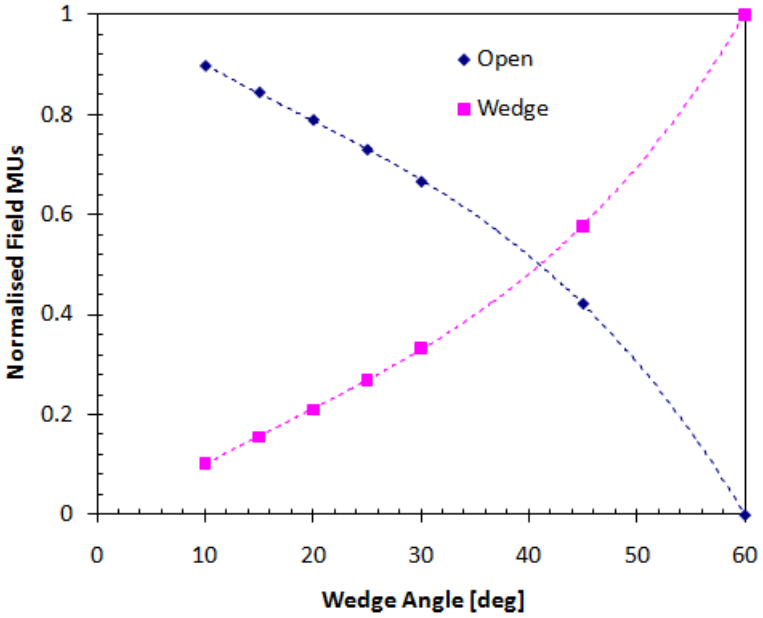

Figure 4.5: MUs are delivered partly as open and wedge fields as a function of wedge angle. The larger the wedge angle, the lesser number of MUs are delivered as an open fields.

The other wedge angle MUs are calculated as weighted average of the MUs in the open field MU and wedge field MU of the 60° wedge field.

$$(\mathrm{MU}_\theta) = (MU_{0^\circ})W_{0^\circ} + (MU_{60^\circ})W_{60^\circ} \tag{4.3}$$

4.2.8 Correction for backscatter from the jaws

The dose backscattered to the monitor Ion Chamber (IC) from the jaws affect the output of certain linac models. Studies in the past have shown that Varian clinac series is prone to be affected by the backscattered dose [170–173]. The monitor chambers present in these linacs collect the necessary monitor units earlier due to the dose back scattered to the chamber by the jaws which would in turn switch off the beam without delivering the intended dose. The contribution of the dose backscattered to the IC is larger for smaller fields as the jaws are much closer to the central axis and up to 2-3% increase in back scattered dose with decreasing field sizes are reported in the literature [174]. Studies have shown that the major contribution of the back scattered dose to monitor IC are the upper Y jaws whereas the X jaws which are further below the monitor IC contributes only 10% of the total back scattered dose [173]. The amount of dose back scattered to the monitor IC depends upon the machine design in particular the design of the collimator and the monitor IC.

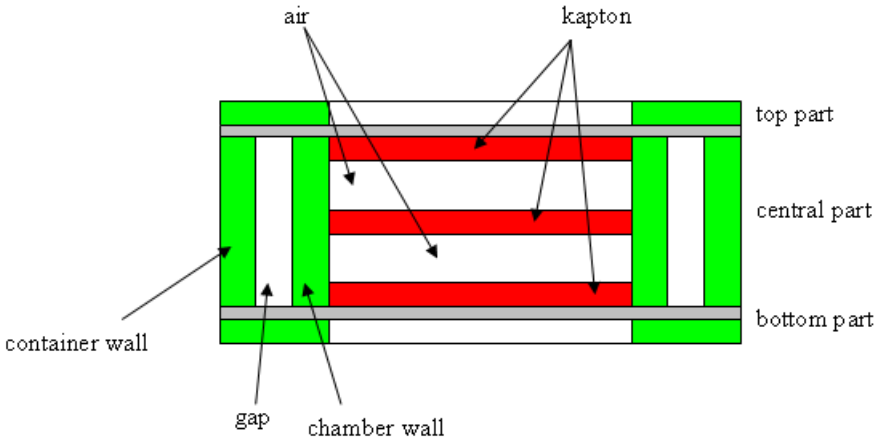

Figure 4.6: Schematic diagram of the MC modelled monitor ionisation chamber with kapton walls and air gaps.

As mentioned in section 4.2.1 the CM CHAMBER of BEAMnrc code has been used to model the monitor IC which has a cylindrical geometry. The dose is scored in two air slabs between three equidistant kapton windows which are oriented

perpendicularly to the beam axis and are surrounded by chamber wall, chamber gap and container wall along the direction of the beam [110]. A schematic diagram of the monitor IC is shown in figure 4.6.

Open, conformal, intensity modulated and rapidarc fields

The total dose, both forward and back scattered dose accumulated in the monitor IC were scored together for open, conformal, and intensity modulated fields as all of our MC calculations were done as full BEAM simulations starting from the target to the phantom or patient geometry. The correction for back scattered dose is done at a later stage with a python script written by Tony Teke[12] after obtaining the *.3ddose file which has the doses in all the voxels of the phantom or patient geometry.

Wedged fields

There was no explicit correction applied for the dose back scattered to the monitor IC in case of wedge fields as the EDW routine automatically accounts for it using the linear relationship with the jaw position as calculated by Liu *et al.* [173]. This correction is applied to the CPDF function of the particular wedge angle derived from the golden STT,

$$\mathrm{CPDF(y)} = STT(y) f_{back}(y) \tag{4.4}$$

$$\mathrm{f_{back}(y)} = a + b|y - yi| \tag{4.5}$$

The parameters a and b are 1.03 and -7.50$\times 10^{-4}$ cm^{-1} for the 6 MV beam as derived by Liu *et al.* [173] and Verhaegen *et al.* [174].

4.2.9 Coordinate transformations

The coordinate system (CS) of the IEC/DICOM CT data set and that of DOSXYZ are not the same.It is essential to convert the CS of DICOM to DOSXYZ format when an MC simulation is carried out using an MC phantom created from DICOM CT data sets that are exported from a TPS. Three different angles are

[12]Physics and Astronomy, University of Columbia, Vancover, Canada.

to be specified in the DOSXYZ input file in order to perform the full BEAM simulations in our study. The angle θ is the angle between the z direction and the line joining the centre of the beam where it meets the phantom surface to the isocentre. The angle ϕ is the angle between the positive x axis and the x-y plane of the line joining the centre of the beam on the phantom surface to the isocentre on the x-y plane. ϕ_{coll} is the collimator angle. The directions x, y, z are incremented by variable i, j, k in the DICOM CS and DOSXYZ CS as shown in figure 4.7.

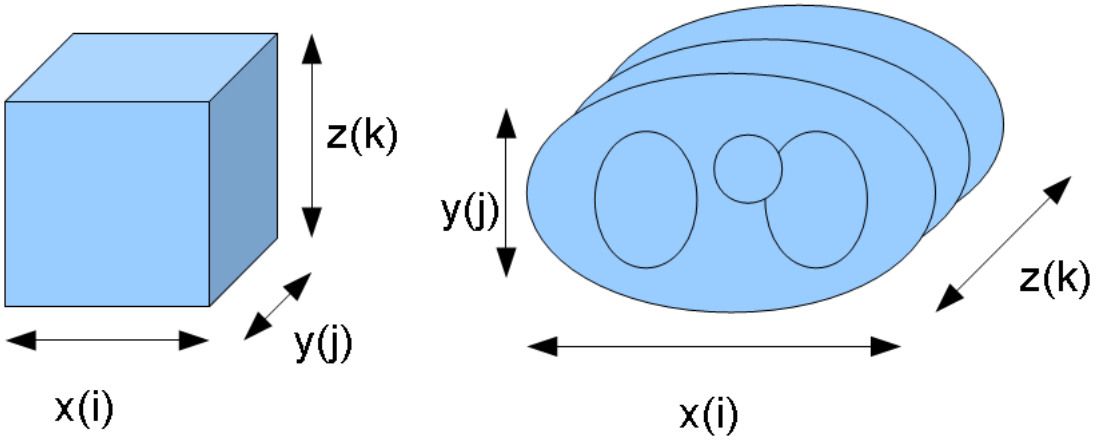

Figure 4.7: Coordinates of a phantom created with DOSXYZ including five materials namely air, lung, soft tissue, soft bone or spongiosa and cortical bone with *ctcreate* by replacing the HUs of each voxel of the DICOM CT images with material densities and material numbers.

For a phantom created with a beam facing the z direction from the top, θ=180°, ϕ=0°. In case of a DOSXYZ phantom created from DICOM CT data set using *ctcreate*, these angles would be θ=180°, ϕ=0°.

4.2.10 DICOM CT phantom

DOSXYZnrc package has two different options to create phantoms, one is without CT data input and the other created with CT data input. The former option was used to create water phantom for validating the accelerator head and the latter option was used for calculating patient plans. The *ctcreate* option has the capability to convert DICOM CT data set to MC phantom with predefined materials. In order to perform this, the CT data set of each patient was exported from Eclipse treatment planning system in DICOM format to a stand alone PC

on which DOSXYZnrc was installed. The data were read with *ctcreate* and the dimensions of the MC phantom and the resolution along the x, y and z directions were input which included a sub volume of original.

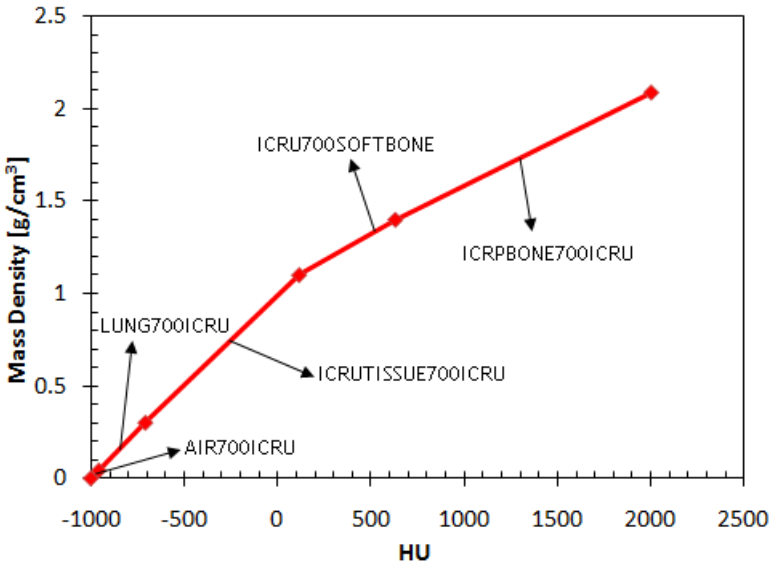

Figure 4.8: CT Hounsfield units to material density calibration curve used in *ctcreate* to convert the DICOM CT data set to MC phantom

It is possible to designate different materials to create the MC phantom and in our study we used five materials namely AIR700ICRU, LUNG700ICRU, ICRUTISSUE700ICRU, ICRU700SOFTBONE, ICRPBONE 700ICRU with lower and upper bound densities ranging from 0.001 - 0.044 g/cm^3, 0.044 - 0.302 g/cm^3, 0.302 - 1.101 g/cm^3, 1.101 - 1.4 g/cm^3 and 1.4 - 2.088 g/cm^3 respectively. The CT upper bound in terms of Hounsfield Units (HUs) was specified for all the five materials. The HU to material density calibration curve is shown in figure 4.8. The MC phantom file is output as *.egsphant which contains the number of materials defined, name of the materials, the type of material in voxels of each slice followed by the average material density of the voxels in all the slices. This is in the form of a 3D matrix of 512×512 along the x, y direction and number of slices along the z direction.

4.2.11 Launching MC simulations

The full BEAM simulations were run both in the condor and the cluster of the University of Liverpool. The infrastructure and hardware of the condor and the cluster are elaborately described in the section 4.2.12. To perform these simulations, the beam and DOSXYZ files were used and the jobs were launched using the DOSXYZ GUI with the BEAM simulation running concurrently. There was no separate phantom file as the phantom was created using the DOSXYZ GUI itself. The depth doses along the central axis of the beam and the beam profiles across the field at various depths for a range of field sizes were scored together by explicitly defining the voxels in which the dose had to be scored and listed at the end of each simulation for further analysis. These jobs were run in parallel as a batch on 25 processors at a time.

The condor system was being set up during the course of the project and became available for full fledged use by the time the validation of the accelerator model was completed. The patient plans run on the condor consists of two main input files similar to those used for the accelerator validation, a BEAM input file with the specification of the accelerator head and the DOSXYZ input file. The patient phantom was given as a separate input file called *.egsphant which was created from the DICOM CT data set as explained in section 4.2.10. The BEAM library file which is required for running the BEAM and DOSXYZ simulation concurrently was also included. The data file containing the cross section data of various materials, 700icru *pegs4* file, DOSXYZnrc executable were also included. A DOSXYZ simulation submission file which specifies the above mentioned files was used to run the jobs in parallel. It was not possible to access the GUIs in the condor because of which the jobs were submitted to the nodes from the command line. These simulations were launched in 250 nodes at a time.

4.2.12 Hardware

The biggest challenge to do MC dose computation is the time and computing power required as it might take extremely long time to simulate a single field. This is due to the fact that the MC dose calculation does the radiation transport in a detailed fashion as it actually tracks each and every interaction, the photons

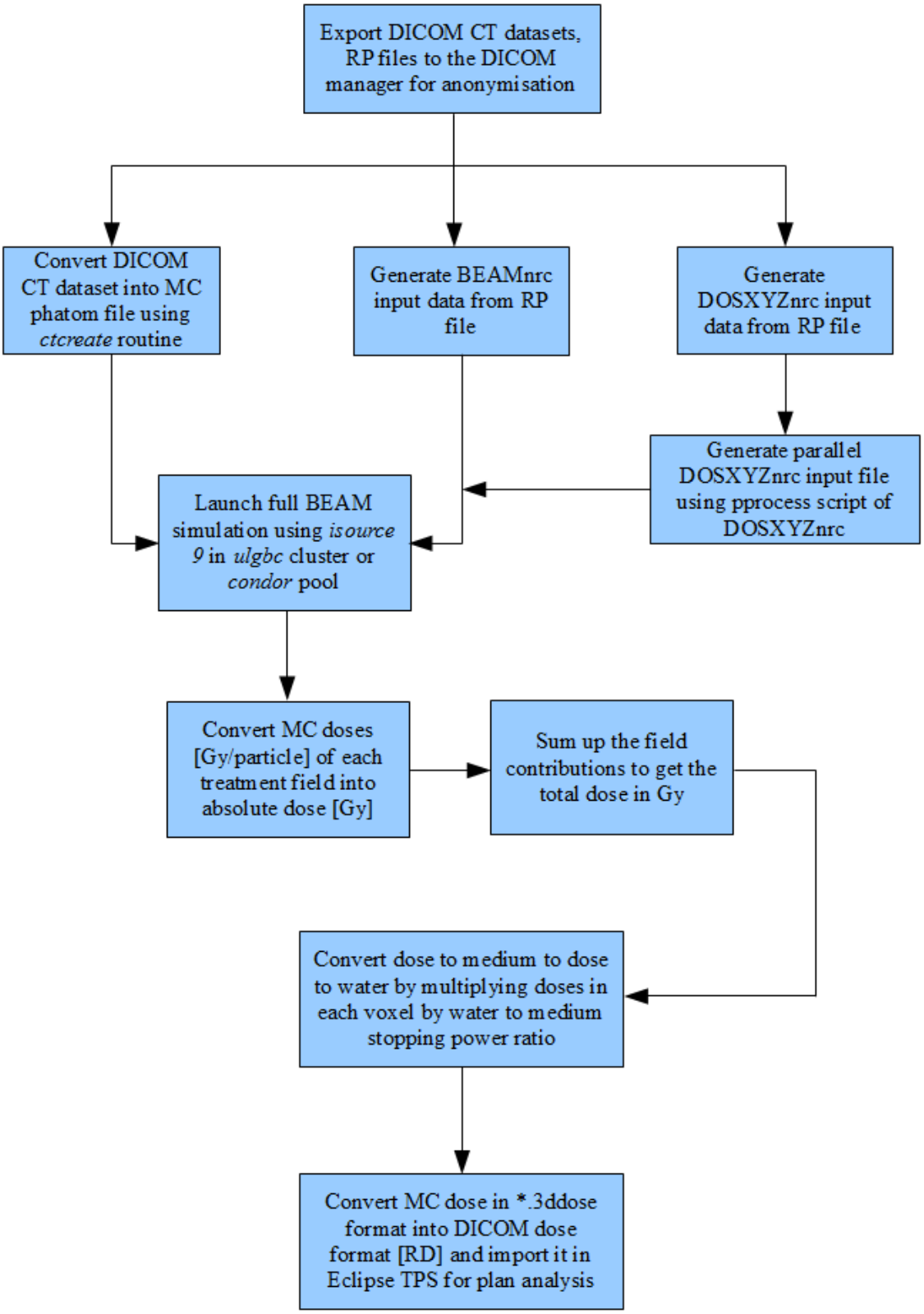

Figure 4.9: Work flow of MC dose calculation

and charged particles undergo until they are totally absorbed or leave the geometry of interest. This study involves two steps of MC calculation, the modelling of the accelerator head as a whole with all its components and the transport of radiation in phantom or patient geometry. Electron histories of the order of millions or billions are necessary in order to compute dose in a voxel with acceptable uncertainties. Parallel computing in the form of high performance computing (HPC) clusters and high throughput computing condor pools present means to tackle the time required to do these computer intensive simulations.

Our simulations were performed in the *ulgbc* and the condor system both of which will be henceforth simply denoted as cluster and condor respectively. The cluster is a dedicated system used for parallel computing whereas the condor is a system that uses idle or unused networked computer processors for computing.

The grid computing hardware of *ulgbc* comprises of systems that use Intel Xeon processors and a 32-bit Redhat Enterprise 4 operating system. There are 94 nodes in total, 32 of which have dual 3.0 GHz processors and 62 nodes have dual 2.4 GHz processors. All of the nodes on this cluster have 70 GB of local hard disk memory space and communicate using a Myrinet 2 interconnect high speed local area networking system. A general parallel file system (GPFS) storage space of 5.7 GB is available to share between the nodes. The condor pool of University of Liverpool consists of the computers in the LAN, most of it have Intel core 2 Duo 2.4 GHz processors and 2 GB memory per machine. A memory of 1 GB is allocated on each of the node during the simulation run time.

4.2.13 Statistical uncertainties

MC dose calculation is associated with statistical uncertainties owing to its stochastic nature of radiation transport. Earlier the statistical uncertainties in BEAMnrc and DOSXYZnrc simulations were calculated using the batch method by splitting the calculation into 10 batches by estimating the uncertainty in the average of the scored quantity of interest. This method proved to have three main disadvantages. The first limitation is that significant fluctuations were found in the estimated statistical uncertainty if small number of statistical batches are used. Secondly, the correlation between particles produced is ignored by grouping the

histories into batches. Finally it results in mass storage of the results of each batch which becomes a problem when dose quantities are scored in a large number of voxels. To overcome these limitations, a history by history method of estimating uncertainties was conceived by Salvat *et al.* [175]. A similar approach has been conceived by Sempau *et al.* [176].

The history by history methods estimates the statistical uncertainty on the scored quantity as expressed in equation.

$$S_{\overline{X}} = \sqrt{\frac{1}{N-1}\left(\frac{\sum_{(i=1)}^{N} X_i^2}{N} - \left(\frac{\sum_{(i=1)}^{N} X_i^2}{N}\right)^2\right)} \tag{4.6}$$

where N is the number of individual histories or events, and X is the scored quantity. The quantities are tracked during the simulations on run time at the end of which the uncertainty is estimated without having the necessity to store quantity in batches.

4.2.14 Absolute dose conversion

This study involves the quantification of differences in absolute doses calculated by various photon dose calculation algorithms. The TPS algorithms automatically calculate the number of MUs required to deliver the prescribed dose whereas MC dose calculation using BEAM/DOSXYZnrc package results in doses expressed as Gy/particle in each and every voxel of the 3D phantom dataset. A method described by Popescu *et al.* [93] was used in our study to convert the MC normalised dose from Gy/particle to Gy. The method for converting MC dose to absolute dose is same for open, conformal, and IMRT plans where correction towards the back scattered dose was included. In case of fields involving dynamic wedges, this term was omitted as the dose back scattered to the monitor IC from the jaws have been automatically accounted for in the EDW routine as explained in section 4.2.8.

The output of the Varian 2100 CD machine is 1 cGy/MU under reference conditions i.e. calibrated to deliver 100 cGy when 100 MUs are set on the linac control console for a 10x10 cm^2 field size at 100 cm source to surface distance

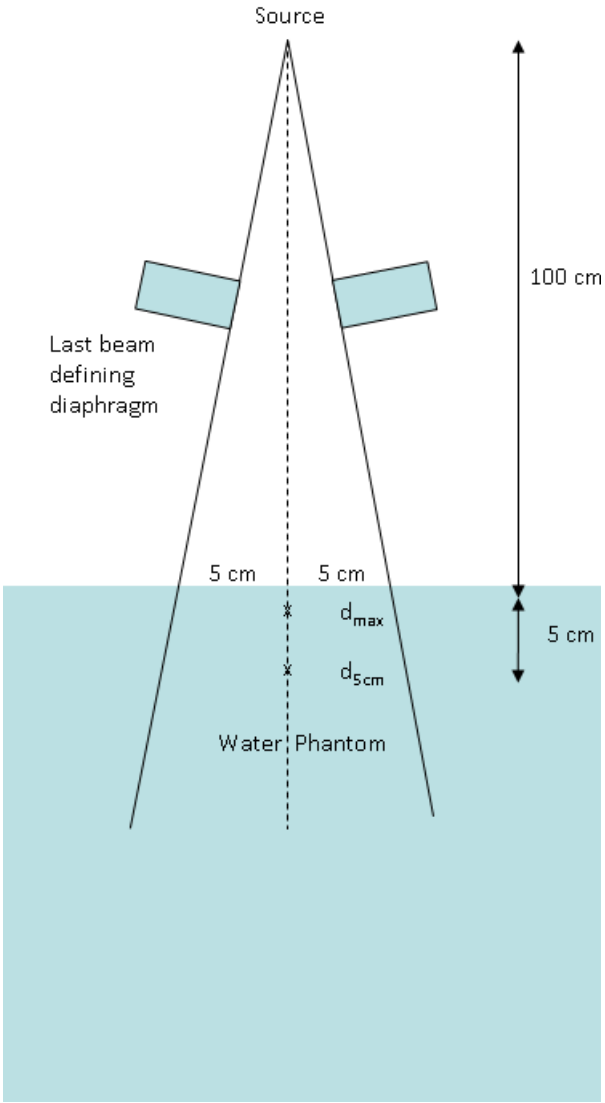

Figure 4.10: Virtual linear accelerator set up for absolute dose calibration using a reference field of 10×10 cm^2 at a depth of d_{max} and SSD of 100 cm. The MC Gy/particle equivalent to deliver 1 MU at reference conditions was determined using this set up.

(SSD) at 1.5 cm which is the depth of maximum dose d_{max} for a 6 MV beam. In order to do the Gy/particle to Gy conversion, it is essential to determine the MC Gy/particle required to deliver 1 cGy at reference conditions given above. A virtual calibration run was performed in a 50×50×50 cm^3 water phantom, where a simulation was done with a field size of 10×10 cm^2, 100 cm SSD.

Open and conformal fields

The following formula has been used for all the calculations performed through out the thesis for open, conformal fields,

$$\mathrm{D_{xyz,abs}} = D_{xyz} \frac{D_{ch}^{forward+back}(10\times10)}{D_{ch}^{forward+back}(x\times y)} \frac{D_{xyz,abs}^{cal}}{D_{xyz}^{cal}} MU \tag{4.7}$$

where D_{xyz} is the MC dose in Gy/particle , D_{xyz}^{cal} is the MC dose at the calibration point in Gy/particle, $D_{ch}^{forward+back}(10\times10)$ and $D_{ch}^{forward+back}$ $(x\times y)$ is the total dose including the forward and back scattered dose accumulated in the monitor chamber for the reference field 10×10 cm^2 and the test field with jaw setting x and y, $D_{xyz,abs}^{cal}$ is the measured absolute dose at 5 cm, MU is the monitor units delivered for that field.

Wedge Fields

For the wedge fields, as explained earlier the back scatter correction term was omitted in the above formula as it has already been included in the EDW routine.

$$\mathrm{D_{xyz,abs}} = D_{xyz} \frac{D_{xyz,abs}^{cal}}{D_{xyz}^{cal}} MU \tag{4.8}$$

where D_{xyz} is the MC dose in Gy/particle , $D_{xyz,abs}^{cal}$ is the MC dose at the calibration point in Gy/particle, D_{xyz}^{cal} is the percentage depth dose at 5 cm, MU is the monitor units delivered for that field.

4.2.15 Dose to medium to dose to water conversion

The MC dose calculation system essentially calculates the dose to the material defined in each voxel. As explained in section 4.2.10 every voxel in the MC

phantom or patient geometry is associated with a pre defined material type and average density specified explicitly by the user or derived from the DICOM CT phantom data set in order to obtain the cross section data to perform radiation transport. It is necessary to convert the dose to medium of each voxel to dose to water in order to compare with the TPS calculated doses. All the TPS algorithms used in this study calculate dose to water except for the CCC algorithm of Oncentra which calculates dose to medium instead. The reason why most of the commercially available TPS algorithms calculate dose to water is because at the beam modelling stage, the input given to these TPSs are depth doses and beam profiles of various field sizes measured in a water phantom. The other reasons being, up to 80% of the human body is composed of water and also many of the radiotherapy dosimetry formalisms such as Technical Report Series (TRS) 398 and Task Group (TG) report 67 recommend determination of absorbed dose to water and not dose to medium [177, 178]. The absorbed dose to medium can be converted to absorbed dose to water as described by Siebers *et al.* [179] by the following equation,

$$\mathrm{D_w} = D_{med} S_{w,med} \tag{4.9}$$

where D_w is dose to water, D_{med} is dose to medium, $S_{w,med}$ is the unrestricted water to medium mass collision stopping power ratio. The unrestricted water to medium stopping power ratio averaged over the energy spectra of secondary electrons is calculated as below.

$$\mathrm{S_{w,med}} = \int_0^{E_{max}} (\Phi_E)_m (S/\rho)_w dE \Big/ \int_0^{E_{max}} (\Phi_E)_m (S/\rho)_{med} dE \tag{4.10}$$

where $(S/\rho)_w$ and $(S/\rho)_{med}$ are unrestricted mass collision stopping powers for water and the voxel medium respectively, $(\Phi_E)_m$ is the energy fluence of the secondary electrons, E_{max} is the maximum energy in the $(\Phi_E)_m$ distribution. As mentioned in the section 4.2.10 in our study we used five materials for the MC phantom derived from DICOM CT dataset namely air, lung, tissue, soft bone and

cortical bone. Fernández-Varea *et al.* [180] have reported differences of up to 3.5% and 14% in the absorbed dose calculated to soft bone and cortical bone between MC and TPS algorithms if the dose to medium to dose to water conversion is not applied. Siebers *et al.* [179] have shown that the stopping power ratio (SPR) is dependent on the beam energy but remains constant throughout a particular material inside and outside the treatment field in the phantom and is insensitive to its dimensions. The SPR of lung and tissue are very close to unity which is that of the water itself and the percentage differences are 0.1% and 1% respectively. The water to medium stopping power ratios used for various materials are given in table 4.1.

Table 4.1: Average water to medium stopping power ratio for 6 MV photon beam (reported by Siebers *et al.*, 2000

Material	Density range [g/cm^3]	$S_{w,med}$
Air	0 - 0.044	1.117
Lung	0.044 - 0.302	0.999
ICRU tissue	0.302 - 1.1	1.010
Soft bone	1.1 - 1.4	1.035
Cortical bone	1.4 - 2.088	1.116

4.2.16 Conversion of 3ddose file to DICOM dose file

The MC dose output file *.3ddose lists the doses in Gy/particle in all the voxels of the MC patient phantom. After converting the doses into absolute doses to water it is necessary to convert this file into DICOM format so that it can be imported in Eclipse TPS for further comparison with dose distributions calculated by other TPS algorithms and also to extract the DVHs and other required plan information. It is to be noted that the MC patient phantom which is created from the DICOM CT images does not have any volumes outlined on it. The MC calculation is done based on the material type and density and the corresponding interaction coefficients for various photon and other types of interactions. A

python routine written by Tony Teke[13] was used to do this conversion where a 3D dose matrix file in DICOM format exported from the TPS is replaced with the MC doses by matching the voxels.

[13]Physics and Astronomy, University of Columbia, Vancouver, Canada.

Chapter 5

Validation of accelerator model in homogeneous and heterogeneous phantoms

5.1 Introduction

An MC dose calculation engine based on BEAMnrc and DOSXYZnrc was set up as outlined in chapter 4. The next step was to validate the virtual accelerator model by fine-tuning it to fit measured beam characteristics of the Varian Clinac 2100 C/D clinical accelerator. This was done by comparing depth doses and beam profiles of clinically relevant field sizes starting from 3×3 cm^2. It was essential to compare measurements and MC calculated doses of open and wedged fields in both homogeneous and heterogeneous cases in order to validate the performance of the MC model in simple and complex geometries and ensure that the assignment of various materials in the MC phantom result in precise dose distribution. This chapter is attributed to the validation of our 6 MV Varian accelerator model in a homogeneous water phantom done with ionisation chambers and in a heterogeneous wooden lung phantom with radiochromic films.

5.2 Methods and Materials

5.2.1 Fine tuning the initial electron parameters

The head of the accelerator was defined according to manufacturer specification as explained in chapter 4. In our model a photon beam of nominal energy 6 MV was generated using a mono-energetic electron beam of energy 6.2 MeV incident on the tungsten target of the accelerator with a radial Gaussian spatial distribution characterised by a full width at half maximum (FWHM) of 1.0 mm. A mono-energetic Gaussian source instead of a spectrum was chosen as previous studies have shown that the influence of the energy spread on the absorbed dose is insignificant [181–183]. This also simplifies the process of bench marking the MC beam model against measurements as it is straight forward to change the electron energy without having to include a new energy spectrum. The initial electron energy and the FWHM values were determined as a process of rigorous bench marking of the virtual linac model to match the beam quality of our treatment unit.

The manufacturer specified electron parameters of 6.0 MeV initial electron energy and 1.0 mm FWHM values were used initially to calculate depth doses of both 10×10 cm^2 and 40×40 cm^2 in water which were compared to the measurements. The initial electron energy was varied in steps of 0.2 MeV and the procedure of computing the MC calculated depth doses were repeated until they matched the measurements within tolerance limits. Once the initial electron energy was fixed, the FWHM was varied in steps of 0.1 mm to match the flatness of the beam profile measurements at 10 cm depth. Once both the depth doses and beam profiles were found to be in reasonably good agreement with the measurements, fine tuning of these parameters were done to match them within tolerances recommended by Venselaar *et al.* [14] over a range of field sizes.

5.2.2 MC calculated depth doses, beam profiles and relative output factors

A water phantom of dimension $50\times50\times50$ cm^3 was constructed with the non-CT phantom option of DOSXYZnrc which was surrounded uniformly by air in all

directions. The voxels along x, y and z directions were defined as groups and the dimensions of the voxels along the x direction were 2.5 mm, 2.0 mm, 1.0 mm and 5.0 mm within the flat region, along the central axis, in the penumbra region and outside the penumbra region respectively. The voxel dimensions along the y and z direction were 2 mm wide. For all the beam profiles, dose in the penumbra region were measured with voxel dimensions $0.1\times0.1\times0.25$ cm^3 in order to precisely record the fall off along the edges of the field. A diagram depicting the virtual MC water phantom in which the depth doses and beam profiles were calculated is shown in figure 5.1.

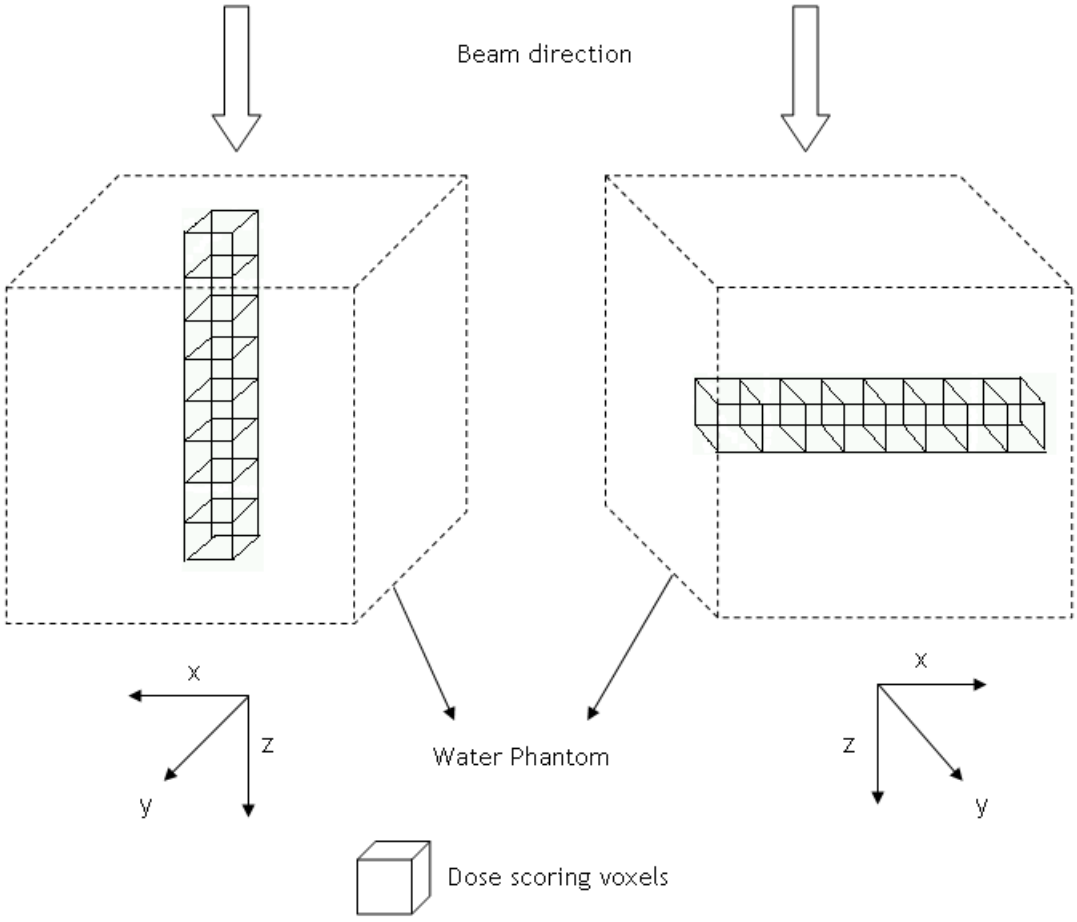

Figure 5.1: MC water phantom and the voxels along which the depth doses and beam profiles were calculated. The phantom dimensions were $50\times50\times50$ cm^3, the depth doses were measured along the central axis of the beam whereas the beam profiles were measured across the central axis at depths d_{max}, 5 cm, 10 cm, 20 cm and 30 cm.

The depth doses and beam profiles of open fields were calculated for field sizes

3×3 cm^2, 4×4 cm^2, 5×5 cm^2, 8×8 cm^2, 10×10 cm^2, 12×12 cm^2, 15×15 cm^2, 20×20 cm^2, 25×25 cm^2, 30×30 cm^2, 35×35 cm^2, 40×40 cm^2 along the central axis and at depths 1.5 cm (d_{max}), 5.0 cm, 10.0 cm, 20.0 cm, 30.0 cm respectively. It would be appropriate to mention here that none of the treatment fields used in the patient plans presented in the following chapters of this thesis were larger that 20×20 cm^2.

The absolute dose conversion of the doses calculated with MC were done using the method proposed by Popescu *et al.* [93] which is described in section 4.2.14 of chapter 4. The relative output factor (ROF) is defined as the ratio of output of the field of interest to that of the reference field at a reference depth in a water phantom. According to the recommendation these were measured at 10 cm depth of each field defined at 100 cm SSD on a homogeneous water phantom. The ROF is calculated by the formula below,

$$\mathrm{ROF} = \frac{D_{xyz,abs}(x\times y)}{D_{xyz,abs}(10\times 10)} = \frac{D_{xyz}(x\times y)}{D_{xyz}(10\times 10)}\frac{D_{ch}(10\times 10)}{D_{ch}(x\times y)} \tag{5.1}$$

where $D_{xyz,abs}(x\times y)$, $D_{xyz}(x\times y)$ and $D_{ch}(x\times y)$ are the absolute dose [Gy], relative dose [Gy/particle] and the dose accumulated in the monitor IC of the field of investigation [Gy/particle] respectively. Similarly, $D_{xyz,abs}(10\times 10)$, $D_{xyz}(10\times 10)$ and $D_{ch}(10\times 10)$ are the absolute dose, relative dose and the dose accumulated in the monitor IC of the reference field 10×10 cm^2 respectively.

The uncertainties 1σ of the dose scored in the monitor IC of all the field sizes were kept as low as 0.2% and the uncertainties of the dose scored in the voxel at 10 cm depth for the range of field sizes were less than 1% except for the 40×40 cm^2 field for which the uncertainty was 1.7%. The percentage differences of the ROFs for all of the fields were well within 2% which is similar to those reported by Popescu *et al.* [93].

The EDW of the Varian 2100 C/D was modelled using the CM EDW as explained in section 4.2.7 of chapter 4. The depth doses along the central axis and beam profiles at d_{max}, 5 cm and 10 cm of 6 MV photon beam incident on a water phantom at 95 cm SSD were calculated using the MC simulations. The minimum wedge field possible was 4×4 cm^2 and the maximum being 20×20 cm^2.

Two wedge angles, 30° and 60° , both IN and OUT orientations in which the Y1 jaw and the Y2 jaw sweeps across the fields respectively until they touch the other jaw of the same pair of three field sizes 4×4 cm^2, 10×10 cm^2 and 20×20 cm^2 were simulated. The depth doses of the EDW fields of 30° and 60°, in both IN and OUT orientations were calculated along the voxels of dimensions 0.2×0.2×0.2 cm^3 along the central axis up to 30 cm depth from the surface of the phantom. The beam profiles of the EDW fields of both 30° and 60°, IN and OUT orientation for all the three field sizes were calculated at depths d_{max}, 5 cm and 10 cm.

5.2.3 Water tank measurements

The depth dose and beam profile measurements which were done in our clinic as a part of routine QA were used as the golden data set to match the MC calculated doses. A 3D radiation field analyser (RFA) MP3-M phantom[1] was used along with two RK ionisation chambers[2] of volume 0.12 cm^3, length 10 mm and inner diameter 4 mm, out of which one was used as a field chamber and another as a reference chamber. The depth doses along the central axis and the beam profiles at depths d_{max}, 5 cm, 10 cm, 20 cm and 30 cm of open fields ranging from 3×3 cm^2 to 40×40 cm^2 with an SSD of 100 cm were measured. MEPHYSTO mc^2 software[3] was used to record these measurements. The output factors of the open fields were measured at 10 cm depth. The above measurements were all in relative units.

The treatment unit was tuned to deliver 100 cGy at d_{max} when 100 MUs are set on the control console for an open field of 10x10 cm^2 defined by the jaws at 100 cm SSD. The d_{max} of 6 MV beam of our treatment unit is 1.5 cm. The relative depth doses and beam profiles were converted into absolute doses using the absolute dose conversion explained in section 4.2.14 of chapter 4 and the measured output factors of non-reference field sizes.

The measurements for the EDWs[4] were done by a linear detector array, LDA99[5]. made of 99 p-type semiconductor diodes with 5 mm spacing between the diodes.

[1]PTW, Frieburg, Germany.
[2]Scanditronix-Wellhöffer, Schwarzenbruck, Germany.
[3]PTW, Frieburg, Germany.
[4]Varian Medical Systems, Palo Alto, CA, USA.
[5]IBA Dosimetry GmBH, Schwarzenbruck, Germany.

The depth doses along the central axis and the beam profiles at depths d_{max}, 5 cm and 10 cm of field sizes 4×4 cm^2, 10×10 cm^2, 20×20 cm^2 for 30° and 60° wedges of both IN and OUT orientations were measured.

5.2.4 Wooden lung phantom geometry

A wooden thorax phantom made of medium density fiber board (MDF) of dimensions 30×30×30 cm^3 (ρ=0.6 g/cm^3) with lung inserts in the shape of lung made of balsa wood (ρ=0.16 g/cm^3) was constructed in the work shop. A relatively high density spherical tumour made of MDF of density 0.55 g/cm^3 and diameter 2 cm was inserted inside the left lung at its centre. 3D conformal single anterior field treatment plans were done with 0 mm and 17 mm (denoted as GTV0 and GTV17 respectively) MLC margins around the GTV with a prescription dose of 2.75 Gy to the at the isocentre which was positioned at the centroid of the GTV. In addition, a five field SABR plan (GTVSABR) with tight margins around a new PTV created with 5 mm margin around the GTV (the PTVs were created with two margins in order to cater to 3DCRT and SABR treatment techniques). A prescription dose of 2.75 Gy to the 75% isodose line in a single fraction was given. The relative dose at the geometric centre of the GTV was up to 100%. The treatment plans were done with PBC_{MB} and the resulting MUs were used to recalculate the dose with other *type a*, *type b* and MC algorithms.

5.2.5 EBT2 films

Gafchromic film dosimetry was chosen for the measurements attributing to the characteristics such as high spatial resolution, lack of energy dependence, tissue equivalence, insensitivity to visible light, no post-exposure film processing [184–186]. The version of gafchromic films called as EBT2[6] films were used in this study. The EBT2 films are made of a polyester substrate of 175 μm over which there is an active film layer of 28 μm. An adhesive layer and a polyester over-laminate of thickness 25 μm and 50 μm respectively sit on the active layer. Figure 5.2 depicts the layers of an EBT2 film. A yellow marker dye is added to the EBT2 film which makes it different from the previous EBT films. This marker

[6]ASHLAND specialty ingredients, New Jersey, USA.

dye enables the possibility to correct for the imperfections in the thickness of the active layer coating when the analysis is done using the response of the red green blue (RGB) channels [187, 188]. The effective atomic number Z_{eff} of EBT2 films is 6.84 and the densities of its components range from 1.2-1.35 g/cm^3.

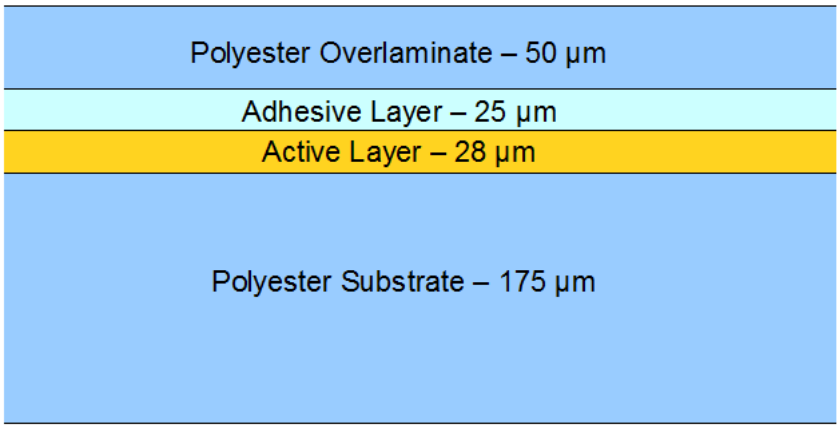

Figure 5.2: Layers of polyester laminate, adhesive and active component on a polyester substrate of an EBT2 film (reproduced from the Gafchromic EBT2 white paper).

5.2.6 Film calibration and irradiation of verification films in solid water and wooden lung phantoms

To begin with pieces of gafchromic films of dimensions 5x5 cm^2 were cut out from the same batch and irradiated with known doses. The 0 Gy film represents the unirradiated or the control film. The films were irradiated with our MC modelled 6 MV Varian 2100 CD[7] linac beam in a solid water phantom at 5 cm depth, 95 cm SSD and a field size of 10×10 cm^2. A solid water slab of thickness 5 cm was placed under the film for back scatter. Prior to irradiation of the films the output of the accelerator on the day of measurement was noted down in order to account for any discrepancy in the daily output of the machine. This was done in a water phantom with an SSD of 100 cm, field size 10×10 cm^2, depth 5 cm with a farmer ionisation chamber of volume 0.625 cm^3. The output of the machine at d_{max} was calculated by applying necessary correction factors to the dose measured at 5 cm depth.

Along with the calibration films, square films of dimensions 5×5 cm^2, 7×7 cm^2,

[7]Varian Medical Systems, Palo Alto, CA, USA.

12×12 cm^2 were cut out and irradiated with a pre-planned dose of 2.75 Gy with field sizes 3×3 cm^2, 5×5 cm^2, and 10×10 cm^2 at an SSD of 95 cm at 5 cm depth with the film sandwiched between solid water phantom slabs of thickness 5 cm each. This was done in order to cross verify the accuracy of gafchromic film doses in homogeneous cases before doing the irradiation on the heterogeneous thorax phantom. For the thoracic phantom irradiation, the EBT2 films were cut out into 'D' shapes in order to fit into the lung insert. The D shaped films were placed in between two equal sized lung inserts with half of the tumour at the centre of each of them. Before irradiating the films, the thorax phantom was scanned in Brilliance[8] CT scanner. The scanned images were transferred to the Eclipse TPS[9] in DICOM format where the GTV was contoured based on the spherical tumour insert seen on the transverse sections of the CT images. The GTV was expanded with a margin of 10 mm isotropically to create a PTV. The PTV was essentially the low density lung volume of balsa wood surrounding the high density MDF tumour insert. Both the lungs were contoured as a single organ using the auto contouring option of Eclipse.

5.2.7 Irradiation, scanning and analysis of the films

All the treatment plans were exported to ARIA[10], record and verify (R&V) system and the plans were delivered on the solid water and thorax lung phantom with the gafchromic films with Varian 2100 CD linac 6 MV beam which was used for the MC modelling. Care was taken while handling the films in order to avoid mechanical stress or strain and gloves were worn at all times to prevent the registration of finger prints on the films which will alter the results. The calibration films and the homogeneous phantom were irradiated first which was then followed by the heterogeneous phantom plan irradiation. Except for the calibration films, all the other films were irradiated isocentrically with single and multiple fields corresponding to 3DCRT and SABR plans. The films were stored in light and moisture tight envelopes for 24 hours before analysis to account for any post-irradiation changes. The active layer of gafchromic films contain a

[8]Philips Healthcare, Andover, MA, USA.
[9]Varian Medical Systems, Palo Alto, CA, USA.
[10]Varian Medical Systems, Palo Alto, CA, USA.

monomer gel which upon irradiation undergoes a polymerisation reaction which results in darkening of the films. The higher the dose, the darker the film.

The films were scanned using an EPSON Perfection V750 Pro[11] flatbed scanner. All the films were scanned in landscape mode with the notch of the film oriented in the same position. The scanner was warmed up 30 minutes before the scan and the total scanning time was less than one hour. The scanner settings were in place according to those suggested by the manufacturer of gafchromic films so as to keep any discrepancies arising from scanning of the films to a minimum. The films were scanned in professional mode, 48-bit colour, 16-bit per channel, with a resolution of 240 dpi (measurement 1) 72 dpi (measurements 2 and 3 as recommended by Matrtišíková *et al.* [189]) and all the colour correction options were turned off in order to measure the true optical density (OD). The scanned films were saved as tagged image file format (TIFF) images and were analysed using Gafchromic reader developed by Colin Baker[12], an in-house film scan reader and analysis software written in MATLAB v.7.6.0 R2008a[13] to compare the MC calculated doses with measurements. Micke *et al.* [190] have recommended the use of triple channel dosimetry for radiochromic film evaluation in order to separate the dose dependent and dose independent components that arise due to the variation in the thickness of active layer of the film and artefacts associated with scanning. This improves the dosimetric accuracy. In our study, three different sets of measurements were performed at different times, two with dual channel and one with single channel dosimetry as the first set of measurements did not give satisfactory results. Triple channel dosimetry was not performed as the in-house gafchromic reader did not have the capability of correcting dose response differences due to scanning related artefacts. The descriptions of the procedures of all three measurement sets are listed below.

Measurement 1: 13 film pieces of 5×5 cm^2 were irradiated with 0.5 Gy equal intervals from 0-6 Gy. The first set of measurements include open field measurements in a homogeneous solid water phantom along with GTV0 and GTV17 plans in the wooden lung phantom, only red channel OD was used for analysis.

[11]Sieko Epson Corporation, Nagano, Japan.
[12]Department of Physics, Clatterbridge Cancer Centre, Wirral, UK.
[13]MathWorks, Natick, MA, USA.

The calibration films and test films were placed at the centre of the scanner and scanned using film area guide by grouping them together depending upon the number of pieces the scanner could hold at a time.

Measurement 2: The second set of measurements were done for open fields in homogeneous phantom along with GTV0, GTV17, GTVSABR plans (anteriorly) and GTV0inv, GTV17inv in which case the single direct fields were irradiated by turning the wooden lung phantom upside down. The scanning protocol was similar to the one used for measurement set 1. Only in this case, both red and blue channels were used for analysis. Three different sheets of film from the same batch were used in this trial. Three small cut outs of 5×5 cm^2 similar to the calibration films were taken off from each of the three sheets and were irradiated to low, medium and high doses to which the calibration films were irradiated in order to account for differences in the response of different films of the same batch.

Measurement 3: Finally, measurements similar to the second set (measurement 2) were repeated except for a different scanning procedure done according to the scanning protocol established in the department recently which is based on Huet *et al.* [191]. After warming up the scanner for 30 minutes for 5 times with a gap of 2-5 minutes between previews, each film piece was placed at the centre of the scanner using customised transparent acetate jigs which were made to increase the reproducibility of placement of the film pieces at the centre of scanner bed. Preview of the scan area was done only with the jig placed on the scanner as the warming up of the film during the preview process might influence the OD when scanned. The films are slightly concave and hence were scanned with the curved side (centre) up in order to avoid formation of Newton's rings. Calibration films were irradiated to 0.1, 0.5, 1.0, 5.0 and 8.0 Gy with the same set up as explained in section 5.2.7. Consecutive scans were done with a gap of 2-5 minutes and any scan with a larger gap in between was done after repeating the scanner warm up procedure. Only red channel OD was used for the analysis.

The ODs of the RGB channels were read separately for all the films. In case of measurements 1 and 3 only red channel OD were used whereas for measurement

2, the ODs corresponding to the red channel were recorded and corrected by the OD of the blue channel according to the method explained by Micke *et al.* [190]. Individual calibration curves were plotted with dose in Gy along the x-axis and OD along the y-axis. The red channel OD corresponds to changes in the colour of the film due to the dose delivered whereas the blue channel OD accounts for the differences in the response of the films that arise due to other factors like non-uniform thickness of the active layer coating. A third order polynomial function was used to fit to the points and the plotted calibration curve was saved in the form of a text file. These calibration curves were used to analyse the test plans using the Gafchromic reader. In case of measurement set 3, only red OD was used and a rational function was used to fit to the points. In all the cases, horizontal (along x axis) and vertical profiles (along y-axis) through the central slice of the tumour were recorded and exported for analysis.

5.3 Results and Discussion

5.3.1 Depth doses and beam profiles of open fields

The depth doses and beam profiles of open fields of MC and measurements are shown in this section. The results of only the fields 3×3 cm^2, 4×4 cm^2, 5×5 cm^2, 10×10 cm^2, 20×20 cm^2, 40×40 cm^2 are shown. The doses and the corresponding differences between MC and measurements are expressed in terms of Gy/MU as in our study we are comparing the absolute doses calculated by various analytical algorithms and MC with same number of MUs. The dose at each point along the central axis of the beam and across the central axis is tied to the number of MUs delivered per each beam. The following MC depth doses and beam profiles were calculated with 100 MUs and the measurements in terms of absolute dose units were derived from the relative measurements, output factors and absolute dose for which the accelerator is tuned to deliver at the isocentre at reference conditions.

Venselaar *et al.* [14] have recommended that the match between the measured and calculated depth doses beyond the depth of maximum dose should be less than or equal to 2% dose difference (DD) within a distance to agreement (DTA)

of 2 mm. The combination of dose difference and distance to agreement analysis is necessary as the former is extremely sensitive to the differences at places where there are steep dose gradients and the latter is extremely sensitive to shallow dose gradients. Considering just one of the above two criteria may lead to either over estimation or under estimation of the differences and hence in this study both have been considered together. It is evident from the plots below that relative differences between the measured and calculated local doses satisfy the criteria of 2%/2mm over the range of investigated field sizes. As this study involves the comparison of absolute doses, plot of differences in the dose rate at each point along the central axis of the beam is also shown in the following figures. Our MC beam commissioning results show that the differences in the calculated and measured output values in each dose voxel is $\pm$ 0.02 cGy/MU.

Overall, excellent match between the measurements and the MC calculated open field depth doses and beam profiles were found. For the open field beam profiles, Venselaar *et al.* [14] have recommended a match criteria of 3%/3mm over the range of field sizes and depths. A detailed analysis of the results show that the MC overestimates the doses for smaller field sizes of 3×3 cm^2, 4×4 cm^2, and 5×5 cm^2 whereas it underestimates the doses for the field sizes larger than the reference field size 10×10 cm^2. This could be due to the effect of correction for back scattered dose in the monitor IC. The JAWS CM models the movement of the jaws along an axis perpendicular to the central axis of the beam whereas in reality in the accelerator Varian 2100 C/D, the jaws are pivoted and move along a sphere. The effective distance of the jaws from the monitor IC is not the same due to this movement.

The choice of the initial electron parameters such as the energy of the electron incident on the tungsten target, the radial intensity distribution and the energy spread of the electron beam are crucial in order to match the MC calculated doses with the measurements for a range of field sizes. Previous studies have shown that the depth doses are sensitive to the mean electron energy while they remain insensitive to the radial intensity Gaussian distribution, FWHM and the energy spread of the electron source [181–183]. On the other hand, the flatness of the beam profiles are sensitive to both the initial electron energy and radial intensity

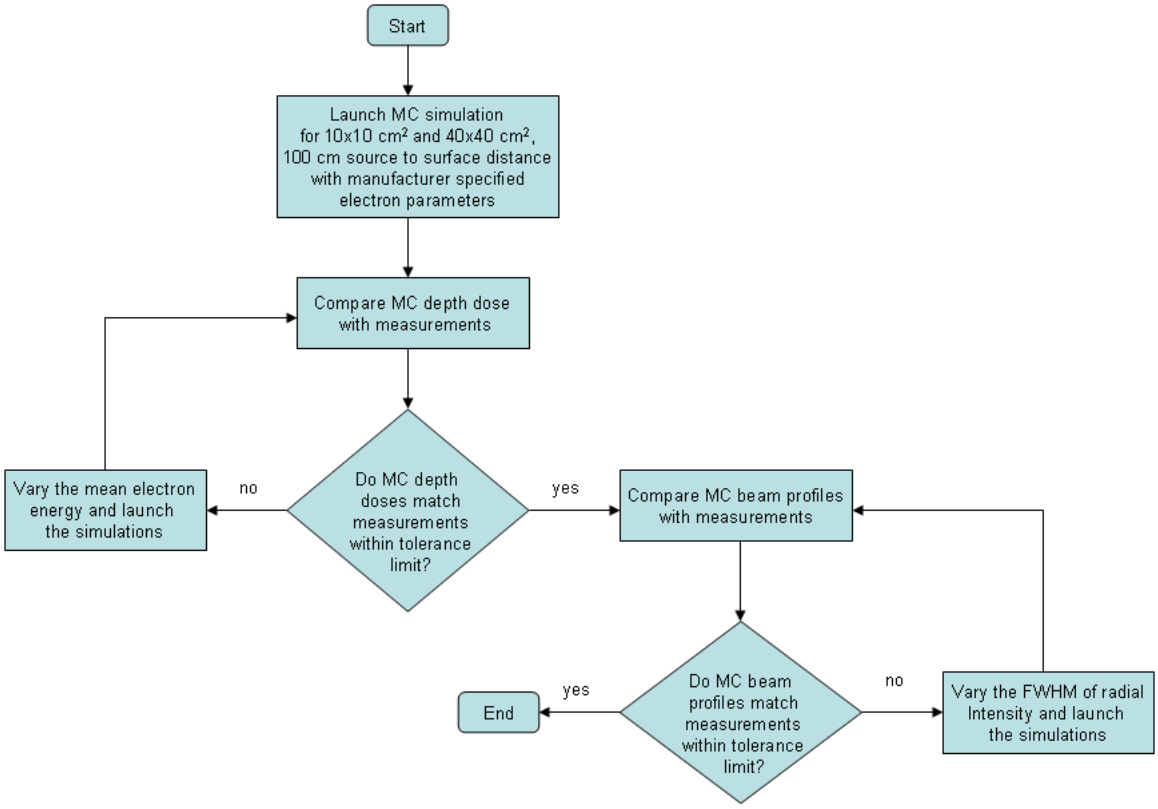

Figure 5.3: Workflow of the validation of the accelerator model. The initial electron parameters, mean electron energy and FWHM were assigned as 6 MeV and 0.1 cm according to the manufacturer specifications. Best match of these two parameters were found iteratively by comparing the MC depth doses and beam profiles against measurements.

distribution of the electron source but is insensitive to the energy spread of the electrons. They are not totally insensitive to the initial electron energy as the height of the horns decrease with increasing electron energy. The reason for such an effect on the horns is three fold: (1) the angular deflection of the electron decreases (2) the resulting photon spectrum is harder (beam hardening) which increases the transmission at the centre of the flattening filter (3) the angular distribution of the bremsstrahlung photons produced in the target is narrower as discussed by Sheikh-Bagheri *et al.* [181].

All the calculations were performed with sufficient number of initial histories in order to achieve statistical uncertainty 1σ less than 1% in all the voxels along the central axis of the beam to plot the depth dose and across the central axis of the beam at various depths except for the 40×40 cm^2 field where 1σ was within 2%. The number of histories simulated increased with increasing field sizes, or

the 3×3 cm^2 field the initial number of electron histories were 1 billion, 7 billion for 10×10 cm^2 and 22 billion for 40×40 cm^2. The number of histories required is a function of the side of the field, size of the voxel in which the dose is scored and the uncertainty limit set.

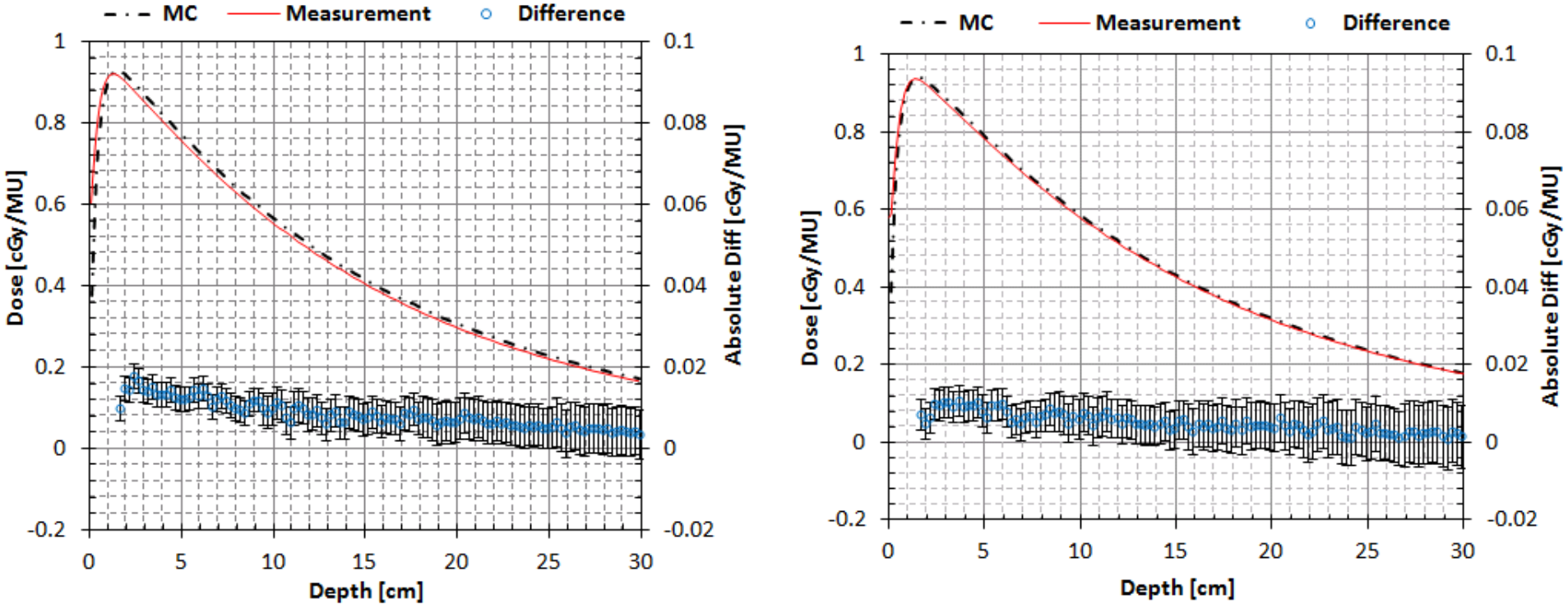

(a) (b)

Figure 5.4: Depth doses along the central axis of 6 MV photon beam of open fields with field sizes (a) 3×3 cm^2 (b) 4×4 cm^2. The dashed black lines represent MC depth doses, solid red lines represent the measured depth doses and the blue scatter points and solid line represent the differences between the measured and MC depth doses. The error bars denote the statistical uncertainty 1σ of MC dose calculation.

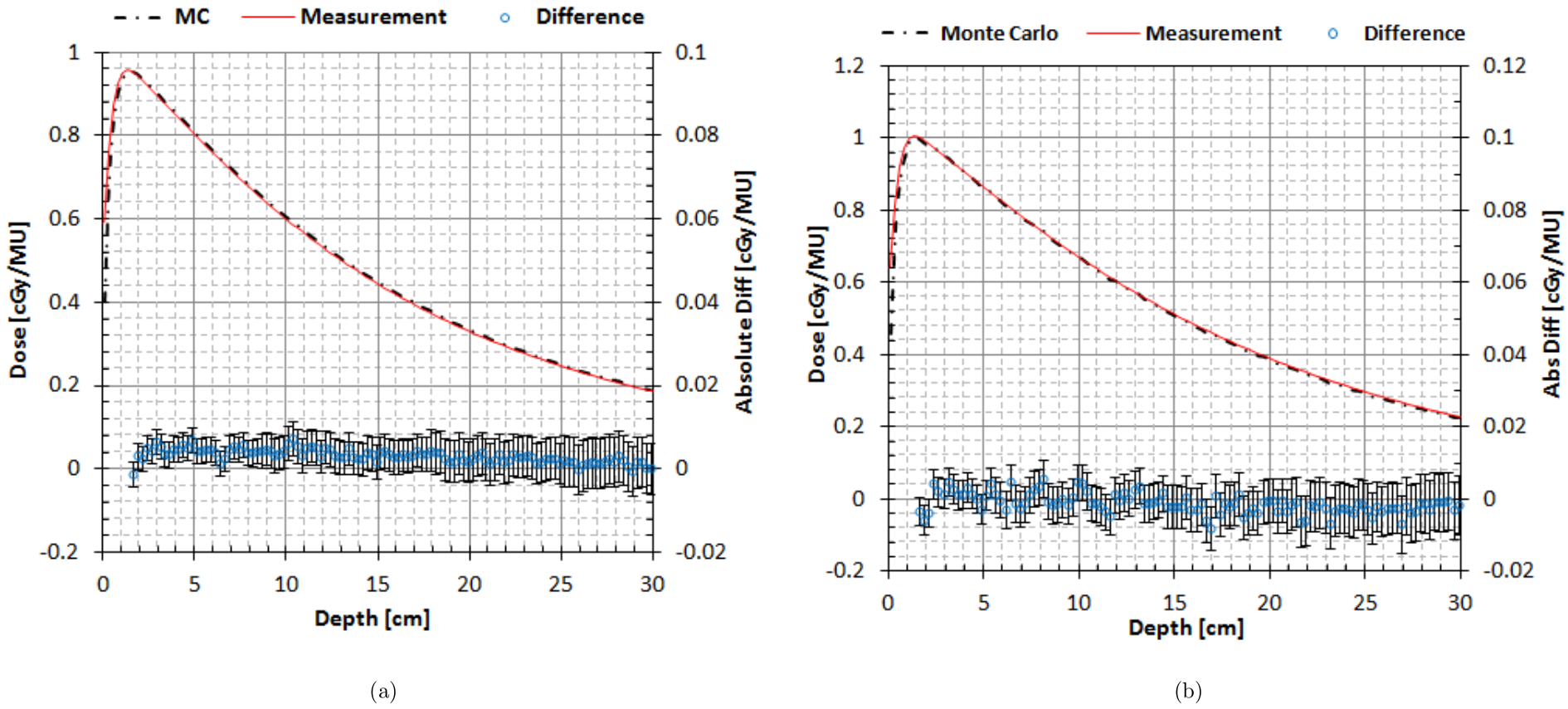

(a) (b)

Figure 5.5: Depth doses along the central axis of 6 MV photon beam of open fields with field sizes (a) 5×5 cm^2 (b) 10×10 cm^2 . The dashed black lines represent MC depth doses, solid red lines represent the measured depth doses and the blue scatter points and solid line represent the differences between the measured and MC depth doses. The error bars denote the statistical uncertainty 1σ of MC dose calculation.

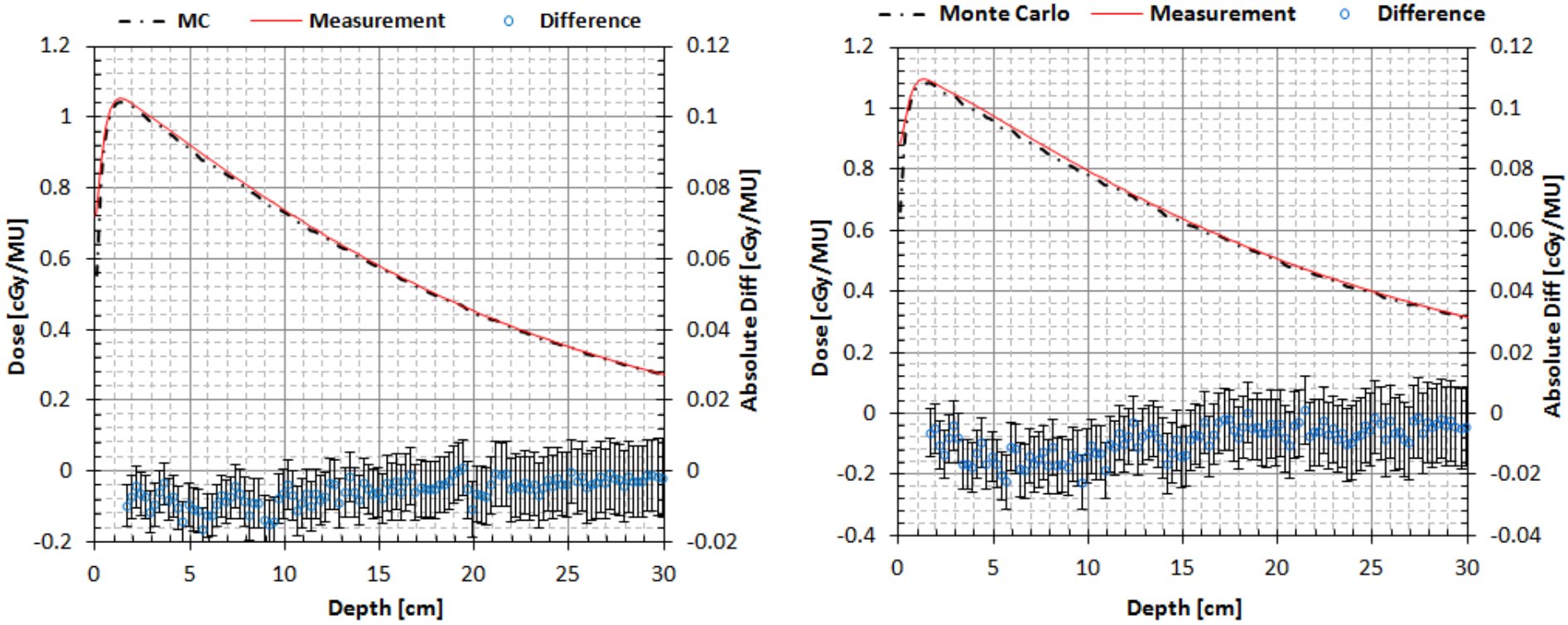

(a) (b)

Figure 5.6: Depth doses along the central axis of 6 MV photon beam of open fields with field sizes (a) 20×20 cm^2 (b) 40×40 cm^2. The dashed black lines represent MC depth doses, solid red lines represent the measured depth doses and the blue scatter points and solid line represent the differences between the measured and MC depth doses. The error bars denote the statistical uncertainty 1σ of MC dose calculation.

Sheikh-Bagheri *et al.* [181] have performed an extensive study to show the sensitivity of the MC calculated dose distributions in terms of depth doses and beam profiles to various parameters like the mean electron energy, radial intensity distribution of the electron beam, divergence of the electron beam, energy distribution of the electron beam, upstream opening of the primary collimator, material and density of the flattening filter, angle of incidence of the electron beam, and lateral dimensions of the target. Out of all of these parameters, for our accelerator model we had to select the first two parameters by trial and error and the rest of the parameters did not influence much the dose distributions or were taken care of by the accurate specification of the accelerator head CMs.

The depth dose curves along the central axis of 6 MV photon beam incident on a homogeneous water phantom at 100 cm SSD with field sizes 3×3 cm^2, 4×4 cm^2, 5×5 cm^2, 10×10 cm^2, 20×20 cm^2, 40×40 cm^2 are shown in figures 5.4 to 5.6. The depth doses were calculated in 0.2×0.2×0.2 cm^3 voxels along the central axis of the beam up to 30 cm depth from the surface of the phantom. The beam profiles of the open fields were calculated at depths d_{max}, 5 cm, 10 cm, 20 cm and 30 cm and the results are shown in figures 5.7 to 5.9. Good agreement between the calculated and measured doses in all the points except for the build up region in the depth dose curves and the field edges of the beam profiles. The depth doses predicted by MC in the build up region are always smaller that that of the measured doses owing to the wall thickness and finite size of the ionization chamber used for measurements. The uncertainties in the voxels along the central axis of the beam increases with increase in depth. The deviations between the measured and MC calculated absolute values of the depth doses are larger in the shallower depths after the d_{max}, the region where transient charged particle equilibrium (TCPE) is established and decreases with increasing depths for all the field sizes reported. This is due to the fact that the magnitude of the absolute doses delivered per MU are larger at shallower depths than at the deeper depths and the differences are plotted in terms of absolute differences rather than relative differences in local doses. If the same plots were drawn with relative differences the deviations would be smaller for shallower depths and larger for deeper depths.

The deviations at the shallower depths decrease with increasing field sizes and

the differences are positive for the fields smaller than the reference field whereas negative for the larger fields. The differences of the smaller and the larger fields at deeper depths tend to converge towards the axis.

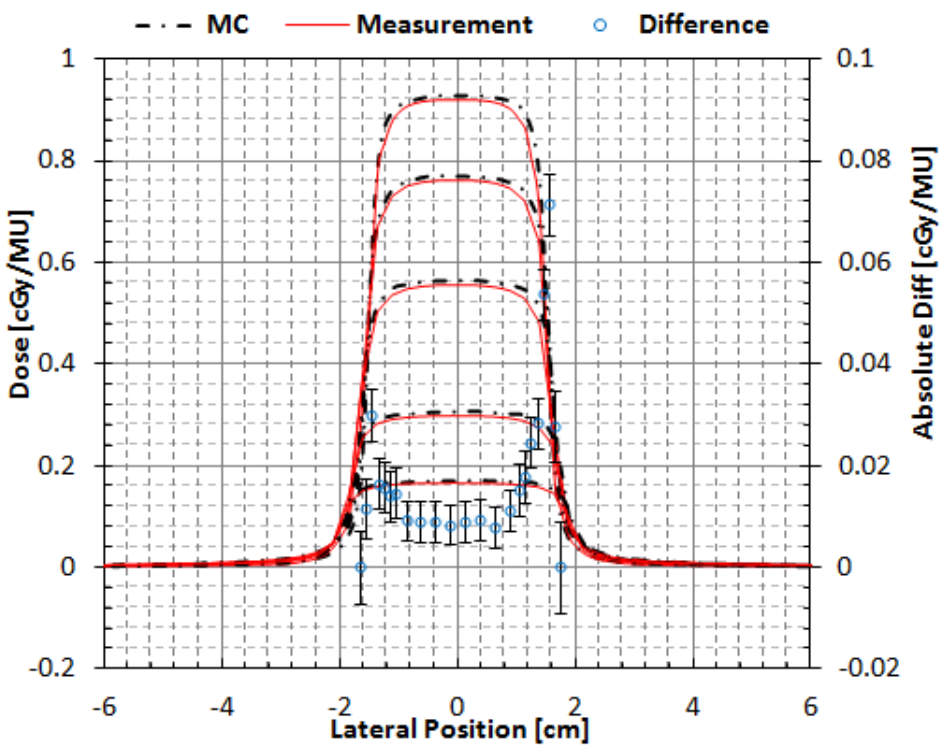

(a)

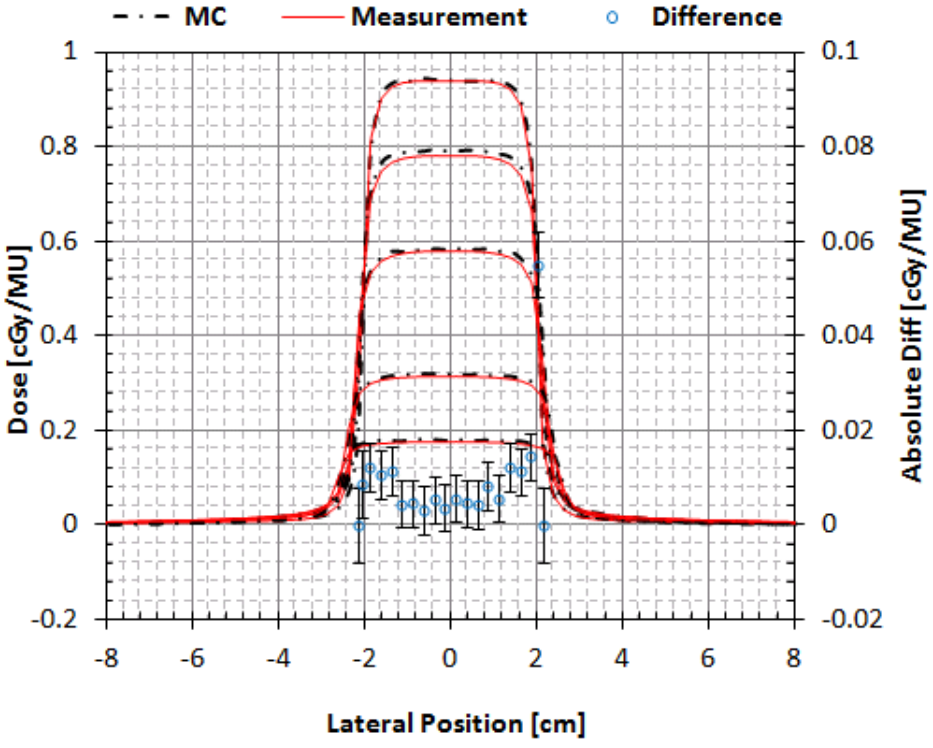

(b)

Figure 5.7: Beam profiles across the central axis of 6 MV photon beam of open fields with field sizes (a) 3×3 cm^2 (b) 4×4 cm^2. The dashed black lines represent MC depth doses, solid red lines represent the measured depth doses and the blue scatter points and solid line represent the differences between the measured and MC depth doses. The beam profiles were measured at d_{max}, 5 cm, 10 cm, 20 cm and 30 cm.

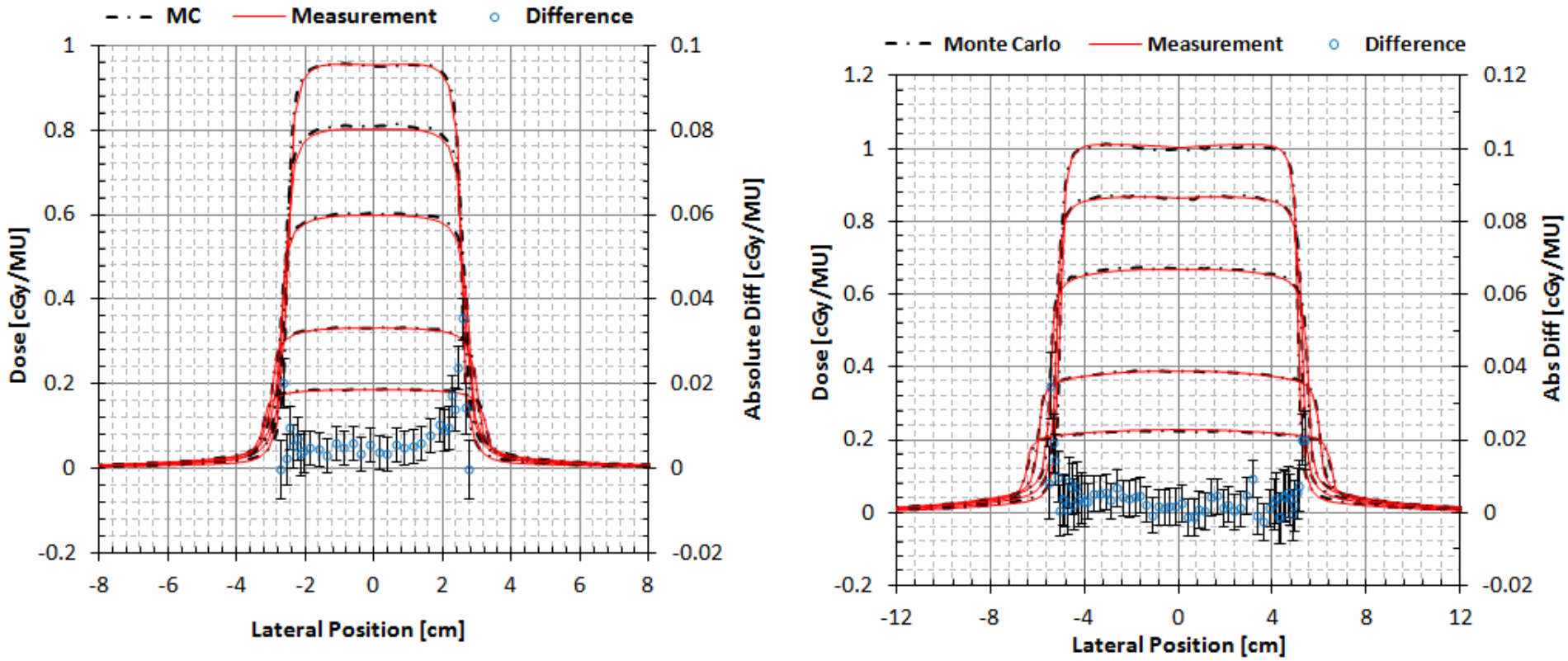

(a) (b)

Figure 5.8: Beam profiles across the central axis of 6 MV photon beam of open fields with field sizes (a) 5×5 cm^2 (b) 10×10 cm^2. The dashed black lines represent MC depth doses, solid red lines represent the measured depth doses and the blue scatter points and solid line represent the differences between the measured and MC depth doses. The beam profiles were measured at d_{max}, 5 cm, 10 cm, 20 cm and 30 cm.

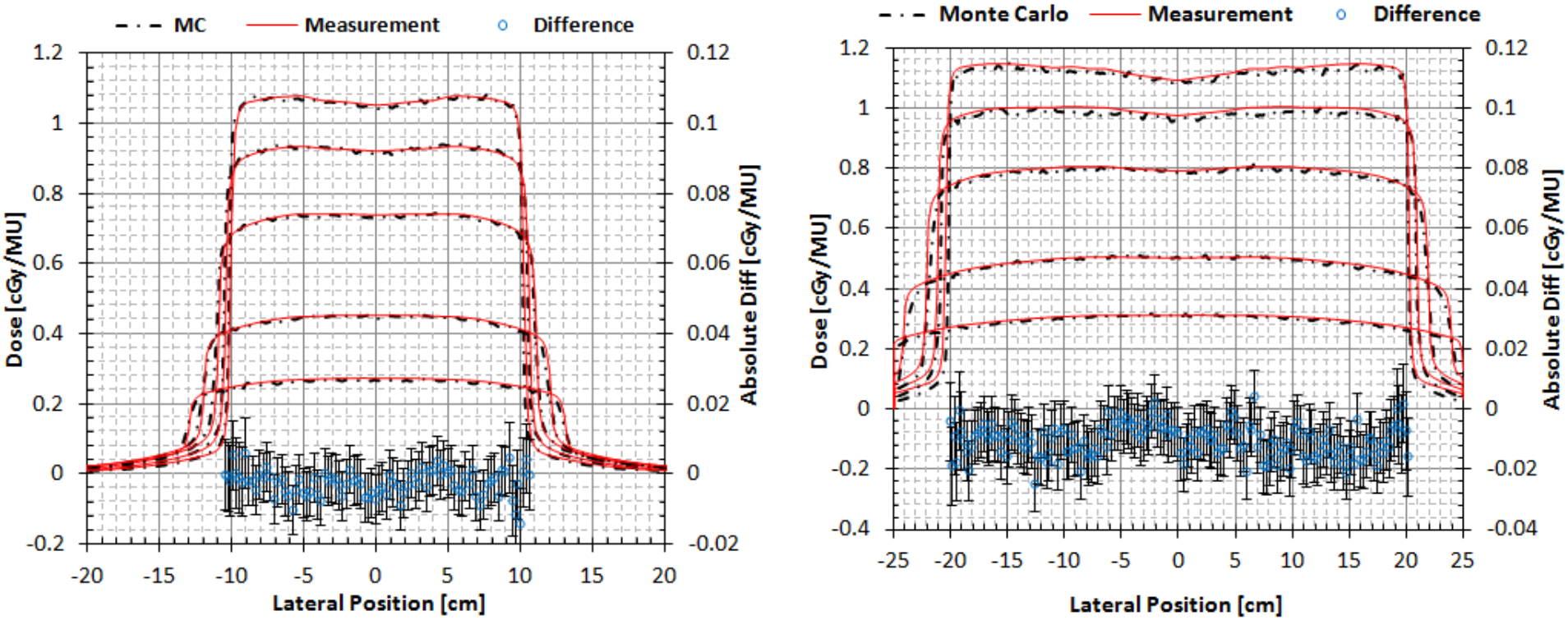

(a) (b)

Figure 5.9: Beam profiles across the central axis of 6 MV photon beam of open fields with field sizes (a) 20×20 cm^2 (b) 40×40 cm^2. The dashed black lines represent MC depth doses, solid red lines represent the measured depth doses and the blue scatter points and solid line represent the differences between the measured and MC depth doses. The beam profiles were measured at d_{max}, 5 cm, 10 cm, 20 cm and 30 cm.

5.3.2 Output factors of open fields

Figure 5.10 shows the ROFs plotted as a function of the field size. From the graph it is evident that the MC calculated ROFs are higher than the measured ROFs for fields smaller than the reference field size 10×10 cm^2 whereas it is lower for larger fields.

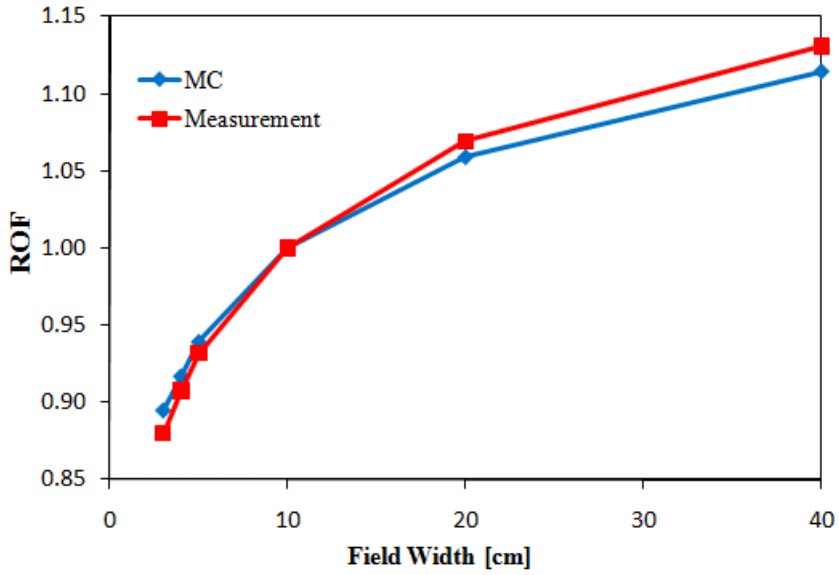

Figure 5.10: MC output factors of field sizes 3×3 cm^2, 4×4 cm^2, 5×5 cm^2, 10×10 cm^2, 20×20 cm^2, and 40×40 cm^2 against measurements. MC overestimates the output factors smaller than the reference field 10×10 cm^2 and underestimates that of the larger fields. The statistical uncertainties of the MC dose calculation was within 1% (1σ) for all the fields except 40×40 cm^2 in which case it was up to 2%.

5.3.3 Depth doses and beam profiles of enhanced dynamic wedges

The plots comparing the depth doses of EDW fields for the range of above mentioned field sizes are shown in figures 5.11 to 5.16. The depth dose curves of a particular wedge angle and field size with different orientations seem to match very well. The results of the beam profiles are shown in figures 5.17 to 5.22. The beam profiles of a given field size and wedge angle for two different orientations IN and OUT are mirror images of each other with the heel and toe region interchanged as in the former the Y1 jaw sweeps across the field and reaches the Y2 jaw whereas in the latter it is vice-versa. Similar to the results of the open

field depth doses and beam profiles, the wedge field dose distributions exhibit a trend where in the doses of smaller field size are over estimated and the field size larger than the reference field of 10x10 cm^2 are under estimated due to the short comings in modelling of the pivoted jaws of the Varian accelerator. The back scatter to the monitor IC is modelled as a linear function of the dynamic jaw position across the field. The differences in the absolute doses between the measured and MC calculated depth dose values at shallower depths are larger than that of those at deeper depths similar to the open fields.

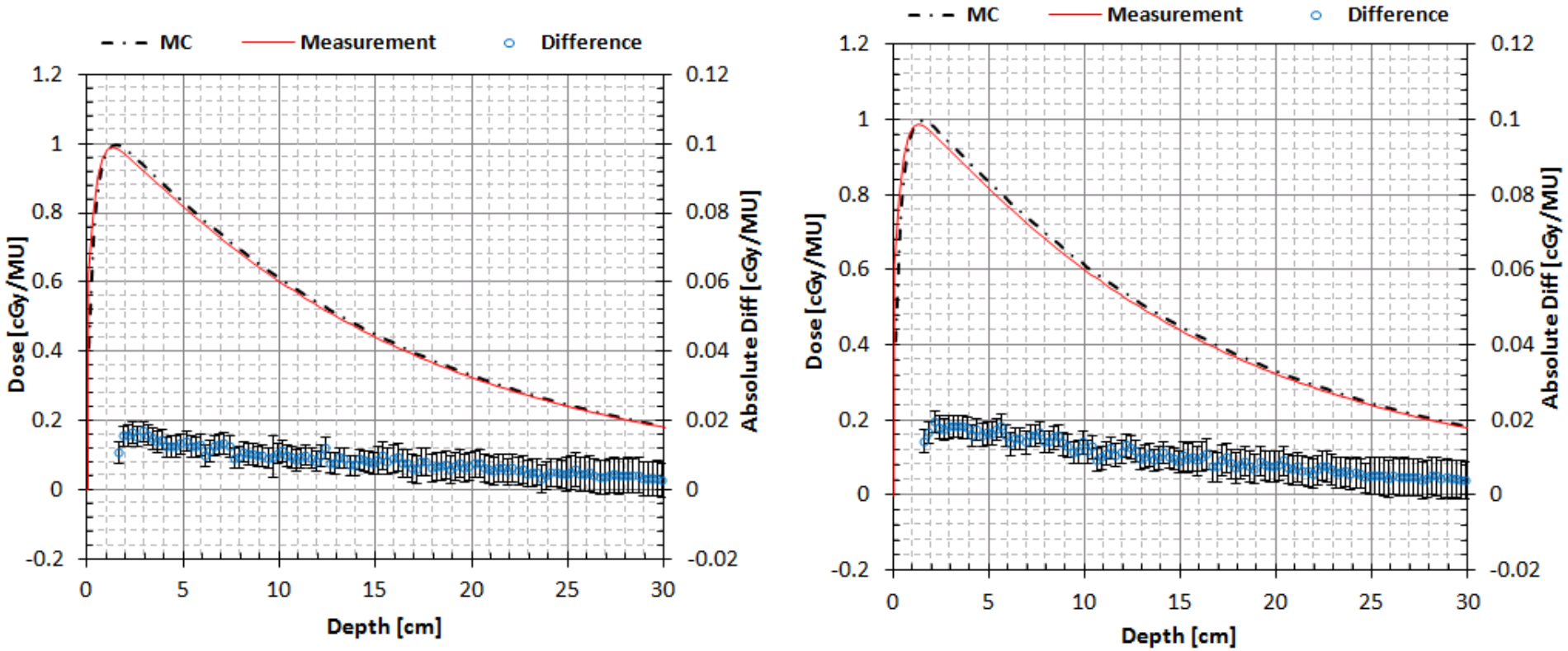

(a) (b)

Figure 5.11: Central axis depth doses of EDW fields (a) 30° IN 4×4 cm^2 (b) 30° OUT 4×4 cm^2. The black dashed lines represent the MC depth doses, the solid red lines represent the measured depth doses and the blue triangular symbols represent the differences between them in cGy/MU.

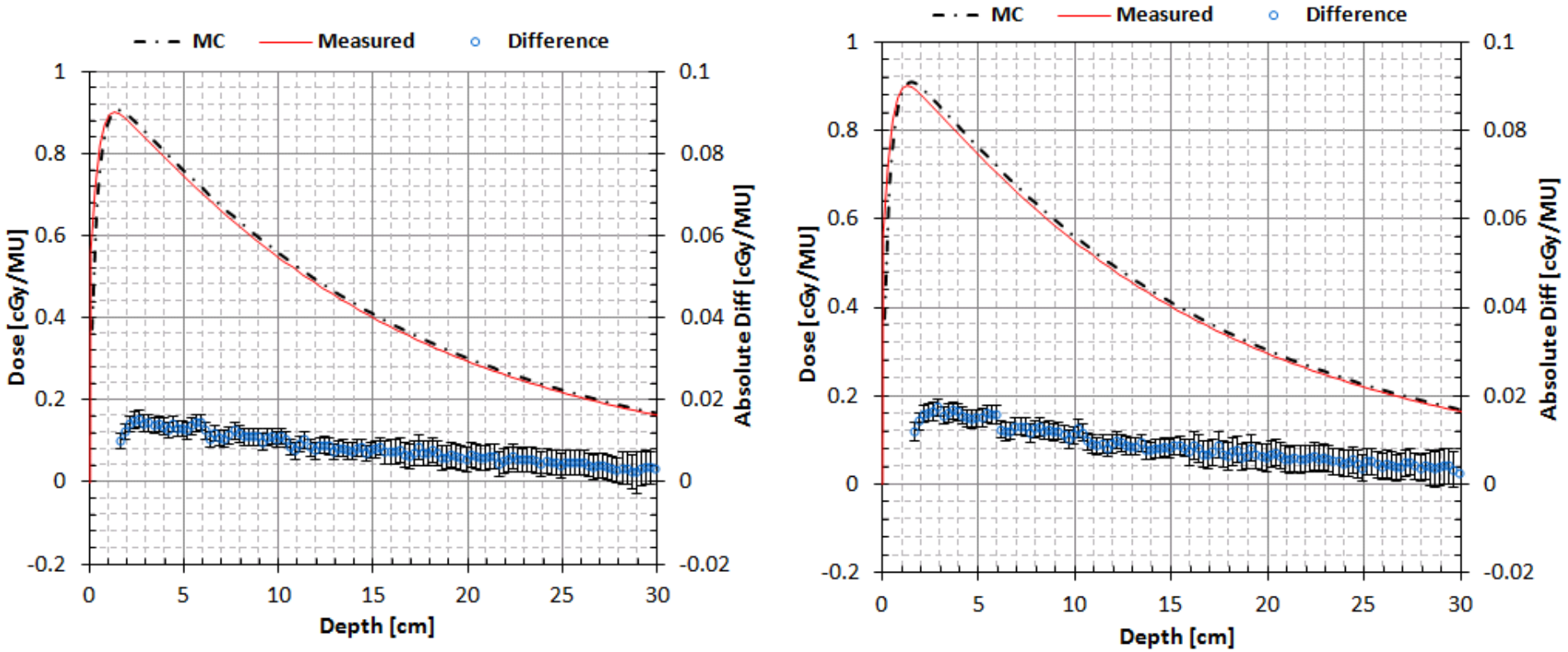

(a) (b)

Figure 5.12: Central axis depth doses of EDW fields (a) 60° IN 4×4 cm^2 (b) 60° OUT 4×4 cm^2. The black dashed lines represent the MC depth doses, the solid red lines represent the measured depth doses and the blue triangular symbols represent the differences between them in cGy/MU.

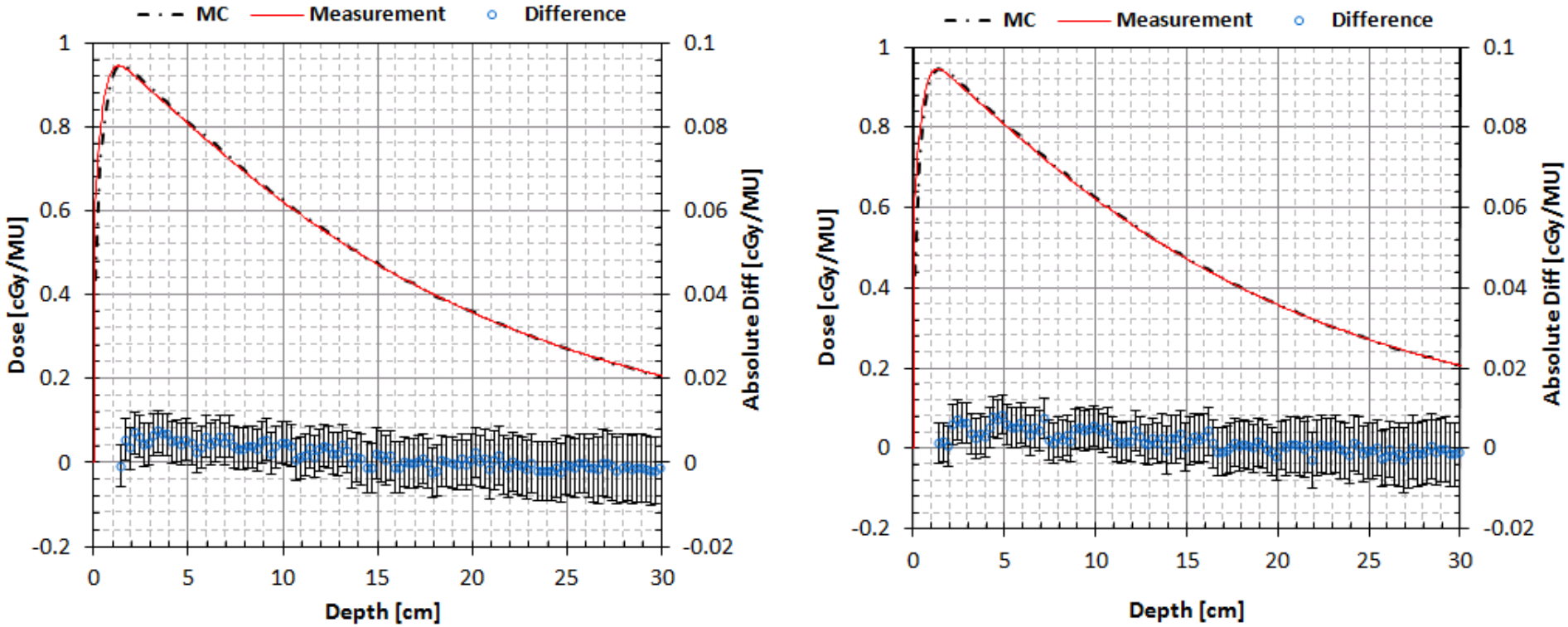

(a) (b)

Figure 5.13: Central axis depth doses of EDW fields (a) 30° IN 10×10 cm^2 (b) 30° OUT 10×10 cm^2. The black dashed lines represent the MC depth doses, the solid red lines represent the measured depth doses and the blue triangular symbols represent the differences between them in cGy/MU.

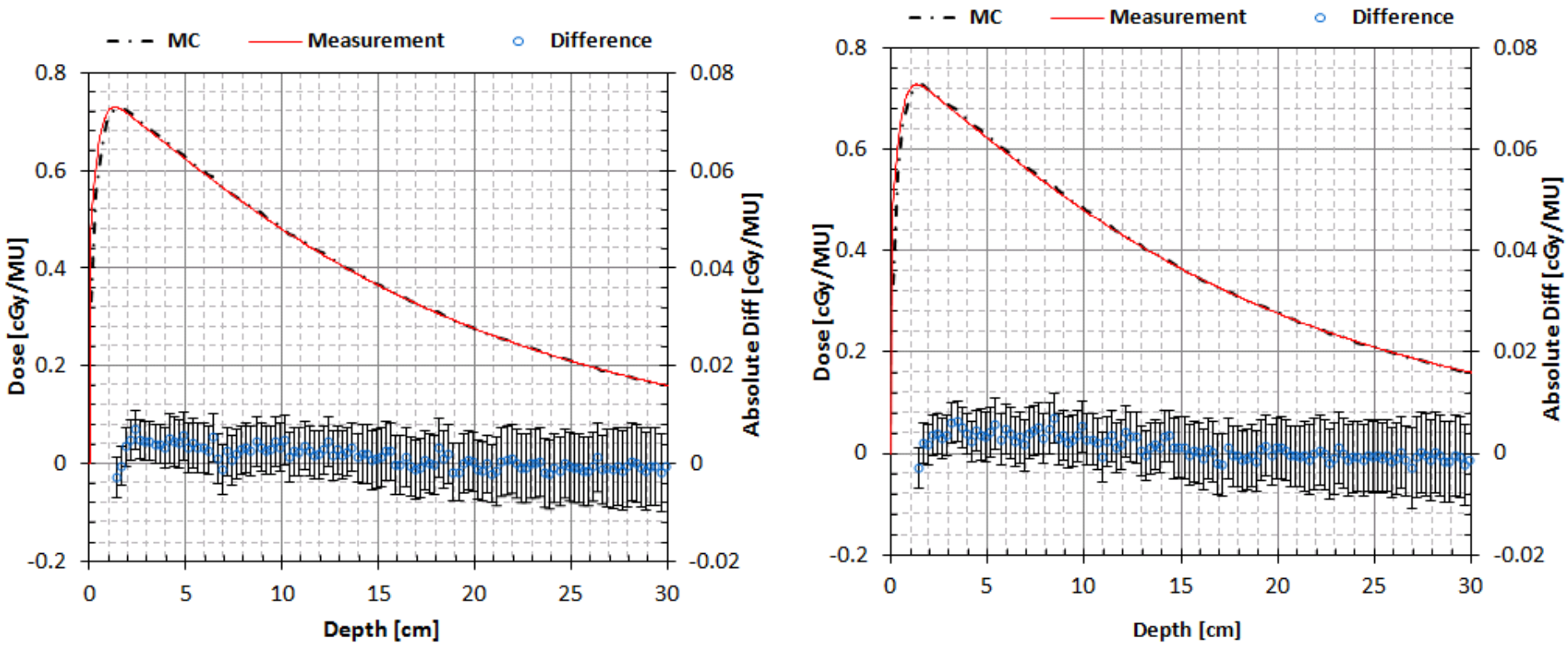

(a) (b)

Figure 5.14: Central axis depth doses of EDW fields (a) 60° IN 10×10 cm^2 (b) 60° OUT 10×10 cm^2. The black dashed lines represent the MC depth doses, the solid red lines represent the measured depth doses and the blue triangular symbols represent the differences between them in cGy/MU.

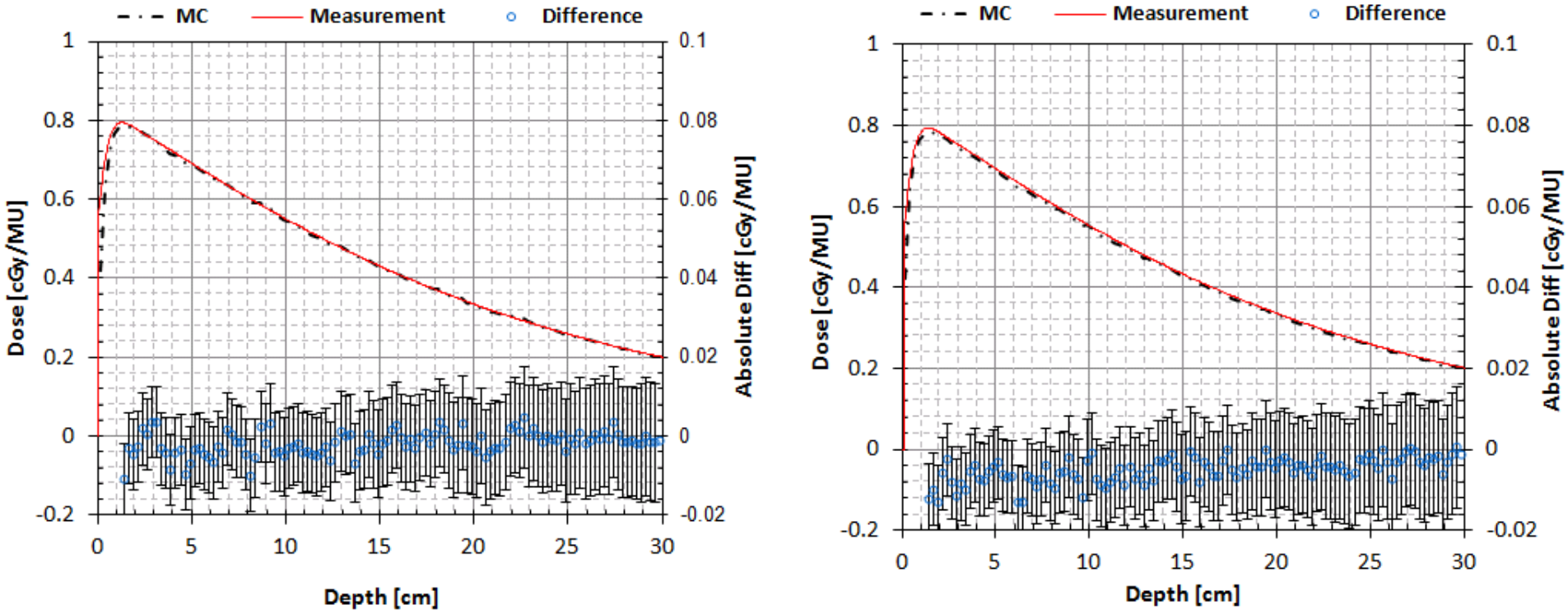

(a) (b)

Figure 5.15: Central axis depth doses of EDW fields (a) 30° IN 20×20 cm^2 (b) 30° OUT 20×20 cm^2. The black dashed lines represent the MC depth doses, the solid red lines represent the measured depth doses and the blue triangular symbols represent the differences between them in cGy/MU.

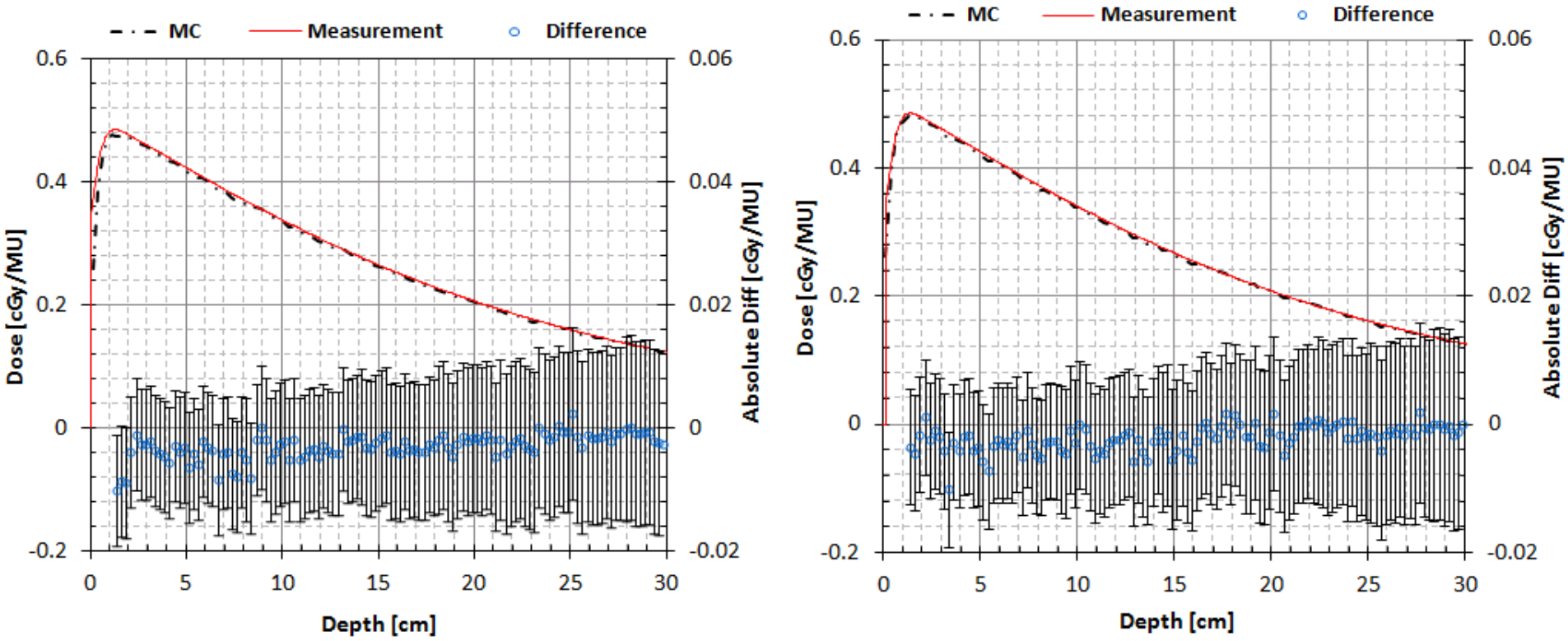

(a) (b)

Figure 5.16: Central axis depth doses of EDW fields (a) 60° IN 20×20 cm^2 (b) 60° OUT 20×20 cm^2. The black dashed lines represent the MC depth doses, the solid red lines represent the measured depth doses and the blue triangular symbols represent the differences between them in cGy/MU.

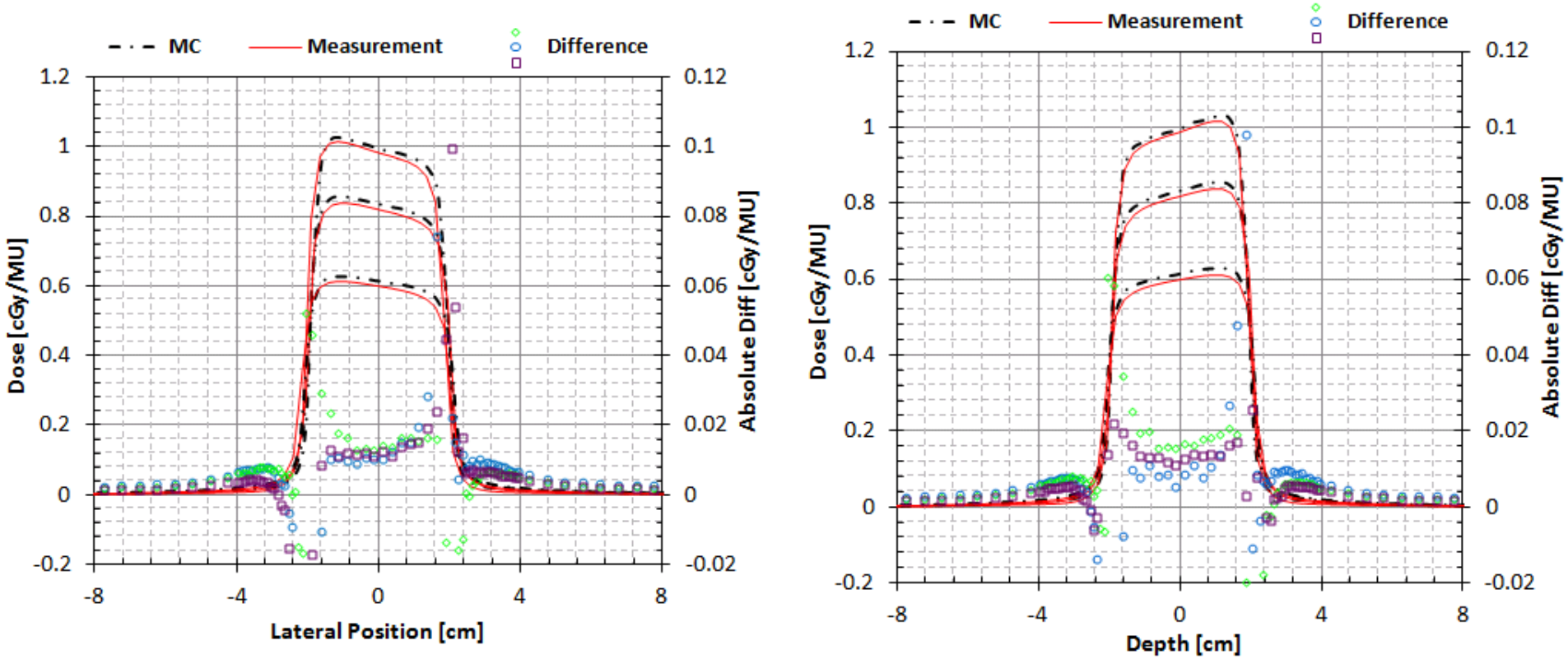

(a) (b)

Figure 5.17: Beam profiles across the central axis of EDW fields at depths d_{max}, 5 cm and 10 cm (a) 30° IN 4×4 cm^2 (b) 30° OUT 4×4 cm^2. The black dashed lines represent the MC depth doses, the solid red lines represent the measured depth doses and the blue, green and purple symbols represent the differences between them in cGy/MU.

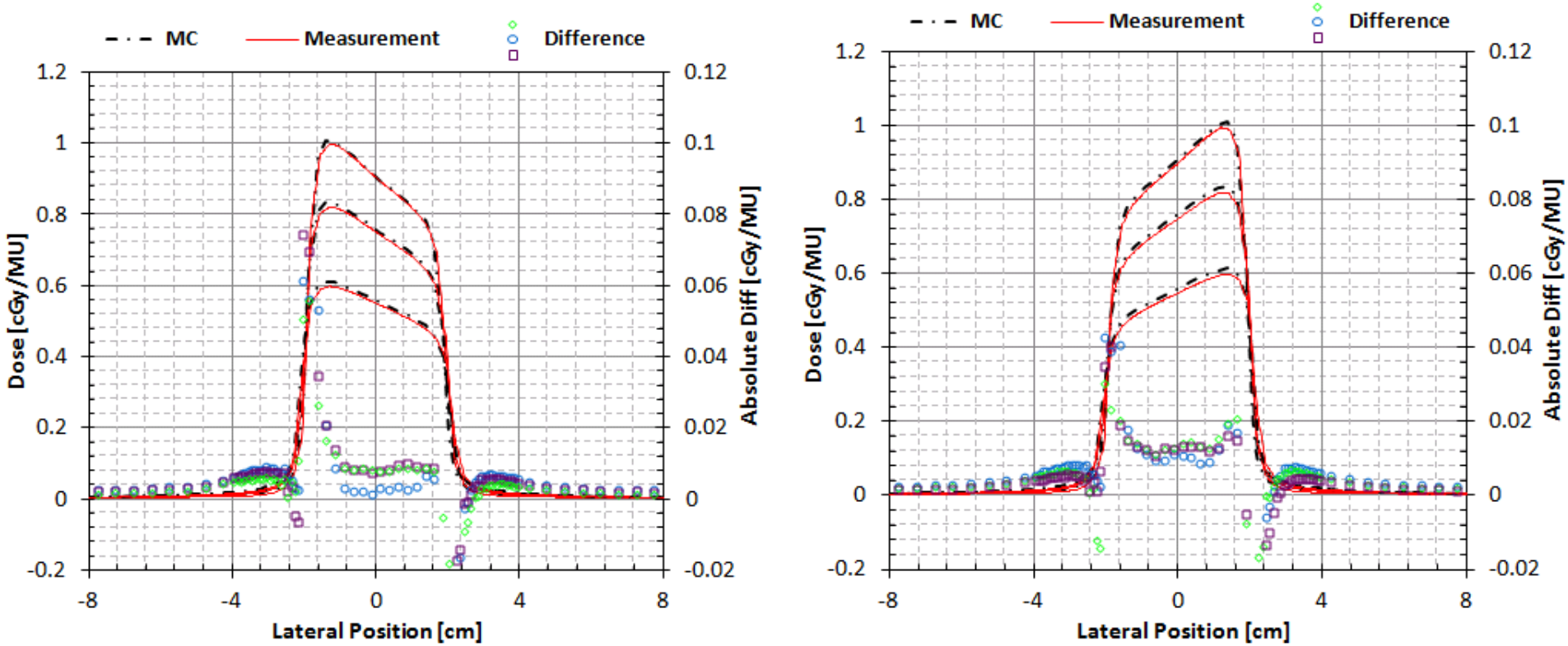

(a) (b)

Figure 5.18: Beam profiles across the central axis of EDW fields at depths d_{max}, 5 cm and 10 cm (a) 60° IN 4×4 cm^2 (b) 60° OUT 4×4 cm^2. The black dashed lines represent the MC depth doses, the solid red lines represent the measured depth doses and the blue, green and purple symbols represent the differences between them in cGy/MU.

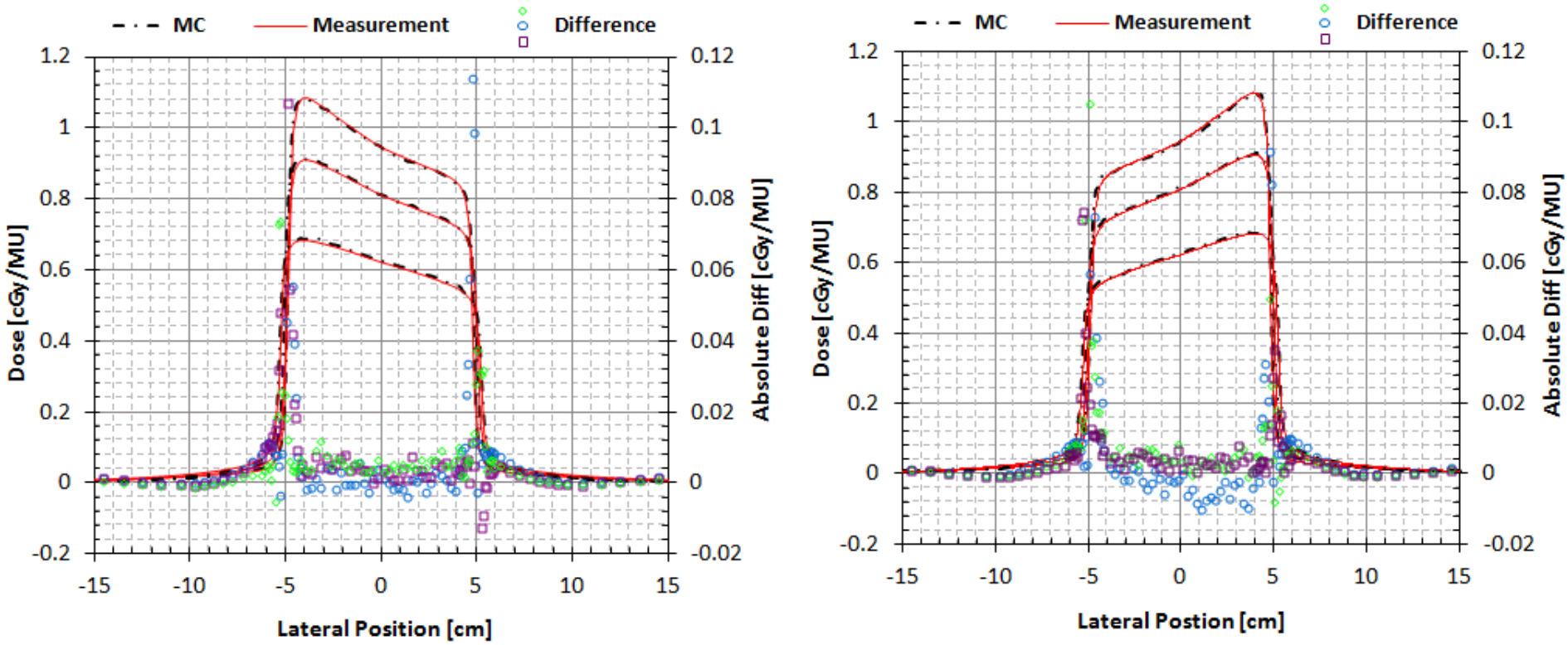

(a) (b)

Figure 5.19: Beam profiles across the central axis of EDW fields at depths d_{max}, 5 cm and 10 cm(a) 30° IN 10×10 cm^2 (b) 30° OUT 10×10 cm^2. The black dashed lines represent the MC depth doses, the solid red lines represent the measured depth doses and the blue, green and purple symbols represent the differences between them in cGy/MU.

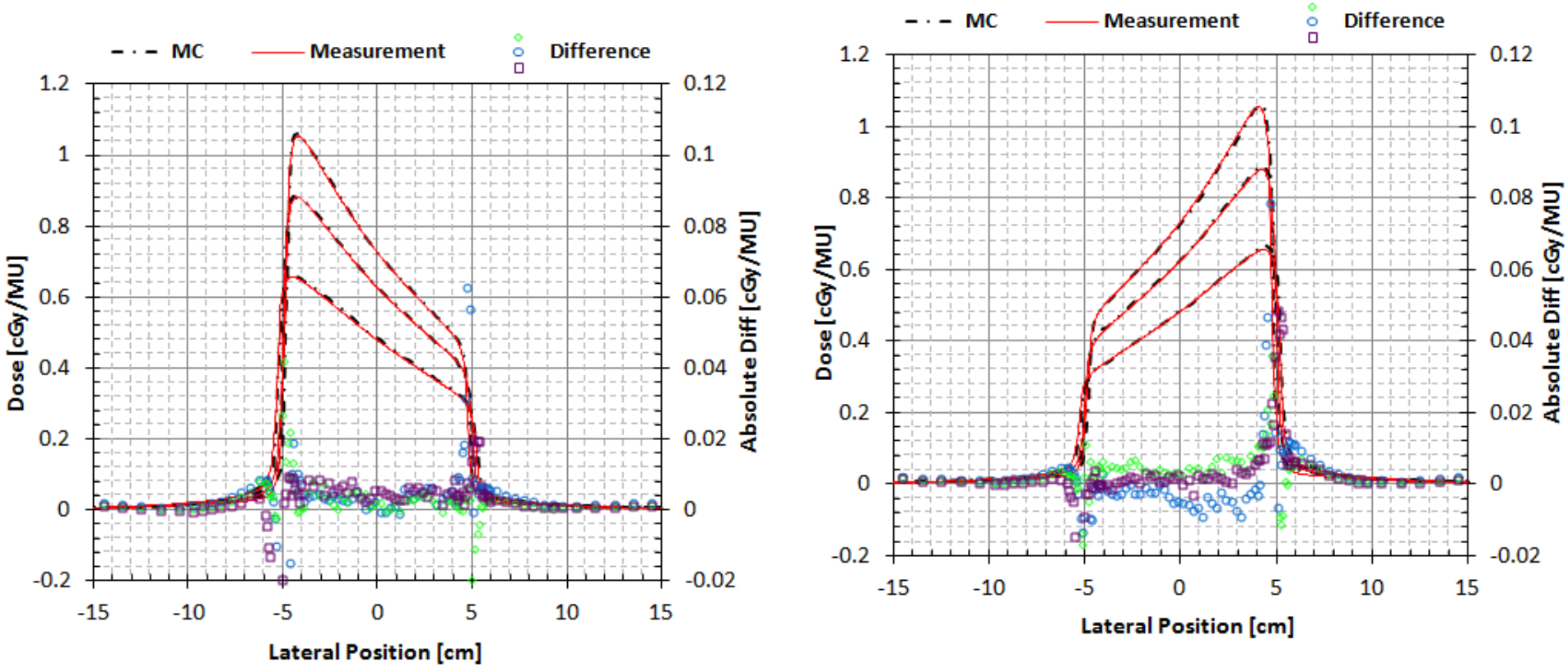

(a) (b)

Figure 5.20: Beam profiles across the central axis of EDW fields at depths d_{max}, 5 cm and 10 cm (a) 60° IN 10×10 cm^2 (b) 60° OUT 10×10 cm^2. The black dashed lines represent the MC depth doses, the solid red lines represent the measured depth doses and the blue, green and purple symbols represent the differences between them in cGy/MU.

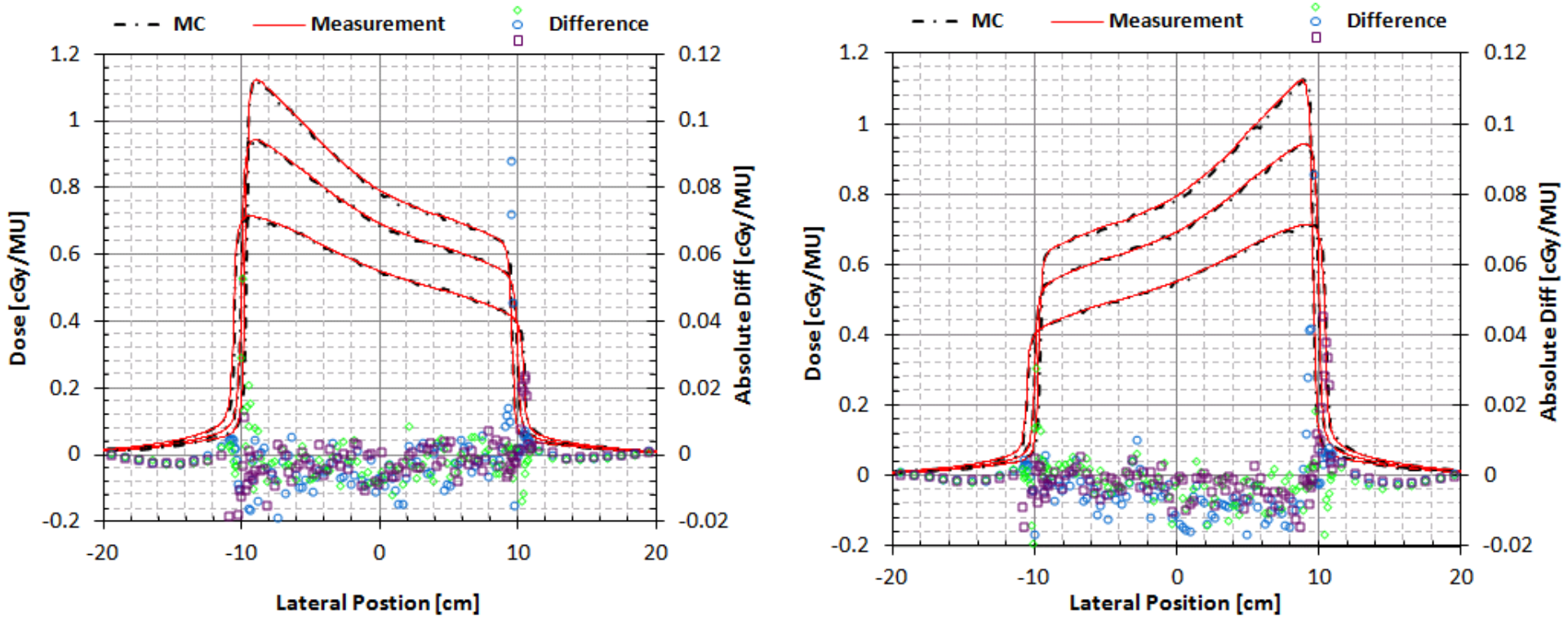

(a) (b)

Figure 5.21: Beam profiles across the central axis of EDW fields at depths d_{max}, 5 cm and 10 cm (a) 30° IN 20×20 cm^2 (b) 30° OUT 20×20 cm^2. The black dashed lines represent the MC depth doses, the solid red lines represent the measured depth doses and the blue, green and purple symbols represent the differences between them in cGy/MU.

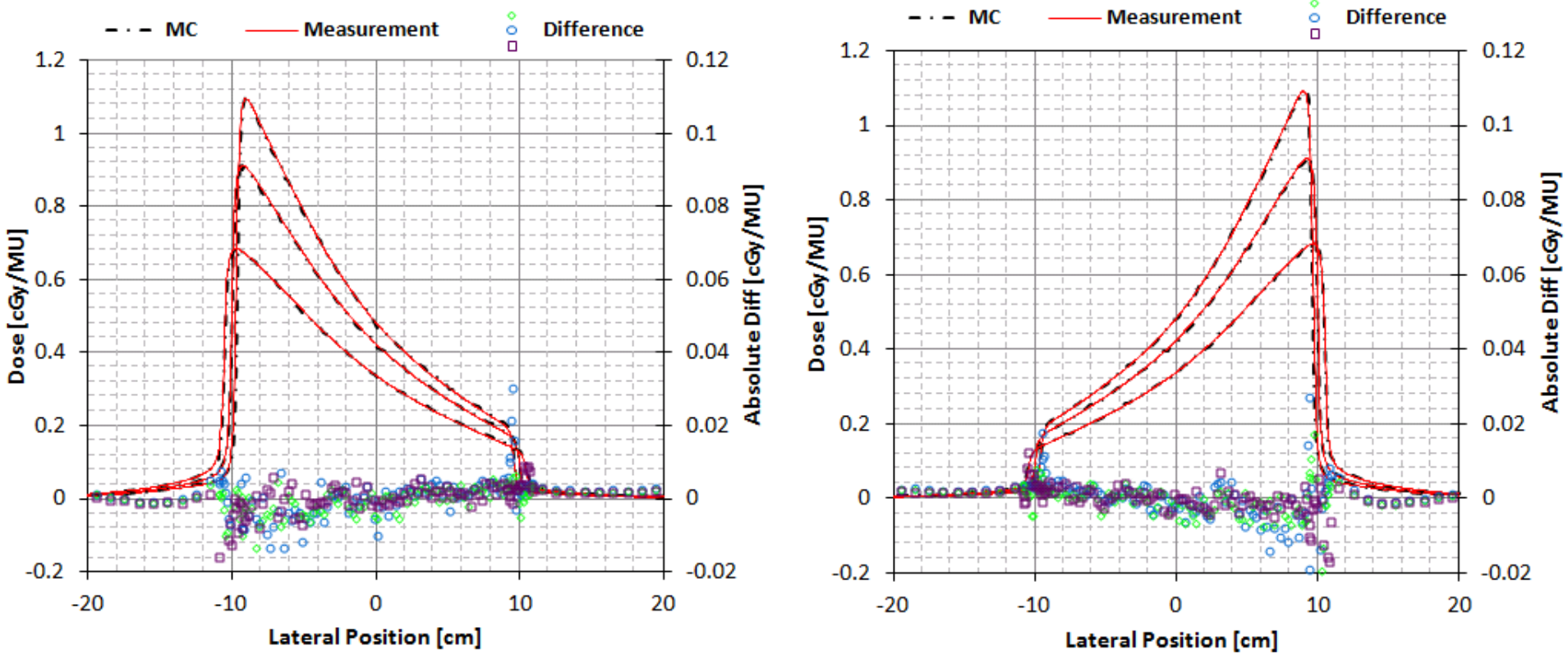

(a) (b)

Figure 5.22: Beam profiles across the central axis of EDW fields at depths d_{max}, 5 cm and 10 cm(a) 60° IN 20×20 cm^2 (b) 60° OUT 20×20 cm^2. The black dashed lines represent the MC depth doses, the solid red lines represent the measured depth doses and the blue, green and purple symbols represent the differences between them in cGy/MU.

5.3.4 Gafchromic film dose-OD calibration curve

Figure 5.23 shows the calibration curves of the red channel OD with (measurements 2) and without (measurement 1 and 3) blue channel correction plotted against the doses in Gy. The plotted ODs represent the average behaviour of the scanner as these are derived by averaging the response of a small defined area at the centre of the calibration film patch. The advantage of correcting the red channel OD by red/blue OD ratio is to eliminate any differences that arise due to non-uniformity in the coating of the active layer of the film. The yellow marker dye added to the EBT2 film enables to account for the dose independent component via the blue channel OD.

The discrete points in figure 5.23 indicate the corrected OD of patches cut from all the three different films irradiated to doses 1, 3, and 5 Gy of measurement set 2. Differences of upto 4.8% in OD exist between the films that were irradiated with the same known doses. Hartmann *et al.* [192] have reported differences of upto ±3.7% and 4.5% in the pixel values and net ODs within one film. Although all three calibration curves are plotted from the results obtained from films of same batch, significant differences were found in the ODs corresponding to same doses. This could be a result of above reported differences in the pixel values or OD between films.

5.3.5 TPS vs EBT2 open field profiles

The open field dose profiles of TPS against EBT2 films for field sizes 3×3 cm^2, 5×5 cm^2 and 10×10 cm^2 irradiation in a solid water phantom at 95 cm SSD, 5 cm depth is shown in figures 5.24, 5.25 and 5.26 respectively. This was done in order to evaluate the performance of gafchromic films in a simple homogenous geometry. TPS profiles were used instead of the ones derived using MC dose calculation as both have been matched and found to be within tolerance limits in homogeneous water phantoms as shown in section 5.3.1. There is good agreement of 2%/2 mm between the TPS calculated and measured profiles for the investigated field sizes 3×3 cm^2, 5×5 cm^2. The slightly tilted behaviour of the profile of larger field size 10×10 cm^2 could be due to lateral distortion during the scanning process which is a well known effect [190,192,193]. This is caused as a result of partial polarization

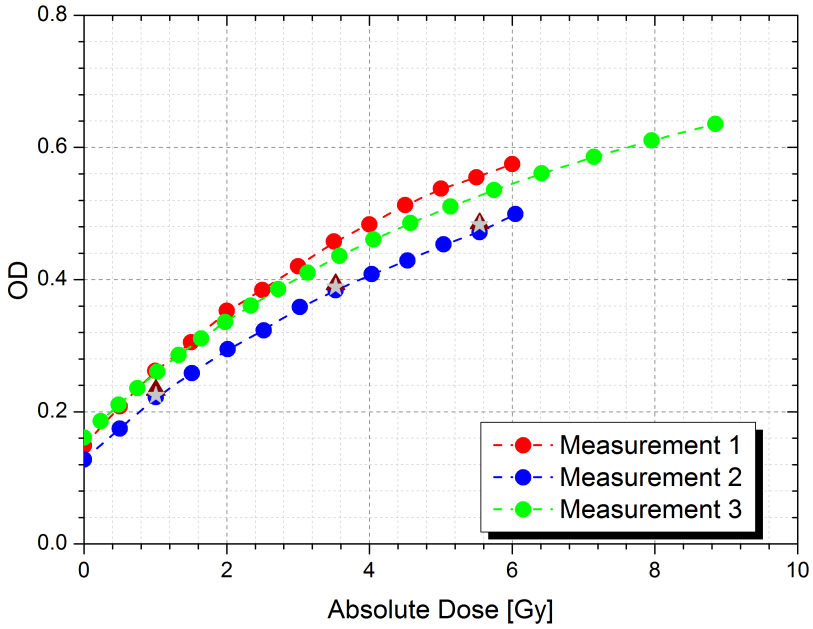

Figure 5.23: Dose in Gy vs OD. Red and blue curves (measurements 1 and 2) were fit using a third order polynomial whereas the green curve (measurement 3) was fit using a rational function. The discrete grey and purple points corresponding to 1, 3 and 5 Gy show the ODs of the patches cut from two different films of measurement set 2.

of the micro crystals present in the film that are aligned randomly which results in alteration of reflective and refractive properties of the light transmitted away from the centre of the scanner [188]. This effect is larger at lateral edges of the scanner in the direction perpendicular to the scan and for doses above 1 Gy which can be eliminated by using triple channel dosimetry [190].

5.3.6 Wooden lung phantom profiles

The depth doses and beam profiles of GTV0, GTV0inv, GTV17, GTV17inv and GTVSABR are shown in figures 5.27 to 5.31 in the same order. GTV0 and GTV17 depth doses and beam profiles include all three measurement sets whereas the results of GTV0inv, GTV17inv and GTVSABR were from measurements 2 and 3 (see section 5.2.7). In general, the agreement between MC calculated depth doses and beam profiles and those measured with EBT2 films of all the wooden lung phantom plans were within 3.5% at the centre of the tumour.

Excellent agreement of with 3% was found in case of GTV0 and GTV0inv plans in both tumour and the lung region. Results of measurement 3 were the

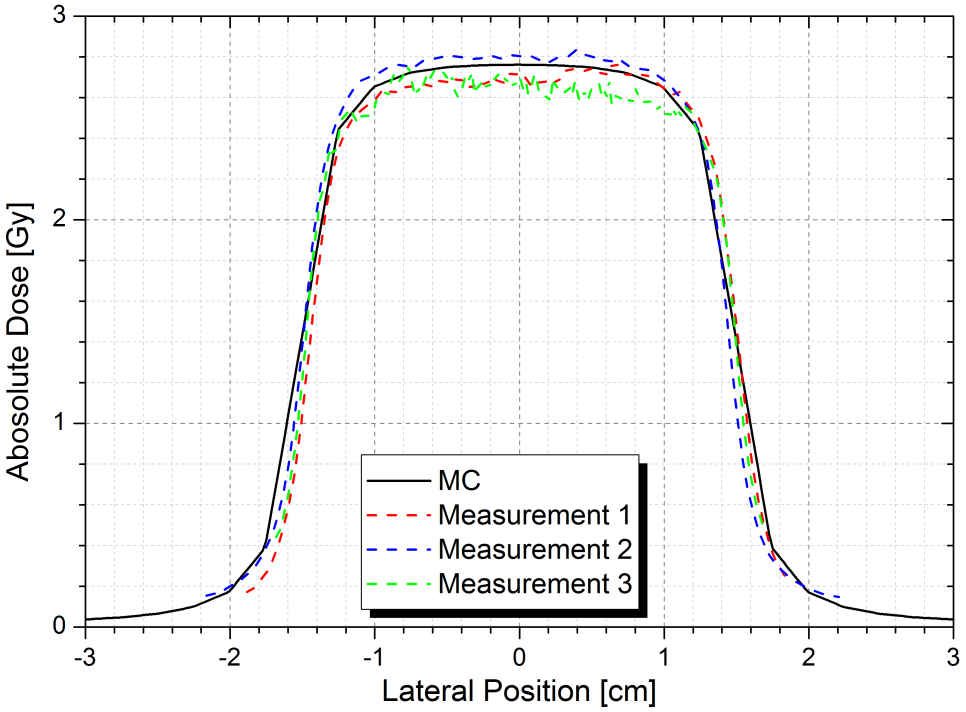

Figure 5.24: PBC and measured beam profiles of 3×3 cm^2 field in a homogeneous solid water phantom at 5 cm depth, 95 cm SSD.

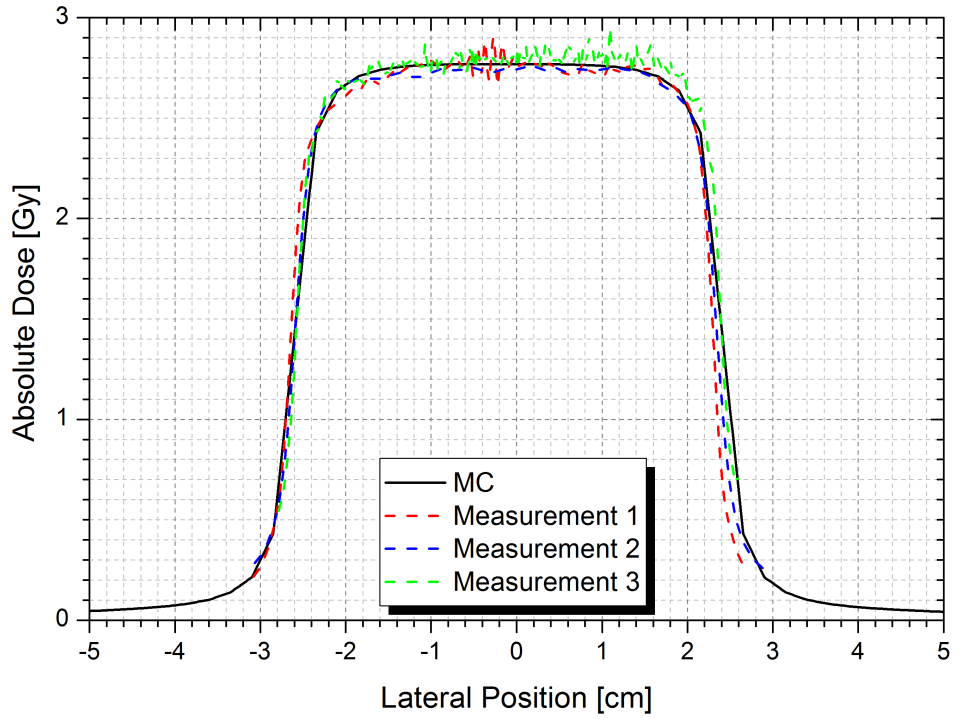

Figure 5.25: PBC and measured beam profiles of 5×5 cm^2 field in a homogeneous solid water phantom at 5 cm depth, 95 cm SSD.

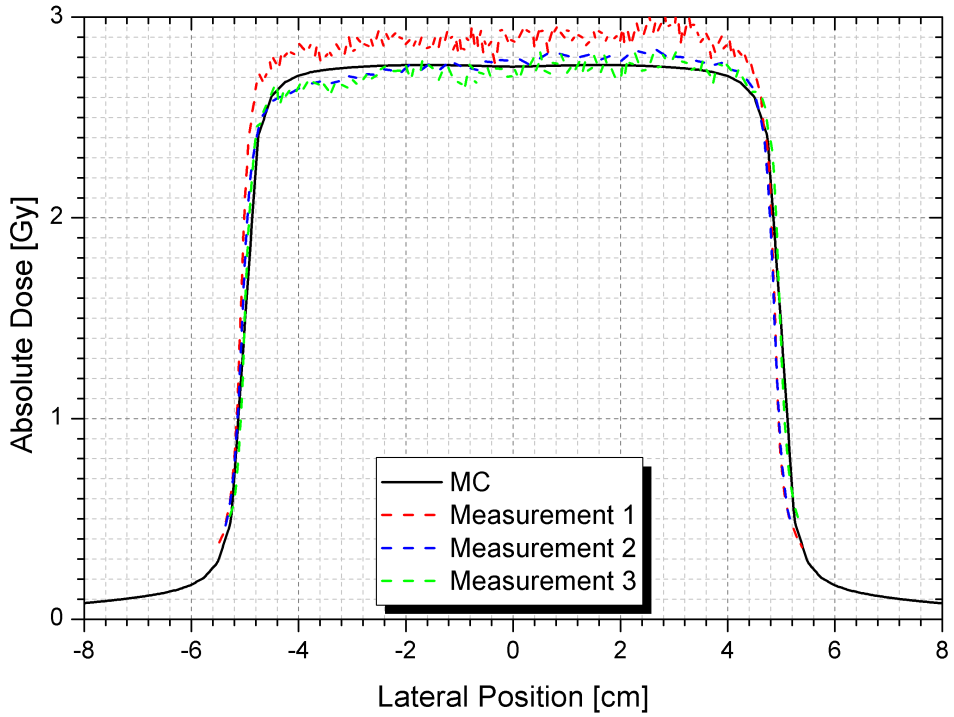

Figure 5.26: PBC and measured beam profiles of 10×10 cm^2 field in a homogeneous solid water phantom at 5 cm depth, 95 cm SSD.

closest to MC out of all three trials GTV0, GTV0inv plans are concerned. This could be due to increased reproducibility in positioning of the film pieces at the centre of the scanner window by using customised acetate jigs.

On the other hand, the differences between measured and MC calculated doses are larger for the GTV17, GTV17 inv plans. The agreement between the lateral or x profiles are better than the longitudinal or y profiles which could be a result of orientation of the film on the scanner. In all the cases, the longitudinal direction of the film was perpendicular to the scan axis as a result of which the response of the pixels that are away from the either side of the centre of the scanner are distorted due to differences in polarization. Although this effect is visible from the longitudinal profiles of the GTV0 and GTV0inv plans its magnitude is small whereas the differences are larger when GTV17, GTV17inv plans are considered. This could be due to higher absolute doses of 2.1 Gy in the plans with 17 mm margin than that of the zero margin plans (1.4 Gy). Another possible reason is self attenuation in the gafchromic film which is of a higher relative density 1.2-1.35 g/cm^3 than the tumour and lung inserts (0.55 g/cm^3 and 0.16 g/cm^3

respectively). It is to be noted that the MC dose calculation of all the plans in the wooden lung phantom were done without gafchromic film inserted in it.

Finally, the lateral and longitudinal profiles of the GTVSABR phantom plan shows differences of up to 3.5% at the centre of the tumour and up to 16% in the lung region. The measured doses are systematically higher than that of the MC calculated doses. This might be a result of additional uncertainties in the set up due to use of asymmetric fields where the isocentre is at the centre of the wooden lung phantom and the treatment fields are away from the isocentre[14]. The MLCs do overleaf travel in order to form apertures off-axis to irradiate the tumour.

A possible way to improve matching between MC calculated and measured depth doses and beam profiles measured by EBT2 films would be to use a phantom of simpler geometry. Another method is to use triple channel dosimetry which can essentially correct for dose-independent factors such as the artifacts that arise concerning the scanning process [188, 190].

[14]This set up was used in order to reproduce a clinical SABR patient plan/treatment done at our centre. The isocentre is placed along the mid line of the patient to avoid couch movement between online cone beam computed tomography (CBCT) acquisition and the treatment. If the isocentre is place at the centre of the tumour which is right or left sided, treatment couch has to be moved to enable full rotation of the linac gantry and CBCT arm around the patient without collision.

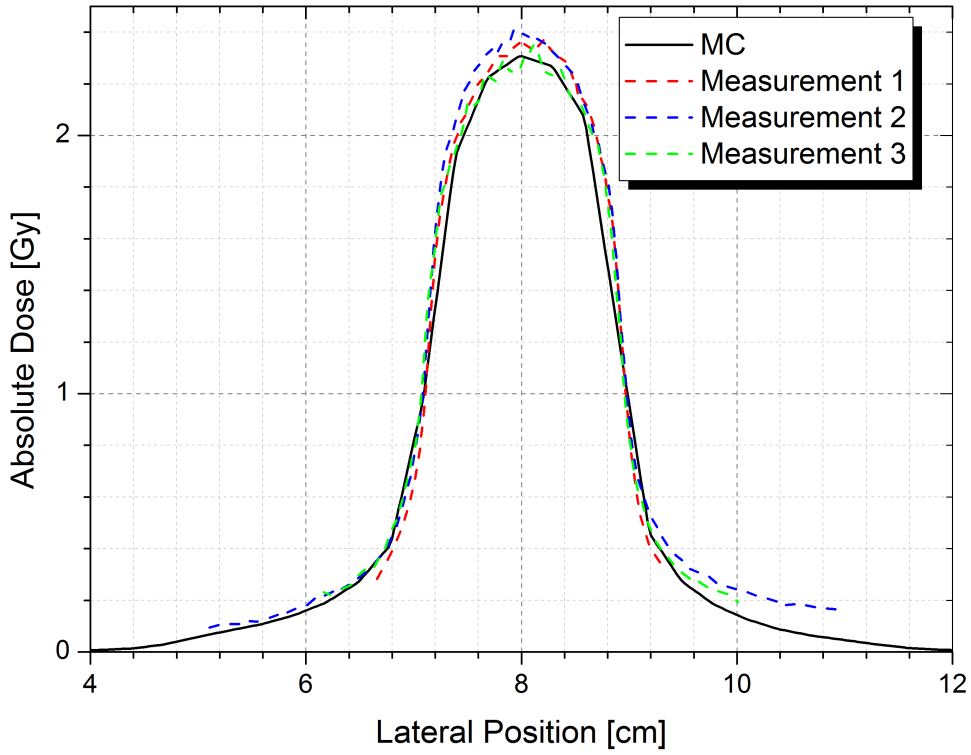

(a)

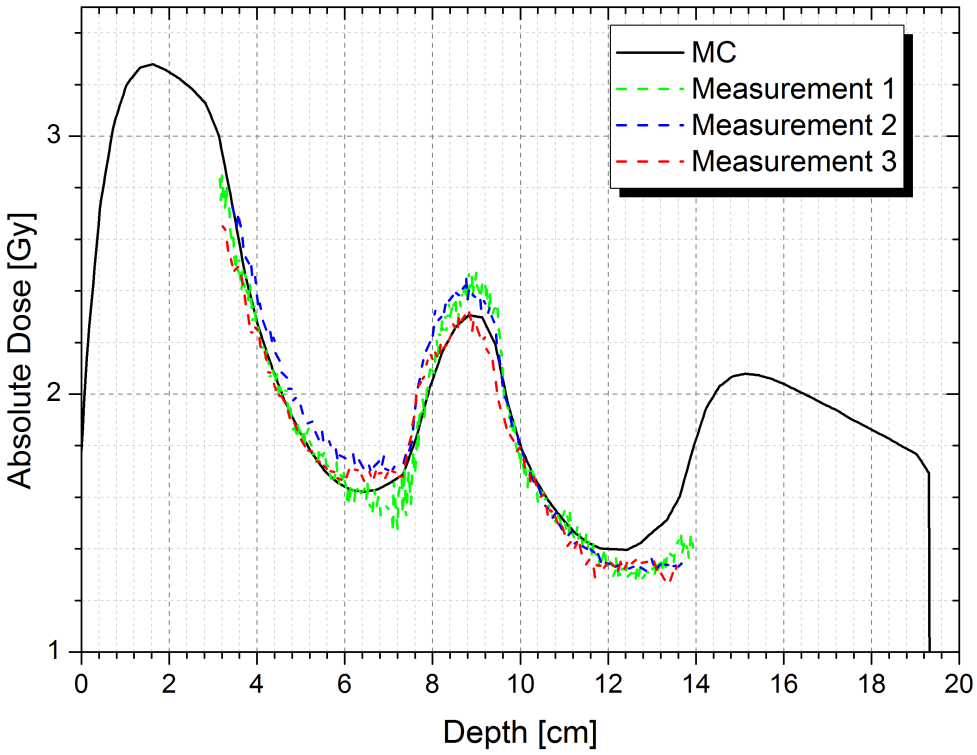

(b)

Figure 5.27: Lateral (along x-axis) and longitudinal (along x-axis) profiles of a plan with GTV + 0 mm MLC margin

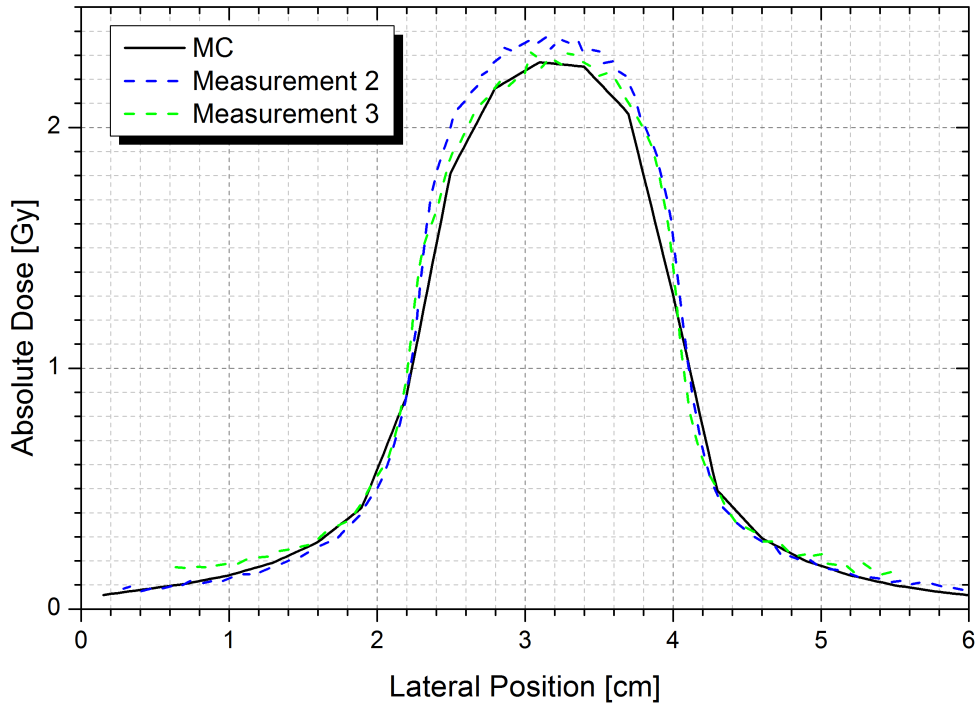

(a)

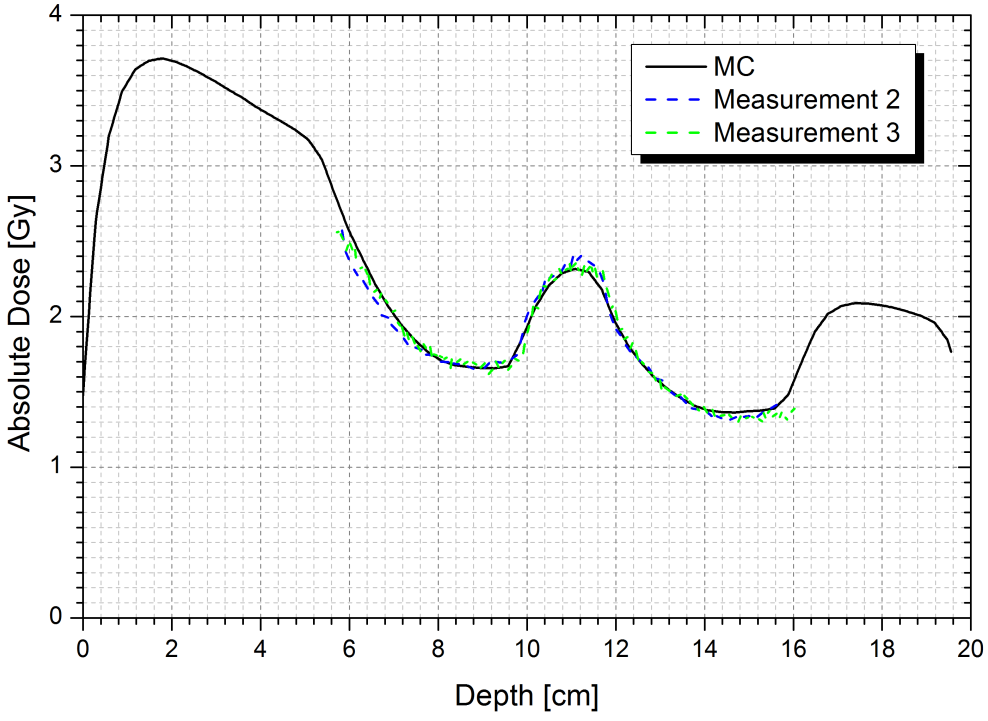

(b)

Figure 5.28: Lateral (along x-axis) and longitudinal (along x-axis) profiles of a plan with GTV + 0 mm MLC margin of the inverted phantom

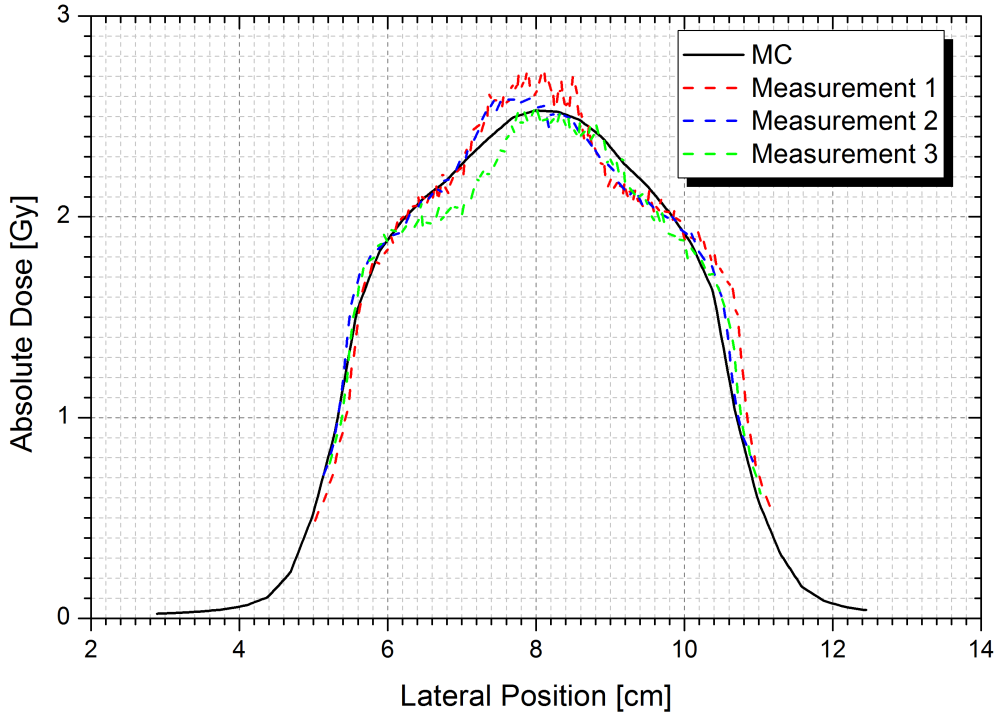

(a)

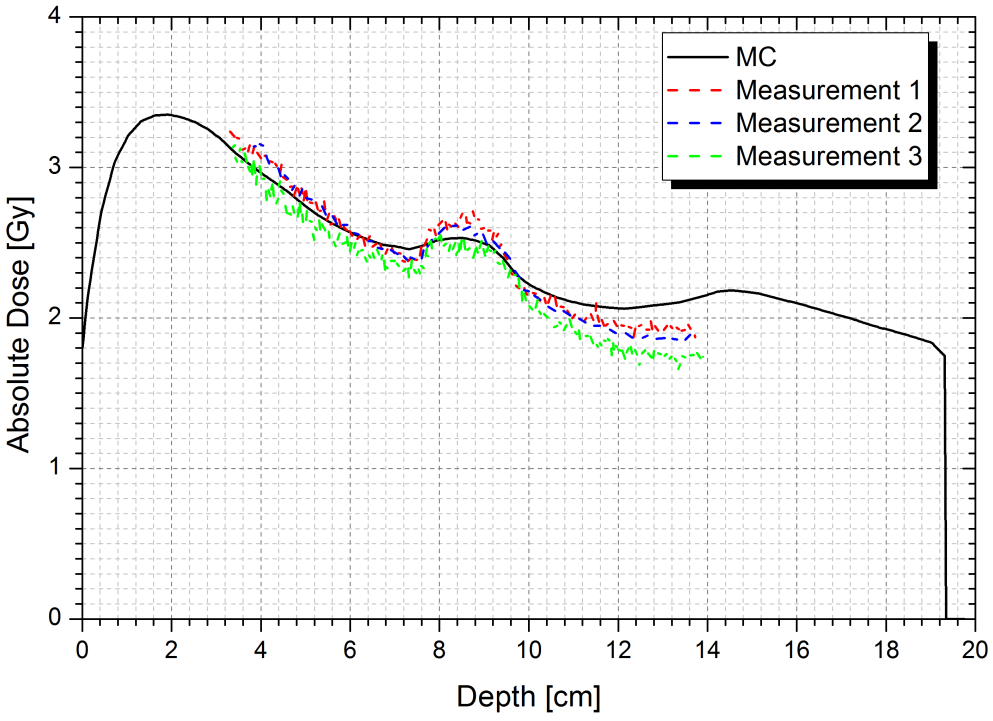

(b)

Figure 5.29: Lateral (along x-axis) and longitudinal (along x-axis) profiles of a plan with GTV + 17 mm MLC margin

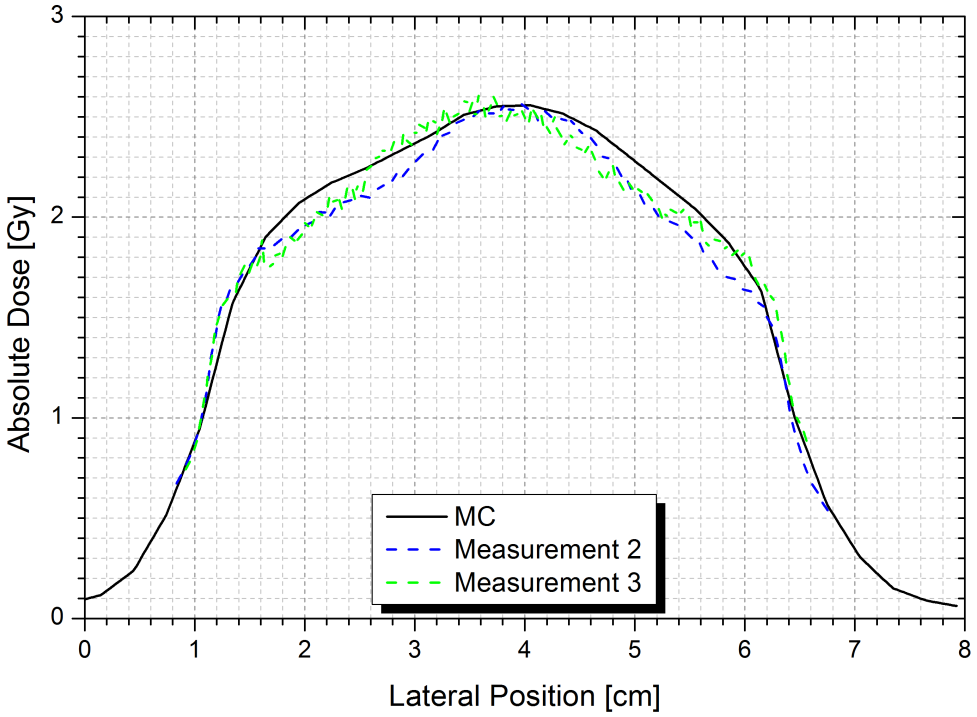

(a)

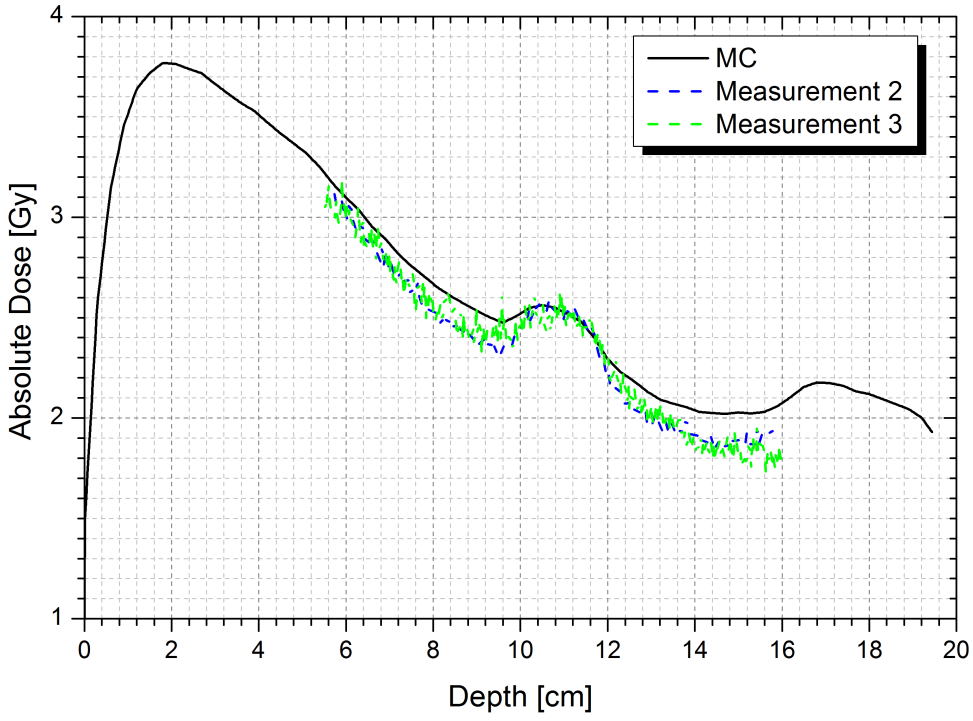

(b)

Figure 5.30: Lateral (along x-axis) and longitudinal (along x-axis) profiles of a plan with GTV + 17 mm MLC margin of the inverted phantom

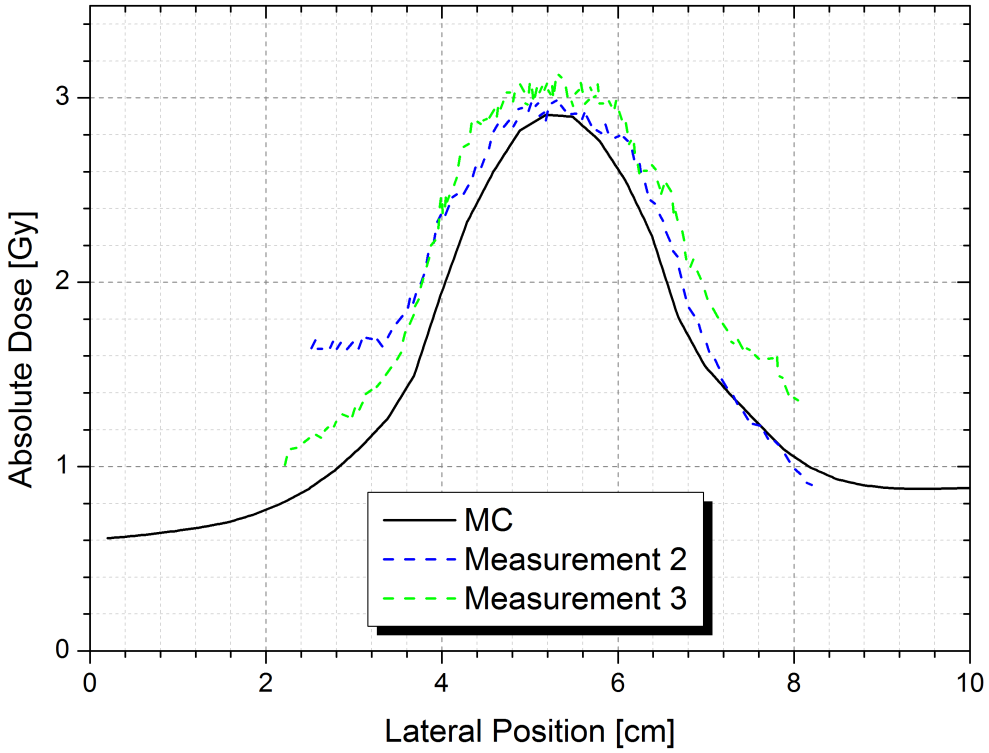

(a)

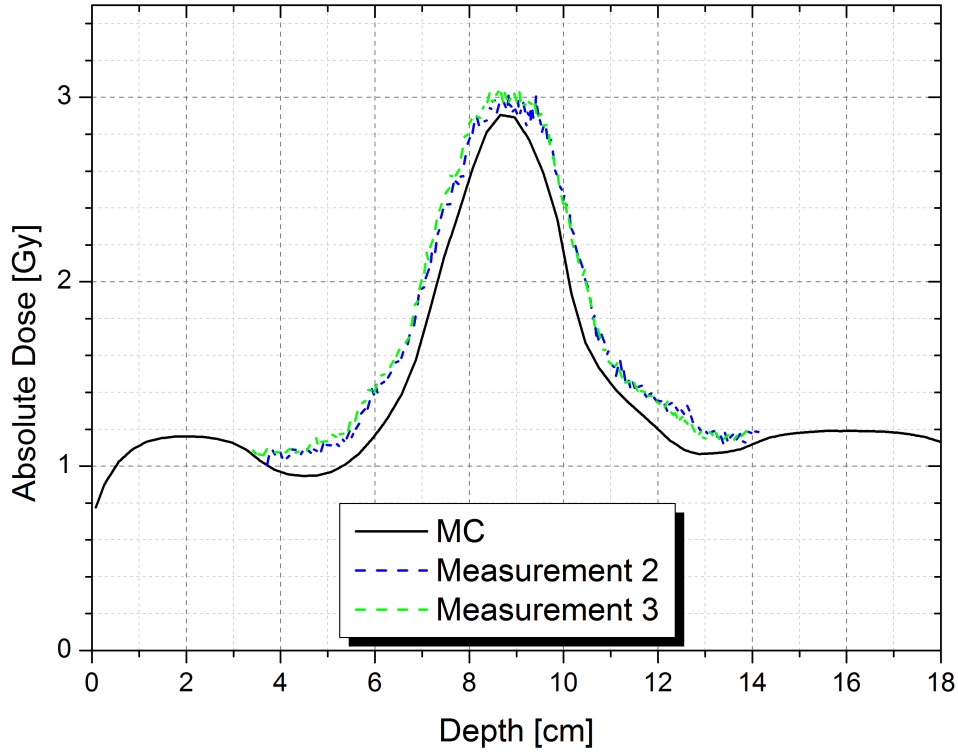

(b)

Figure 5.31: Lateral (along x-axis) and longitudinal (along x-axis) profiles of SABR plan

5.4 Conclusions

A MC model of Varian 2100 C/D was built which is found to be in good agreement with that of the measurements. Comparison of depth doses and beam profiles of the open and dynamic wedge fields shows that the overall match is excellent within the recommended tolerances of 2%/2mm and 3%/3mm respectively. However, the doses of the smaller fields are over estimated and the larger fields being under estimated by the MC which can attributed to the inadequacy in modelling the jaws of the accelerator.

EBT2 films are proven to be useful for the validation of the performance of the accelerator model in heterogeneous media. Differences of up to 5% exist between MC calculated and doses measured by gafchromic films in most of the cases. Although differences of up to 16% are found in some cases which could be due accumulated uncertainties arising from MC dose calculation, scanning, non-uniformity of the film response, complex design of the wooden lung phantom, inclusion of a high density material at the time of measurement, air gaps between the lung inserts and film, the agreement is still within preferable range.

Chapter 6

Influence of photon dose calculation algorithms on the clinical outcome of lung radiation therapy

6.1 Introduction

The type of photon dose calculation algorithm employed in the TPS strongly influences the dose delivered to thoracic tumours such as non-small cell lung carcinoma (NSCLC). This is due to the presence of a unit density tumour of density close to that of water within the low density lung which is approximately one-third of the density of water. The interfaces at the high and low densities present challenges to the accurate calculation of dose distribution in thoracic tumours such as NSCLC. A typical lung tumour treatment field may traverse from high density tissue to low density lung and or low density lung to high density tumour depending upon the beam arrangements. NSCLC tumours of stage I and II that are often medically inoperable and stage III locally advanced tumours are widely treated with 3DCRT using 4 or 6 MV photon beams with curative intent. The dose fractionation depends upon the protocol followed in a particular institute or country. For example, in our institute, majority of the patients with NSCLC are commonly treated with a total dose of 55 Gy in 20

fractions over 4 weeks with a daily dose of 2.75 Gy [194].

Many investigators have studied the differences between various photon dose calculation algorithms in treating thoracic tumours such as lung and breast [69–71, 85–87, 195–198]. Convolution algorithms such as PBC with EPL, ETAR, MB heterogeneity correction methods and CS algorithms such as CCC and AAA of various commercially available TPSs have been compared against either against MC or measurements extensively. The convolution and CS algorithms are also called as *type a* and *type b* algorithms as classified by Knöös *et al.* [87]. *Type a* algorithms do not model the lateral electron transport whereas *type b* algorithms model the changes in lateral electron transport in an approximate way. PBC algorithms are proven to over-estimate the dose to the unit density lung tumour owing to its inability to accurately model the electron transport in regions where there is no charged-particle equilibrium [69–71, 85–87, 195–198]. The range of secondary electrons are larger in low density medium such as lung and they tend to scatter laterally. PBC algorithms still exist in most of the commercial TPSs owing to their faster dose calculation. Although they have been replaced by more accurate CS or *type b* algorithms such as CCC and AAA, the PBC algorithms are still commonly used in the process of IMRT plan optimisation, the dose calculation of which is replaced by a *type b* algorithm at the final dose calculation step.

On the other hand, the CS or *type b* algorithms model the lateral electron transport in a crude way that includes many approximations. The *type b* algorithms are far superior than the *type a* algorithms. However they have shortcomings in predicting the dose distributions at the lung-soft tissue interfaces as they use rectilinear density scaling in accounting for changes in lateral electron transport [87, 115, 195]. The MC dose calculation algorithm is considered as the gold standard; it is often used to compare the validity of various photon dose calculation algorithms in addition to measurements [69–71, 85–87, 195–198]. A detailed overview of the physics of these algorithms is given in chapter 2 of this thesis.

Various authors [69–71, 85–87, 115, 195–198] have quantified the influence of heterogeneities on the accuracy of doses predicted by various photon dose calcu-

lation algorithms in terms of physical doses in relative and absolute quantities. To our knowledge, the implications of these dose differences on the predicted clinical outcome of a radiotherapy regimen have not been been studied in depth. In this work, the differences between the TPS algorithms and MC algorithm are presented in terms of physical doses in absolute units and their biological consequences in terms of radiobiological indices such as TCP and NTCP. Seven photon dose calculation algorithms of three commercial TPSs were studied against MC for 3DCRT and SABR techniques.

6.2 Materials and Methods

The aim of this study is to evaluate the differences between the absolute doses calculated by analytical algorithms present in the TPSs against the MC doses in terms of clinical outcome using radiobiological models such as TCP and NTCP. The differences in the TCP and NTCP values of treatment plans done with various photon dose calculation algorithms in a simple virtual phantom geometry and clinical NSCLC patients were studied.

6.2.1 Virtual lung phantom

Two phantoms each of 30(L)×20(W)×20(H) cm^3 were created in the Eclipse TPS with a lung insert of 30(L)×20(W)×10(H) cm^3 of density 0.3 g/cm^3 (Hounsfield Unit, HU = -722) sandwiched between water slabs of dimensions 30(L)×20(W)×5(H) cm^3 and density 1.0 g/cm^3 (HU = 0). Spherical gross tumour volumes (GTVs) of unit density (HU = 0) of diameters 2 cm and 8 cm were delineated at the centre of the phantom in the lung insert as shown in figures 6.1(a) and 6.1(b). Two different volumes of GTVs were chosen in order to study the influence of photon dose calculation algorithms for small and large tumours. Planning target volumes (PTVs) of 1 cm margin were created by expanding the GTVs isotropically in both the cases. Each structure of the phantom including the body, lung insert, the spherical GTV and PTV volumes were drawn as separate "organs" or "structures" using the segmentation tools in Eclipse v.10.0[1] TPS and the HUs were

[1]Varian medical systems, Palo Alto, USA.

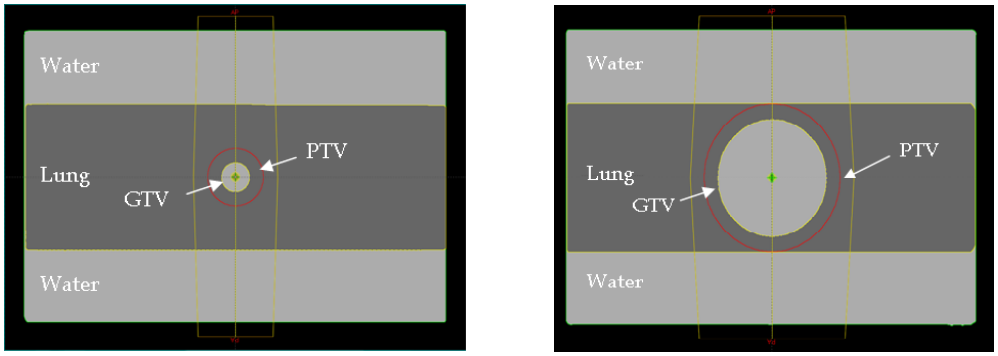

(a) (b)

Figure 6.1: Virtual lung phantoms with a lung slab of thickness 10 cm sandwiched between two water slabs of 5 cm each. A spherical tumour of diameter (a) 2 cm and (b) 8 cm of unit density surrounded by a PTV of 1 cm margin was delineated at the centre of the lung volume of density 0.3 g/cm^3. Parallel opposed, isocentric, conformal fields of field size 6×6 cm^2 and 12×12 cm^2 with an MLC margin of 7 mm were applied in case of small and large tumours respectively with a prescription dose of 55 Gy in 20 fractions.

over ridden to assign the corresponding densities for each of the above mentioned structures. The empty DICOM-RT CT data set and the DICOM-RT structures were exported to Pinnacle v.9.0[2] and Oncentra v.4.0[3] TPSs where the densities of the structures were over-ridden again separately as this information was lost during the export.

6.2.2 NSCLC patient cases

CT simulation and segmentation

Treatment plans of ten patients with NSCLC stage I, II, and III who underwent 3D conformal radical lung radiotherapy were used in this retrospective study. All the patients underwent CT simulation head first, supine on a Brilliance[4] scanner on which they were imaged in the treatment position with a flat couch top and additional immobilisation devices. The CT images were under taken in the thorax region covering the entire lung. The scans were taken in normal breathing and

[2]Philips Healthcare, Andover, MA, USA.
[3]Nucletron, Veenendaal, The Netherlands.
[4]Philips Healthcare, Andover, MA, USA.

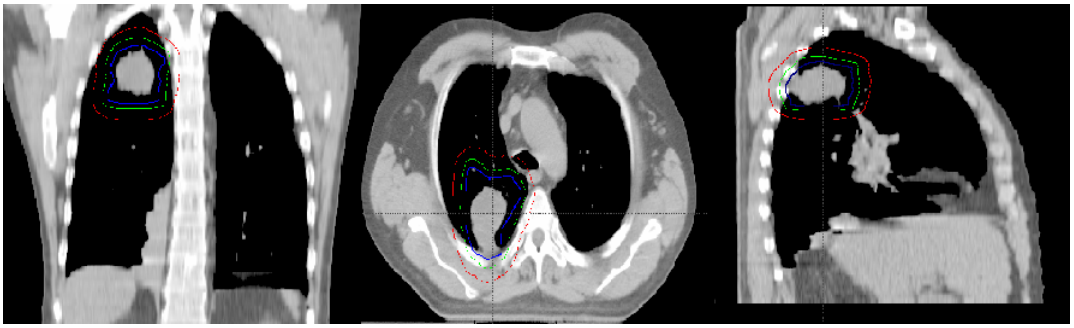

Figure 6.2: Coronal, axial and sagittal CT images of a patient with delineated target volumes GTV (blue), CTV(green) and PTV(red)

no breath-hold techniques were employed. The slice thickness of all the patient scans was 5 mm in the superior-inferior or cranio-caudal direction. The CT scans were exported to the ProSoma[5] contouring work station where the segmentation of body, target volumes and organs at risks (OARs) were done by a Radiation Oncologist. The target volumes included the GTV, CTV and the OARs were normal lung, oesophagus, heart and spinal cord. Both lungs were delineated as a single organ. Total lungs excluding the GTV (TL-GTV) volumes were created using inbuilt Boolean operators.

The GTVs were the gross tumour volumes which were visible on the CT scan and the GTVs were expanded by a margin of 5 mm to include any microscopic extent of the tumour to form the clinical target volume (CTV). The CTVs were further expanded by 10 mm isotropically in order to account for systematic and random errors including both the inter- and intra- fraction tumour motion during irradiation.

Tumour location and geometry

Out of the 10 patients, all patients except 3 had right-sided tumour among which the tumours of 6 patients were attached to the mediastinum. Tumours of 7 patients were situated in the upper lobe of the lung with the other 3 right-sided lung tumours present in the middle lobe. Tumours in the lower lobe near the diaphragm are not included in this study as conventional 3DCRT plans are not sufficient as these tumours tend to move to a greater extent than the ones found

[5]MedCom GmbH, Darmstadt, Germany.

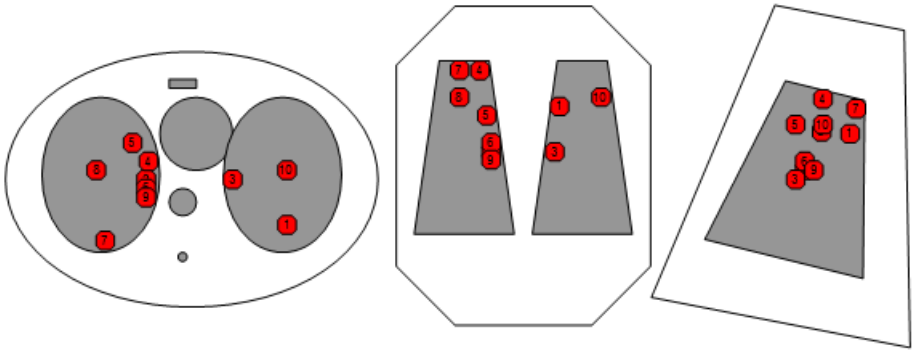

Figure 6.3: Location of the tumours of all the 10 NSCLC cases in axial, coronal and sagittal orientations of the thorax

in the middle or upper lobe. In general, the patients with lower lobe tumours undergo a 4DCT scan and they are treated based on 4D planning in our centre. The tumours were classified into 3 types depending upon their volumes: small (1-60 cm^3), medium (61-120 cm^3) and large (121-180 cm^3). 8 patients had small and medium tumours, 4 in each group and the remaining 2 had large tumours. The location of all the tumours in the thorax in axial, coronal and sagital sections is shown in figure 6.3. In addition to 10 3DCRT patient plans, an SABR patient plan was included in the study. Stereotactic ablative body radiotherapy (SABR) of lung is a hypo-fractionated treatment which involves delivery of a high dose per fraction of 11 Gy in 5 fractions (total dose of 55 Gy). Generally, small peripheral tumours are treated with SABR where there is a possibility to give high dose to the tumour. In this case, 5 ipsi-lateral ribs were contoured out of which 3 were in close proximity to the tumour.

6.2.3 Dose calculation with TPS algorithms and MC

Virtual lung phantom study

In case of the virtual phantom, the treatment plans were done in the Eclipse TPS with conformal fields using 6 MV photon beams from a Varian Clinac 2100 C/D with jaw settings 6×6 cm^2 and 12×12 cm^2 in case of the 2 cm and 8 cm GTV phantom cases respectively. The beams were shaped to cover the PTVs with Varian Millennium 120 MLC with a margin of 0.7 cm. Parallel opposed

treatment plans with a prescription dose of 55 Gy in 20 fractions to the ICRU reference point, which was the centroid of the PTV(95% isodose line just covering the PTV) were created using PBC with MB heterogeneity correction, PBC_{MB} and the same MUs for each beam were used to recalculate the dose with two other *type a*, four *type b* algorithms and MC. The classification of the algorithms are given below:

1. Models that do not account for changes in lateral electron transport - PBC with modified Batho heterogeneity correction method (PBC_{MB}), equivalent tissue air ratio method (PBC_{ETAR}) of Eclipse, equivalent path length correction (PBC_{EPL}) of Oncentra - *type a* algorithms.

2. Models that account for changes in electron transport in an approximate way - AAA_{Ecl} of Eclipse, AC_{Pin}, CCC_{Pin} of Pinnacle, CCC_{Onc} of Oncentra - *type b* algorithms.

3. Full MC - EGSnrc, BEAMnrc, DOSXYZnrc based MC dose calculation.

The differences between the algorithms will be henceforth mentioned separately when necessary and grouped as *type a* and *type b* algorithms in other circumstances in order to refer to convolution- and CS-based algorithms respectively. The MC dose calculation algorithm is always denoted explicitly. The plan characteristics including gantry, collimator, couch angle, jaw and MLC settings and weighting of the beams were kept identical in all the plans. A dose grid of dimensions $0.25 \times 0.25 \times 0.5$ cm^3 was used for the computation in all the cases. Treatment plans were done on the heterogeneous virtual lung phantom.

NSCLC 3DCRT patient plans

In case of 3DCRT patient plans, 6 MV photon beam 3D conformal treatment plans with three fields using Varian Millennium 120 leaves were done for all ten patients. All the patient plans included EDWs in two or more fields where it was necessary. The field margins or in other words, PTV to MLC margins were 7 mm in all the cases and the leaves were manually edited in some plans to ensure PTV coverage. Similar to the phantom study, the treatment plans were done with PBC_{MB} to begin with. Isocentric treatment plans with the isocentre at the

centroid of the PTV with a prescription dose of 55 Gy in 20 fractions was used. The dose was prescribed to the ICRU reference point which in this study was the centroid of the PTV. The MUs of the PBC_{MB} were used to recompute the doses with 7 TPS algorithms and MC.

NSCLC SABR patient plan

An SABR lung patient plan with 9 fields with a GTV volume of 1 cm^3 was considered. In our clinic, we choose the weighting of the beams by optimising the patient plan with strict MLC margins around the PTV, each beam with one segment (an SABR patient plan is essentially a 3DCRT plan but in order to differentiate the conventional and hypo-fractionated treatments investigated in this study these two notations are used). A total dose of 55 Gy in 5 fractions, with a daily dose of 11 Gy was prescribed to the 75% isodose line covering the PTV. The dose distribution along the periphery of the PTV is close to 75% and it increases up to 100% as we go towards the centroid of the PTV. In our institute, the isocentre of the SABR patients is usually set at the mid line irrespective of which side the tumour is located, in order to enable maneuverability of the cone beam computed tomography (CBCT) gantry around the patient without any couch movement. The treatment beams were conformed by asymmetric jaws and MLC fileds with over leaf travel and the dose normalisation point was chosen in the region with uniform, shallow dose gradients, usually inside the GTV. Similar to the 3DCRT NSCLC plans, the SABR plan was calculated with PBC_{MB} with the prescription dose as explained above and then the plans were recalculated with other algorithms including MC. The MC dose calculation of the virtual phantom, 3DCRT and SABR NSCLC patient plans were performed as explained in section 4.2 of chapter 4. The workflow of MC dose calculation is summarised in the form of a flow chart in figure 4.9 (see section 4.2.11 of chaper 4).

6.2.4 Radiobiological evaluation of treatment plans

The differential dose volume histograms (dDVHs) of the GTVs and TL-GTVs of treatment plans created with analytical algorithms and MC were exported from Eclipse, Pinnacle and Oncentra TPSs for radiobiological analysis. In case

of clinical patient plans, the PTV DVHs were exported additionally. The TCPs were calculated with the dDVHs of the GTVs in case of virtual lung phantom and with both GTVs and PTVs in case of clinical patient plans. The NTCPs of the normal lung volume were calculated with dDVHs of the TL-GTV volume. The dDVHs were exported in terms of absolute units of dose and volume. The Marsden TCP model [27,31,32] (see section 3.5.1 of chapter 3) based on Poission statistics was used along with the TCP parameters for lung derived by Nahum *et al.* [130] (see section 3.5.2 of chapter 3) to compute the TCPs. The LKB model [139] (see section 3.6.2 of chapter 3) was used to compute the NTCPs of normal lung with radiation pneumonitis parameters reported by De Jaeger *et al.* [40] (see section 3.6.4 of chapter 3). The pair of lungs was considered as a single organ. The dDVHs of GTV, PTV and TL-GTV were imported in Bio-Suite, an in-house radiobiological evaluation tool developed by Uzan *et al.* [199]. The TCP and NTCP models with appropriate parameters were used, a detailed account of which is given in sections 3.5.2 and 3.6.4.

6.3 Results

6.3.1 Dosimetrical and radiobiological evaluation of the virtual lung phantom study

Lateral profiles

The lateral or x profiles and longitudinal or y profiles of plans calculated with all the TPS algorithms and MC of both the small and large tumour of the virtual lung phantom are shown in figures 6.4(a), 6.4(b) and 6.5(a), 6.5(b) respectively. The comparison of lateral or x profile at the central slice of the phantoms with small and large tumour calculated with *type a* and *type b* algorithms with MC shows that the former type of algorithms including PBC_{MB} , PBC_{ETAR} and PBC_{EPL} generally tend to over estimate the doses both at the isocentre and across the field. In case of the small tumour, differences of up to 1 Gy are found at the isocentre and slightly more than 1 Gy across the tumour whereas differences of up to 6 Gy are found in the lung region when PBC_{MB} doses are compared against

MC algorithms. The magnitude of these differences are reduced in case of the large tumour: less than 0.5 Gy at the isocentre and 4 Gy in lung.

The lateral profiles of the *type a* algorithms are characterised by pronounced horns in the low density lung region, PBC_{MB} predicts 4 Gy and 3 Gy higher in small and large tumour respectively at a distance of 1 cm lateral from the periphery of the tumour or tumour-lung interface. The *type b* algorithms predict doses that are closer to the MC algorithm. Although these algorithms predict very similar dose at the isocentre with a spread of 0.5 Gy and across the tumour along the line perpendicular to the central axis of the beam there is an underestimation of up to 1 Gy at the lung-tumour interface by AAA_{Ecl} and a small overestimation in the order of 0.5 Gy in the lung by AC_{Pin} and CCC_{Pin} when compared to MC. In case of the large tumour, the differences between the algorithms are in the same direction but the absolute values of these differences are smaller.

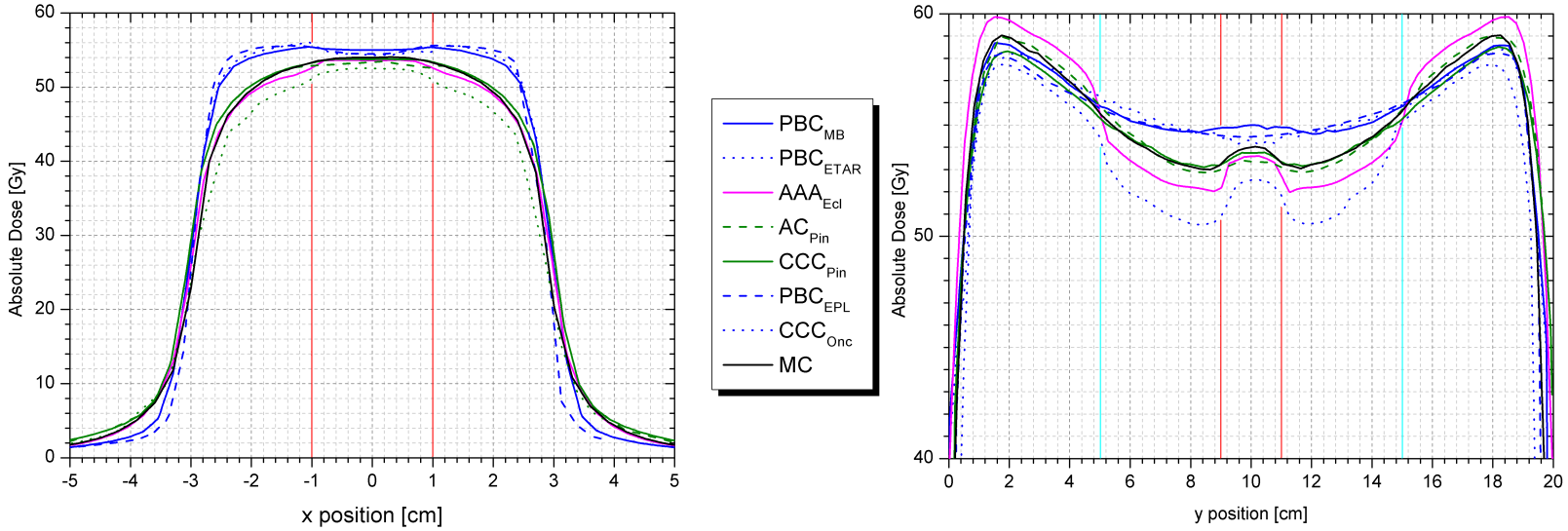

(a) (b)

Figure 6.4: (a) Lateral or x profile and (b) longitudinal or y profile of the virtual lung phantom calculated using *type a*, *type b*, and MC algorithms with spherical tumour of diameter 2 cm. The red lines indicate the boundary of the GTV and the blue lines (seen only in the longitudinal plot as everything outside the red lines in the lateral plot is lung) represent the lung.

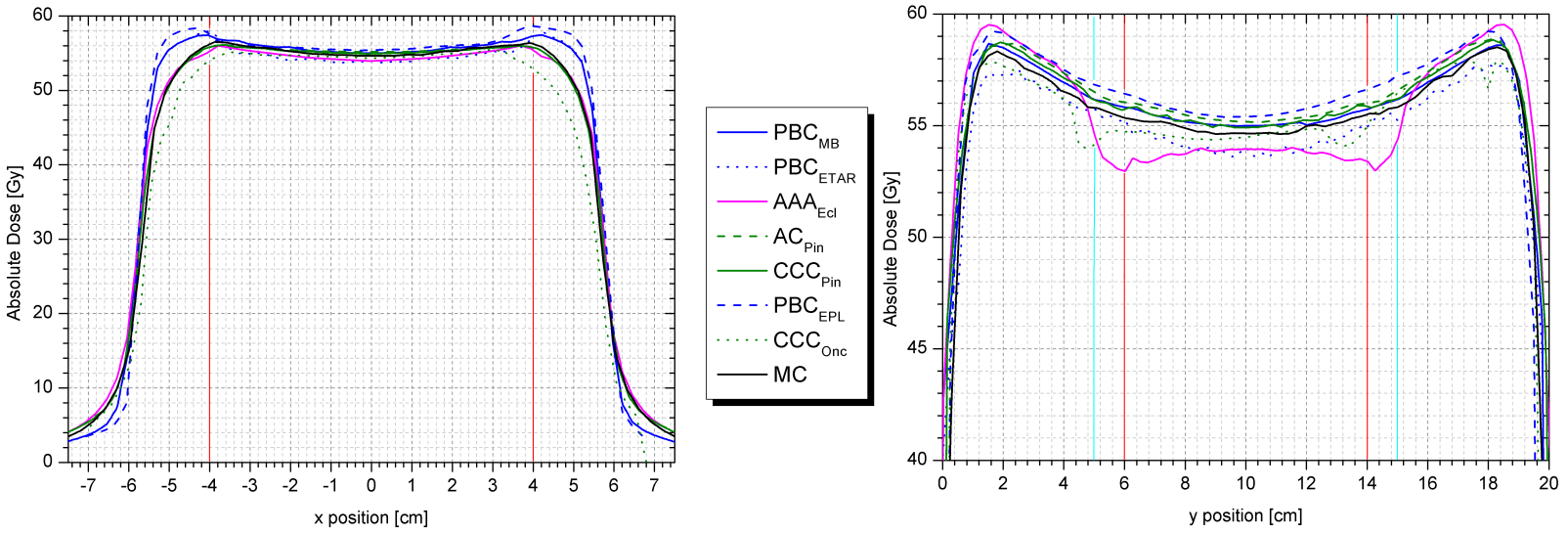

(a) (b)

Figure 6.5: (a) Lateral or x profile and (b) longitudinal or y profile of the virtual lung phantom calculated using *type a*, *type b*, and MC algorithms with spherical tumour of diameter 8 cm. The red lines indicate the boundary of the GTV and the blue lines (seen only in the longitudinal plot as everything outside the red lines in the lateral plot is lung) represent the lung.

Longitudinal profiles

From the longitudinal or y profile of the 2 cm phantom, it is evident that *type a* algorithms overestimate the dose both in the tumour and in the lung region. The longitudinal profile extracted from dose distributions of PBC_{MB} algorithm indicates that, the dose is over predicted by 1 Gy (2%), up to 1.5 Gy and slightly less than 2 Gy at the isocentre, along the beam central axis in the tumour, and at the tumour-lung interface respectively. In lung, the differences are up to 2 Gy in the region close to the tumour and the dose profile starts converging in the direction towards the water slabs above and below lung where it underestimates the dose to a small degree. Among the *type b* algorithms, AAA_{Ecl} behaves strikingly different than AC_{Pin} and CCC_{Pin}, by under estimating the dose in the tumour and lung but overestimating the dose in the unit density water slabs; the differences in the doses are less than 0.5 Gy, up to 1.5 Gy, and 1 Gy respectively. The difference in the dose profiles between AC_{Pin} and CCC_{Pin} are insignificant and are much closer to MC in the small tumour phantom plan whereas consistent difference of up to 1 Gy exist between the two CS algorithms of Pinnacle TPS and MC in case of the large tumour.

DVHs of the small and large tumour

The differential and cumulative DVHs of GTVs and PTVs of the small and large tumours are shown in figures 6.6(a), 6.6(b) and 6.8(a), 6.8(b) respectively. From the differential and cumulative DVHs, it is evident that the *type a* algorithms over estimate the dose systematically in both the cases i.e. virtual lung phantoms with 2 cm and 8 cm diameter tumours.

The differences in the DVHs between *type a* and *type b* algorithms with respect to MC are larger for the small tumour plans; this is because the ratio of the secondary electron ranges to the field size is greater. Also, the differences are larger for the DVHs of PTVs than the GTVs as a consequence of large differences in predicted dose distributions at the periphery of the GTV, GTV-PTV interface, and within the shell volume between GTV and PTV. When the plan is recalculated using MC with PBC_{MB} derived MUs, the absolute mean dose D_{mean}

of GTV and PTV is lower by 1.5 Gy and 4 Gy; a 3% and 7% relative reduction respectively. On comparing PBC_{MB} and PBC_{EPL} algorithms, both yield similar GTV and PTV DVHs; for the small tumour PBC_{EPL} underpredicts the low doses and overpredicts the high doses whereas in the large tumour it consistently overestimates both the low and high doses. While AAA_{Ecl} and CCC_{Pin} agree well with MC, two of the other *type b* algorithms AC_{Pin} and CCC_{Onc} systematically underestimate the doses to both target volumes of the small tumour. The variation in doses of the large tumour DVHs are smaller, the difference in D_{mean} between convolution algorithms and MC is less than 1 Gy. The DVHs of the *type b* algorithms are very similar to that of MC excluding AAA_{Ecl} which consistently deviates from MC in case of the large tumour, but is reasonably close to MC for the small tumour.

In both the cases, the differential DVHs of *type b* algorithms and MC were broader than that of the *type a* algorithms which indicates that the actual delivered dose distribution in the target volumes are less uniform. Although *type b* algorithms agree well with MC in most of the cases, differences still exist.

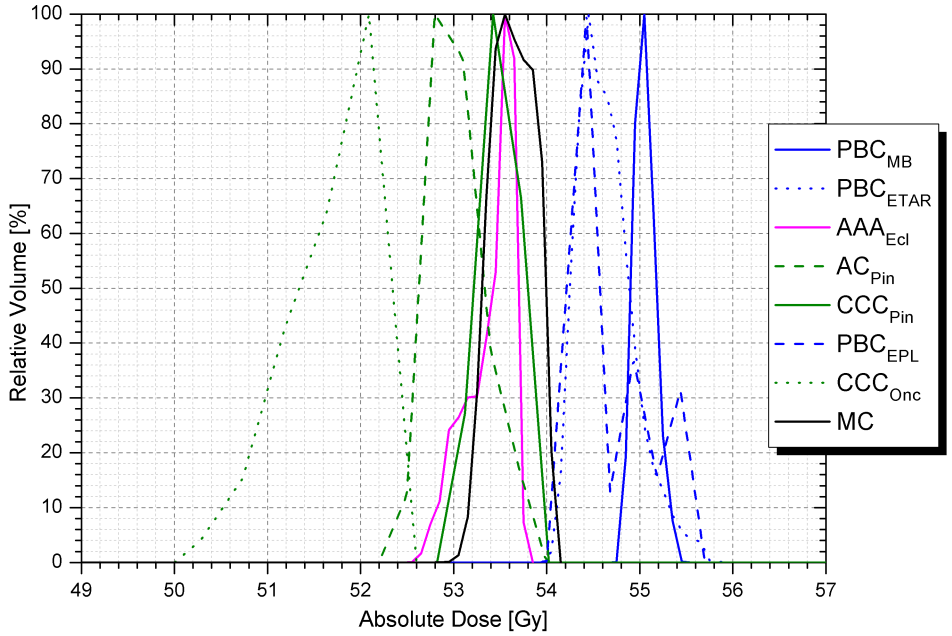

(a)

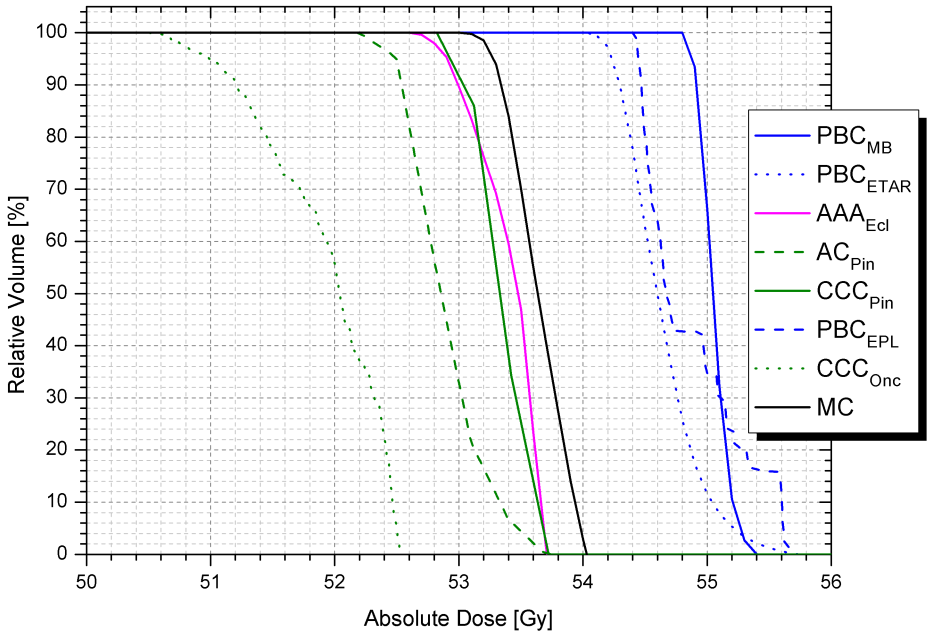

(b)

Figure 6.6: (a) Differential and (b) cumulative dose volume histogram of GTV of Lung phantom with a spherical tumour of diameter 2 cm

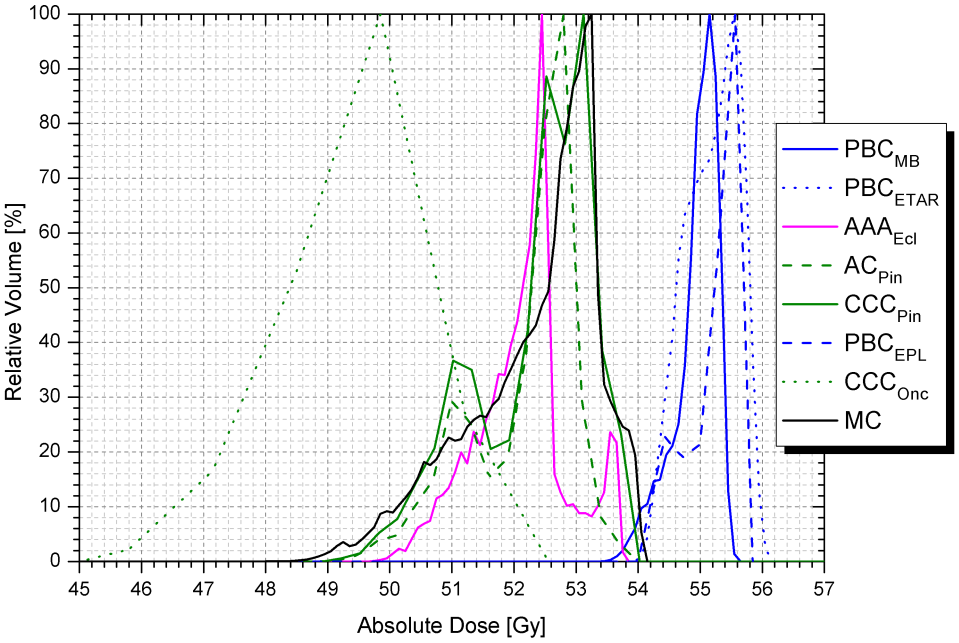

(a)

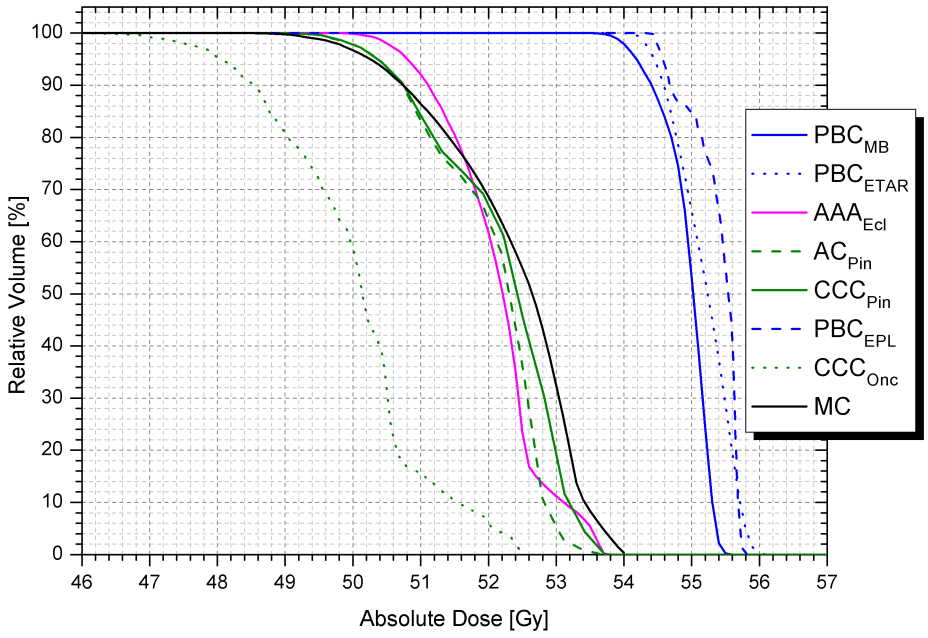

(b)

Figure 6.7: (a) Differential and (b) cumulative dose volume histogram of PTV of Lung phantom with a spherical tumour of diameter 2 cm

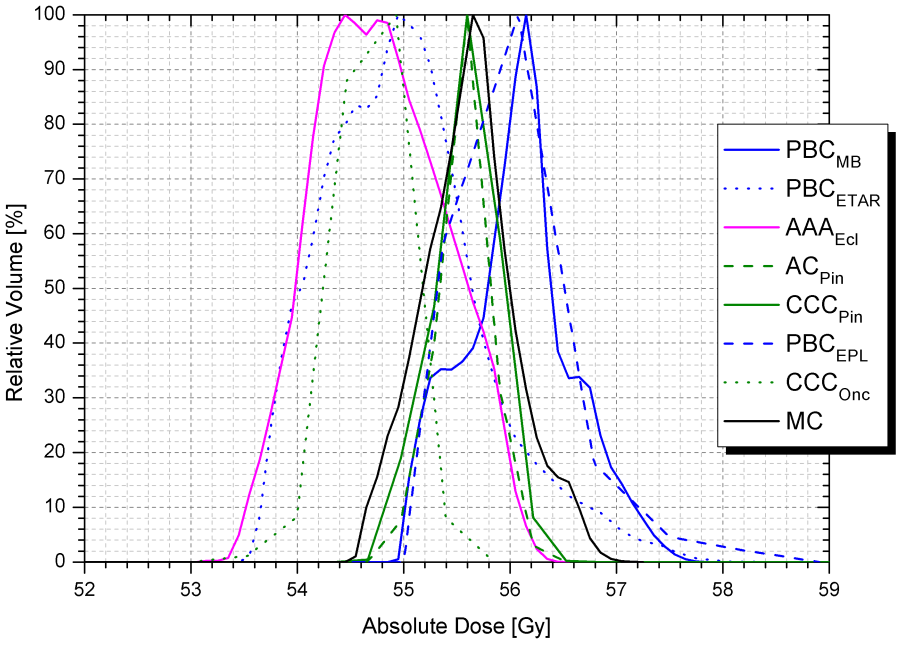

(a)

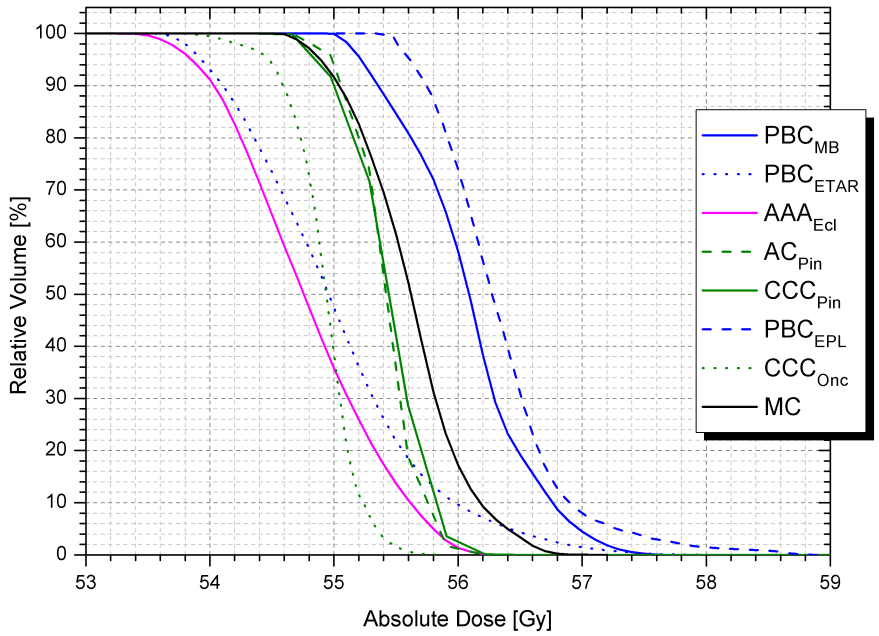

(b)

Figure 6.8: (a) Differential and (b) cumulative dose volume histogram of GTV of Lung phantom with a spherical tumour of diameter 8 cm

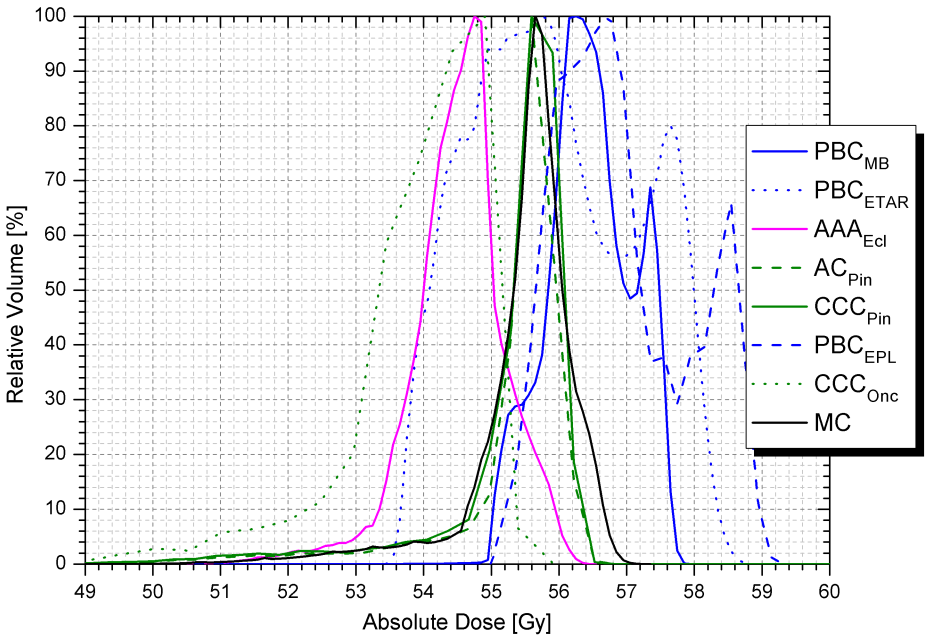

(a)

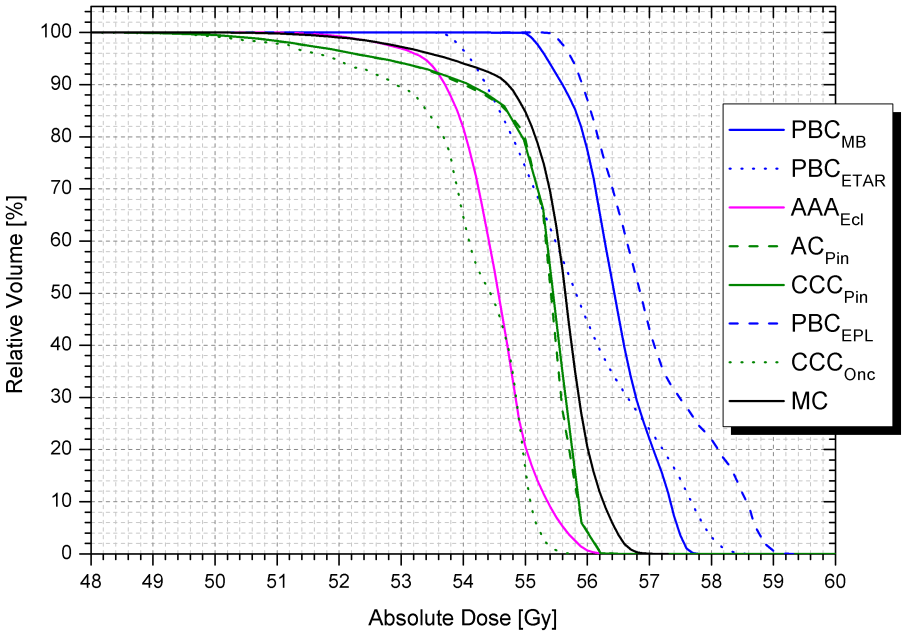

(b)

Figure 6.9: (a) Differential and (b) cumulative dose volume histogram of PTV of Lung phantom with a spherical tumour of diameter 8 cm

TCPs of small and large tumour

The TCPs of the small and large tumour of diameters 2 cm and 8 cm respectively are shown in the table 6.1. Differences of up to 10% in terms of absolute units are found in the TCP of the small tumour, whereas in case of the large tumour the differences reduce to 5% or less. The probability of controlling the small tumour is far higher than that of the large tumour; there is approximately a 45% greater chance of controlling the small tumour than the large one as the number of clonogens in the small tumour are far less than the large tumour[6]. The differences in the DVHs calculated by *type a*, *type b* and MC algorithms are reflected in the TCP values. Table 6.1 shows that *type a* algorithms of Eclipse and Oncentra TPSs over predict the TCPs with the PBC_{EPL} algorithm of Oncentra yielding the highest TCP followed by PBC_{MB}. In case of the small tumour, all the *type b* algorithms except CCC_{Onc} predict TCP values very close to that of MC. CCC_{Onc} results in a low TCP value which is 10% less than MC. In contrast, for the large tumour, the absolute differences in TCP values are relatively small. AC_{Pin}, CCC_{Pin} and MC dose distributions yield similar TCPs whereas AAA_{Ecl} and CCC_{Onc} underestimate the TCP by 6% and 4% respectively.

Table 6.1: TCPs [%] calculated using the dDVHs of GTVs of diameter 2 cm and 8 cm of the virtual lung phantom

	TCP [%]	
Algorithm	Small tumour	Large tumour
PBC_{MB}	81.9	34.0
PBC_{ETAR}	80.1	36.8
AAA_{Ecl}	74.1	25.6
AC_{Pin}	70.6	30.9
CCC_{Pin}	73.6	30.9
PBC_{EPL}	81.0	35.7
CCC_{Onc}	65.4	26.9
MC	75.4	31.1

[6]The TCP is predicted by taking into account the initial number of clonogens which is in turn calculated by multiplying the volume of GTV and clonogenic cell density (10^7 g/cm^3).

Cumulative DVHs and NTCPs of uninvolved normal lung

The cumulative DVHs of total lungs excluding the GTV volume, TL-GTV for both tumour sizes are shown in figures 6.10(a) and 6.10(b) respectively. In both cases, the doses in the low dose region are underestimated by *type a* algorithms and slightly over estimated by CCC_{Pin} and AC_{Pin}. The doses calculated by AAA_{Ecl} are far higher in the low dose regions in both small and large tumour plans. The CCC_{Onc} predicts a dose distribution which is very close to MC throughout, except in the high dose region where it tends to underestimate the dose. In case of the large tumour all the *type b* algorithms are very close to MC except for minor differences in the high dose region.

The NTCP values with radiation pneumonitis as the end point, calculated using the LKB model calculated with De Jaeger *et al.* [40] (TD_{50}=29.2 Gy, m=0.45, n=1, α/β=3 Gy) are given in table 6.5. NTCPs are smaller for the small tumour plans and larger for large tumour plans due to the differences in the volume of lung involved in the treatment field. In both the cases, the differences between the NTCP values calculated based on treatment plans done by various dose calculation algorithms are insignificant. The maximum absolute differences between the NTCPs predicted by *type a*, *type b* and MC algorithms were well below 1% for the small tumour plans, and just above 1% for the large tumour plans.

Table 6.2: NTCPs [%] with radiation pneumonitis as the end point calculated using the dDVHs of TL-GTVs of diameter 2 cm and 8 cm in the virtual lung phantom

	NTCP [%]	
Algorithm	Small tumour	Large tumour
PBC_{MB}	2.4	7.1
PBC_{ETAR}	2.4	7.1
AAA_{Ecl}	2.6	6.7
AC_{Pin}	2.3	6.2
CCC_{Pin}	2.3	6.2
PBC_{EPL}	2.4	7.5
CCC_{Onc}	2.2	6.5
MC	2.3	6.6

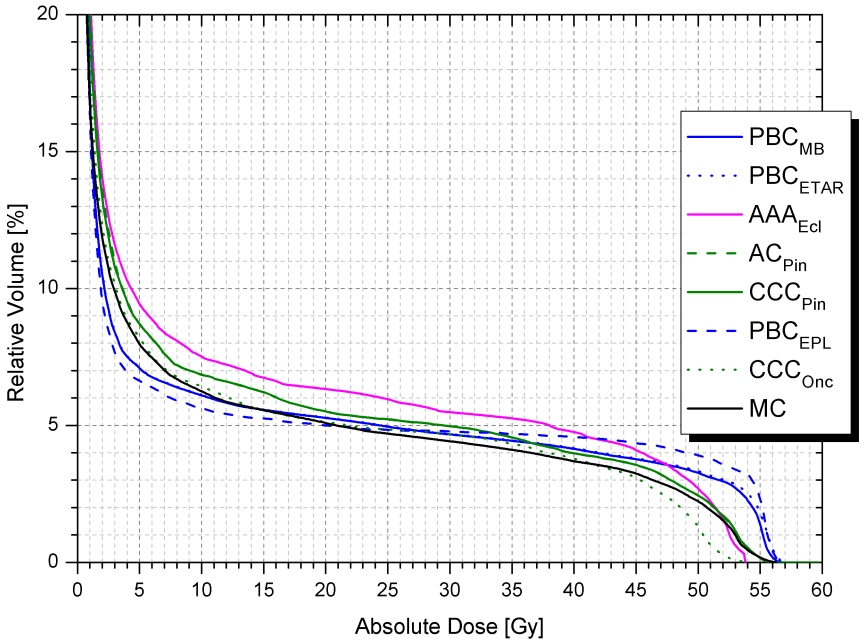

(a)

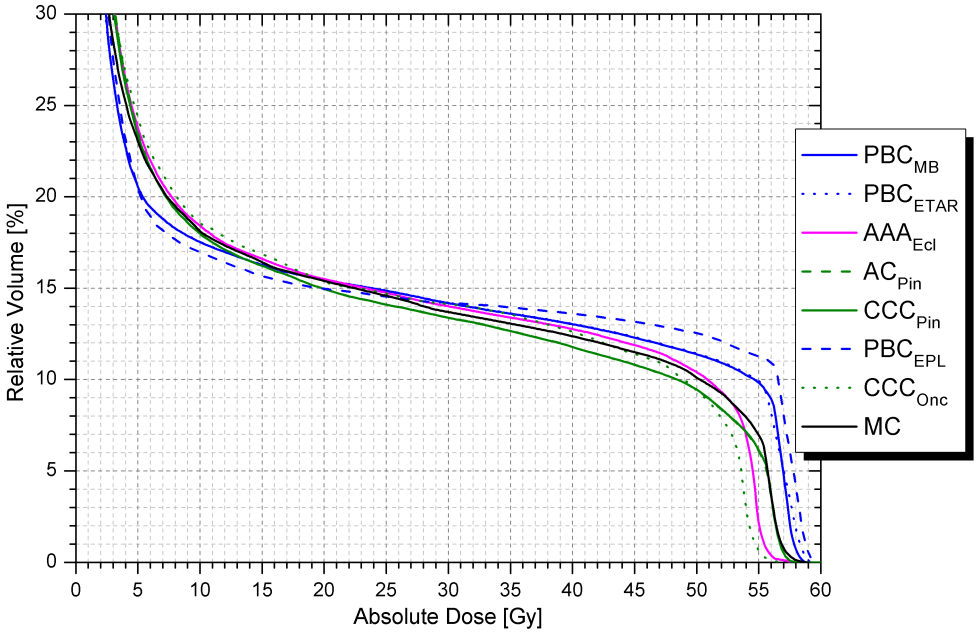

(b)

Figure 6.10: Cumulative dose volume histogram of TL-GTV of Lung phantom with a spherical tumour of diameter (a) 2 cm and (b) 8 cm

6.3.2 Dosimetrical and radiobiological evaluation of the NSCLC patient study

Dose calculation without heterogeneity correction

NSCLC patient treatment plans were also done by switching off the heterogeneity correction in order to separate the differences that arise due to beam modelling and the way different TPS algorithms handle the contour irregularities. It is to be noted that in the lung study we used the MUs of each field calculated by PBC_{MB} of Eclipse and recalculated the dose distribution with other algorithms. The TPS algorithms were modelled with beam data measurements done in a water phantom including relative measurements depth doses, beam profiles of open and wedge fields at various field sizes and depths, output factors and absolute doses are calculated by the calibration factor where 100 MUs delivers 100 cGy at d_{max} for a 10×10 cm^2 field at 100 SSD. These measurements were done according to the requirements of the TPS vendor.

In case of calculations without heterogeneity corrections, two different methods were used: in the first method the dose calculation was done with PBC_{Ecl} algorithm without heterogeneity correction for a prescription dose of 55 Gy in 20 fractions and the MUs of each treatment field was used to recalculate the doses with other algorithms. In the second method, dose prescription was done separately with each algorithm with their respective MUs. It was found that differences in MUs of up to ±2 existed when the doses were calculated without heterogeneity correction which could be attributed to the differences in beam modelling, handling the contour irregularities of the patient.

When the doses were recalculated by other TPS algorithms using the PBC_{MB} MUs differences of upto 2%/2mm for rectangular fields and 3%/3mm for asymmetric, MLC, wedged fields were found which is well within the recommendation by Van Dyk *et al.* [13] and Fraass *et al.* [200]. Cumulative DVHs of GTV and PTV volumes of plans done without heterogeneity correction with all the investigated photon dose calculation algorithms are shown in figures 6.11(a) and 6.11(b) respectively.

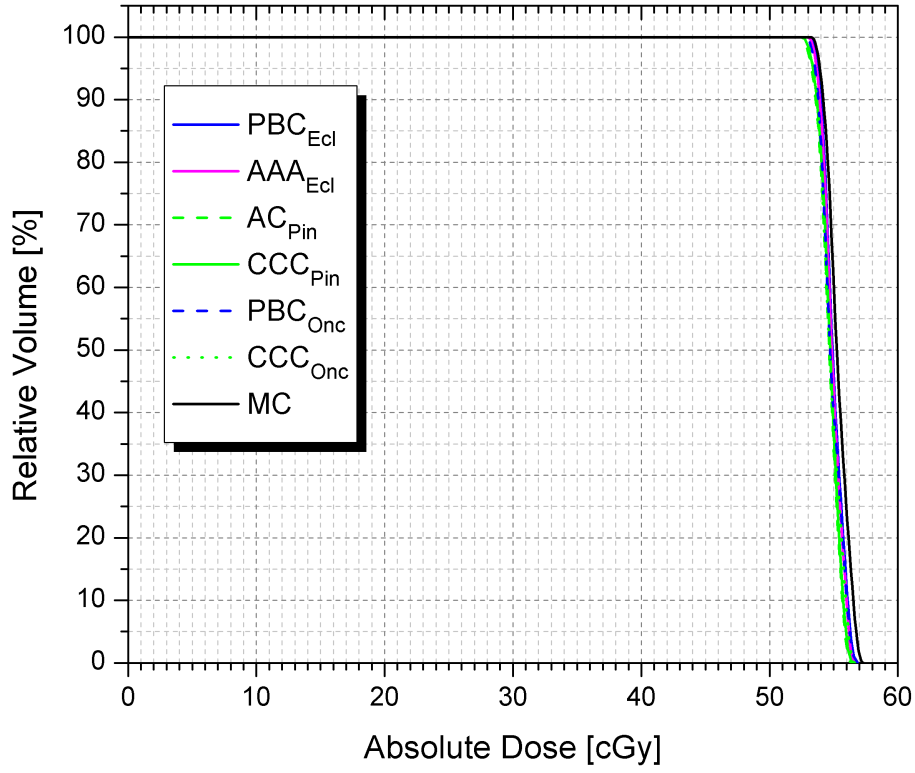

(a)

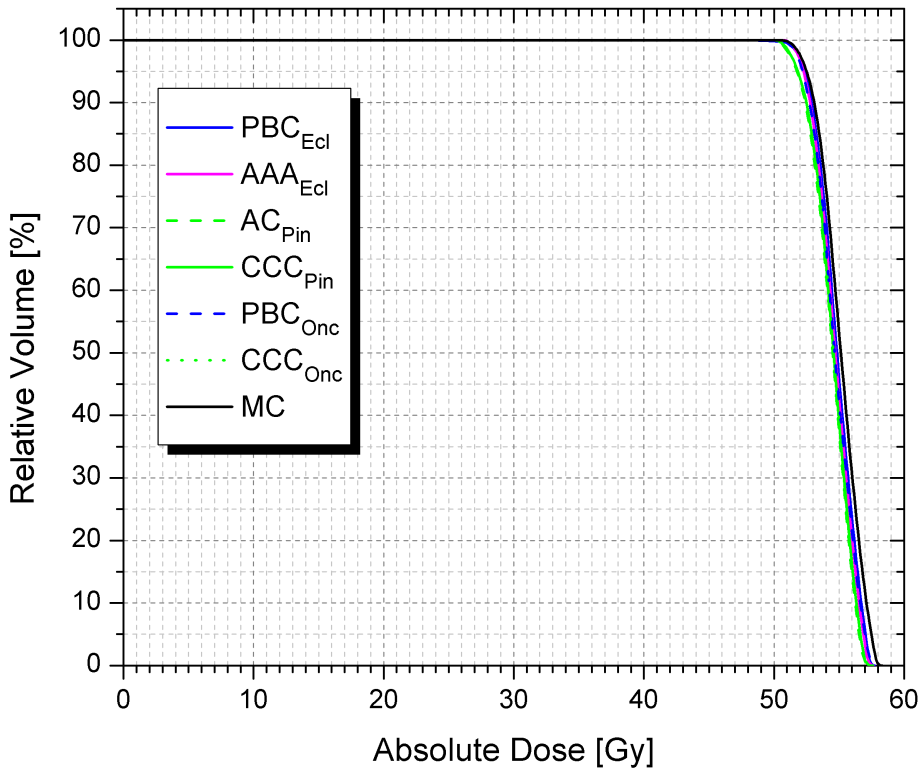

(b)

Figure 6.11: Cumulative DVHs of (a) GTV and (b) PTV of one of the 3DCRT NSCLC treatment plans done without heterogeneity correction. [145]

DVHs of GTV and PTV of 3DCRT patient study

The differential and cumulative DVHs of the GTV and PTV volumes of a patient plan with a small tumour of volume 26 cm^3 are shown in figures 6.12 and 6.13. The DVHs of the patient plan with a small tumour show a trend similar to that of the virtual phantom plan with a small tumour where all 3 PBC algorithms overestimate the dose delivered to the GTV and PTV. AAA_{Ecl} predicts doses that are closer to MC whereas the variants of collapsed cone algorithms in Pinnacle and Oncentra overestimate and underestimate the doses respectively. When the DVHs of the PTV calculated by various algorithms are compared to MC, the low dose region is overestimated by both *type a* and *type b* algorithms.

In general, the results of all 10 patients shows that *type a* algorithms predict higher doses to both the target volumes in all the cases, irrespective of the size and location of the tumours. Among the *type b* algorithms AAA_{Ecl} underestimates doses in most cases whereas AC_{Pin} and CCC_{Pin} overestimate the doses compared to MC. In contrast, CCC_{Onc} underestimate the doses systematically in all cases in comparison to MC predicted doses. The differences in the dose distributions within the TPS algorithms and between the TPS algorithms and MC is larger for the PTV than the GTV. In all 10 patients, *type a* algorithms overestimated the dose to the GTV volumes whereas *type b* algorithms resulted in doses similar to that of the MC. However, considerable differences were found between the *type b* algorithms and MC algorithm when PTV DVHs were evaluated, owing to approximations in the modelling of electron transport by the *type b* algorithms. The differences in the dose distribution calculated by the algorithms widely depend on a number of factors such as the volume of the tumour, field size, density of the medium, location of the tumour, and path length of the beam in lung.

Mean doses of GTV and PTV of 3DCRT patient study

D_{mean} values of GTV and PTV volumes are shown in figures 6.14(a) and 6.14(b) respectively. In general, the largest differences in D_{mean} is observed between *type a* algorithms and MC. The differences between the D_{mean} values estimated by

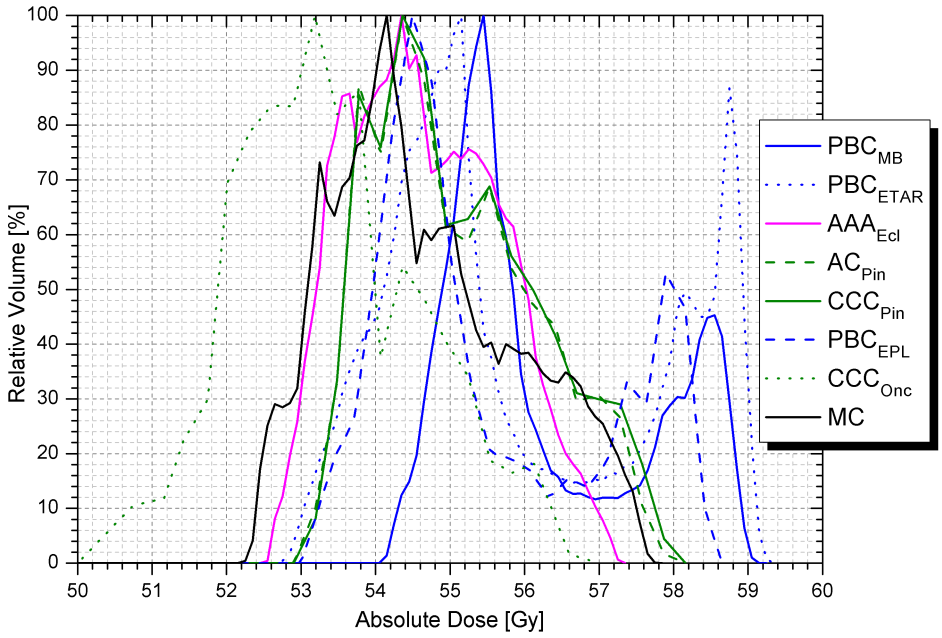

(a)

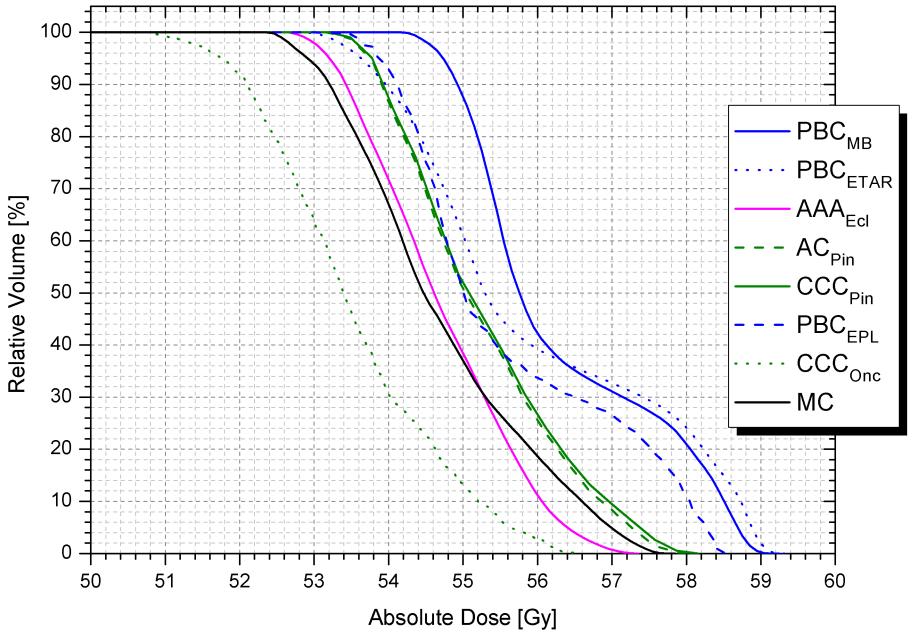

(b)

Figure 6.12: (a) Differential and (b) cumulative dose volume histogram of GTV of a patient with a small NSCLC tumour

type b algorithms and MC are smaller. The higher the D_{mean}, higher is the TCP. However, for DVHs which result in the same D_{mean} values, the one that receives a lower minimum dose will result in a lower TCP and vice versa.

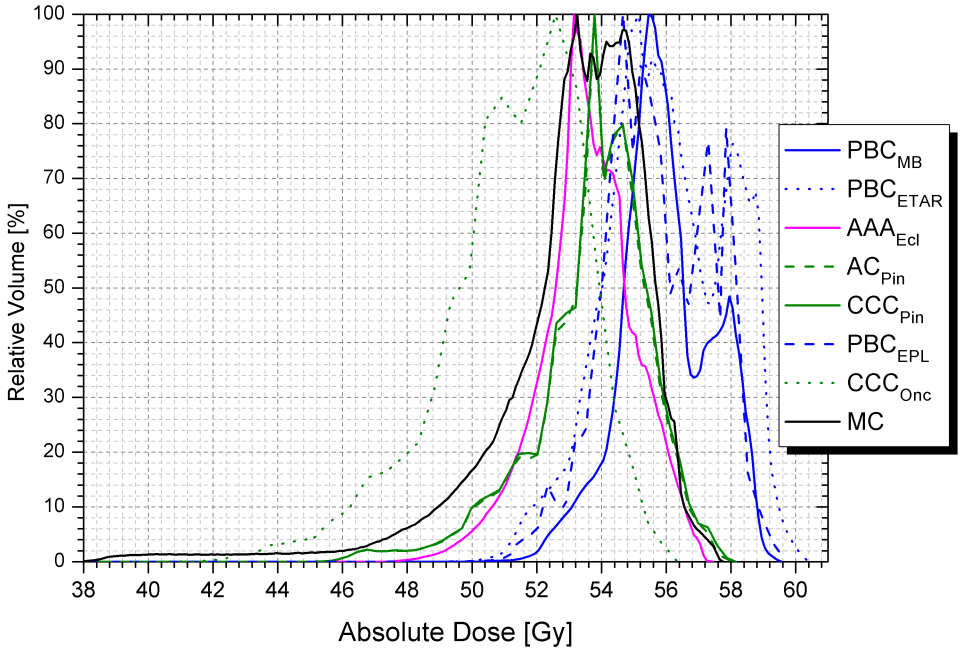

(a)

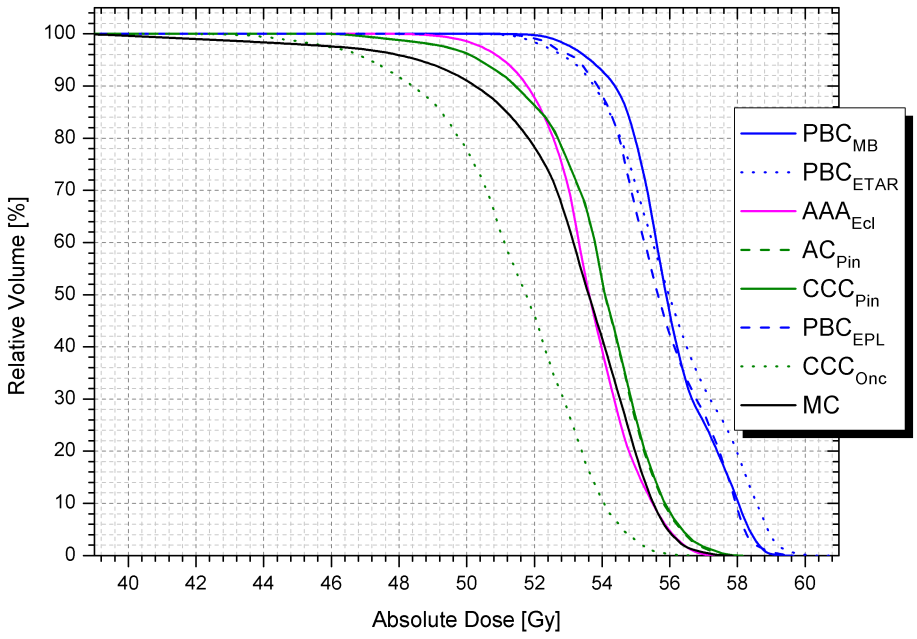

(b)

Figure 6.13: (a) Differential and (b) cumulative dose volume histogram of PTV of a patient with a small NSCLC tumour

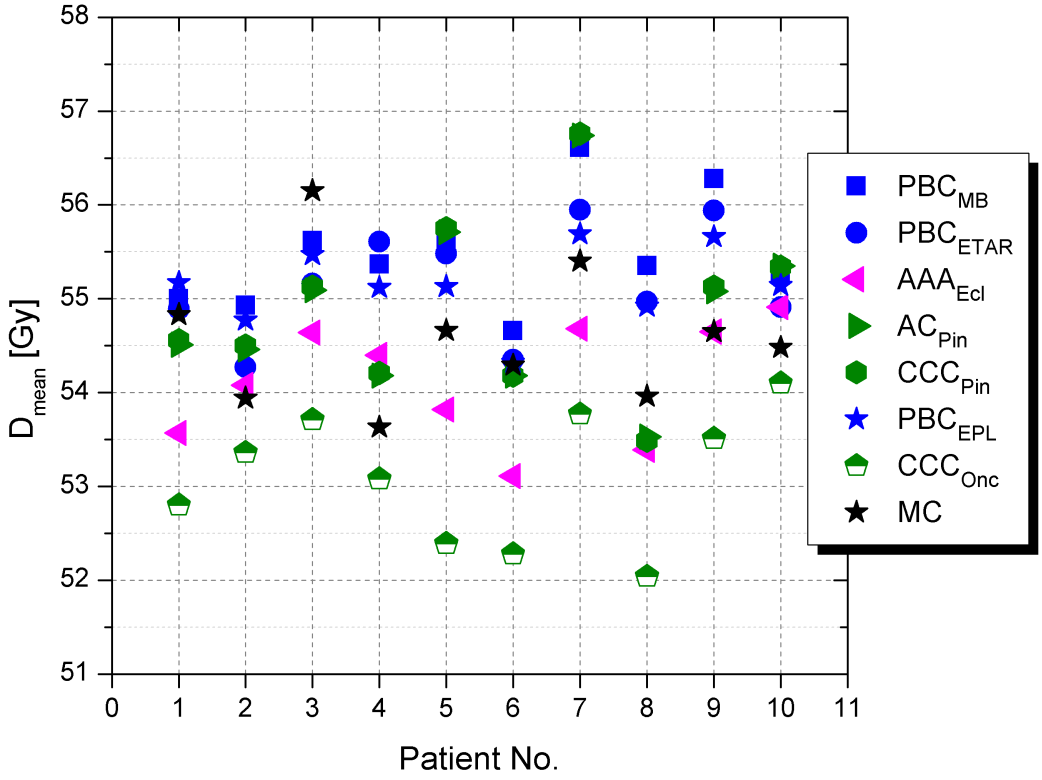

(a)

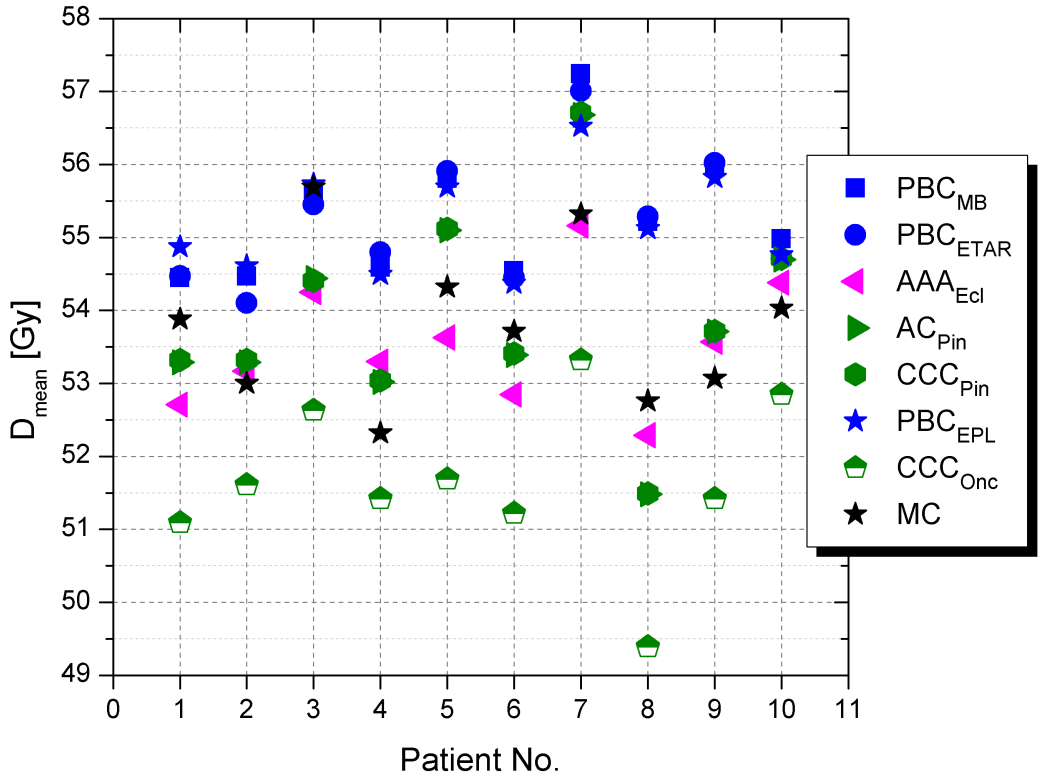

(b)

Figure 6.14: D_{mean}, mean dose received by (a) GTV and (b) PTV volumes

TCPs of the 3DCRT patient study

Figures 6.15 and 6.16 show the TCP values of the 3DCRT patient plans calculated from GTV and G-PTV DVHs against the GTV volume. The second sub figure in both cases is to enhance the visualisation of the differences in TCPs of three patient plans with GTV volumes closer to each other. Tables 6.3 and 6.4 show the TCP values of all the 10 patient plans calculated with various photon dose calculation algorithms estimated using the GTV and G-PTV dDVHs respectively. The volumes of the GTV ranged from 26 cm^3 to 175 cm^3 and the absolute TCPs varied according to the size of the tumour, the smaller the volume of tumour, the higher is the TCP. Other factors like the dose distribution or dose coverage of the tumour, mean and minimum doses received, also influence the local control. Generally, the TCPs obtained from the GTV DVHs of a patient are larger than that obtained by using the G-PTV DVHs as the dose coverage of the GTV is better than that of the PTV.

The differences between the TCP values calculated with various algorithms are larger when calculated with G-PTV DVHs as the differences in the doses calculated are larger at the interface, the shell volume between the GTV and PTV and the periphery of the PTV. Differences of up to 38% are found between GTV_{TCP} (TCP calculated with GTV DVHs) and G-PTV_{TCP} (TCP calculated with G-PTV DVHs) of when calculated using DVHs of same algorithm. The differences between GTV_{TCP} and G-PTV_{TCP} are larger for *type b* algorithms than *type a* algorithms. When the GTV_{TCP} and G-PTV_{TCP} of *type a* and *type b* algorithms are compared against MC, the variation in small, medium, large tumours rise from 10% to 45%, 14% to 21%, and 5% to 27% respectively.

DVHs of uninvolved lungs of 3DCRT patient study

The cumulative DVHs of uninvolved lungs, which excludes the GTV volume, are shown in figure 6.21. It is seen from the DVHs that all the algorithms predict fairly similar doses to the lung volume, except for slight overestimation and un-

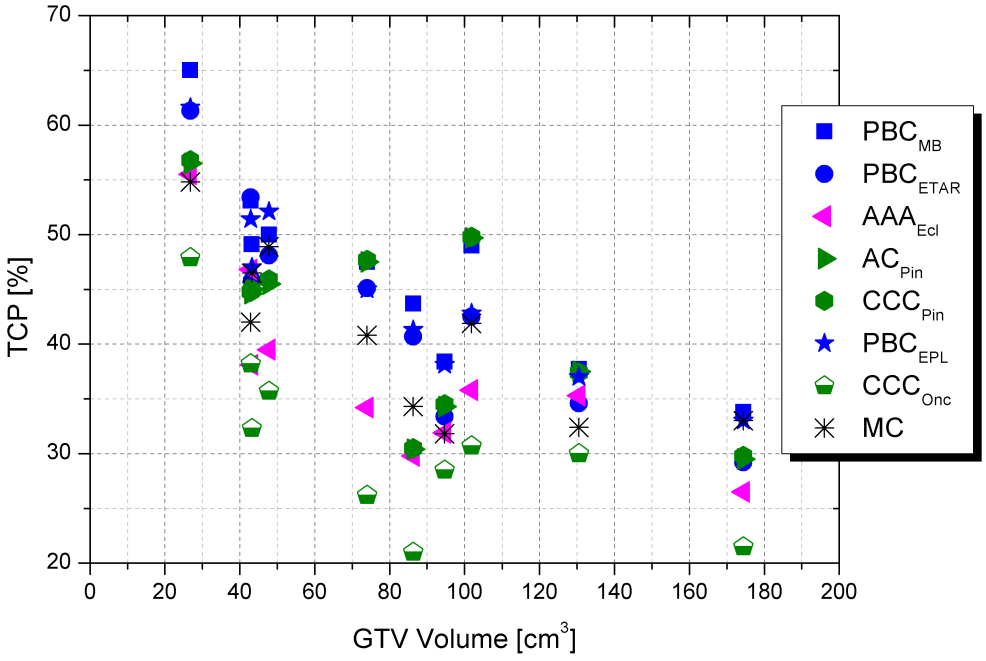

(a)

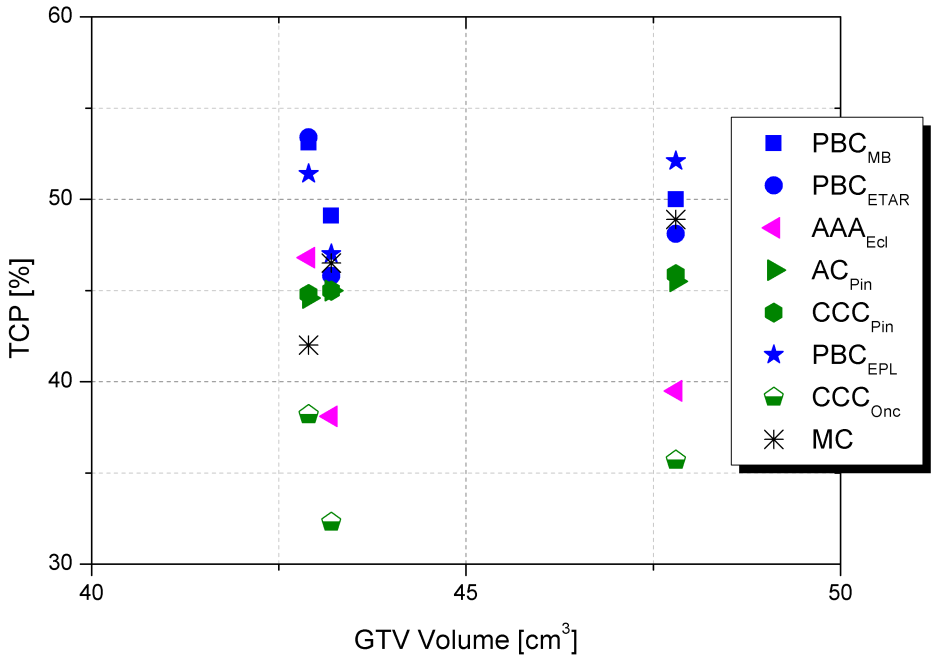

(b)

Figure 6.15: TCPs calculated using Marsden-Poisson model with the GTV dDVHs. The Marsden model parameters used were clonogenic cell density, $\rho_{cl} = 10^7$ cm^3, mean intrinsic radiosensitiviy over a patient population $\bar{\alpha}$=0.307 Gy^{-1}, σ_α=0.037 Gy^{-1}, α/β=10 Gy. (a) TCP$_{GTV}$ of all 10 patients and (b) TCP$_{GTV}$ of 3 patients with similar volumes (this plot is included for better visualisation of the differences)

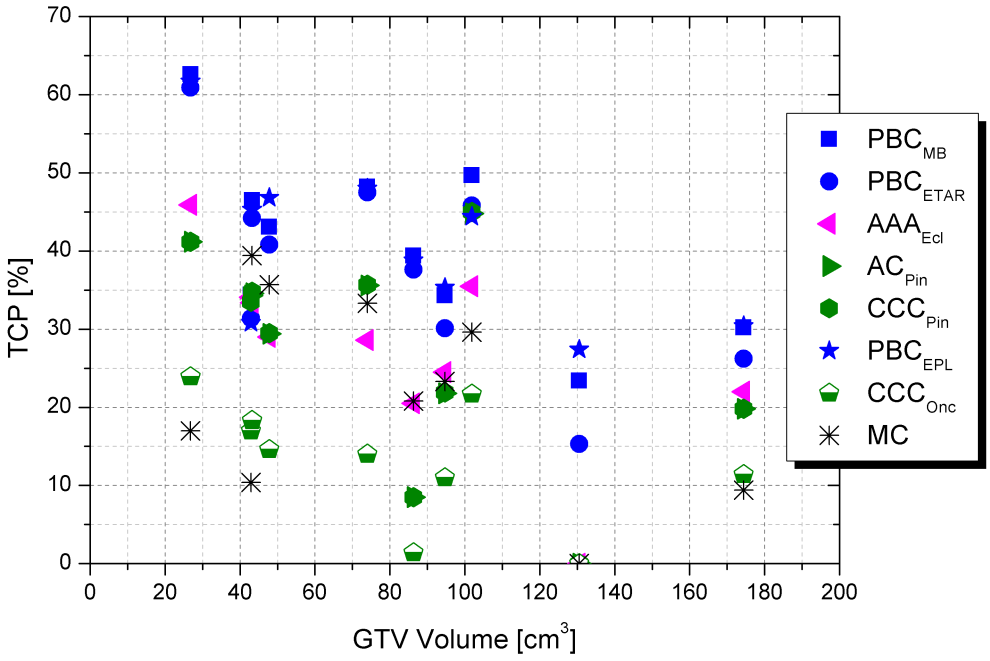

(a)

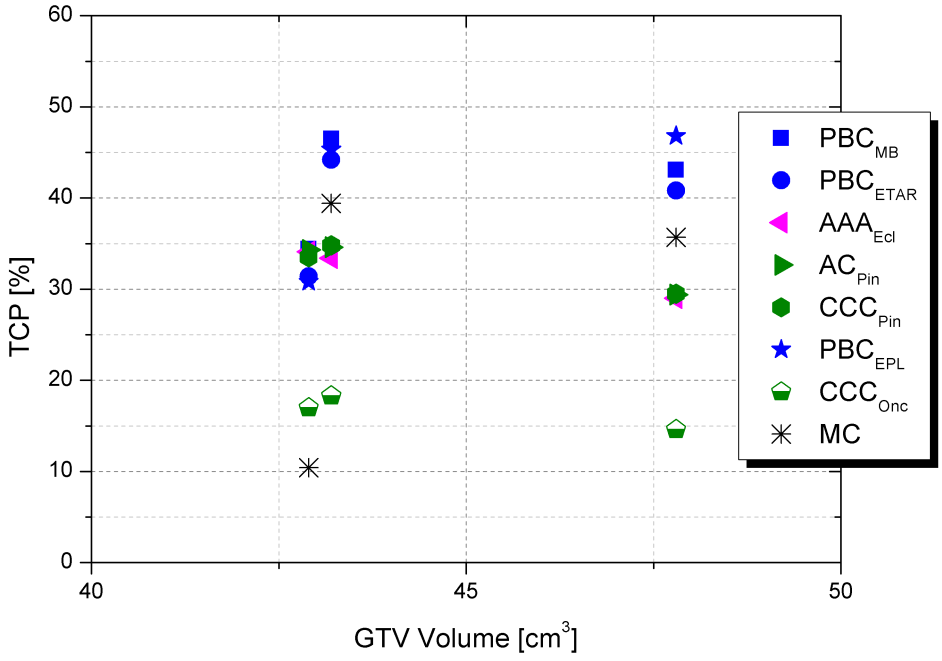

(b)

Figure 6.16: TCPs calculated using Marsden-Poisson model with the G-PTV dDVHs. The Marsden model parameters used were clonogenic cell density, $\rho_{cl} = 10^7$ cm^3, mean intrinsic radiosensitivity over a patient population $\bar{\alpha}$=0.307 Gy^{-1}, σ_α=0.037 Gy^{-1}, α/β=10 Gy. (a) TCP$_{G-PTV}$ of all 10 patients and (b) TCP$_{G-PTV}$ of 3 patients with similar volumes (this plot is included for better visualisation of the differences)

Table 6.3: TCPs [%] calculated using the dDVHs of GTVs for all the 10 NSCLC 3DCRT patients.

Algorithm	P1	P2	P3	P4	P5	P6	P7	P8	P9	P10
PBC_{MB}	50.0	38.4	33.8	53.1	47.5	49.1	49.0	43.7	65.0	37.7
PBC_{ETAR}	48.1	33.4	29.2	53.4	45.1	45.8	42.5	40.7	61.3	34.6
AAA_{Ecl}	39.5	31.9	26.5	46.8	34.2	38.1	35.8	29.8	55.5	35.3
AC_{Pin}	45.5	34.3	29.5	44.6	47.5	45.0	49.7	30.4	56.5	37.5
CCC_{Pin}	45.9	34.5	29.8	44.8	47.7	45.0	49.8	30.5	56.8	37.4
PBC_{EPL}	52.1	38.1	33.0	51.4	45.0	47.0	42.8	41.3	61.6	37.0
CCC_{Onc}	35.7	28.5	21.5	38.2	26.2	32.3	30.7	21.0	47.9	30.0
MC	48.9	31.8	33.0	42.0	40.8	46.5	41.9	34.3	54.8	32.4

Table 6.4: TCPs [%] calculated using the dDVHs of G-PTVs for all the 10 NSCLC 3DCRT patients.

Algorithm	P1	P2	P3	P4	P5	P6	P7	P8	P9	P10
PBC_{MB}	43.1	34.3	30.2	34.4	48.2	46.5	49.7	39.4	62.6	23.4
PBC_{ETAR}	40.8	30.1	26.2	31.4	47.5	44.2	45.8	37.6	60.9	15.3
AAA_{Ecl}	29.0	24.5	22.0	34.1	28.6	33.4	35.5	20.5	45.9	0
AC_{Pin}	29.4	21.8	19.8	34.3	35.6	34.6	44.8	8.5	41.2	0
CCC_{Pin}	29.5	21.9	19.8	33.5	35.7	34.8	45.0	8.5	41.3	0
PBC_{EPL}	46.8	35.3	30.4	30.8	48.0	45.3	44.4	38.8	61.7	27.4
CCC_{Onc}	14.6	11.0	11.4	17.0	14.0	18.3	21.7	1.4	23.9	0
MC	35.7	23.3	9.4	10.4	33.3	39.4	29.6	20.8	17.0	0

derestimation of doses in the high dose region (shell volume between GTV and PTV) by *type a* algorithms and CCC_{Onc} respectively. There is also systematic underestimation of the low dose region by the PBC_{EPL} algorithm. All other *type b* algorithms results in doses similar to that of MC.

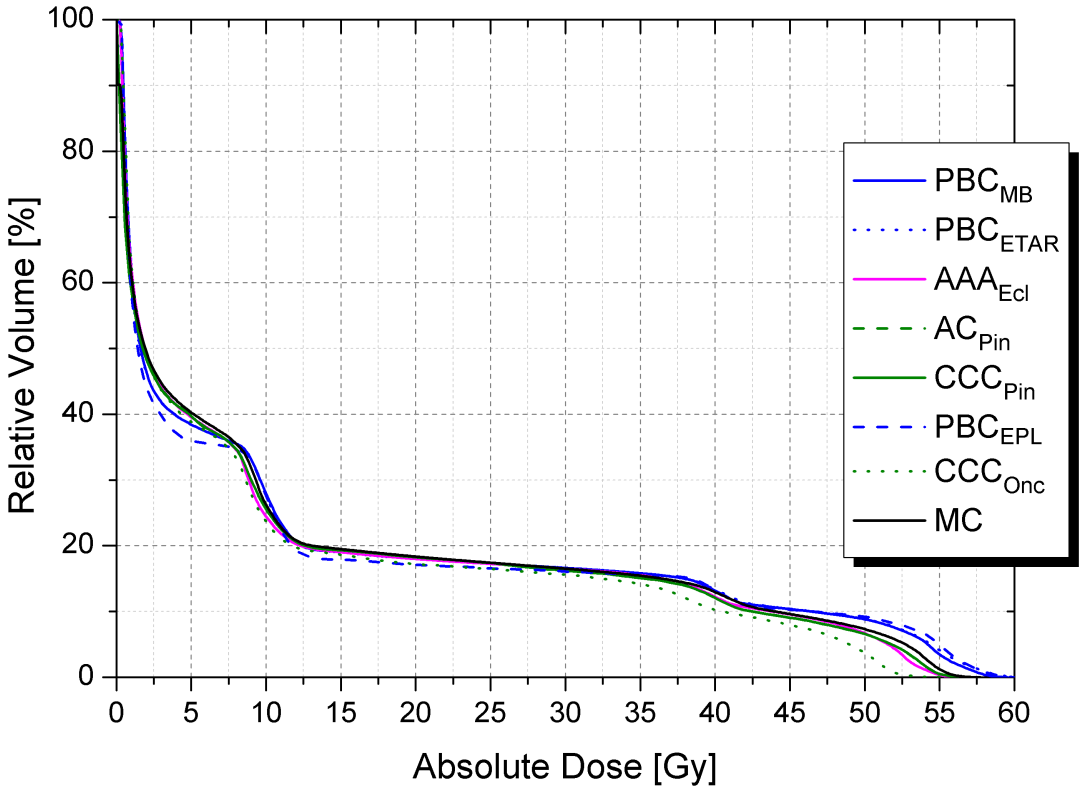

Figure 6.17: DVHs of TL-GTV of a patient with a small tumour

V_{20} and MLD of uninvolved lung of 3DCRT patient study

Dosimetric quantities such as MLD and V_{20} of the uninvolved lung are used as predictors to estimate lung toxicity. Absolute values of MLD and V_{20} obtained from dose distributions calculated by various dose calculation algorithms are shown in figures 6.18(a) and 6.18(b). Tolerance limits for V_{20} and MLD recommended by Marks *et al.* [57] are <30-35% and <20 Gy respectively. In all the patient plans, the above dosimetric quantities derived from dose distributions calculated by all the investigated photon dose calculation algorithms were well below the recommended tolerance limits. The differences between the V_{20} values predicted by all

the algorithms were small and were up to 4% in terms of absolute differences. In case of MLD, MC predicted values were larger in most of the cases, the maximum difference being 7 Gy.

NTCPs of uninvolved lung of 3DCRT patient study

Table 6.5 shows the absolute values of NTCPs for all the 10 patient plans based on the DVHs of *type a*, *type b* and MC algorithms. The NTCPs were less than 10% for most of the patients except two where the probability of the patients developing radiation pneumonitis was 16% and 21% as predicted by MC dose calculation. Higher NTCP values were predicted by MC followed by *type a* algorithms and *type b* algorithms. The differences in absolute NTCP values were insignificant similar to the results of the virtual phantom study. The results of our study differ from that of Nielsen *et al.* [201] who showed differences of up to 12% between the mean NTCP values of 20 patients. This could be due to the fact that their patient cohort received a total dose fractionation of 60-66 Gy in 2 Gy fractions which is significantly different from that of our study; also the stated mean NTCP values were four times larger. Also, they used a totally different set of LKB model parameters from ours. The differences between the NTCPs were greater for patient plans that yielded higher absolute NTCP values.

Table 6.5: NTCP values calculated using TL-GTV DVHs

Algorithm	P1	P2	P3	P4	P5	P6	P7	P8	P9	P10
PBC_{MB}	8.1	19.9	13.4	3.5	5.1	8.0	6.3	8.5	6.9	9.6
PBC_{ETAR}	8.2	20.0	13.4	3.5	5.1	8.1	6.3	8.5	7.0	9.6
AAA_{Ecl}	7.5	18.9	12.4	3.4	4.7	7.3	5.9	7.5	6.3	9.1
AC_{Pin}	7.3	17.5	11.9	3.3	4.6	6.9	5.8	6.1	6.1	9.1
CCC_{Pin}	7.3	17.5	11.9	3.3	4.6	6.9	5.8	6.1	6.1	9.1
PBC_{EPL}	7.8	18.4	12.6	3.3	4.9	7.3	5.8	6.4	6.4	9.2
CCC_{Onc}	6.5	15.3	10.5	3.1	4.3	6.3	5.1	5.4	5.4	8.0
MC	9.1	21.4	15.6	3.4	5.0	9.2	11.8	10.0	6.1	10.8

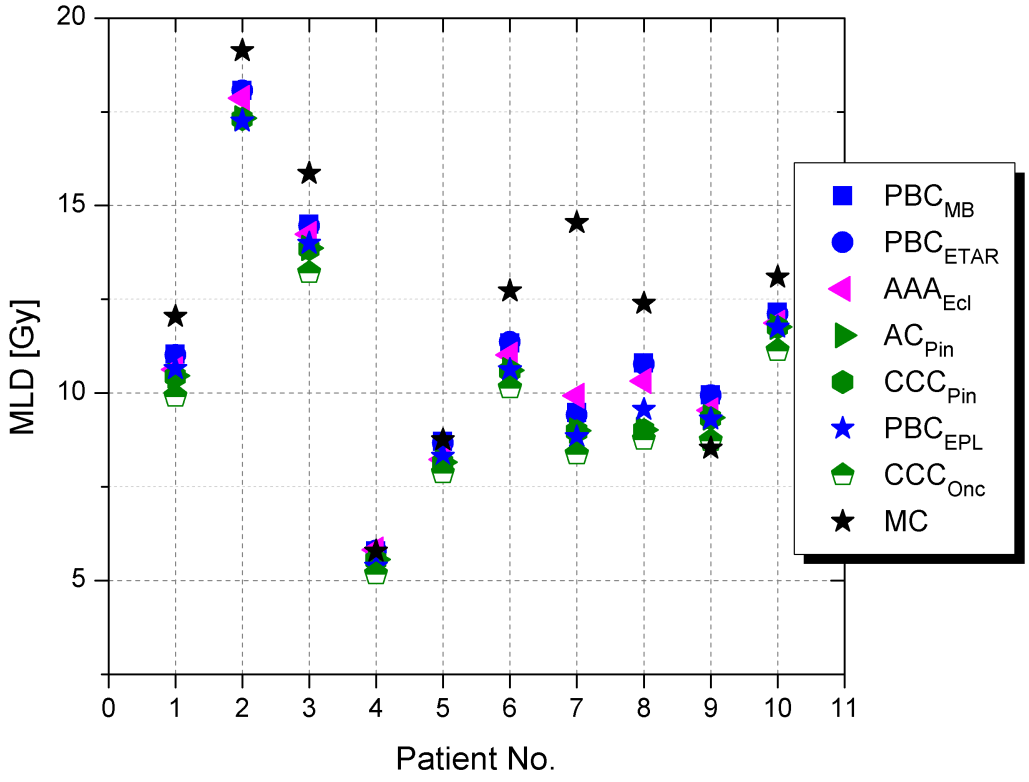

(a)

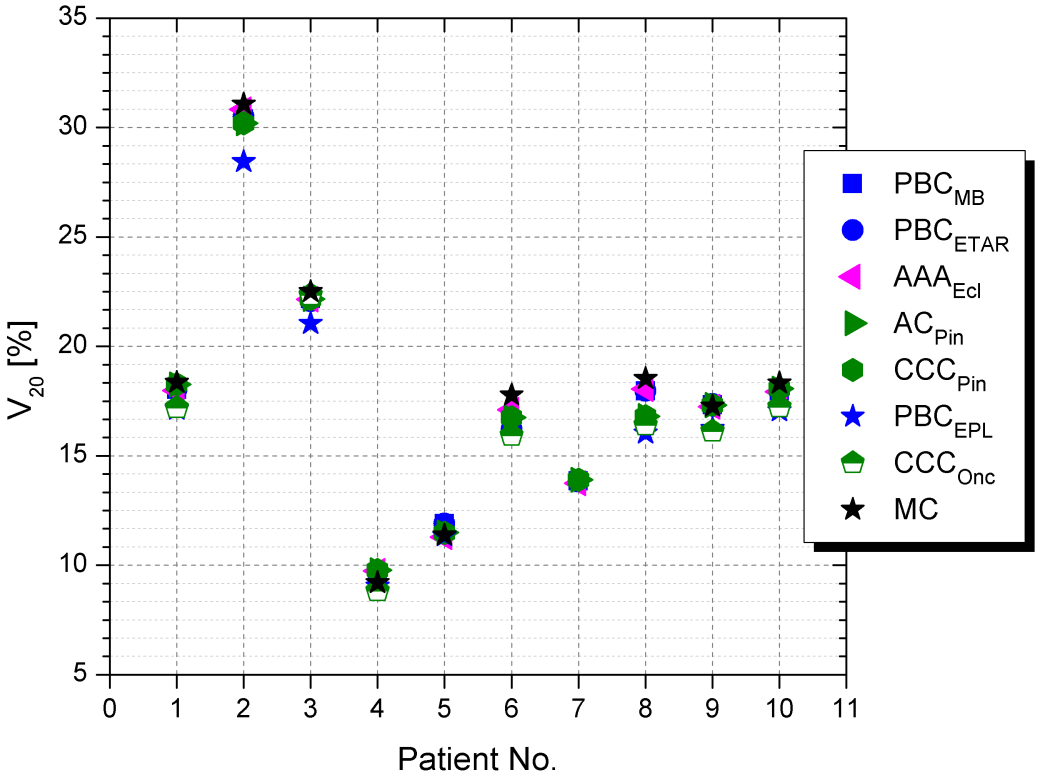

(b)

Figure 6.18: (a) MLD and (b) V_{20} values of all 10 NSCLC 3DCRT patient plans

DVHs of GTV and PTV of SABR patient plan

The cumulative and differential DVHs of the GTV and PTV of SABR patient plan calculated with all the algorithms are shown in figures 6.19(a), 6.19(b) and 6.20(a), 6.20(b). The cumulative DVHs of the TL-GTV and rib volumes are shown from figures 6.20. The dose to the GTV and PTV are overestimated by both the *type a* algorithms, similar to the 3DCRT plans. The AC_{Pin} and CCC_{Pin} algorithms result in similar DVHs which are very close to MC. The AAA_{Ecl} and CCC_{Onc} algorithms tends to underestimate the doses to the GTV. When the dose calculation is done with heterogeneity correction with the same number of MUs as the PBC_{Ecl}, the doses are under-estimated in the GTV but yields a PTV DVH similar to that of MC and other analytical algorithms. The GTV received a fairly uniform dose whereas the PTV received a non-uniform dose ranging from 55 Gy to 74 Gy. The differences in the dose distributions between the *type a* and *type b* algorithms in case of SABR plan are found to be larger than for the 3DCRT plans due to the fact that the tumour volume and dimension and hence the field sizes are smaller. The AC_{Pin} and CCC_{Pin} algorithms result in a dose distribution very close to MC both in the GTV and the PTV volumes, whereas the AAA_{Ecl} algorithm under estimates the dose in the GTV. The results were found to be similar to those shown by Panettieri *et al.* [197], where differences were shown between the doses calculated by MC and analytical dose calculation algorithms both in case of static and dynamically moving tumours.

TCPs of the SABR patient plan

TCPs calculated with GTV and G-PTV DVHs of the NSCLC SABR patient plan based on TPS and MC dose calculations are shown in table 6.6. The TCPs estimated with GTV and PTV DVHs with parameters for the Marsdel TCP model as derived by Nahum *et al.* [32] were all 100% irrespective of the differences in the calculated dose distribution by various TPS algorithms and MC. The combination of smaller tumour volume, and hence smaller numbers of initial clonogens to kill and hypo-fractionated doses, results in a very high tumour control which is oth-

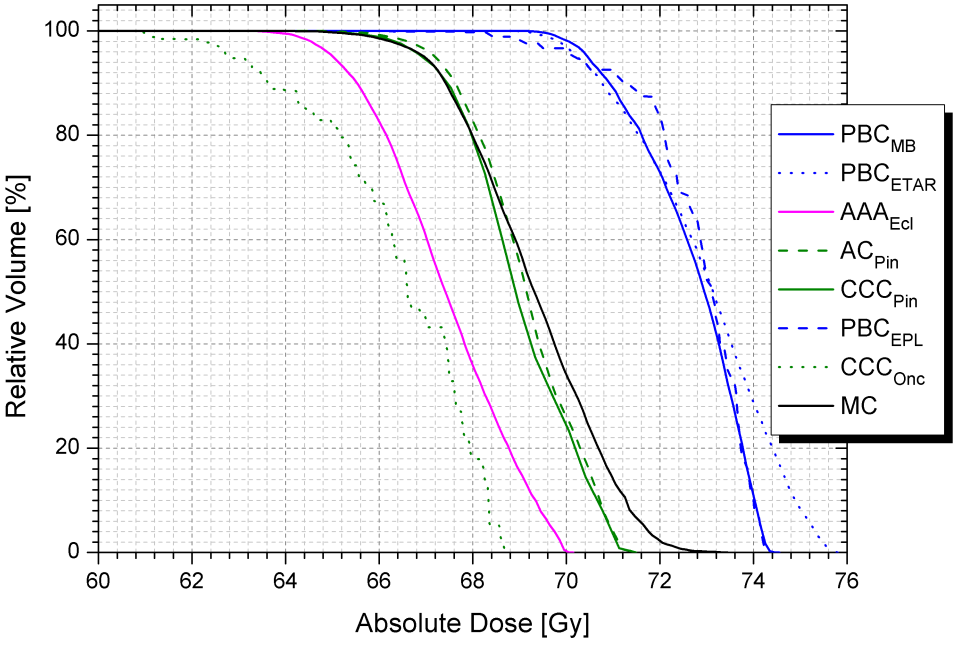

(a)

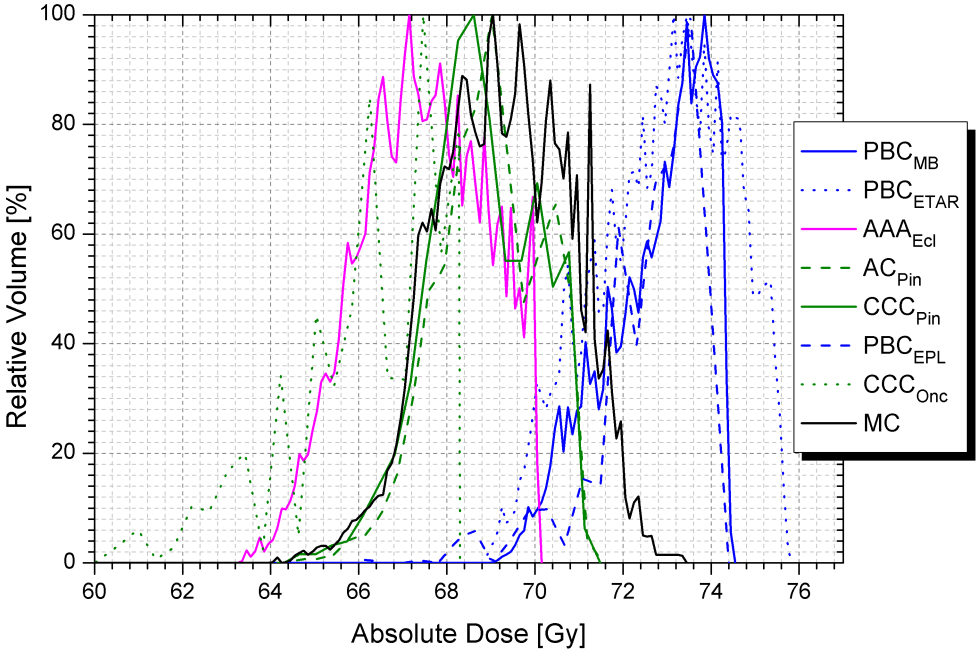

(b)

Figure 6.19: (a) Cumulative and (b) differential DVHs of GTVs of SABR patient plan

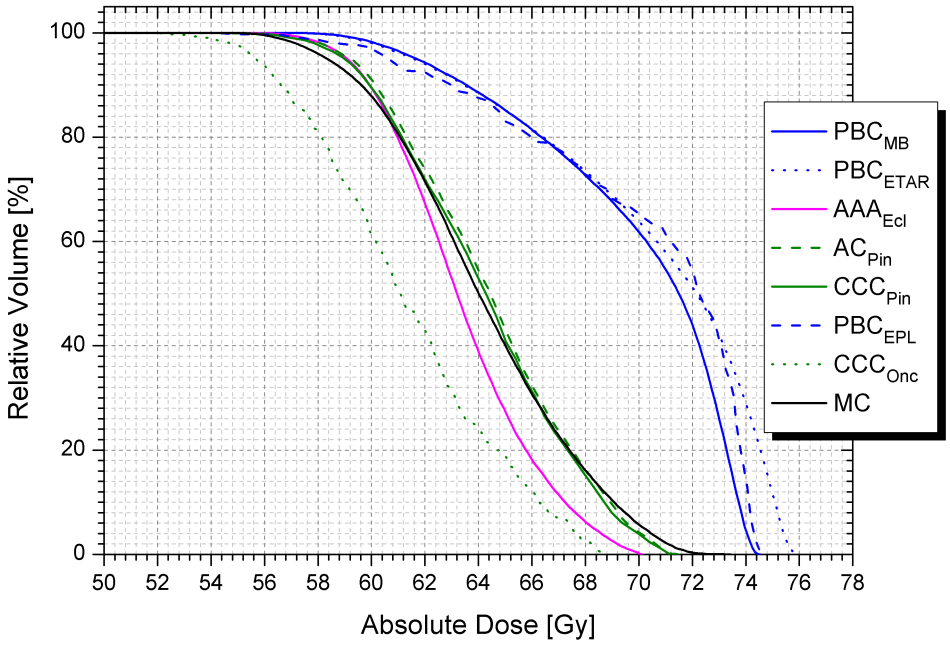

(a)

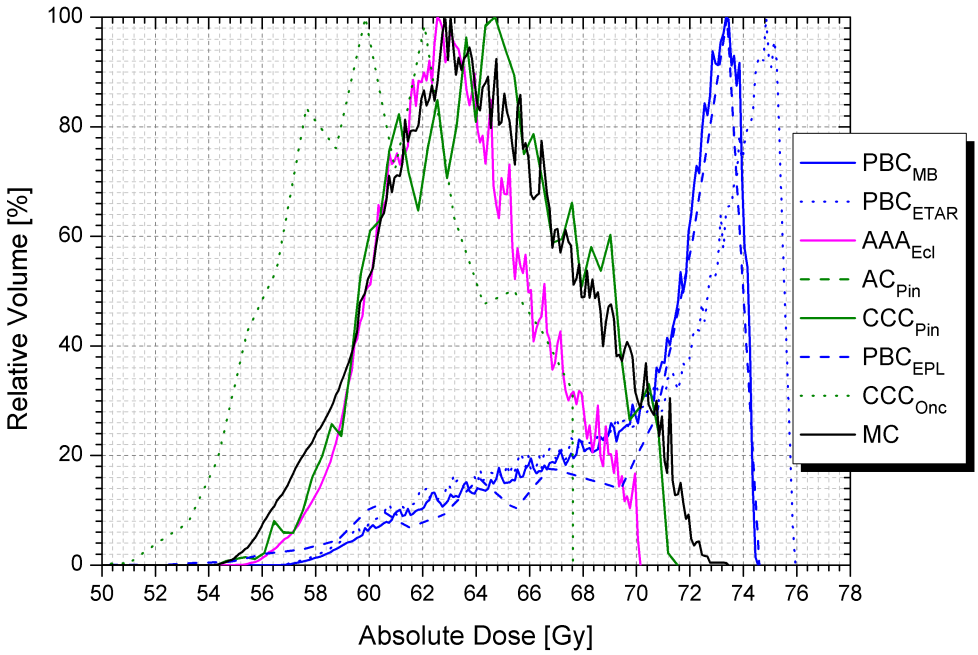

(b)

Figure 6.20: (a) Cumulative and (b) differential DVHs of PTVs of SABR patient plan

erwise difficult to achieve with conventional fractionation. When the TCPs were calculated with a new set of parameters with a lower alpha value, the differences in TCP_{GTV} and TCP_{G-PTV}between TPS algorithms and MC were considerably larger, up to 12% and 28% respectively.

Table 6.6: TCP values calculated using the dDVHs of GTV and G-PTVs of the investigated SABR patient plan with parameters: $\bar{\alpha}$=0.14 Gy^{-1}, σ_α=0.017 Gy^{-1}, ρ_{cl} = 10^7 cm^3, α/β=10 Gy, T_k=3 days, T_d=21 days.

Algorithm	TCP_{GTV} [%]	TCP_{G-PTV} [%]
PBC_{MB}	95.7	75.2
PBC_{ETAR}	95.7	74.9
AAA_{Ecl}	96.0	68.5
AC_{Pin}	80.1	48.3
CCC_{Pin}	84.6	45.7
PBC_{EPL}	83.9	44.1
CCC_{Onc}	74.6	26.8
MC	87.2	47.4

DVHs and NTCPs of uninvolved lungs of SABR patient plan

In SABR plans the lung volume involved in the treatment fields is generally smaller due to the small volume of the tumour and in this particular patient plan the tumour was at the periphery of the lung and the width of the field sizes used was not more than 3.5 cm. The differences in the DVHs of the TL-GTV volume of various algorithms were insignificant and so were the differences between the the complication probabilities of lung with radiation pneumonitis as an end point as given in table 6.7. The NTCP of lung was evaluated using the three parameter LKB model (TD_{50}=29.2 Gy, m=0.45, n=1, α/β=3 Gy).

DVHs and NTCPs of ribs of SABR patient plan

The cumulative DVHs of 3 ribs present close to the tumour are shown in figure 6.22. D_{2cm3} and NTCP values calculated for one of the ribs which is closest

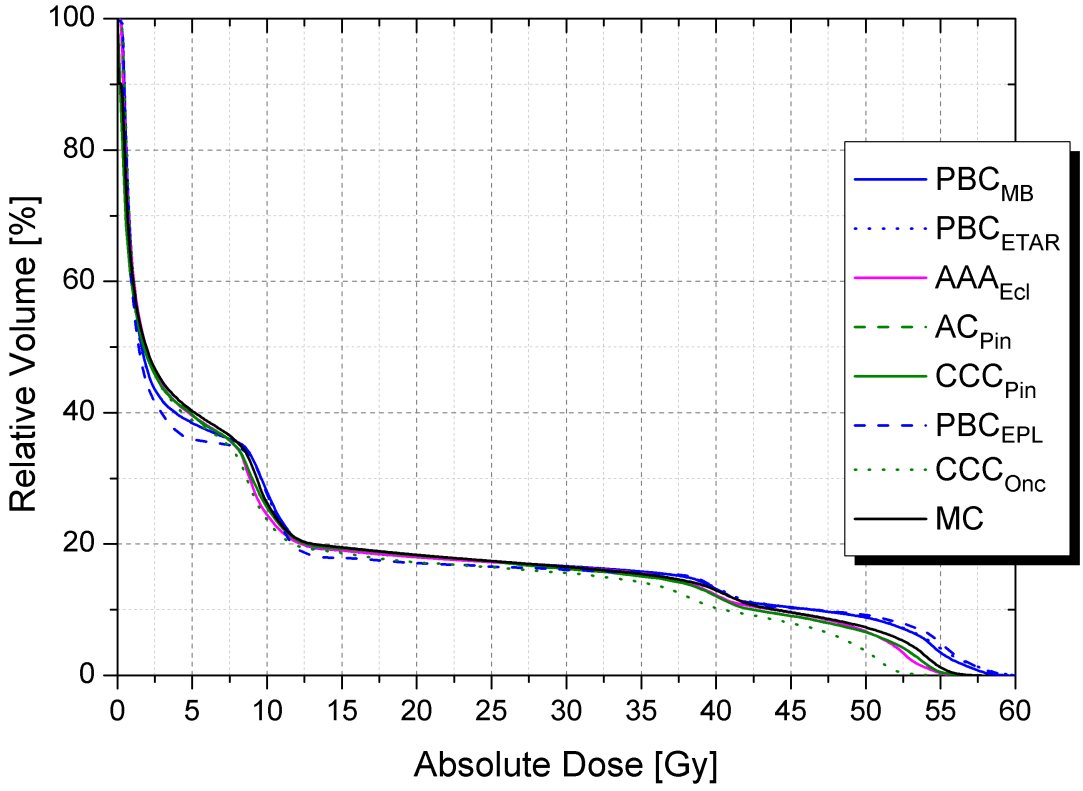

Figure 6.21: DVHs of TL-GTV of the investigated SABR patient with a small tumour of volume 1 cm^3

Table 6.7: NTCP values calculated using the dDVHs of TL-GTV of SABR patient plan with radiation pneumonitis as the end point with LKB model parameters: TD_{50}=29.2 Gy, m=0.45, n=1, α/β=3 Gy, De Jaeger, 2003.

Algorithm	$NTCP_{RP}$
PBC_{MB}	2.6
PBC_{ETAR}	2.6
AAA_{Ecl}	2.3
AC_{Pin}	2.3
CCC_{Pin}	2.3
PBC_{EPL}	2.6
CCC_{Onc}	2.2
MC	2.7

to the tumour, with rib fracture as the end point are shown in table 6.8. Differences of up to 2 Gy and 7.5% in D_{2cm3} and NTCPs are found between the analytical dose calculation algorithms and MC.

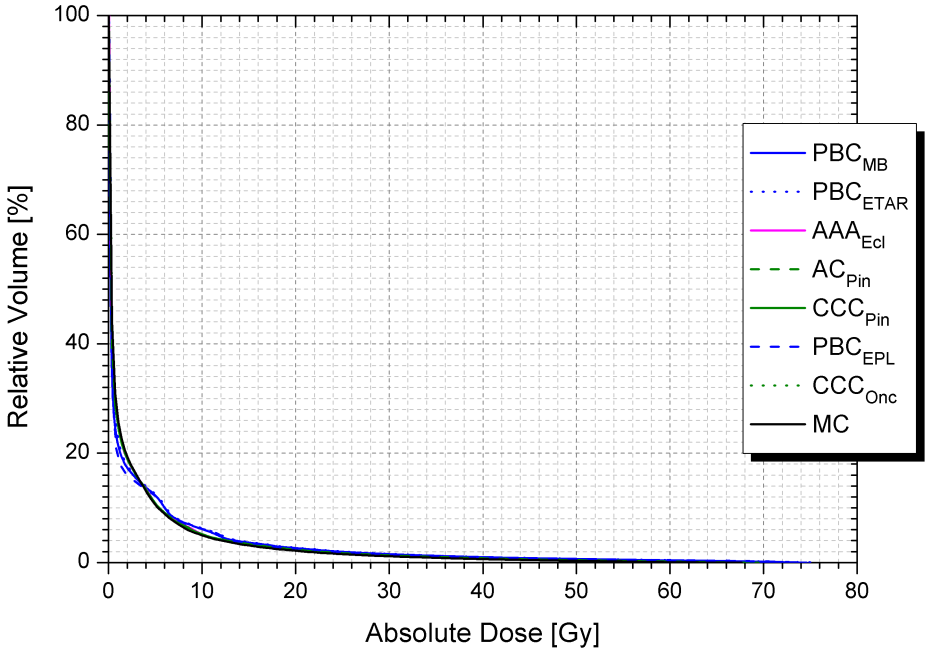

Figure 6.22: Cumulative dose volume histogram of TL-GTV of an SABR patient plan

6.4 Discussion

Virtual Phantom Study

This study succinctly highlights the influence of differences in photon dose calculation algorithms on the predicted dose distributions and its effect on the clinical outcome in a simple virtual lung phantom. The results of the study show that in general *type a* algorithms overestimates the doses to the tumour when compared to *type b* algorithms and MC. The main reason for the over estimation of the doses by *type a* algorithms is because they do not accurately model or account for change in lateral electron transport during the dose calculation process. They underestimate the lateral range of secondary electrons when they traverse from a high density medium to a relatively low density medium. In reality, the range

Table 6.8: NTCP values of SABR patient plan with rib fracture as the end point calculated using logistic model with parameters: D_{50}=49.8 Gy, γ_{50}=2.05, Petterson, 2009.

Algorithm	D_{2cm3}	$NTCP_{RF}$
PBC_{MB}	45.2	32.6
PBC_{ETAR}	45.0	31.9
AAA_{Ecl}	44.7	31.0
AC_{Pin}	45.3	32.9
CCC_{Pin}	46.1	35.7
PBC_{EPL}	43.9	28.5
CCC_{Onc}	43.5	27.2
MC	45.7	34.3

of electrons in the lateral direction are longer which results in broadening of the penumbra [202]. This effect is larger at the tissue interfaces is clearly seen in the lateral and longitudinal profiles given in sections 6.3.1 and 6.3.1. The results of lateral and longitudinal profiles between the TPS algorithms and MC are similar to that presented by various other authors [69–71, 85, 108, 196, 197, 203].

The differences in predicted TCPs of the virtual phantom plans are directly related to the differences in DVHs calculated by TPS algorithms and MC. The differences in TCPs of the small tumour were larger than that of that found in large tumour owing to the use of smaller field sizes in the former case. When same set of TCP parameters are used to calculate TCPs based on dose distribution data generated from various photon dose calculation algorithms, *type a* algorithms in general predict a higher tumour control than that realistically achievable, due to their nature of overestimating the doses delivered. For a given number of MUs, TCPs predicted by *type a* algorithms are significantly larger than that of *type b* algorithms. The separation in the DVHs and hence the TCP values between *type b* algorithms and MC converges in case of large fields in which the magnitude of error in doses reduce as only a smaller fraction of the tumour volume that receives a low dose along the periphery of the tumour when recalculated with *type b* algorithms and MC. If the tumour is sufficiently large enough, charged-particle equilibrium is restored partially.

3DCRT NSCLC patient study

In the patient study, in order to evaluate the clinical outcome of the treatment plans calculated with various algorithms, the TCPs were calculated using the DVHs created by applying the GTV volume to the PTV DVHs (denoted as G-PTV DVHs) in order to approximately account for the tumour motion. During the segmentation process, the internal target volumes (ITVs) which account for the motion of the CTV during the respiration were not created explicitly but sufficient CTV to PTV margins were used so as to not 'miss' the moving CTV during the treatment. We might be either overestimating or underestimating the TCPs if the GTV DVHs or PTV DVHs were used to calculate the TCP. The 'true' TCP lies somewhere in between. As the GTV moves within the PTV volume due to breathing during the treatment delivery, the DVHs created by applying GTV volumes to the PTV DVHs were used to calculate the TCPs which is represents an extreme case. The effect of tumour motion due to breathing on predicted dose distribution, which is technically termed as dose blurring [204,205], can be studied by accumulating the dose based on 4DCT data sets (some commercially available TPSs such as Pinnacle have the capability of performing 4D dose calculation) but is beyond the scope of this thesis.

Overall, systematic differences were found between the DVHs of *type a* and *type b* algorithms, the former always overestimated the doses and hence the TCPs. Irrespective of the type of heterogeneity correction method used, none of the *type a* algorithms 'see' the presence of low density lung when lateral electron transport is concerned, which is proven by its narrow penumbra and gradual fall off of depth doses in a water-lung-water geometry that accounts only for photon attenuation. The tendency of electrons to scatter with a longer range in the lateral direction, when they encounter a medium of relatively low density is not explicitly accounted for by *type a* algorithms.

The AAA_{Ecl} underestimates the doses in lung and overestimates the doses in the build-up region in unit density tissue adjacent to lung, and the magnitude of overestimation increases with increasing field size, which is observed in the phantom study reported in sections 6.3.1 and 6.3.1 of this chapter. The high

dose region of the DVHs of GTVs are overestimated in most of the cases whereas the low doses are underestimated. Tillikainen *et al.* [108] has reported similar behaviour of AAA_{Ecl} algorithm. On the other hand, the other two CS algorithms, CCC_{Pin} and AC_{Pin} resulted in fairly similar DVHs and they were always closer to MC. This shows that the AC_{Pin} algorithm, which is a faster version of CCC_{Pin}, proves sufficient for calculations in the thoracic region without compromising the accuracy of the dose distribution. The results are similar to that shown by Chow *et al.* [70] in which they showed that AC_{Pin} and CCC_{Pin} match well within $\pm$ 1% in handling heterogeneities.

It is observable from the results of the NSCLC patient studies that CCC_{Onc} systematically underestimates the doses delivered to the target volumes, both GTVs and PTVs, and hence underestimates the resulting TCPs. Nisbet *et al.* [115], Fogliata *et al.* [85] and Fotina *et al.* [206] have shown that CCC_{Onc} underestimates the doses both in lung especially at the high dose region adjacent to the tumour, the envelope between the GTV and PTV volumes and also in the build-up region at the lung-water/tumour interface. Aarup *et al.* [69] demonstrated that although CCC_{Onc} performs well in 'light' lung densities comparing to other *type b* algorthms like AAA_{Ecl}, its performance is less good in the normal lung densities as it tends to underestimate the doses. Knöös *et al.* [87] have reported similar behaviour in their study. Asparadakis *et al.* [114] have shown that the CCC_{Onc} overestimates the penumbra width in lung due to discretisation effects of the fluence matrix as a result of which it tends to spread out the dose in the lateral direction more than what happens in reality. In the study done by Paelinck *et al.* [116], up to 5.6% of differences were found between MC and CCC_{Onc} in the lung regions when fields with smaller width are used.

The differences in the D_{mean} are systematically larger for *type a* algorithms in comparison to MC. Recalculation of the treatment plans using *type b* algorithms and MC with the same MUs as predicted by PBC_{MB} resulted in inferior or clinically unacceptable GTV and PTV dose coverage. D_{mean} and the minimum dose received by the target volumes and the number of clonogenic cells present in the tumour volume determine the probability of controlling the tumour. This is evident from the results of one of the NSCLC patients planned with the 3DCRT

technique for which the TCP_{G-PTV} values predicted by all of the *type b* algorithms is 'zero' or in other words there is no possibility of controlling the tumour due to a cold spot in the PTV volume (see table 6.4). In our study, the clonogens are assumed to be uniformly distributed and concentrated in the GTV and no clonogens are assigned to CTV or PTV volumes. The differences in the TCPs calculated based on dose distribution computed by TPS and MC algorithms depend upon the steepness of the relevant dose-response curve. The steeper the curve is, larger are the differences. The steepness of the dose-response curve is defined by σ_α in our study as it employs the Marsden TCP model, in other cases for eg. in case of a logistic model γ_{50} defines the steepness of the curve. In this study, the σ_α value used was obtained from the parameter set published by Nahum *et al.* [130] which was derived from data of a cohort of 25 patients. The patient plans included in this lung study is a subset of the patient cohort used by Nahum *et al.* [130]. As the aim of this study is to evaluate the influence of the differences in physical doses calculated by various photon dose calculation algorithms on the differences in predicted TCPs, the parameter sets used prove sufficient.

MC predicted higher MLD values due to higher minimum doses and slightly higher V_{20} values but the differences in these values calculated based on TL-GTV DVHs of TPS algorithms are minor. The absolute differences in the predicted incidence of radiation pneumonitis (RP) by plans calculated using various TPS algorithms are less than 5%. Yorke *et al.* [207] showed that both MLD and V_{20} are equally important predictors of incidence of RP in the treatment of NSCLC, the tolerance limits being 20 Gy and 30% respectively and Chang *et al.* [208] showed that heterogeneity correction does not affect V_{20} but there is a change in MLD of up to 4%.

SABR NSCLC patient study

In case of the SABR plan, although large differences exist between the DVHs calculated by the TPS algorithms and MC, differences in TCP values are minor when estimated using the parameters derived by Nahum *et al.* [130]. The predicted TCPs are close to 100% as a result of high biologically effective dose (BED_{10}). The BED_{10}s (calculated with α/β 10 Gy) are 115.5 Gy and 56.5 Gy

when a total dose of 55 Gy is delivered in 5 and 20 fractions respectively. SABR treatment regimes are characterised by their high tumour control. Both the TCP_{GTV} and TCP_{G-PTV} of the SABR patient plan were still close to 100% when calculated with the same parameter set derived by Nahum *et al.* [130] except for a higher α/β of 20 Gy. When another set of TCP estimation was performed using a different parameter set (see section 3.5.2 of chapter 3) by lowering $\bar{\alpha}$ (0.14 Gy^{-1} instead of 0.307 Gy^{-1}) and σ_α (0.017 Gy^{-1} instead of 0.037 Gy^{-1}) values but keeping the slope of the curve constant and retaining the original α/β of 10 Gy, large differences were found in the predicted TCPs. However, the ideal method would be to use parameter sets derived specifically for a hypofractionated treatment regime, which is beyond the scope of this work.

As the volume of lung in the treatment field of the SABR patient plan was significantly lower than that of 3DCRT plans, the NTCP values for radiation pneumonitis were not influenced by differences in the dose calculation algorithms. On the other hand, differences of up to 5% were found between the NTCP values of ribs with rib fracture as the end point. The CCC_{Onc} algorithm calculated dose to medium whereas all the other TPS algorithms calculate dose to water. MC dose calculation also calculates dose to medium which is converted into dose to water using a MATLAB routine by multiplying each voxel by water-medium stopping power ratio. The GTV and G-PTV and TL-GTV DVHs report doses received by tumour and lung, the dose to water conversion factors are 1.01 and 0.999 respectively which when not applied results in 0.1-1% error which is negligible. On the other hand, the ribs which are constituted by soft bone has a dose to water conversion factor of 1.035 which when not accounted for would incur an error of -3.5%. The D_{2cm3} value of the ribs were converted to dose to water by multiplying the dose to medium by 1.035. Fernández *et al.* [180] have reported errors of up to 3.5% and 14% in case of spongiosa or soft bone and cortical bone respectively due to lack of dose to water conversion. In this work, the doses of GTV, G-PTV, TL-GTVs were not converted to dose to water due to insignificant differences but the doses of the ribs were converted to dose to water.

6.5 Conclusions

This work comprehensively summarises the influence of the differences in absolute doses calculated by photon dose calculation algorithms on the predicted TCPs and NTCPs of NSCLC tumours. Although both *type a* and *type b* algorithms predict similar doses at the centre of the unit density tumour, significant differences exists at the tumour periphery and between the delineated GTV and PTV volumes which is a result of lack or insufficient modelling of electron transport. *Type a* algorithms overestimate the doses and hence predict higher TCPs than that actually achievable with a plan generated by such algorithms. As a result, the patients are under dosed compared to the doses in treatment plan and hence the chance of controlling the tumour is reduced to an extent which might lead to tumour recurrence. The magnitude of reduction of TCP is larger for small tumours which are treated by employing relatively smaller field sizes. Although, *type b* algorithms predict doses and TCPs closer to that of MC, differences still exist and the limitations of using these algorithms must be kept in mind for treatment planning of thoracic tumours. SABR treatments have a high probability of controlling the tumour, although the validity of LQ model is in doubt for hypofractionated treatments with daily dose fractions larger than $\sim$7 Gy [135].

Both *type a* and *type b* algorithms underestimate the lung toxicity when treated with large numbers of fractions eg. 20 fractions. The differences in the predicted NTCP of lung for radiation pneumonitis depends upon the total dose and dose per fraction employed. On the other hand, there is no significant difference in the incidence of radiation pneumonitis due to use of various heterogeneity correction methods in case of SABR treatments as the lung doses are significantly lower. The NTCP of ribs is not very sensitive to the choice of the dose calculation algorithm used.

Chapter 7

Influence of photon dose calculation algorithms on the predicted clinical outcome of nasopharyngeal IMRT

7.1 Introduction

Radiotherapy serves as the primary management for nasopharyngeal carcinoma (NPC) along with chemotherapy which is an endemic in East Asian countries such as China and in some parts of Africa [209]. Patients usually present with stage III, IV tumours. The concave shape of the tumour, high and low risk nodal volumes, the large number of critical organs surrounding it, and density variations in the tissues around it make it one of the most difficult tumour sites to plan. In recent years, NPC patients have been treated with step-and-shoot or dynamic IMRT and very recently intensity modulated dynamic arc treatment techniques due to their proven superiority over conformal treatments [210–212]. This enables dose escalation without causing complications to nearby critical structures [212].

The airways and sinuses present in the proximity of NPC can cause dose perturbation as a result of which charged-particle equilibrium may be disturbed in these regions: there is less attenuation of the beam and the ranges of secondary electrons produced are longer compared to in water. Accounting for the changes

which occur due to presence of air cavities is crucial in order to accurately calculate the doses delivered to the target volumes and surrounding critical organs. Many authors have addressed the dose calculation accuracy issues associated with various photon dose calculation algorithms in and near low density air volume and at the air-tissue interfaces [80, 120, 213–218].

However, the effect of these differences on the predicted tumour control and normal tissue complication has not been investigated in the published literature. Also, techniques such as IMRT add to the necessity for accurate prediction of dose calculations due to the steep dose gradients and complex dose distributions. The IMRT fields are composed of many segments with apertures smaller than that of the field sizes used in conventional or conformal treatments; these small apertures are main sources of dose discrepancies between different photon dose calculation algorithms, as the range of secondary electrons can be much larger than the aperture size. Another source of error is inadequacy in modelling the MLC leakage by TPS algorithms. MC models developed by Siebers *et al.* [219] and Heath and Sentjuens [166] have the capability to fully model the leaf gaps and tongue and groove of MLCs.

In this study, the influence of the choice of photon dose calculation algorithms - *type a*, *type b* and MC on predicted local control values of NPC and probability of complication to parotids (with xerostomia as the end point) is investigated using radiobiological models, and the preliminary results are presented. To our knowledge, such a study has not been done before.

7.2 Methods and Materials

7.2.1 Patient simulation and segmentation

The first step of patient simulation was done on the Acuity[1] conventional x-ray simulator in order to choose the isocentre and plan the lower neck field. The treatment portal was split into two (known as the split-field technique), the upper primary tumour which is treated with IMRT and lower neck nodes treated conventionally. During this simulation process the isocentre was chosen

[1] Varian Medical Systems, Palo Alto, CA, USA.

and is generally placed between the upper and lower neck fields. The patient then underwent a CT simulation procedure in which a CT scan (with a contrast agent) of the head and neck region was acquired on the Brilliance[2] CT scanner with a slice thickness of 3 mm. In some cases, MRI images were acquired in addition to CT images. The images were then transferred to the ProSoma[3] contouring work station where the target volumes and OARs were delineated on the planning CTs, along with the use of fused MR images in some cases, and diagnostic CT images of the patient that were taken before the administration of chemotherapy.

The GTV volume was delineated along with the positive nodes (nodes $>$ 1 cm in diameter) which were expanded isotropically by 5 mm to form CTV1. This margin was reduced by 1 mm if it overlapped with a critical organ present in its proximity. The adjacent involved structures, including the entire nasopharynx, base of skull, sinuses, the posterior third of the nasal canal depending upon the invasion and the high-risk nodes, were contoured to form CTV2. The low-risk sub-clinical nodes were contoured as CTV3. PTV1 and PTV2 were formed by expanding the corresponding CTVs isotropically by 5 mm unless they overlap on critical structures such as brain stem or optic chiasm in which case the contours are slightly modified. The conventional lower neck field forms the PTV3 volume. In addition to the target volumes, critical organs such as brain stem, optic nerve, optic chiasm, lens, larynx, ipsi-lateral and contra-lateral parotids, mandible and temporal lobe were also delineated. A 5 mm skin volume was delineated from the body contour in order to enable skin sparing.

7.2.2 Dose fractionation and prescription

Two nasopharyngeal IMRT patient plans were chosen for this study. The treatment plans were done according to the clinical protocol followed at our centre for radical radiotherapy of tumours. For one of the patients, radiotherapy was given as a definitive treatment (without any form of chemotherapy) with a daily dose of 2.2 Gy in 30 fractions to a total dose of 66 Gy while the other patient (administered to concurrent chemotherapy) who was given a daily dose of 2 Gy in 35 fractions to a total dose of 70 Gy. The primary tumour along with all positive

[2]Philips Healthcare, Andover, MA, USA.
[3]MedCom GmBH, Darmstadt, Germany.

nodes and adjacent high risk nodes was treated with IMRT whereas the lower neck nodes were treated conventionally either with a single anterior field or with parallel opposed anterior-poster fields. The gap between the upper IMRT fields and lower conventional neck fields are determined carefully so as to avoid over or under dosage and to reduce the dose to the larynx [220]. This junction is usually set above the vocal cords. PTV2 and PTV3 are treated with doses lower than that of PTV1. Table 7.1 shows the doses delivered to all three PTV volumes in the case of patients undergoing IMRT with chemotherapy and definitive IMRT alone.

The treatment plans were done using 7 IMRT fields with gantry angles 0°, 36°, 76°, 116°, 160°, 200°, 244°, 284° and 324° in order to cover at least 95% of PTV by the prescription dose, 99% of PTV receives $\geq$ 93% of prescribed dose, only $\leq$ 5% of PTV to receive more than 108% of prescribed dose.

Table 7.1: Dose fractionation schemes employed at our centre for treating target volumes of nasopharyngeal carcinoma with and without chemotherapy. PTV1 represents the primary tumour along with any positive nodes, PTV2 denotes surrounding involved structures with high risk nodal volume and PTV3 includes the low risk neck nodes. PTV1 and PTV2 were treated using an IMRT technique whereas PTV3 was treated conventionally (split field technique).

Target	IMRT with chemo-radiation	Definitive IMRT alone
PTV1	70 Gy in 35 fractions	66 Gy in 30 fractions
PTV2	63 Gy in 35 fractions	60 Gy in 30 fractions
PTV3	40.5 Gy in 15 fractions	40.5 Gy in 15 fractions

7.2.3 IMRT plan optimisation and dose calculation

Nasopharyngeal treatment plans were done with step and shoot IMRT. These IMRT fields were optimised using the direct machine parameter optimization algorithm (DMPO) which derives the photon fluences for the generation of the intensity modulated fields. This was done by inverse optimization where objective functions and dose constraints were set. High priority was given to organs that overlap with GTV or CTV volumes which might result in compromise of dose to

these target volumes and low priority was given to those which are far away from the target volumes. A detailed list of dose-volume objectives and constraints are given in table 7.2.

Table 7.2: Dose-volume objective functions and constraints set during the optimisation process based on which the IMRT segments, their fluences and weights were determined.

Structure	Description	Dose
PTV1 (definitive IMRT alone)	Min dose	65.5 Gy
	Max dose	66.5 Gy
PTV1 (IMRT with chemoradiation)	Min dose	69.0 Gy
	Max dose	71.0 Gy
PTV2 (definitive IMRT alone)	Min dose	60.0 Gy
	Max dose	61.0 Gy
PTV2 (IMRT with chemoradiation)	Min dose	63.0 Gy
	Max dose	64.0 Gy
Brain stem	Max dose	54.0 Gy
Spinal cord	Max dose	50.0 Gy
Temporal lobe	Max dose	54.0 Gy
Optic Chiasm	Max dose	64.0 Gy
Mandible	Max dose	70.0 Gy
Parotid (one parotid)	Mean dose	26.0 Gy
Larynx	Max dose	45.0 Gy
Lens	Max dose	12.0 Gy

Similar to the treatment planning done in the lung study given in section 6.2.5 of chapter 6, the PBC_{MB} algorithm was initially designated to determine the number of MUs delivered by each field but unlike 3DCRT plans IMRT treatment planning posed challenges in retaining the plan characteristics between the three TPSs, Eclipse, Pinnacle and Oncentra. Transferring DICOM RT data from Eclipse to Pinnacle was not possible and therefore the treatment plans were created and IMRT optimisation was performed in Pinnacle TPS using its finite-size pencil beam (TPB_{Pin}) dose calculation algorithm during the optimisation process. Generally, when clinical IMRT treatment plans are done in Pinnacle TPS, the less accurate faster TPB_{Pin} algorithm is used at the optimisation stage and

the final dose calculation is performed with a more accurate algorithm like AC_{Pin} or CCC_{Pin}. In this study, the segments of the plans and their corresponding MUs were determined by the TPB_{Pin} algorithm by skipping the final dose calculation step. These plans were then transferred to Eclipse and Oncentra for recalculation with same MUs. The doses were recalculated with 7 other TPS algorithms and MC. A comprehensive description of photon dose calculation algorithms investigated in this study is given in chapter 2. The MC dose calculation was done as per the steps explained in section 4.2 of chapter 4. The only difference between MC 3DCRT and IMRT dose calculation is that an additional input file was generated which contains the MLC leaf sequences for each gantry angle along with the weights of their respective segments. This file was included as an input file which was retrieved by the BEAMnrc program at run time.

7.2.4 MC IMRT dose verification in a homogenous phantom

The MC modeling of the accelerator was performed as explained in chapter 4 and the validation of the virtually built accelerator head was done in a homogeneous cubical water phantom for open and wedged fields and in a heterogeneous wooden lung phantom for 3DCRT and SABR treatment plans as described in chapter 5. Before carrying out the MC IMRT plans on patient DICOM CT datasets it was essential to validate the dose calculation in a homogeneous phantom.

Therefore, in order to verify the performance of the MC IMRT, one of the patient treatment plans was transferred on to a Delta4 phantom[4] without altering the original beam segments, weights and MUs. The Delta4 phantom is made of poly-methyl-metha-acrylate (PMMA) which has a density of 1.19 g/cm^3. The density of the phantom was over ridden and assigned to that of water, 1 g/cm^3 in order to avoid dose to medium to dose to water step to keep the calculations simpler. The Eclipse TPS calculated and MC calculated IMRT dose distributions in a unit density assigned Delta4 phantom were compared in terms of absolute doses.

[4]Scandidos, Uppsala, Sweden.

7.3 Results

7.3.1 Verification of MC IMRT dose calculation in a homogeneous phantom

Figures 7.1(a), 7.1(b), and 7.1(c) shows the IMRT dose distribution on a homogeneous delta^4 phantom calculated by PBC, AAA of Eclipse and MC algorithms respectively. Dose distribution of the nasopharyngeal IMRT plan in a transverse plane of the Delta4 phantom calculated by PBC, AAA and MC algorithms are shown in figure 7.1. The PBC and AAA plans were within 2%/2mm whereas the MC plan satisfied a gamma criteria of 3%/3 mm and 4%/4 mm when compared to PBC and AAA algorithm calculated doses respectively. The MC calculated doses were systematically ∼2.5% less than PBC and AAA algorithms. Although this is within the recommended tolerance limits set for IMRT plans by Venselaar [14], the MC beam model was observed to under predict the doses in a systematic fashion. In order to eliminate the difference in doses due to beam modeling between TPS and MC a correction factor of 1.025 was introduced in the MC calculation as the aim of this study is to quantify the impact of the photon dose calculation algorithms on predicted clinical outcome as a result of the differences in the way they handle heterogeneities.

7.3.2 Dosimetric differences between dose calculation algorithms

Target volumes

The differential and cumulative DVHs of the GTV of one of the nasopharyngeal IMRT patient plans calculated with *type a*, *type b* and MC algorithms are shown in figures 7.2(a) and 7.2(b) respectively. Similarly, the differential and cumulative DVHs of PTV1 are shown in figures 7.3(a) and 7.3(b). The mean doses received by the GTVs of both the patients are shown in table 7.3. It has to be noted that, a correction factor of 1.025 has been applied to the MC doses in order to eliminate the differences that arise due to beam modelling as explained in section 7.3.1.

From the DVHs of the GTV, it is observed that *type a* algorithms overestimate the doses by up to 3 Gy (mean dose, D_{mean}). Out of all the type a

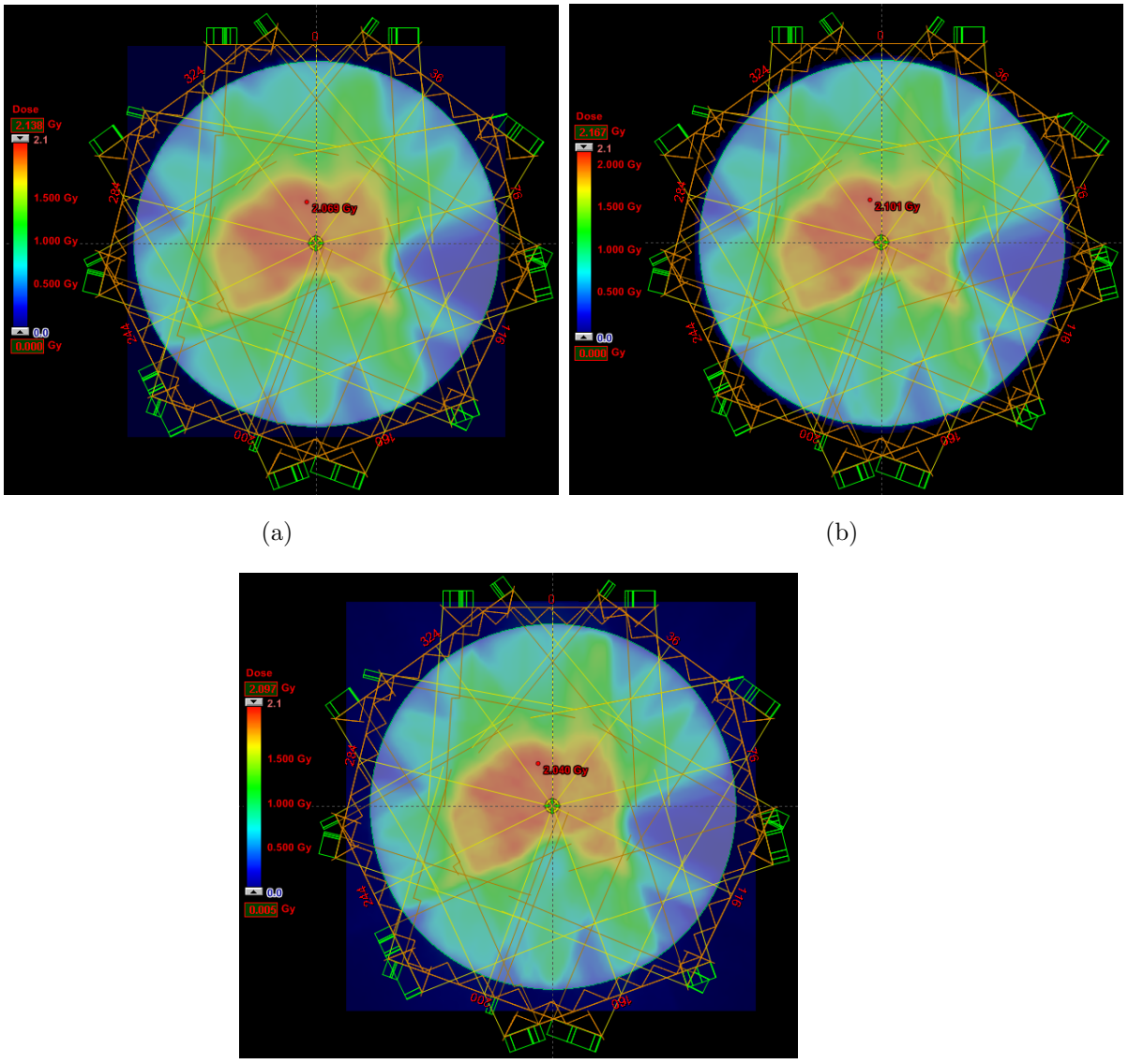

(a) (b)

(c)

Figure 7.1: Verification of MC IMRT model in a homogeneous Delta4 phantom. The dose distribution calculated by (a) PBC, (b) AAA are compared with that of (c) MC. The were in good agreement of within 4%/4mm tolerance limit recommended by Venselaar, 2001.

algorithms, PBC_{EPL} of Oncentra predicts the highest doses, followed by PBC_{MB} and PBC_{ETAR}. Dose-volume characteristics of AAA_{Ecl} are very close to those of PBC_{ETAR}. However, the low doses of AAA_{Ecl} are lower and the high doses are higher than that of PBC_{ETAR}, a difference of up to ~1.5 Gy (2%) and 0.5 Gy (<1%) is found in the minimum and maximum doses respectively. Among the algorithms of Pinnacle, TPB_{Pin} yields higher doses than AC_{Pin} and CCC_{Pin}. Both AC_{Pin} and CCC_{Pin} result in very similar dose distribution which shows

that AC_{Pin} is a good alternative to CCC_{Pin} for a faster dose calculation without compromising on the accuracy in handling complex IMRT plans. The DVH of CCC_{Onc} is closer to that of TPB_{Pin}. The GTV DVH of MC algorithm shows the lowest doses out of all the investigated algorithms, among which CCC_{Pin} results in the DVH closest to that of MC. However, CCC_{Pin} overestimates the doses by up to ∼2.0 Gy (3%). The differences in the primary PTV DVHs exhibit a similar trend of differences with a maximum D_{mean} difference of 2 Gy between PBC_{EPL} and MC. Figure 7.4 depicts the dose distribution on axial, coronal and sagittal orientations of one of the IMRT patient plans used in this study.

PBC_{EPL} or PBC_{MB} predict highest D_{mean} values in both the patients followed by the third *type a* algorithm PBC_{ETAR}. Among *type b* algorithms AAA_{Ecl} predicts the highest mean dose which is followed by CCC_{Onc}. Differences of up to 1.5 Gy is found between PBC_{EPL} and AAA_{Ecl}. The two CS algorithms of Pinnacle, AC_{Pin} and CCC_{Pin} produce the same dose quantities.

Table 7.3: Dose-volume characteristics of GTV of nasopharyngeal IMRT patient plans derived from dose distributions calculated by *type a*, *type b* and MC algorithms.

Algorithms	D_{mean} P1 [Gy]	D_{mean} P2 [Gy]
PBC_{MB}	67.09	70.95
PBC_{ETAR}	66.82	70.52
AAA_{Ecl}	66.68	71.35
AC_{Pin}	65.86	69.81
CCC_{Pin}	65.86	70.43
TPB_{Pin}	66.11	69.80
PBC_{EPL}	67.67	68.95
CCC_{Onc}	66.24	72.56
MC	62.78	70.04

Parotids

The cumulative DVHs and D_{mean} values of both the parotids drawn as a single paired organ are shown in figure 7.5 and table 7.4 respectively. D_{mean} values of the parotids, estimated by PBC_{EPL} algorithms were the highest, 36.1 Gy and

42.04 Gy for both the patients. Differences of up to 3.5% were found in D_{mean} values calculated by PBC_{EPL} and MC. PBC_{MB}, TPB_{Pin} predictions are very similar to each other whereas PBC_{ETAR} results in D_{mean} values lower than those of both *type a* and *type b* algorithms. Among the *type b* algorithms, all except CCC_{Onc} predicted similar mean doses within less than 0.5 Gy. CCC_{Onc} DVHs and D_{mean} are closer to that of PBC_{EPL} of the same planning system, Oncentra. In contrast, MC calculated DVHs and D_{mean} are systematically lower than the rest of the algorithms in both the patient plans.

Table 7.4: D_{mean} values of both the parotids as a single organ of the two NPC IMRT patients plans investigated in this study.

Algorithms	D_{mean} (P1) [Gy]	D_{mean} (P2) [Gy]
PBC_{MB}	35.36	40.34
PBC_{ETAR}	34.72	38.73
AAA_{Ecl}	35.78	40.76
AC_{Pin}	35.47	39.49
CCC_{Pin}	35.45	39.48
TPB_{Pin}	35.92	39.85
PBC_{EPL}	36.10	42.04
CCC_{Onc}	35.81	42.04
MC	33.63	38.49

7.3.3 Differences in the predicted clinical outcome

Tables 7.5 and 7.6 show predicted TCPs and NTCPs of both the NPC IMRT patients studied. The GTV volumes of P1 and P2 were approximately 20 cm^3 and 45 cm^3 respectively and hence the TCP of P1 is higher than that of P2 due to lesser number of clonogenic cells. TCPs were calculated by the Marsden model [27, 31, 32] with parameters for NPC derived by Selvaraj *et al.* [136] (see section 3.6 of chapter 3). Amongst *type a* algorithms, PBC_{EPL} of Oncentra TPS predicts the highest TCP in both the patients followed by PBC_{MB} of Eclipse. The performance of PBC_{ETAR} is closer to *type b* algorithms in P1 in particular to AAA_{Ecl} and to AC_{Pin} and CCC_{Pin} in P2. AAA_{Ecl} over predicts the clinical

outcome of P2 and yields a TCP value higher than that of PBC_{ETAR} by 5% in terms of absolute units which is due to over estimation of the low dose region. AC_{Pin}, CCC_{Pin} and CCC_{Onc} yield similar TCPs. Analogous to the D_{mean} values, MC predicts the lowest TCPs in both the patients and is 4% and 1.5% (absolute differences) lower than the collapsed cone convolution algorithms in patient plans P1 and P2 respectively.

Table 7.5: TCPs calculated for two NPC IMRT patients using Marsden TCP model with local tumour control as the end point.The parameter set used was: $\bar{\alpha}$=0.3 Gy^{-1}, σ_{α}=0.048 Gy^{-1}, ρ_{cl}=10^7 g/cm^3, α/β=10 Gy, T_k=21 days, T_d=3 days (Selvaraj *et al.*, 2011).A correction factor of 1.025 was applied to the MC doses in order to ignore the differences in beam modelling.

Algorithms	TCP_{P1} [%]	TCP_{P2} [%]
PBC_{MB}	54.9	24.5
PBC_{ETAR}	53.9	20.0
AAA_{Ecl}	52.8	25.3
AC_{Pin}	48.9	20.3
CCC_{Pin}	48.9	20.3
TPB_{Pin}	50.0	21.3
PBC_{EPL}	57.4	26.0
CCC_{Onc}	51.8	19.3
MC	44.5	18.6

Table 7.6 shows the NTCP values calculated using differential DVHs of both the parotids using the parameter set derived by Semenenko *et al.* [141] (see section 3.6 of chapter 3). The absolute values of predicted NTCPs were highest for PBC_{EPL} followed by CCC_{Onc}. PBC_{MB}, TPB_{Pin} and AAA_{Ecl} resulted in similar NTCP values. There was no difference in the NTCPs resulting from DVHs of AC_{Pin} and CCC_{Pin}. MC predicted probabilities were up to 9% lower than *type a* algorithms and 2.5% lower than that of *type b* algorithms.

7.4 Discussion

The work done in this study summarises the influence of the choice of dose calculation algorithm employed in treatment planning of NPC IMRT on the predicted

Table 7.6: NTCPs calculated for two NPC IMRT patients using LKB NTCP model with xerostomia as the end point.The parameter set used was: TD_{50}=31.4 Gy, m=0.53, n=1, α/β=3 Gy (Semenenko and Li, 2008). A correction factor of 1.025 was applied to the MC doses in order to ignore the differences in beam modelling.

Algorithms	$NTCP_{P1}$ [%]	$NTCP_{P2}$ [%]
PBC_{MB}	53.5	58.3
PBC_{ETAR}	51.5	54.3
AAA_{Ecl}	54.5	59.5
AC_{Pin}	53.2	56.0
CCC_{Pin}	53.1	56.0
TPB_{Pin}	54.1	60.8
PBC_{EPL}	55.4	62.9
CCC_{Onc}	54.1	62.4
MC	48.7	53.6

clinical outcome. The loss of electronic equilibrium due to the presence of air cavities with extremely low densities affects the accuracy of predicted dose distributions. This becomes even more crucial in sites such as head and neck which involve very complex geometry with heterogeneities of densities ranging from 0.01 g/cm^3 (air cavities) to ∼2.0 g/cm^3 (bone). In addition to the heterogeneities, complex treatment planning techniques such as IMRT, which deliberately produce steep dose gradients pose challenges.

7.4.1 Differences in MLC modelling

Accuracy of MLC modelling plays an important role in accurately predicting the dose distributions in IMRT treatment plans due to the 'tongue and groove effect. Deng *et al.* [221] have shown not of accounting for the above effect could lead to errors of up to 10% of the maximum dose when a single IMRT field is used. However, the differences are reduced when multiple IMRT fields are employed as the maximum differences in each field would not appear in the same plane and the combined error is less than 1.6%. In our MC model, the DYNVMLC CM developed by Heath and Seuntjens [166] was used to model Varian Millenium 120

MLCs, as stated in chapter 4. This CM accounts for the interleaf leakage and tongue and groove effect. Heath *et al.* [166] have reported differences of up to 2% and 4% when DYNVMLC results were compared to ion chamber and film measurements respectively. On the other hand, the TPS algorithms of all three TPSs used in this study do not fully model the interleaf leakage and tongue and groove effect.

Francescon *et al.* [217] have demonstrated differences of up to 8% for a narrow segment of an IMRT field when Pinnacle collapsed cone was compared with MC and measurements. However, their study included an older version of the Pinnacle planning system (v.6.0). It would be ideal to study the differences in MLC modelling for IMRT treatment plans by comparing MC and TPS (Eclipse v.10.0, Pinnacle v.9.0 and Oncentra v.4.0) calculated doses with measurements. Due to time limitations, this aspect was not investigated in detail as a result of which a correction factor was incorporated in the MC doses in order to eliminate the differences that occur as a result of variations in beam modelling. The differences in doses and predicted clinical outcomes between MC and TPS algorithms reported in our study arise solely from the differences between these algorithms regarding the handling heterogeneities.

7.4.2 Dosimetric differences and consequences on the clinical outcome

The results of this study indicate significant differences at the tissue interfaces and in the air volume near these interfaces between *type a*, *type b*, and MC algorithms. Overall, two of the *type a* algorithms, PBC_{MB} and PBC_{EPL} overestimate the doses to both target and parotids and hence predict higher tumour control and normal tissue complication. On the other hand; PBC_{ETAR} performs better than the other *type a* algorithms. This could be due to its increased accuracy in modelling the scattering effects as it uses an improved full 3D voxel CT geometry data unlike 1D tracing algorithms such as PBC_{MB} and PBC_{EPL}. In general, the *type a* algorithms account for the tissue density differences only along the longitudinal direction where secondary electron transport is concerned, as a result of which they tend to overestimate the doses to target volumes.

Considering the AAA_{Ecl} algorithm, although it performs better than the other

simple convolution algorithms of Eclipse TPS, it is still limited by its inadequate modelling of lateral electron transport. AAA_{Ecl} models the longitudinal and lateral components of the scatter kernel separately. Whilst doing so, the radiological path length for the longitudinal component is calculated from the point of beam entry on the surface of the patient contour to the calculation point. On the contrary, the latter is obtained by accounting for the radial distance of the beamlet in the same plane where the calculation point lies and hence the scatter element due to heterogeneities from upstream are neglected. Kan *et al.* [218] have reported overestimation of up to 8.3% by AAA_{Ecl} in handling low density heterogeneities. In their experimental comparison with gafchromic measurements they observed extremely large differences at the distal interfaces when field sizes of less than 5×5 cm^2 were used. As a result of the above mentioned uncertainties associated with AAA_{Ecl}, the differences in estimated tumour control are 10% and 6.7% greater than that of MC predicted values for patient plans P1 and P2 respectively.

Amongst the CS or *type b* algorithms of Pinnacle and Oncentra, the performance of AC_{Pin} and CCC_{Pin} are consistently better than CCC_{Onc} and closest to MC. Seco *et al.* [120] have reported similar over prediction in doses by CCC_{Onc} algorithm in an oral cavity tumour.

Where the complication probability of parotids is concerned, this is systematically overestimated by both *type a* and *type b* algorithms by up to 9%. In reality, the predicted complication actually occurs at a lower dose than reported which is an impediment to possibility of dose escalation. In this study, complication probabilities of other structures were not calculated as xerostomia is the most commonly observed side effect of radiotherapy of NPC.

7.4.3 Structures and parameters used for the prediction of clinical outcome

In this study, only the GTV volumes were used to calculate the TCPs. The actual probability of tumour control would also depend upon the nodal status of the patient and chemotherapy administered. Although the positive nodes within the CTV were planned to receive the same dose as received by the GTV, and high- and low-risk nodal volumes were irradiated with lower doses, these volumes

were not considered in estimating TCPs. The version of the Marsden model used in this study assumes a uniform clonogenic cell density within the target volume i.e. GTV. In reality, the microscopic disease present in the CTV1 and CTV2 (see section 7.2.1) would also contribute to the predicted TCP.

The uncertainties associated with the TCP and NTCP model parameters may influence the predicted outcomes based on the investigated photon dose calculation algorithms. However, these uncertainties would not change the direction of these differences. Derivation of reliable model parameters within recommended tolerance level (95% confidence interval) is beyond the scope of this research and we believe the parameter sets used in this study are adequate for our stated purpose.

7.5 Conclusions

The influence of photon dose calculation algorithms on the predicted clinical outcome of nasopharyngeal IMRT treatment plans were studied using radiobiological models of TCP and NTCP. The dose calculation of MC IMRT model was compared against TPS calculations in order to verify the validity of the complexity of the model. Differences of up to 3%/3 mm and 4%/4 mm were found between MC and PBC, AAA of Eclipse TPS respectively. These differences arise due to differences in MLC leakage modelling between the TPS algorithms and MC. The results of clinical nasopharyngeal IMRT plans show that all the TPS algorithms systematically overestimate the doses to the GTV and hence predict a higher chance of controlling the tumour. In case of PBC_{Onc} and MC, the DVHs of which have the maximum separation result in TCP differences of up to 13%. NTCPs are overestimated by up to 9% at the expense of impeding dose escalation. Therefore, simple convolution based algorithms which do not accurately model the electron transport in inhomogeneities such as air cavities are not suitable for clinical use. On the other hand, *type b* algorithms are acceptable alternatives to MC dose calculation algorithms as the differences in dose calculation accuracy can be traded against the longer treatment planning calculation time of MC.

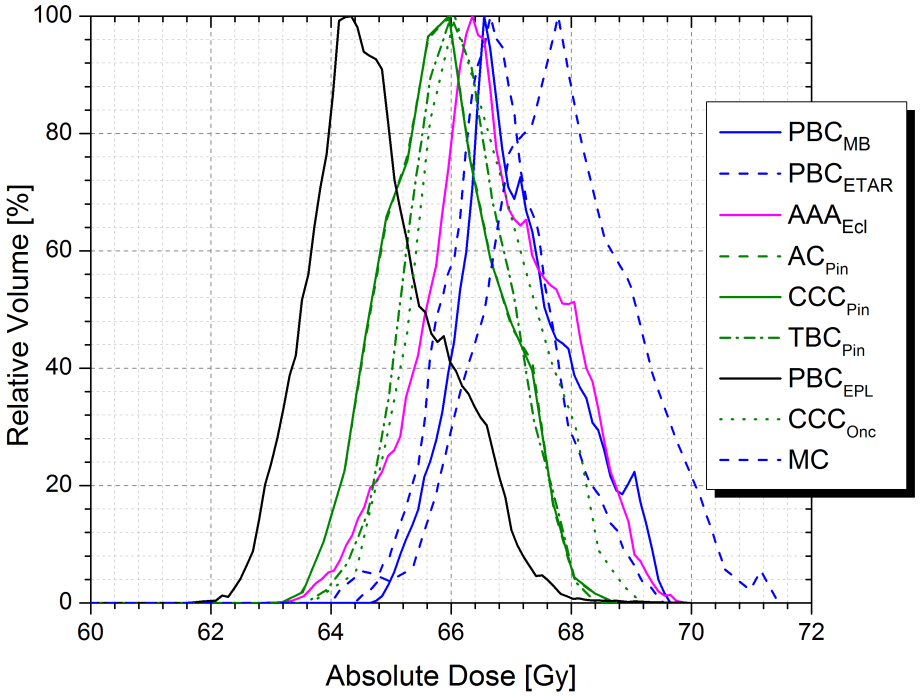

(a)

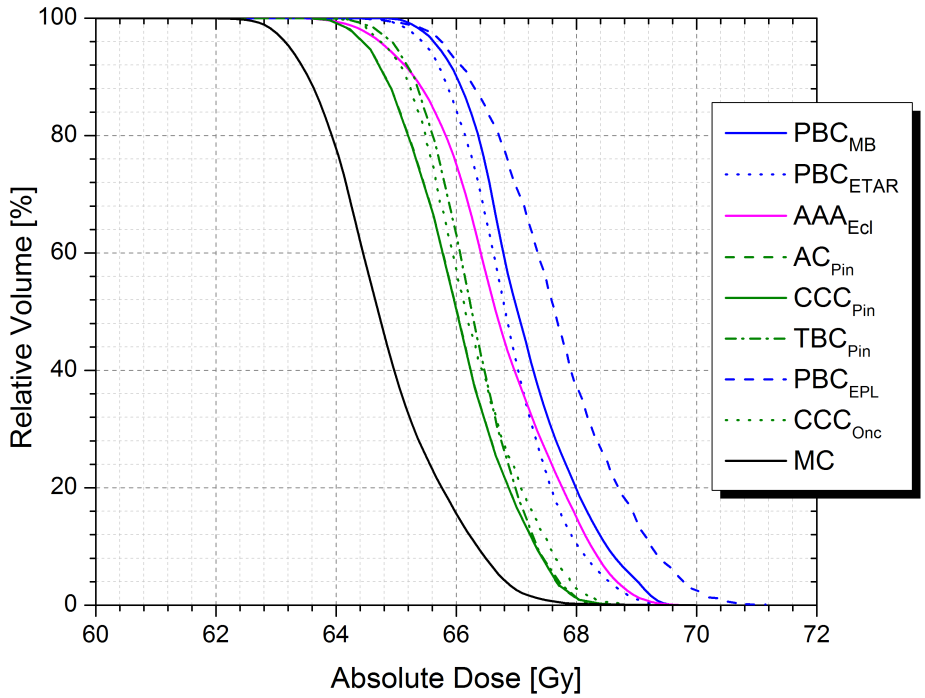

(b)

Figure 7.2: (a) Differential (b) Cumulative DVHs of GTV of nasopharyngeal carcinoma patient plan expressed in terms of absolute dose along x-axis and relative volume along y-axis calculated using TPS algorithms and MC (a correction factor of 1.025 was applied to the MC doses in order to ignore the differences in beam modelling).

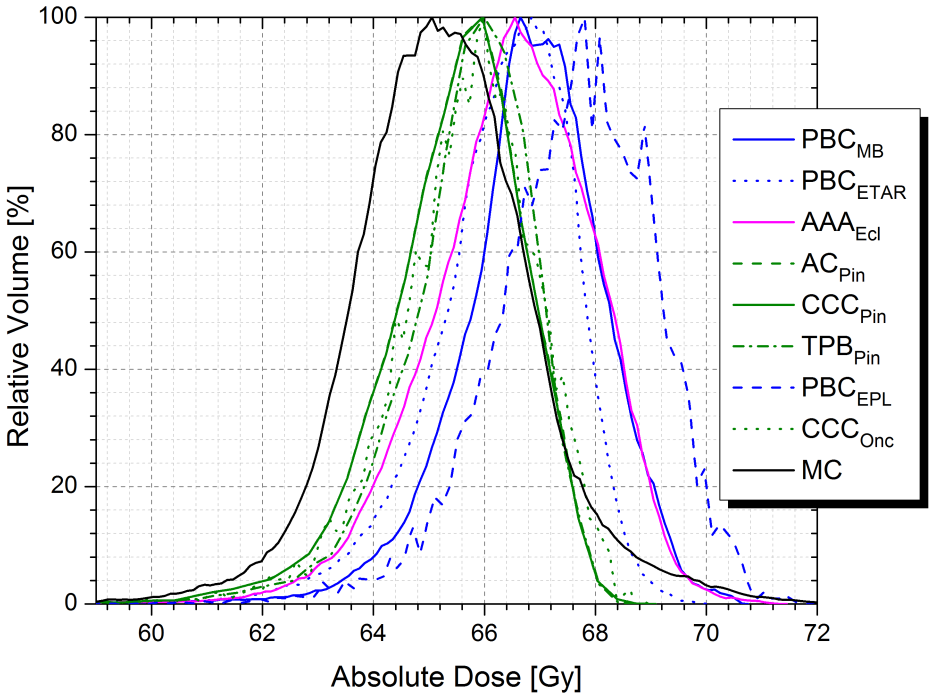

(a)

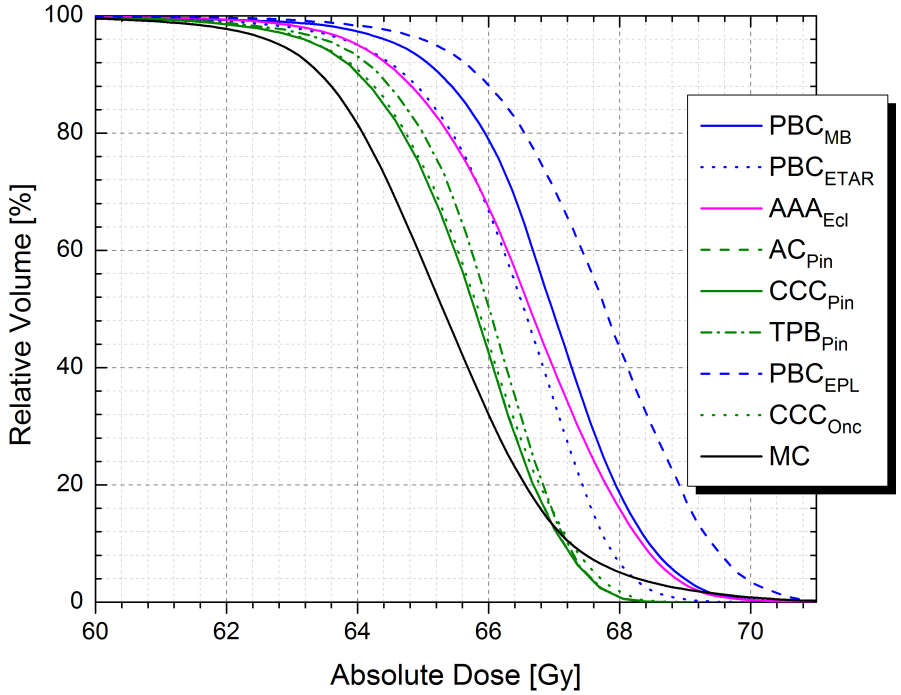

(b)

Figure 7.3: (a) Differential (b) Cumulative DVHs of PTV1 of an NPC patient plan expressed in terms of absolute dose along x-axis and relative volume along y-axis calculated using TPS algorithms and MC (a correction factor of 1.025 was applied to the MC doses in order to ignore the differences in beam modelling).

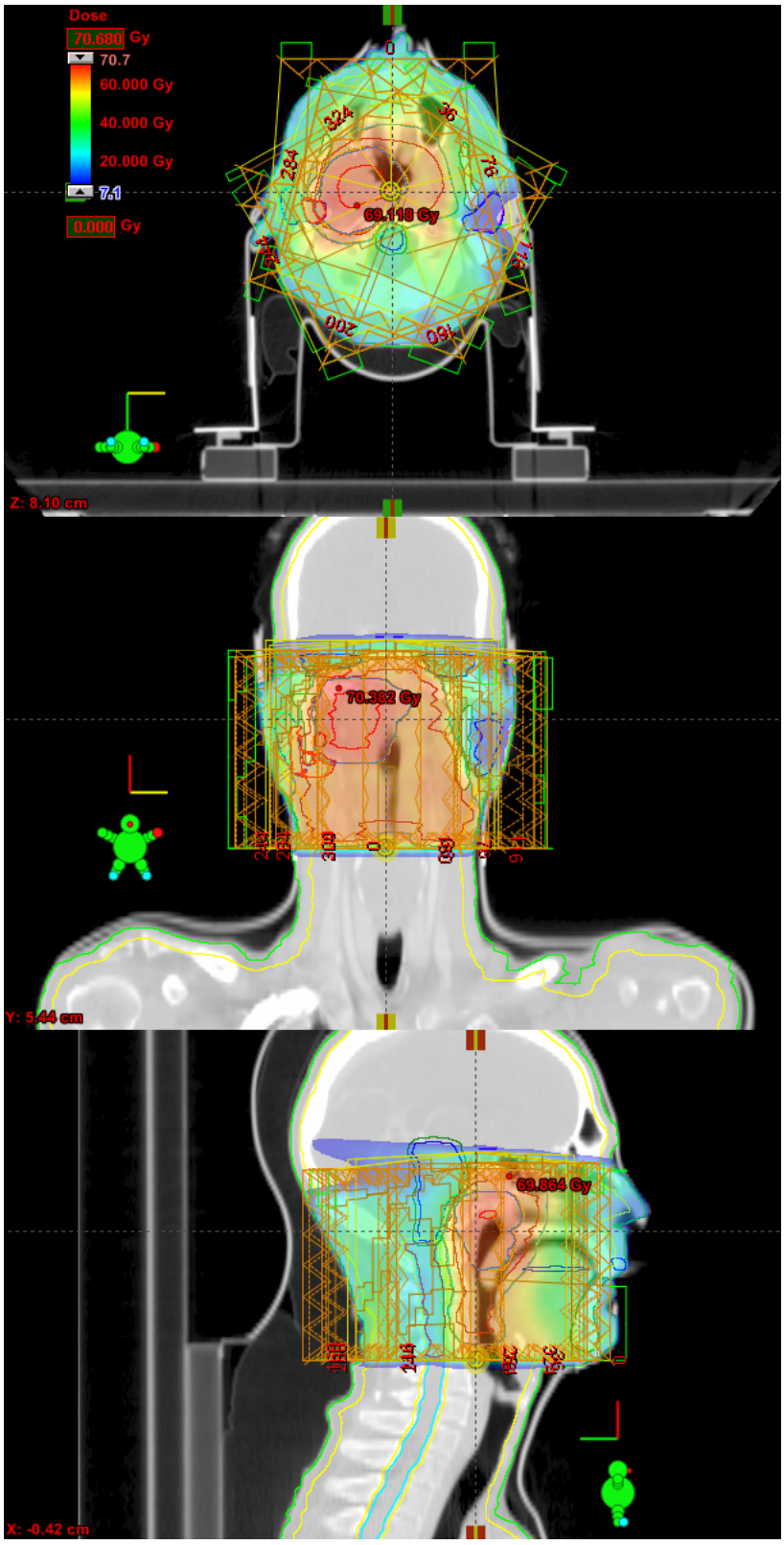

Figure 7.4: IMRT dose distribution of a patient treated for NPC. The top, middle and bottom figures show the dose distribution in axial, coronal and sagittal views. The nodal lower neck field is not shown in the figures.

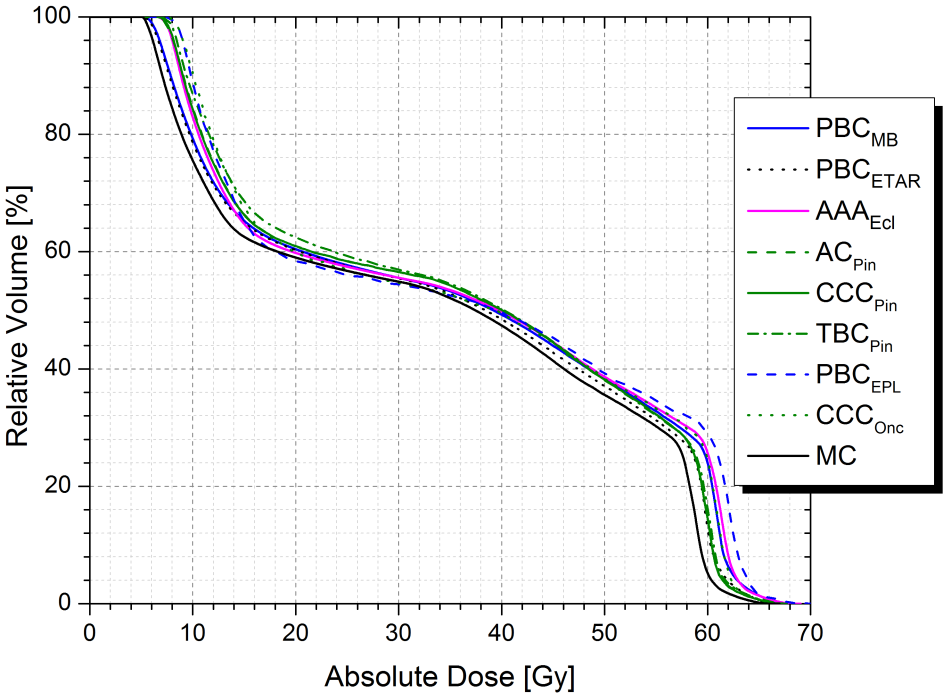

Figure 7.5: Cumulative DVHs of both the parotids (considered as a single paired organ) calculated using TPS algorithms and MC (a correction factor of 1.025 was applied to the MC doses in order to ignore the differences in beam modelling).

Chapter 8

Influence of dose calculation algorithms on TCP parameters

8.1 Introduction

The prediction of clinical outcome of radiotherapy regimens are important in order for us to understand the probability of controlling a particular type of tumour in a patient population. TCP and NTCP models have been reported in the literature which are used to estimate the probability of tumour control and normal tissue complication respectively [23–25, 27, 139]. These models are based on various parameters which are derived by fitting parameters of radibiological models to data sets in the form of DVHs to clinically observed outcome data [38, 41, 42]. Some mechanistic or phenomenological models have been reported in the literature which account for the mechanism involved in cell damage due to radiation [222–225]. Some of these models are based on the damage caused to functional subunits (FSUs) whereas others have employed MC track structure codes [226, 227]. In order to obtain probability of tumour control in a patient population, the clinical outcome data for a particular end point of interest, eg. tumour local control, local progression free survival, disease free survival are obtained by evaluating the response of a patient with a particular tumour treated with certain dose fractionation after a period of time from the last day of treatment [36, 37, 131, 228–230]. The response is either 0 or 1 depending upon no or partial and complete response of the tumour to the treatment received and the

probability of controlling a tumour is expressed as percentage of patients in a patient cohort who have had a complete response at the time of follow-up.

The accuracy of the predicted clinical outcome and the model parameters depend directly upon the accuracy of the dose distributions or the delivered prescription dose. This in turn varies with the dose calculation algorithm employed to do the treatment plan. The choice of the dose calculation algorithm becomes critical when tumour sites with complex geometries including heterogeneities like lung, bone, air passages are considered. These heterogeneities that have densities lower or higher than that of water results in disruption of charged-particle equilibrium. Low density medium such as lung has a lower photon attenuation coefficient than that of water and in addition the electrons that are produced upstream scatter in the lateral direction than in the forward direction due to relatively 'light' scattering medium. Simple pencil beam convolution based dose calculation algorithms do not model the lateral electron transport whereas more sophisticated convolution-superposition algorithms approximately models this effect. A large number of publications are available in the literature that report the differences in physical doses calculated by various analytical algorithms available in commercial TPSs and golden standard MC that accounts for the actual transport of charged-particles in the medium of interaction or measurements done in heterogeneous phantoms [69–71,80,85–87,116,195–198,206]. These studies report considerable differences on doses received by target volumes in NSCLC.

A parameter set that is fit to data set calculated by a particular algorithm can still correctly predict the clinical outcome in terms of probability of controlling the tumour of a treatment plan which is computed by a similar algorithm irrespective of its dosimetric accuracy. However, the same set of parameters may not hold good to evaluate treatment plans that are calculated with an algorithm that is completely different from that of the one based on which the parameters were derived. This will either result in overestimation or underestimation of TCPs. It is therefore essential to use TCP parameters that are derived from the same dose calculation algorithm as that of the treatment plan for which the probability of tumour control needs to be estimated. A study has been done by De Jaeger *et al.* [40] in which NTCP parameters with radiation pneumonitis as the end

point were derived for LKB model based on data sets from an EPL heterogeneity correction based convolution algorithm and more accurate CCC algorithm . The results showed that the complications occur at a much lower dose of 12-14% less than that predicted by EPL algorithm. Significant difference was found in the D_{50} value which reduced to 29.2 Gy from 34.1 Gy.

In this study, we derive the TCP parameters for Marsden model which is a mechanistic model that employs the LQ formalism in order to predict local control for a patient population [27]. This model estimates the surviving number of clonogenic cells after a radiotherapy regimen incorporating inhomogeneous dose distribution in a patient plan accounting for inter patient variability in radiosensitivity. The TCP parameters were obtained by fitting to datasets of various dose calculation algorithms to published clinical outcome data for four different radiotherapy dose fractionation schedules for NSCLC patients treated with curative intent. TCP parameters were derived for eight different photon dose calculation algorithms, out of which seven are available in commercial TPSs; some of which are routinely used in the clinic at present and some in the past. These parameters were compared against the parameters derived from MC dose distributions which is considered as the golden standard dose calculation algorithm. To date, such a study evaluating the influence of photon dose calculation algorithms on TCP parameters has not been performed.

8.2 Methods and Materials

8.2.1 Treatment planning

Ten NSCLC patients with locally advanced, unresectable tumours of stages II-III treated with curative radiation therapy were considered for this retrospective study. All the patients under went CT simulation process before the schedule of treatment. These CT scans were taken in treatment position in normal breathing cycle and the targets including the GTV, CTV and PTV and OARs like normal uninvolved lungs, cord, oesophagus and heart were delineated according to the segmentation protocol. The GTVs were the tumour mass that was visibly seen on the images and the CTV included the microscopic extent of the tumour which

was created by expanding the GTV isotropically by 5 mm. A uniform PTV margin of 10 mm around the CTV was created to account for any errors due to patient positioning, both systematic and random and also due to tumour motion including inter- and intra-fraction motion due to breathing.

3DCRT treatment plans with 6 MV photon beam of Varian Clinac 2100 CD were done with three fields in all the cases with an MLC margin of 7 mm around the PTV. EDWs were used in all the patient plans in two or more fields when necessary in order to get a uniform dose distribution around the PTV. The treatment plan was prescribed to deliver 55 Gy in 20 fractions at the ICRU prescription point which is the centroid of the PTV, according to the NSCLC hypofractionated radiotherapy regimen followed in our clinic [194]. The treatment plans were done with the PBC_{MB} algorithm of Eclipse TPS and the number of MUs to be delivered for each treatment field were kept the same and the doses were recalculated with PBC_{ETAR}, AAA_{Ecl} of Eclipse, AC_{Pin} and CCC_{Pin} of Pinnacle, PBC_{EPL} and CCC_{Onc} of Oncentra TPSs and EGSnrc based MC algorithm. A detailed description of physics of these algorithms are given in chapter 2 of this thesis. The beam parameters of the treatment plans including the field size, beam energy, MLC shapes were kept the same while exporting the plans to other planning systems. As mentioned in Chapter 5, the TPS algorithms fall into two categories, *type a* or convolution and *type b* or convolution-superposition algorithms as enunciated by Knöös *et al.* [87], where *type a* algorithms are convolution based algorithms which do not model the electron transport accurately and *type b* algorithms are those which have the capability of modelling electron transport with approximations. PBC_{MB}, PBC_{ETAR}, PBC_{EPL} fall under *type a* algorithms whereas AAA_{Ecl}, AC_{Pin}, CCC_{Pin}, CCC_{Onc} are *type b* algorithms. The differential DVHs of GTV and PTV volumes of plans done with all of the above mentioned algorithms were exported in terms of absolute dose and volume units in order to fit to known outcome data for NSCLC and TCP parameters for each of these algorithms were derived separately.

8.2.2 Points for fitting

The clinical outcome of radiotherapy of NSCLC based on four fractionation regimens, three published in the literature and our own unpublished data from the Clatterbridge Cancer Centre (CCC) were used to derive the TCP parameters based on the dose distribution and DVHs of the plans done with *type a*, *type b* and MC algorithms. The outcome of the study published by Saunders *et al.* [131] on continuous, hyperfractionated, accelerated radiotherapy (CHART) versus conventional radiotherapy based on a randomised multi-centric trial constituted two of four points of the TCP parameters fitting. In this study, the patients under the conventional arm received a total dose of 60 Gy in 30 fractions as 2 Gy dose per fraction over 6 weeks whereas the CHART patients received a total dose of 54 Gy in 12 fractions. The patients under the CHART arm received a daily dose of 1.5 Gy 3 times per day with a gap of 6 hours, 36 fractions over 12 consecutive days in total. The results of the study showed that the outcome of CHART was superior than that of conventional radiotherapy [131]. The estimated probability of tumour control for CHART and conventional radiotherapy were reported to be 18% and 12% respectively. The outcome data published by Martel *et al.* [37] based on the study done in University of Michigan Medical Center (UMMC) reported tumour control of 43% for a dose fraction ranging from 64 to 82 Gy depending upon the stage and volume of the tumour. These patients were treated daily, 5 days in a week, with daily tumour dose of 1.8 - 2 Gy. The final point to fit was based on our own clinical experience at CCC where the predicted tumour control in patients with NSCLC treated with curative intent is 35%. These patients were treated with a prescription dose of 55 Gy in 20 fractions with a daily dose of 2.75 Gy.

Figure 8.1 shows the four TCP points against corresponding biologically effective doses (BEDs) [129] or equivalent doses in 2 Gy fractions for CHART conventional or control arm, CHART trial arm, CCC and UMMC outcome data. The doses along the x-axis is given in terms of BEDs in order to represent it in terms of isoeffect as the fractionation regimens of the four points are different from each other. The BEDs are calculated using the formula given in equation 8.1.

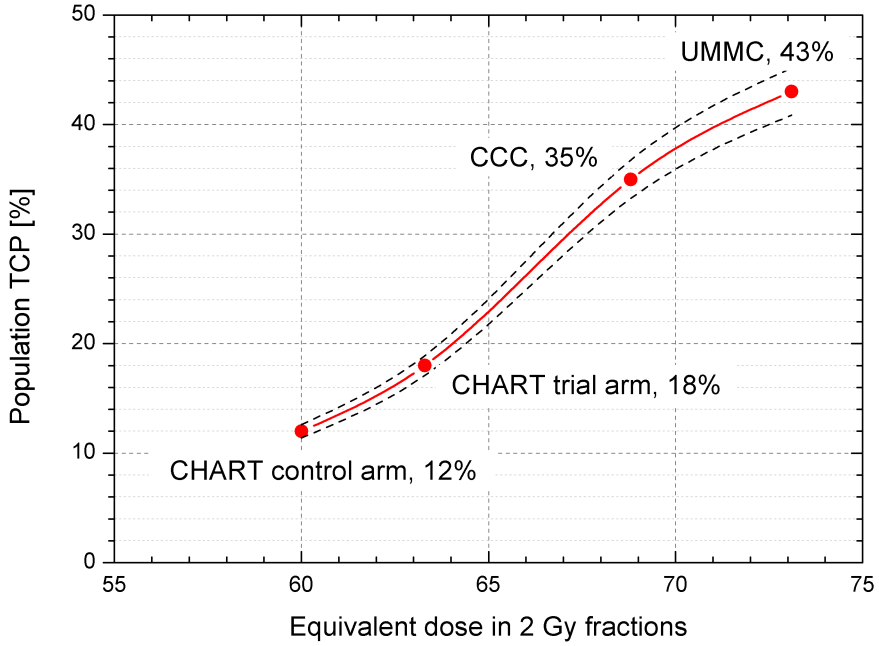

Figure 8.1: Average population TCP against corresponding equivalent doses in 2 Gy fractions based on CHART conventional arm, CHART trial arm, CCO and UMMC clinical outcome data. The dashed black lines show ±5% standand deviation on the TCP points.

$$\mathrm{BED} = D\left[1 + \frac{d}{\alpha/\beta}\right] \tag{8.1}$$

where D is the total dose in Gy, d is the dose per fraction in Gy, α/β accounts for fractionation correction.

8.2.3 Fitting of Marsden TCP parameters

The differential DVHs of the GTV and PTV of plans done with all the photon dose calculation algorithms under investigation and were exported in absolute dose and volume units from all three TPSs. The prescription doses were modified according to Martel *et al.* [37] data depending upon the GTV volume using *Bio-Suite*, in-house radiobiological evaluation software developed by Uzan *et al.* [199]. The volumes of the GTVs ranged from 25 to 175 cm^3. The volumes of the GTVs of patient plans used in this study ranged from 25 to 175 cm^3. A MATLAB v.7.6, R2008a[1] code developed in-house was used to derive TCP parameters by fitting them to the DVH datasets calculated by various dose calculation algorithms to

[1]Mathworks, Natick, US

four points based on published outcome data of cohort of patients who under went radical radiotherapy for NSCLC for four alternative fractionation regimens. The TCP parameters of Marsden model proposed by Webb *et al.* [27] namely $\bar{\alpha}$ (Gy^{-1}), mean radiosensitivity for a patient population, σ_α (Gy^{-1}, population standard deviation on the radiosensitivity, T_k (days), delay in accelerated repopulation and T_d (days), tumour doubling time were obtained by fitting. These parameters were set as variables whereas two other parameters of this model, ρ_{cl} (10^7 clonogens/cm^3), clonogenic cell density and α/β (10 Gy) ratio were kept constant.

Lower ($\bar{\alpha}$=0.1 Gy^{-1}, σ_α=0.001 Gy^{-1}, T_k=1 day, T_d=1 day) and upper ($\bar{\alpha}$=0.5 Gy^{-1}, σ_α=0.005 Gy^{-1}, T_k=50 days, T_d=50 days) bounds were defined for each of the four variable parameters and during each run the initial values or starting points of each of these variable parameters were randomly chosen within the defined parameter boundary space and the fitting was repeated several times to test the robustness of the derived parameters which will ensure a stable or global solution. A standard deviation of $\pm 5\%$ was applied on the TCP points predicted based on CHART, CCC and UMMC data so as to investigate the range of fitted parameters. An objective function was defined for the optimsation process to determine the best fit using least squares fitting of aim or observed and model predicted TCP values. The iteration was continued until the objective function reached at least a minimum value of less than 10^{-9}.

8.2.4 Formalisms employed for fitting the parameters

Mean of the population TCP was calculated for each patient DVH with M dose bins for all four dose fractionation schemes using equation 8.2.

$$\mathrm{TCP}_{\mathrm{pop,j}} = \int_0^1 P(\alpha) e^{-N_c(\alpha)} d\alpha \tag{8.2}$$

Here, j is the patient index, *P(α)* is the log-normal probability of a patient having radiosensitivity α, N_c is the number of clonogens that remain after receiving a dose represented by the dDVH normalised to unit total volume. The remaining number of clonogens is calculated by equation 8.3.

$$\mathrm{N_{c,j}} = [GTV_{\rho_c}] \sum_{i=1}^{M} dDVH_i e^{-n\alpha d_i(1+d_i\beta/\alpha)+ln2(T-T_k)/T_d} \tag{8.3}$$

In all the cases, GTV was used to calculate the total number of tumour clonogens present before irradiation and both the GTV and PTV DVHs were used to account for the dose delivered to the tumour. The predicted population TCP for the patient cohort receiving a given dose fractionation regimen is given by the equation 8.4.

$$\overline{\mathrm{TCP_{pop}}} = \frac{1}{K} \sum_{j=1}^{K} TCP_{pop,j} \tag{8.4}$$

8.2.5 Simplex optimisation algorithm

Simplex optimisation algorithm which is available as a part of the optimisation toolbox of MATLAB, a generic tool for solving linear programming problems was used to find the best fit parameters iteratively. It is based on a simple optimisation algorithm that finds a global solution of an n-dimensional function within a defined parameter boundary space. A simplex of an n-dimensional function starts with *n+1* observations, for eg. a 2D simplex starts with 3 initial observations whereas a 3D simplex has 4 initial observations and so on. It is represented as a line segment in 1D space, triangle in 2D space and as a tetrahedron in 3D space. A simplex is constructed depending upon the number of parameters to be optimised and an objective or target function is defined, the iterations are repeated so as to minimise the objective function for eg. least squares function. Two points in the n-dimensional space, known as worst and best points are defined and the worst point is updated iteratively by four processes namely reflection, expansion, 1D contraction and multiple contraction.

The simplex reflects the worst point W through the centroid, CEN to form the reflection point R. If R is better than the present best point B, simplex is expanded to the new reflected point. On the other hand, if the reflected point R is not better than the present worst point W, it contracts in 1D through CEN to the contraction point C whereas if it is worse than W it contracts on all dimensions towards the present best point B. The sequence of steps is repeated iteratively until an optimal solution is achieved.

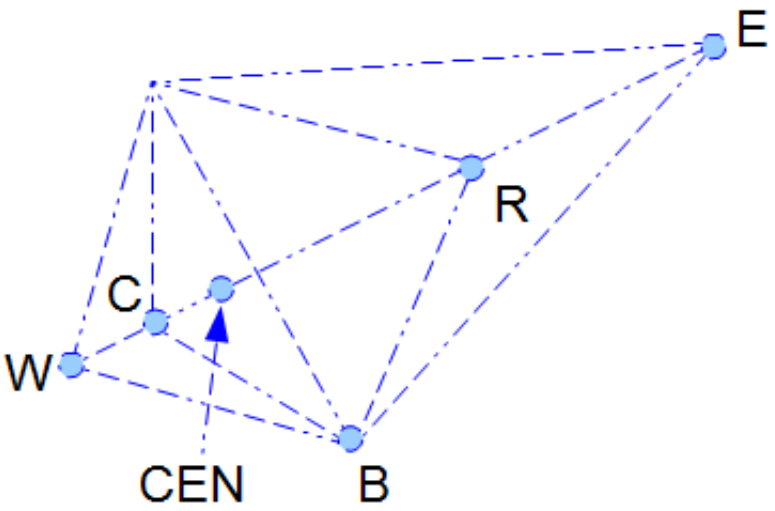

Figure 8.2: Schematic diagram showing simplex optimisation process. CEN, W, B, C, R, E represent the centroid, worst, best, contraction, reflection and expansion points.

8.3 Results

8.3.1 TCP parameters derived from data sets of individual algorithms

Table 8.1 show the Marsden TCP model parameter sets derived from GTV and G-PTV DVHs of plans calculated with *type a*, *type b* and MC algorithms. In case of the parameter sets derived from G-PTV DVHs, significant differences were found in the mean radiosensitivity of the patient population when the parameters were fit to DVHs corresponding to dose distributions calculated by *type a*, *type b* and MC algorithms. The mean alpha value obtained from MC dose distributions were larger than that derived from PBC_{MB} as the absolute doses were over estimated by the *type a* algorithms. PBC_{MB} yielded an $\bar{\alpha}$ value of 0.302, lowest of all the other algorithms. The and PBC_{ETAR} , PBC_{EPL} and algorithms result in $\bar{\alpha}$ values slightly higher than PBC_{MB} with respect to their order of over estimation of the doses to the tumour. Both the convolution-superposition algorithms AC_{Pin} and CCC_{Pin} of Pinnacle TPS result in $\bar{\alpha}$ values closer to each other and to MC, 0.316 and 0.317 respectively. MC algorithm results in a higher $\bar{\alpha}$ which indicates that the tumour is more radiosensitive than predicted by *type a* algorithms. Out of all the investigated dose calculation algorithms CCC_{Onc} yields the highest $\bar{\alpha}$ value as it tends to under estimate the doses to the tumour.

Table 8.1: TCP parameters obtained by fitting to datasets derived from GTV and G-PTV DVHs to published clinical outcome for four radiotherapy regimens (CHART control=12%, CHART trial=18%, CCC=35% and UMMC=43%).

Parameters/ Algorithm	Structure	Mean radiosensitivity $\bar{\alpha}$ [Gy$^-$1]	Standard deviation on mean radiosensitivity σ_α [Gy$^-$1]	Repopulation constant T_k [days]	Tumour doubling time T_d [days]
PBC_{MB}	GTV	0.297	0.037	20.8	3.6
	G-PTV	0.302	0.036	20.7	3.8
PBC_{ETAR}	GTV	0.3	0.037	20.9	3.6
	G-PTV	0.305	0.035	20.9	3.8
PBC_{EPL}	GTV	0.299	0.037	20.8	3.6
	G-PTV	0.305	0.035	20.9	3.8
AAA_{Ecl}	GTV	0.303	0.039	21.0	3.6
	G-PTV	0.313	0.039	21.2	3.7
AC_{Pin}	GTV	0.301	0.038	20.8	3.6
	G-PTV	0.317	0.036	21.3	3.7
CCC_{Pin}	GTV	0.301	0.038	20.8	3.6
	G-PTV	0.317	0.036	21.3	3.7
CCC_{Onc}	GTV	0.312	0.039	21.2	3.6
	G-PTV	0.336	0.037	21.9	3.8
MC	GTV	0.302	0.038	20.9	3.6
	G-PTV	0.324	0.034	21.3	3.9

The differences in the $\bar{\alpha}$ between the algorithms followed a similar trend with *type a* algorithms yielding low $\bar{\alpha}$ values than MC when the parameter sets were derived from the GTV DVHs. *Type b* algorithms resulted in parameters that were closer to the MC derived parameters, AC_{Pin} and CCC_{Pin} being the closest to MC out of all the algorithms. The values obtained by fitting for the standard deviation on the intrinsic radiosensitivity of the patient population $\bar{\alpha}$ which characterises the slope of the sigmoidal TCP curve is shown in the tables. The differences in the tumour doubling time and repopulation constant were not that large and these two parameters does not significantly affect the shape of the TCP curve.

8.3.2 Robustness of the fitted parameters

Figure 8.3 shows the parameter sets derived for the same aim TCP values but with different starting points during the optimisation process. $\bar{\alpha}$, σ_α, T_k, T_d of 10 individual runs were obtained in order to test the robustness of the optimisation process. It is evident from figure 8.3 that a stable solution is achieved at the end of each run irrespective of choosing the starting points of the parameters randomly within the predefined parameter space.

8.3.3 Range of the fitted parameters

Figures 8.4(a), 8.4(b) and 8.5(a), 8.5(b) show the range of $\bar{\alpha}$ and σ_α repectively fit to datasets of eight dose calculation algorithms using GTV and G-PTV DVHs. A standard deviation of $\pm 5\%$ was applied on the four TCP points (CHART control=12%, CHART trial=18%, CCC=35% and UMMC=43%) used in this study and parameter sets were derived for the mininum, mean and maxiumum values of these four TCP points using both GTV and G-PTV DVHs. Another set of parameters were obtained by chosing the 'aim' TCP values randomly to see if they fall within the range. The variation, in $\bar{\alpha}$ was within 1% (1σ) and within 3% in most of the cases when σ_α is concerned.

8.3.4 TCP points recalculated with PBC and MC parameters

The four points based on the clinical outcome data of CHART conventional, CHART trial, Clatterbridge, UMMC fractionation regimes were recalculated us-

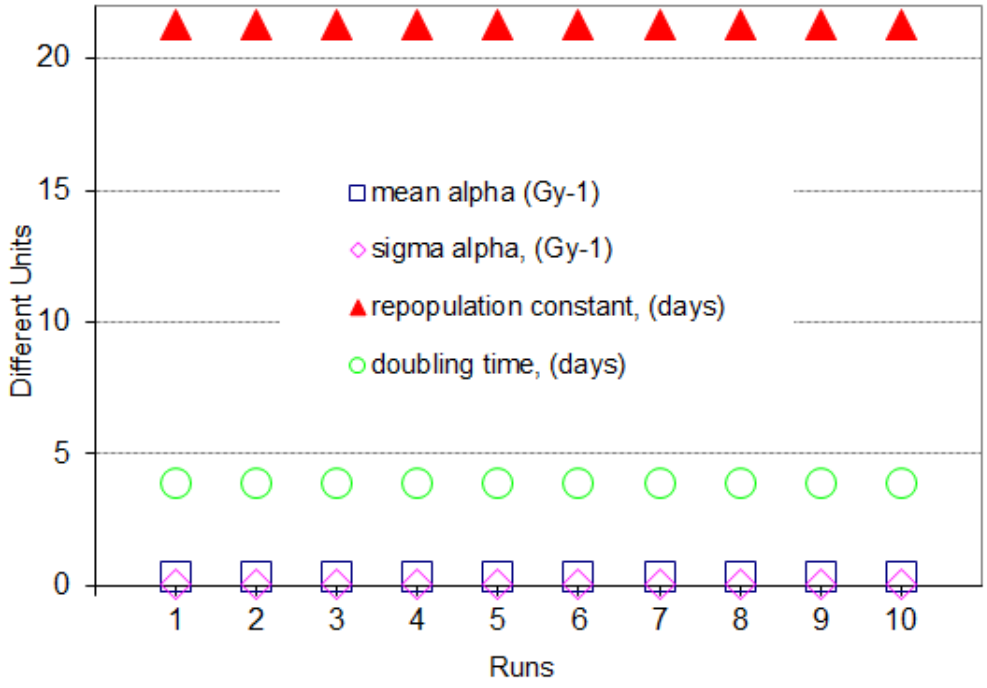

Figure 8.3: Plot showing the robustness of the parameter set fitting. Values of $\bar{\alpha}$, σ_α, T_k, and T_d obtained by fitting with different starting points in the defined parameter space for the same aim TCP values.

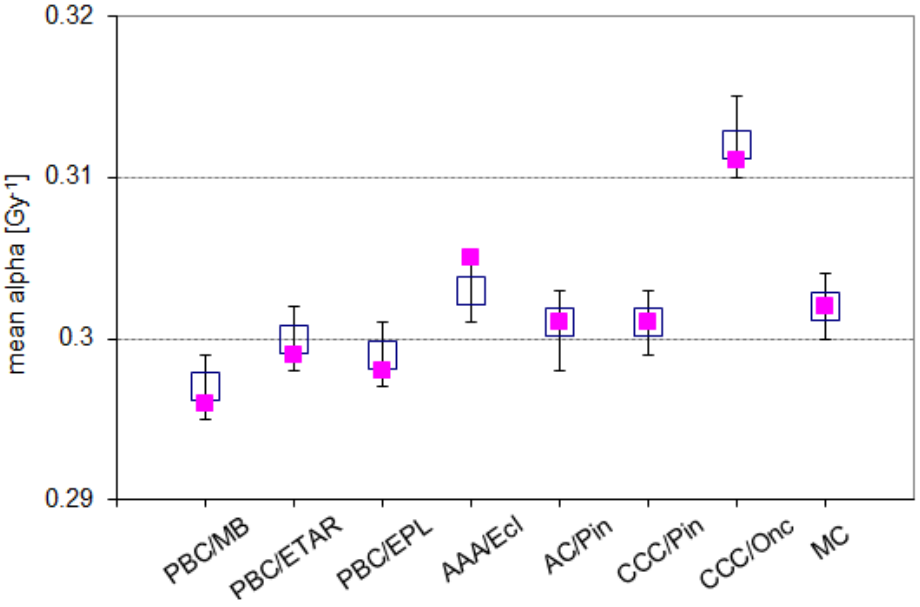

(a)

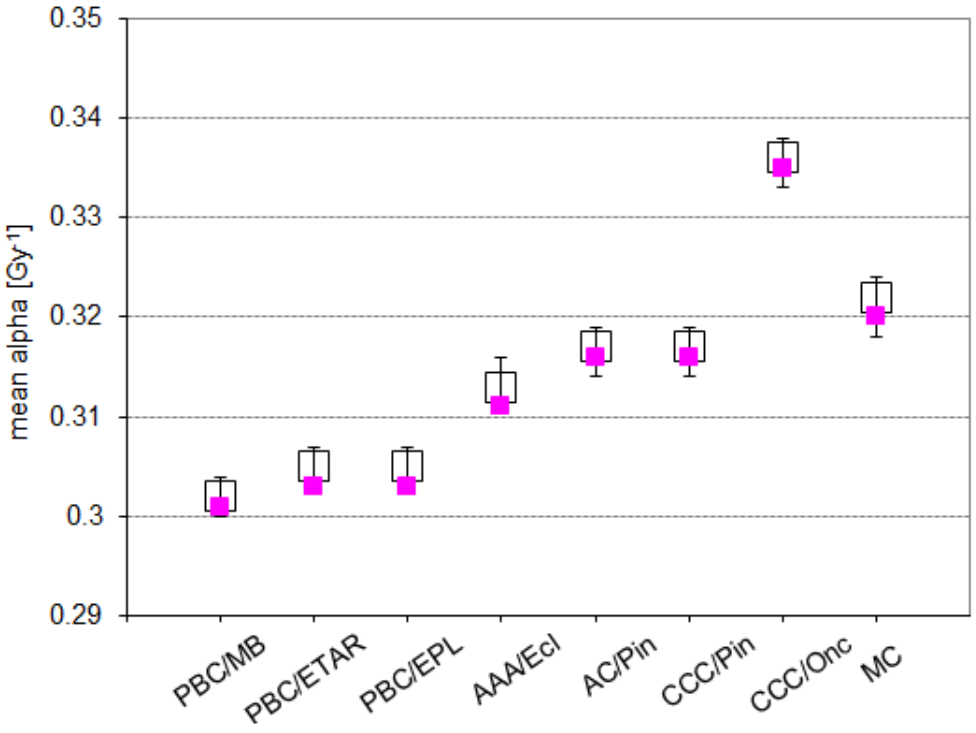

(b)

Figure 8.4: Range of mean alpha, $\bar{\alpha}$ obtained by fitting (a) GTV DVHs (b) G-PTV DVHs to min, mean, max TCP points with a standard deviation of ±5%. Black squares represent the $\bar{\alpha}$ values obtained by fitting to mean TCP points and the error bars represents the range of $\bar{\alpha}$ when fit minimum and maximum TCP points (±5% standard deviation on mean TCPs). Pink squares are $\bar{\alpha}$ values obtained for randomly chosen TCP points.

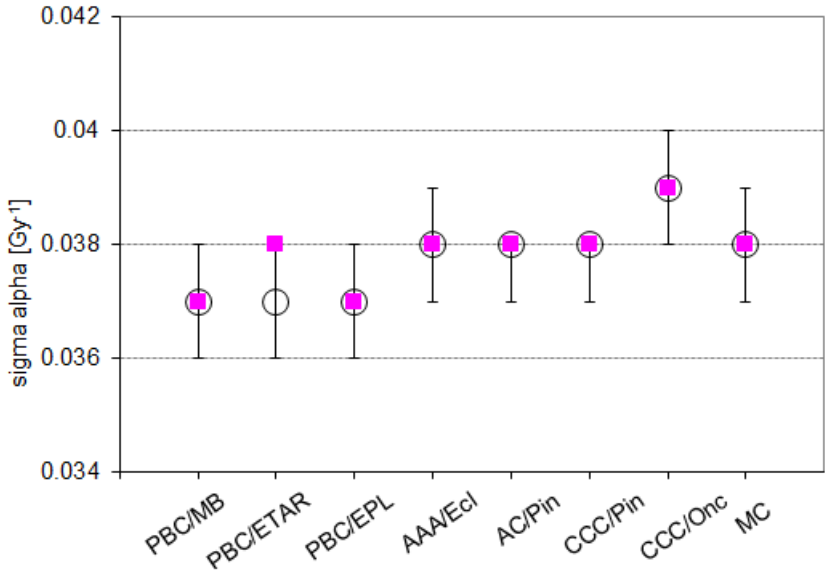

(a)

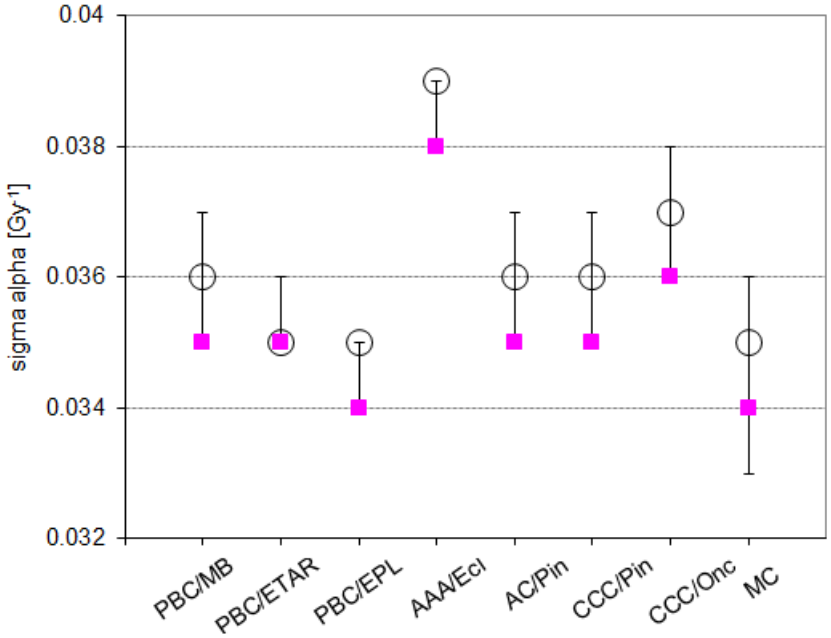

(b)

Figure 8.5: Range of sigma alpha, σ_α obtained by fitting (a) GTV DVHs (b) G-PTV DVHs to min, mean, max TCP points with a standard deviation of $\pm 5\%$. Black circles represent the σ_α values obtained by fitting to mean TCP points and the error bars represents the range of σ_α when fit minimum and maximum TCP points ($\pm 5\%$ standard deviation on mean TCPs). Pink squares are σ_α values obtained for randomly chosen TCP points.

ing the TCP parmaters derived by fitting data obtained from convolution, convolution-superposition and MC algorithms. Figures 8.6(a) and 8.6(b) show the TCP points for a patient population calculated with parameters derived from PBC_{MB} and MC with GTV and G-PTV DVHs respectively. The dose distributions of plans of the patient cohort were calculated by *type a*, *type b* and MC algorithms. When the TCP points were recalculated with PBC_{MB} derived TCP parameters, the points of PBC_{EPL} and PBC_{ETAR} were found to be closer to that of PBC_{MB}. AC_{Pin} and CCC_{Pin} of Pinnacle TPS predicted similar TCP values which were very close to that of the MC points. AAA_{Ecl} predicted TCP points that were second closest to that of MC. CCC_{Onc} under predicted the TCPs as it under estimates the doses to the tumour. The differences between the TCP points predicted based on dose distributions calculated with *type a*, *type b* and MC algorithms are larger when the parameters are derived using the G-PTV DVHs. Similar trend was found when the four points were recalculated with TCP parameters derived from MC calculated dose distribution.

8.3.5 Observed and predicted $\overline{TCP_{pop}}$

In order to ensure the validity of the derived TCP parameters, the average TCP_{pop} of the four different fractionation regimens were recalculated using parameters derived for each algorithm and the DVHs that represent the dose distributions calculated with their respective algorithms. The average TCPpop recalculated based on the GTV and G-PTV DVHs are shown in figures 8.8(a) and 8.8(b) respectively.

Figures 8.9 and 8.10 show the TCP values recalculated with MC and PBC_{MB} using GTV and G-PTV DVHs that represent the dose distributions calculated by convolution, convolution-superposition and MC algorithms for all the 10 NSCLC 3DCRT patients studied. When the TCPs were calculated with MC derived parameters using DVHs of all the 10 patient plans calculated with all the 8 algorithms, the absolute values of TCPs were found to be higher than when calculated with PBC_{MB} derived parameters as the intrinsic radiosensitivity or the mean alpha value was larger when fitted to MC data set.

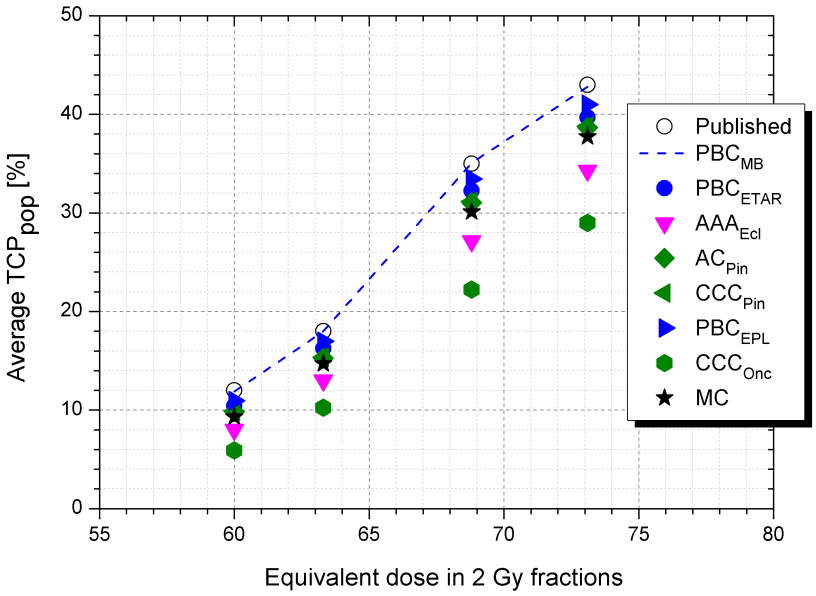

(a) Average TCP$_{pop}$ against equivalent dose in 2 Gy fractions for GTV DVHs based on parameters derived from PBC$_{MB}$ dose distribution

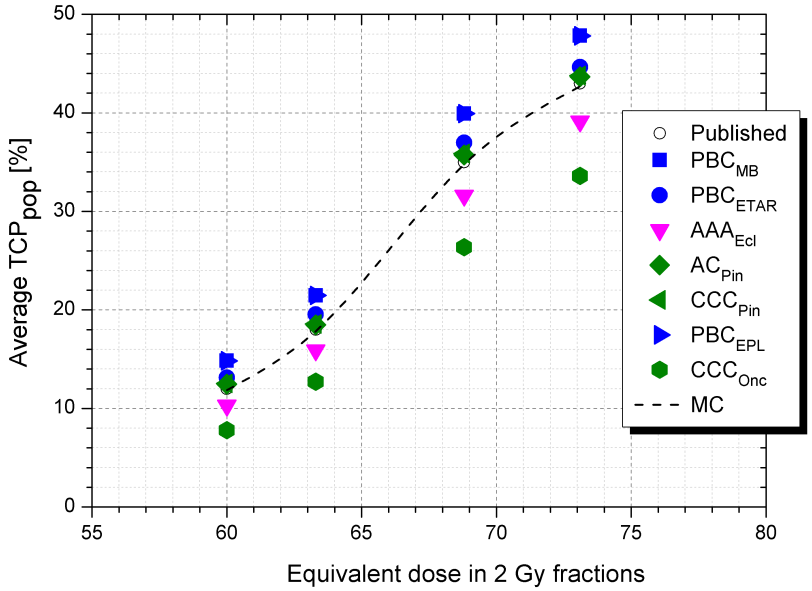

(b) Average TCP$_{pop}$ against equivalent dose in 2 Gy fractions for GTV DVHs based on parameters derived from MC dose distribution

Figure 8.6: TCP points based on outcome data published in the literature for four different dose fractionation regimens derived based on PBC$_{MB}$ and MC dose distribution using GTV DVHs.

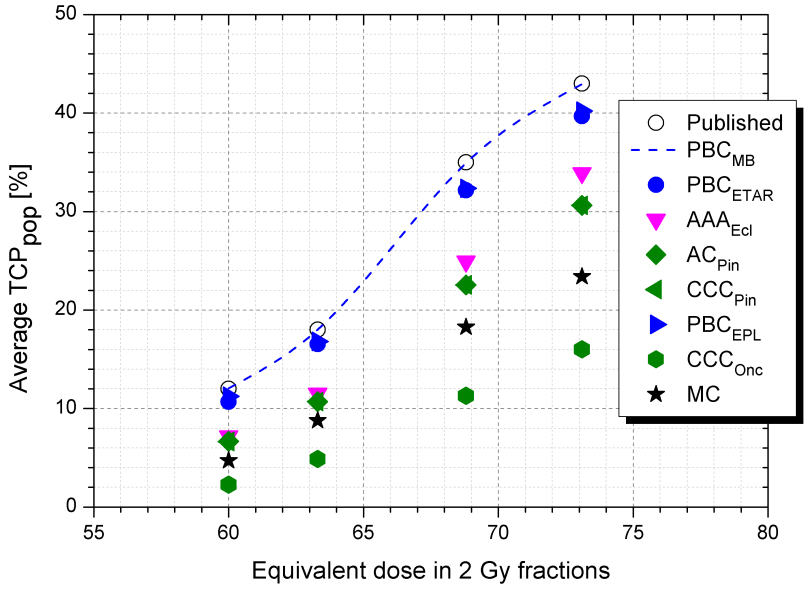

(a) Average TCP$_{pop}$ against equivalent dose in 2 Gy fractions for G-PTV DVHs based on parameters derived from PBC$_{MB}$ dose distribution

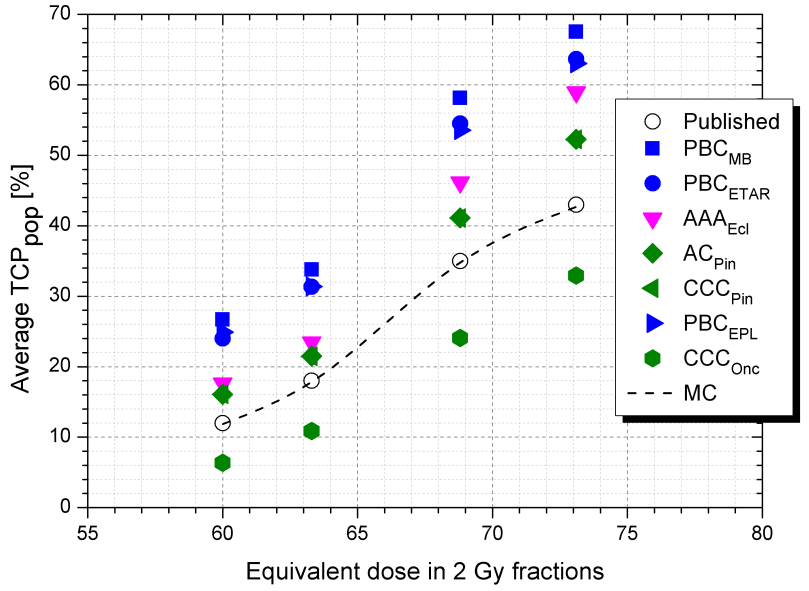

(b) Average TCP$_{pop}$ against equivalent dose in 2 Gy fractions for G-PTV DVHs based on parameters derived from MC dose distribution

Figure 8.7: TCP points based on outcome data published in the literature for four different dose fractionation regimens derived based on PBC$_{MB}$ and MC dose distribution using G-PTV DVHs.

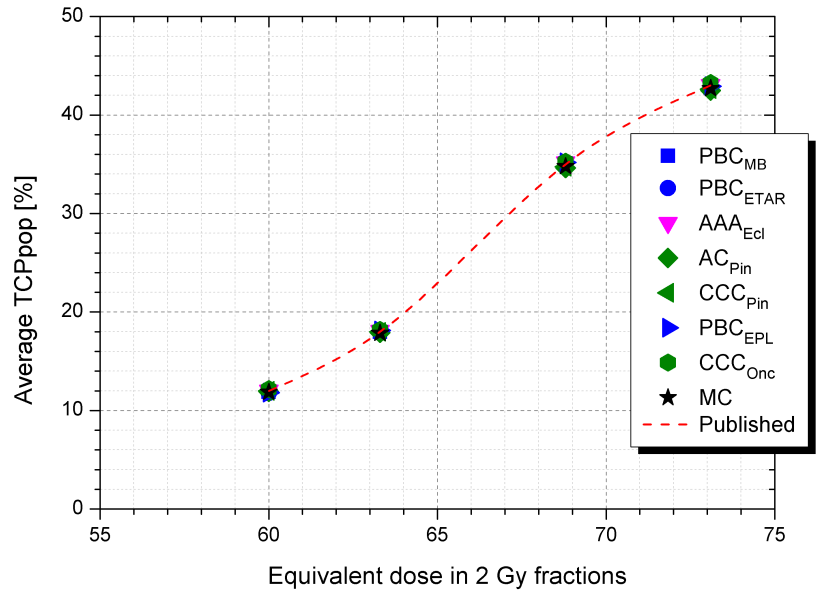

(a) Average TCP_{pop} against equivalent dose in 2 Gy fractions for GTV DVHs

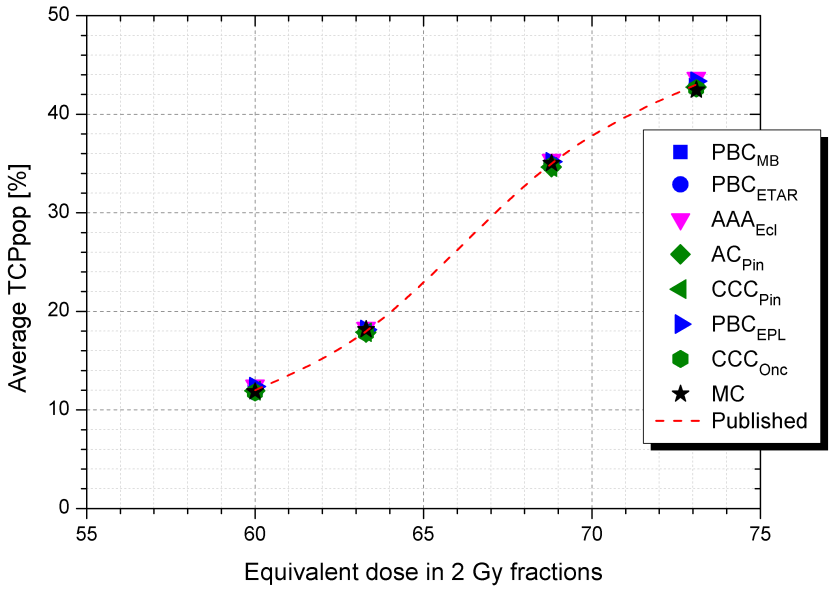

(b) Average TCP_{pop} against equivalent dose in 2 Gy fractions for G-PTV DVHs

Figure 8.8: TCP points based on outcome data published in the literature for four different dose fractionation regimens.

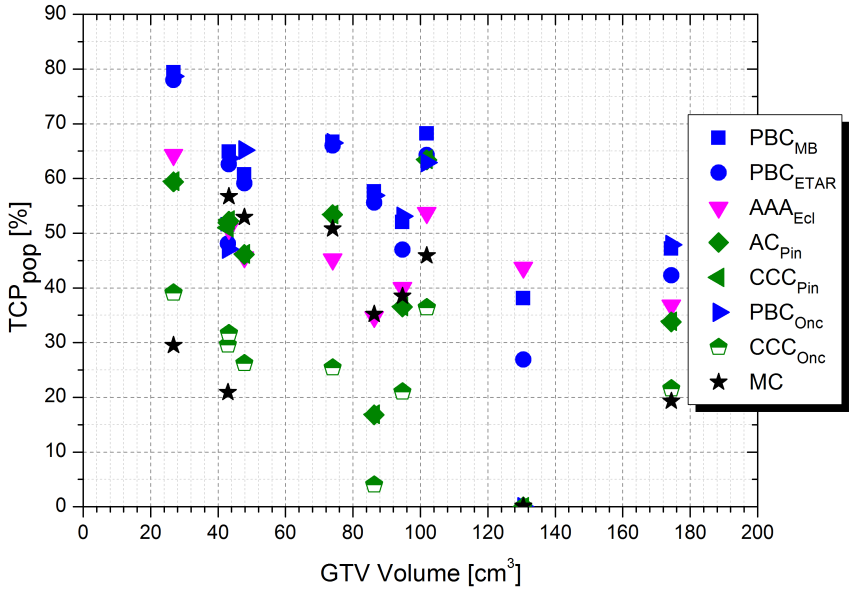

(a)

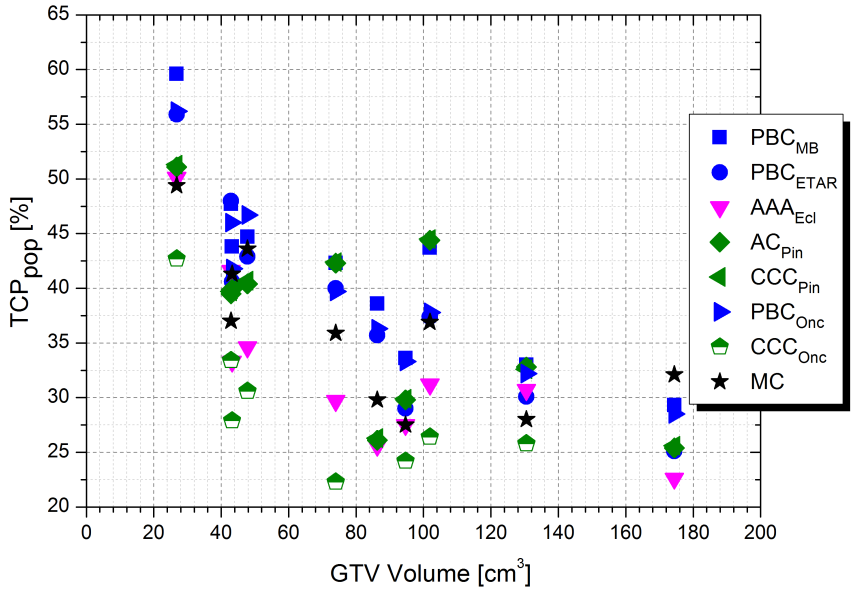

(b)

Figure 8.9: TCP_{pop} recalculated with parameters derived from MC DVHs of (a) G-PTV (b) GTV.

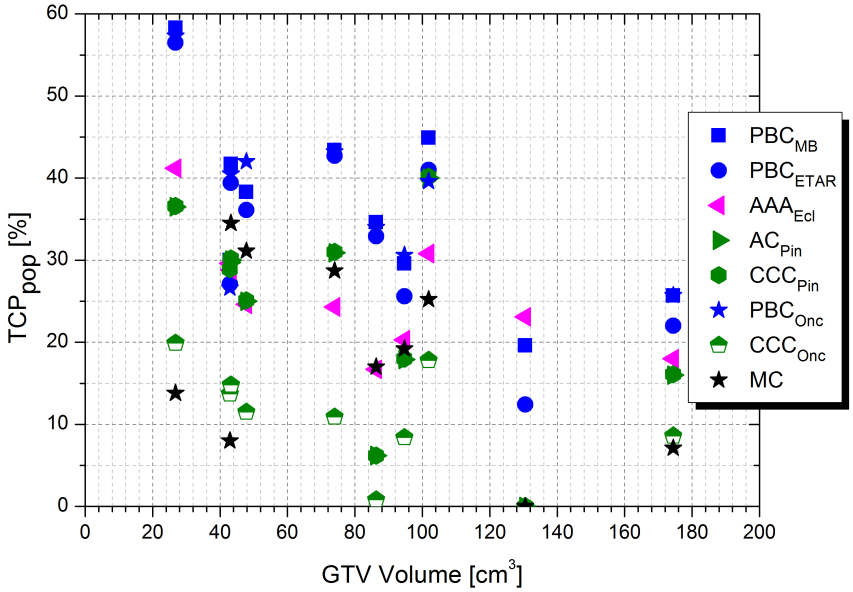

(a)

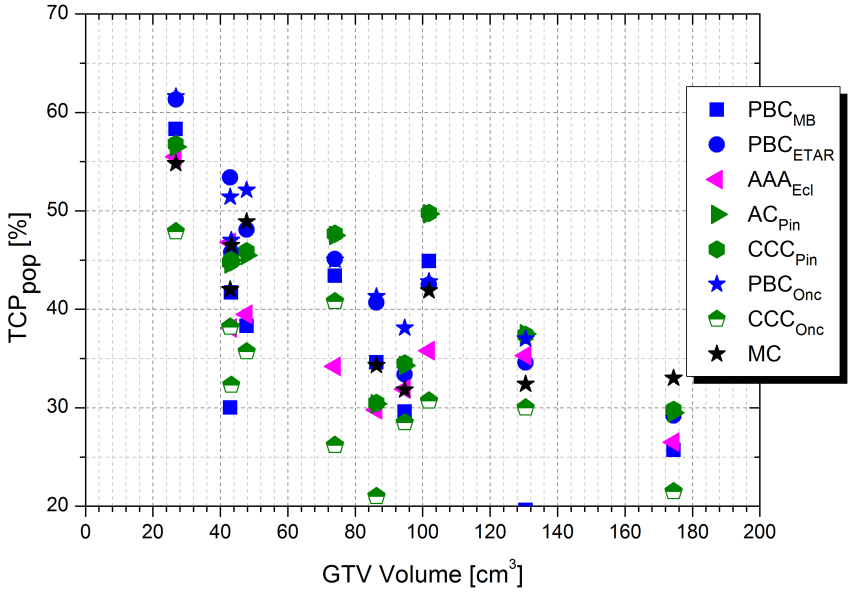

(b)

Figure 8.10: TCP_{pop} recalculated with parameters derived from PBC DVHs of (a) G-PTV (b) GTV.

8.4 Discussion

Customised TCP parameters were obtained by fitting data sets in the form of differential DVHs which represent dose distributions calculated by 7 algorithms that are available in commercial TPSs and MC. DVHs of GTV and PTV with GTV volumes were used to do the fitting. The results of the study indicate significant differences in the intrinsic radiosensitivity of the patient population which determines average sensitivity of the patient cohort to the dose fractionation regimen in question. Over estimation of the prescription dose would result in lower $\bar{\alpha}$ value as it signifies that the patients in the studied cohort will have to receive a higher dose in order to achieve an 'X' response which has been observed clinically. When the patient plan is recalculated with MC, it is evident that the patient has received a much lower dose than that predicted by *type a* algorithms. As a result, when the parameters are reset to the data sets based on the accurate MC dose distributions, the patient cohort seem to have had much higher radiosensitivity. The *type b* algorithms resulted in intrinsic radiosensitivities that were between the values predicted by *type a* and MC algorithms depending upon their degree of accuracy or closeness in calculating dose distributions with respect to MC. A difference of up to 20% and 10% is found when the TCP points are calculated using an inconsistent parameter set when calculated G-PTV and GTV DVHs respectively. It has to be noted that the changes in the patient anatomy during the time of treatment relative to that at the time of planning scan will affect the dose distributions which could in turn result in different parameter sets when fitted.

This study shows that using incompatible set of TCP parameters that were derived from data sets obtained from dose distributions calculated with a particular type of dose calculation algorithms to evaluate the clinical outcome of treatment plans that were calculated using a different algorithm might result in over- or under-prediction of the probability of the tumour control. The direction and magnitude of the discrepancies would depend upon the type of algorithm based on which the parameters were derived and the algorithm that was used to calculate the plan for which TCP is to be predicted.

To our knowledge, the influence of dose calculation algorithms on TCP model parameters has not been reported in literature. De Jaeger *et al.* [40] have studied

the influence of dose calculation algorithms on NTCP parameters for lung with radiation pneumonitis as the end point where the differences in NTCP parameters derived from a simple convolution and convolution-superposition algorithm were evaluated. Their study did not include MC algorithm due to the complexity in dose computation and long calculation time. The number of patient plans which were used to derive the parameters were 10 but it would be a work in the future to include significant number of patients. However, the number of patients included in this study is sufficient as the aim of the study was to quantify the differences in the TCP parameters obtained from data sets based on various photon dose calculation algorithms.

8.5 Conclusions

In this study, customised TCP parameters were derived by fitting DVHs corresponding to *type a*, *type b* and MC algorithms to published clinical outcome data of four different fractionation regimes. It is evident from the results of this study that using an inconsistent set of TCP parameters will lead to over or under estimation of the probability of local control of the tumour. It is therefore necessary to match the dose calculation algorithm of the treatment plan to be evaluated with that of the one from which the model parameters were derived. This is especially significant when considering tumours like NSCLC which is located amidst heterogeneous tissues of varying densities like lung where parameters derived from a simple convolution based dose calculation algorithm may not be applicable to evaluate plans calculated with *type b* or MC algorithms.

The differences between the TCP parameters derived by fitting the G-PTV DVHs were larger than those obtained from GTV DVHs alone. This is due to the fact that the differences between algorithms were larger in case of G-PTV DVHs where there is involvement of low density lung volume and the lung-tissue interface which result in over prediction of doses by *type a* algorithms. Significant differences exist mainly in the parameter, $\bar{\alpha}$ which denotes the mean radiosensitivity of a patient population. The $\bar{\alpha}$ values obtained by fitting MC dose calculation algorithm data is higher than that of *type a* algorithms in general. This study

proves that TCP parameter sets derived from dose distribution calculated by are strictly valid to predict the outcome of plans calculated by a similar dose calculation algorithm.

Chapter 9

Conclusions

The principal aim of this thesis was to quantify the potential impact on clinical radiotherapy outcome of replacing the currently employed convolution (pencil-beam) and convolution-superposition algorithms for patient dose computation by Monte-Carlo based treatment planning. A number of conclusions can be drawn from this thesis based on the results of chapters 5-8 which are summarised here.

9.1 Monte Carlo modelling

The greater part of this project involved extensive background work on setting up a MC dose calculation engine for radiotherapy treatment planning. An EGSnrc, BEAMnrc, DOSXYZnrc based MC system with the capability of performing conventional, 3DCRT and IMRT dose calculation in both phantom and patient CT data sets in a parallel computing environment was assembled as explained in chapter 4. A 6 MV Varian 2100 C/D accelerator head was modelled according to manufacturer specifications. This accelerator model was validated by matching MC calculated with measurements of open fields and dynamic wedged fields in a water phantom, resulting in a good agreement of doses within recommended tolerance limits of 2%/2mm and 3%/3mm respectively. MC calculated relative output factors ROFs were higher than measurements for field sizes smaller than 10x10 cm^2 but were lower for larger fields, as a result of inadequate modelling of the jaws. Additional measurements in a heterogeneous wooden lung phantom were made using radiochromic films to validate the handling heterogeneities by

the MC system. Although, overall there was good agreement between MC and measurements, differences of up to 16% were found in some cases (SABR) which could be attributed to the complex design, geometry and extremely low densities of the balsa and MDF inserts of the wooden lung phantom, the SABR treatment technique which involves asymmetric off-axis beams, statistical uncertainties in MC dose calculation and uncertainties related to scanning of the films as reported in chapter 5.

9.2 Study of radiotherapy of NSCLC and NPC

Chapter 6 was devoted to an exploration of the impact of PBC_{MB}, PBC_{ETAR} and PBC_{EPL} (*type a*), AAAEcl, AC_{Pin}, CCC_{Pin}, and CCC_{Onc} (*type b*) and MC photon dose calculation algorithms on the clinical outcome of lung tumour radiation therapy, for 3DCRT treatment plans done on a virtual lung phantom and for NSCLC patient CT data sets. The results of both the phantom and patient study highlight that PBC_{MB} and PBCOnc overpredict the doses to the tumour by the largest amount, followed by PBC_{ETAR}. Therefore, when an NSCLC patient is treated with a plan created using any of the *type a* dose calculation algorithms there is a chance of under-dosing the tumour, which is evident when the same treatment plans are recalculated for the same MUs with *type b* or MC. Hence, PBC_{MB} predicted higher tumour control; absolute differences of up to 11% and 45% were found when the TCPs were calculated using GTV and G-PTV DVHs respectively.

Out of the three convolution (pencil beam) algorithms, the performance of PBC_{ETAR} was the best owing to its 3D scatter model, in contrast to the other two inhomogeneity correction algorithms that use a 1D ray-tracing method. The differences in the absolute doses and TCPs calculated by AAA_{Ecl}, AC_{Pin}, CCC_{Pin} were much smaller and AC_{Pin} and CCC_{Pin} were consistently the closest to MC. On the other hand, CCC_{Onc} systematically underestimates the doses in the target volumes as it under-predicts the doses in the (re-)build up region and hence the doses along the periphery of the tumour are lower than those predicted by other *type b* algorithms and by MC. The differences in the NTCP values were

insignificant; in general, for the dose-fractionation regimen used in this study, the absolute values of NTCP were far less than 10% in most of the cases but absolute differences of up to 6% were found between PBC_{MB} and MC. However, the MC-predicted NTCPs for lung were systematically higher than those predicted by other algorithms.

In the final section of chapter 6, a hypofractionated NSCLC patient with a very small tumour was treated with a large daily dose of 11 Gy in 5 fractions. The differences in the DVHs calculated by *type a*, *type b* and MC algorithms were larger than those found in the 3DCRT plans. However, these large differences did not influence the TCPs (when calculated with parameter set derived by Nahum *et al.* [130]) (see chapter 3) as the absolute TCP values reached 100%. When the TCP was estimated using lower mean alpha and sigma alpha values (reflecting the suspected failure of the LQ model for large doses per fraction), TCP differences of up to 28% were found between PBC_{MB} and MC. The differences in the estimated probability of occurrence of rib fracture were within 5%.

Chapter 7 investigated another tumour site, this time in the head and neck NPC. The combination of very low-density air, high-density bone, other critical organs surrounding the tumour and three different target volumes, along with the use of a complex IMRT technique, makes it a challenging site for treatment planning. The validity of the MC IMRT model was tested in a $Delta^4$ phantom by comparing an MC calculated plan to PBC- and AAA-based plans from Eclipse. The overall agreement between the plans was within 4%/4mm. However, a systematic difference of 2.5% was found between MC and TPS algorithms at the isocentre, which was attributed to the differences in MLC inter-leaf leakage and tongue and groove modelling. The DYNVMLC model used in this study fully models the geometry of the MLC whereas the TPSs do not. Therefore a correction factor was introduced in the MC clinical NPC plans to correct for the beam modelling differences, in order to yield differences in dose solely to differences in handling heterogeneities.

Similar to the NSCLC study, PBC_{MB} and PBC_{EPL} overestimate the doses and hence result in higher TCP. *Type b* algorithms yield results closer to MC with the latter predicting the lowest TCPs and NTCPs. Although, differences exist

between the doses and consequently the predicted clinical outcome calculated by *type a*, *type b* and MC algorithms, the differences are not as large as that of those found in case of NSCLC tumours reported in chapter 6. In the case of NSCLC, the beams have a long path length in low density lung before entering the relatively high density tumour, in contrast to the NPC situation. Another reason for the NSCLC-NPC differences is that in the head and neck region there is minimal or no intra-fraction tumour motion, whereas this is a potentially large source of error in doses delivered to thoracic tumours (accounted for in chapter 6 by considering G-PTV DVHs). In the case of NPC the TCPs were calculated only using GTV DVHs as the intrafraction tumour motion is minimal.

9.3 Influence of dose calculation algorithms on TCP parameters

Chapter 8 is dedicated to evaluating the differences in the TCP parameters derived from fitting the TCP predictions to published outcome data for four different radiotherapy regimens using data sets in the form of DVHs obtained from treatment plans done with *type a*, *type b* and MC algorithms. Marsden-TCP model parameters mean radio sensitivity ($\bar{\alpha}$), statistical uncertainty on radio sensitivity over a patient population (σ_α), repopulation constant (T_k) and tumour doubling time (T_d) were derived by fitting while the clonogenic cell density ρ_{cl}) and α/β ratio were assumed known and constant.

Differences of up to 10% (GTV DVHs) and 20% (G-PTV DVHs) were found in the TCP values when inconsistent parameters were used i.e. parameters derived from data sets of a particular type of algorithm to evaluate a treatment plan that was calculated with a totally different type of algorithm. The differences between the parameters obtained from PBC_{MB} and MC algorithms were the largest and out of all the analytical algorithms AC_{Pin} and CCC_{Pin} yielded parameters very close to that of MC. The differences were significant for two main parameters namely mean radio sensitivity ($\bar{\alpha}$) and statistical uncertainty on the radio sensitivity over a patient population (σ_α). It has been shown in chapter 6 that algorithms based on simple convolution overestimate the doses to the tumour due

to their lack of modelling of lateral electron transport in low-density media. In reality, the dose delivered is significantly lower than the planned dose calculated with pencil-beam convolution algorithms; this was shown by recalculating the doses for the same MUs with the MC algorithm; a higher value for the mean radiosensitivity σ_α was obtained when the fitting was performed with data sets based on MC dose distributions.

The study shows that parameters pertaining to a specific dose calculation algorithm should be used to obtain valid tumour control probability estimates of plans calculated by the same algorithm. Using inconsistent parameters will result in either over- or under-prediction of TCP.

Chapter 10

Future Work

In this study, the feasibility of using MC dose calculation system for conventional, conformal, intensity modulated treatments for patient plans using DICOM CT data set have been tested extensively and it has been successful. The next step would be to implement MC based QA in the clinic for all of the above mentioned techniques, in particular 3DCRT, SABR of NSCLC, IMRT and also test the possibility for Rapidarc treatments of sites with complex heterogeneities. In our clinic, QA of patient plans done with above mentioned techniques is in practice, except for the fact that, the treatment plans calculated with TPSs are compared with measurements done in a homogeneous phantom. The MC dose calculation system will pave way to check the validity of the treatment plans taking heterogeneities into account without actually having to do any measurements.

The MC simulations were performed using two different parallel computing systems set up in the University of Liverpool namely high throughput condor pool and high performance computing clusters. In case of the patient plans, the total number of histories of each treatment field were split into parallel jobs and executed remotely in nodes in the condor which included class room PCs. The jobs were evicted if the nodes were used by a user located on site. The jobs had to be submitted again or otherwise it would compromise on the statistical uncertainty of the MC dose calculation which would in turn affect the accuracy of the predicted dose distribution. Streamlining of the condor jobs is necessary in order to increase the efficiency of the MC dose computation.

Due to limitation in timing to carry out this project, the testing of MLC

model for IMRT plans were not studied in detail which is will be done in future. Nasopharyngeal tumours are surrounded by air passages, soft tissue and high density bone which presents challenges to the dose calculation algorithms to predict an accurate dose distribution. Also, IMRT treatments are more complex than conventional or conformal radiotherapy due to the fact that these techniques involve steep dose gradients. The influence of dose calculation algorithms on local control, normal tissue complication probabilities of lung radiotherapy treatments were studied for plans done with low energy photon beams. Recently, the nasopharyngeal patients are treated with Rapid arc treatments instead of IMRT owing to its superiority in dose coverage and sparing of normal tissues. MC can prove as an useful QA tool for testing Rapidarc plans in DICOM CT based patient plans.

It has been shown in literature that the differences between the dose calculation algorithms are larger for high energy photon beams as the ranges of secondary electrons are larger than that generated by low energy photons for a given field size and material density. It would be of interest to study the differences in clincal outcome resulting from plans calculated using convolution, convolution-superposition and MC algorithms for high energy photon beams of energy greater than 10 MV.

A new dose calculation algorithm known as Accuros XB (which is based on linear Boltzmann transport equation) of Eclipse TPS which became available in our department recently will be tested against our MC model.

Bibliography

[1] D.I. Thwaites and J.B. Tuohy. Back to the future: the history and development of the clinical linear accelerator. *Phys Med Biol*, 51:R343–R362, 2006.

[2] E.G.A. Aird and J. Conway. Ct simulation for radiotherapy treatment planning. *Br J Radiol*, 75:937–949, 2002.

[3] R.R. Price, J. Allison, R.J. Massoth, G.D. Clarke, and D.J. Drost. Practical aspects of functional mri (nmr task group 8). *Med Phys*, 29:1892–1912, 2002.

[4] Y.E. Erdi. The use of pet for radiotherapy. *Current Medical Imaging Reviews*, 3:3–16, 2007.

[5] M. Lecchi, P. Fossati, F. Elisei, R. Orecchia, and G. Lucignani. Current concenpts on imaging in radiotherapy. *Eur J Nucl Med Mol Imaging*, 35:821–837, 2008.

[6] The role of PET/CT in radiation treatment planning for cancer patient treatment (IAEA technical document).

[7] Prescribing, recording and reporting photon beam therapy: Report 62. Technical report, International Commision on Radiological Units (ICRU), 1999.

[8] A. Brahme. Dosimetric precision requirements in radiation therapy. *Acta Radiol Oncol*, 23:379–391, 1984.

[9] A. Dutreix. When and how can we improve precision in radiotherapy? *Radiat Oncol*, 2:275–292, 1984.

[10] H. Svensson. Quality assurance in radiation therapy: physical aspects. *Int J Radiat Oncol Biol Phys*, 10:59–65, 1984.

[11] B.J. Mijnheer, J.J. Batterman, and A. Wambersie. What degree of accuracy is required and can be achieved in photon and neutron therapy? *Radiat Oncol*, 8:237–252, 1987.

[12] P. Andreo. Uncertainties in dosimetric data and beam calibration. *Int J Radiat Oncol Biol Phys*, 19:1233–1247, 1990.

[13] J. van Dyk, R.B. Barnett, J.E. Cygler, and P.C. Shragge. Commissioning and quality assurance of treatment planning computers. *Int J Radiat Oncol Biol Phys*, 26:261–273, 1993.

[14] J. Venselaar, H. Welleweerd, and B.J. Mijnheer. Tolerances for the accuracy of photon beam dose calculations of treatment planning systems. *Radiother Oncol*, 60:191–201, 2001.

[15] A. Ahnesjö and M. M. Aspradakis. Dose calculations for external photon beams in radiotherapy. *Phys Med Biol*, 44(11):R99–155, Nov 1999.

[16] A. Brahme, J. Chavaudra, T. Landberg, E. McCullough, F. Nusslin, J.A. Rawlinson, G. Svensson, and H. Svensson. Accuracy requirements ad quality assurance of external beam therapy with photons and electrons. *Acta Oncol*, 15 (Supp. 1):1–76, 1988.

[17] G.J. Kutcher and C. Burman. Calculation of complication probability factors for non-uniform normal tissue irradiation: the effective volume method. *Int J Radiat Oncol Biol Phys*, 16:1623–1630, 1989.

[18] B. Emami, J. Lyman, A. Brown, L. Coia, M. Goitein, F.W. Munzenrider, B. Shank, L.J. Solin, and M. Wesson. Tolerance of normal tissue to therapeutic irradiation. *Int J Radiat Oncol Biol Phys*, 21:109–122, 1991.

[19] S.M. Bentzen. *Basic clinical radiobiology*, chapter Dose-response relationships in radiotherapy, pages 94–104. Arnold, London, 2002.

[20] G.G. Steel. *Handbook of radiotherapy physics: theory and practice*, chapter Radiobiology of tumours, pages 127–148. Taylor & Francis, 2007.

[21] G.G. Steel. *Handbook of radiotherapy physics: theory and practice*, chapter Radiobiology of normal tissues, pages 149–162. Taylor & Francis, 2002.

[22] A.E. Nahum and G.J. Kutcher. *Handbook of radiotherapy physics: theory and practice*, chapter Biological evaluation of treatment plans, pages 731–771. Taylor & Francis, 2007.

[23] A.B. Wolbarst, L.M. Chin, and G.K. Svensson. Optimization of radiation therapy: Integral-response of a model biological system. *Int J Radiat Oncol Biol Phys*, 8:1761–1769, 1982.

[24] A. B. Wolbarst. Optimization of radiation therapy ii: The critical-voxel model. *Int J Radiat Oncol Biol Phys*, 10:741–745, 1984.

[25] J.T. Lyman and A.B. Wolbarst. Optimization of radiation therapy, iii: A method of assesing complication probabilities from dose-volume histograms. *Int J Radiat Oncol Biol Phys*, 13:103–109, 1987.

[26] P. Kallman, A. Agren, and A. Brahme. Tumour and normal tissue responses to fractionated non-uniform dose delivery. *Int J Radiat Oncol Biol Phys*, 62:249–262, 1992.

[27] S. Webb and A.E. Nahum. A model for calculating tumour control probability in radiotherapy: including the effects of inhomogeneous distributions of dose and clonogenic cell density. *Phys Med Biol*, 38:653–666, 1993.

[28] B. Jones and R.G. Dale. Mathematical models of tumour and normal tissue response. *Acta Oncol*, 38:883–893, 1999.

[29] A. Ottolenghi, M. Merzagora, F. Monforti, B. Candoni, and H.G. Paretzke. Mechanistic and phenomenological models of radiation induced biological damage. *Phys Med Biol*, 8 (Suppl. 1):282–286, 1997.

[30] A. Ottolenghi, F. Ballarini, and M. Biaggi. Mechanistic and phenomenological models for the estimate of radiation-induced biological damage. *Physica Medica*, 17 (Suppl. 2):3–12, 2001.

[31] A.E. Nahum and D.M. Tait. Tumour response monitoring and treatment planning. In *Maximising local control by customised dose prescription for*

pelvic tumours advanced radiation therapy, pages 425–431, Breit, A., Ed,, 1992. Springer, Heidelberg.

[32] A.E. Nahum and B. Sanchez-Nieto. Tumour control probability modelling: Basic principles and applications in treatment planning. *Physica Medica*, 17 (Suppl. 2):13–23, 2001.

[33] C. Burman, G.J. Kutcher, and B. Emami. Fitting of normal tissue tolerance data to an analytic function. *Int J Radiat Oncol Biol Phys*, 21:123–135, 1991.

[34] S.L. Kwa, J.V. Lebesque, and J.C. Theuws. Radiation pneumonitis as a function of mean lung dose: An analysis of pooled data of 540 patients. *Int J Radiat Oncol Biol Phys*, 42:1–9, 1998.

[35] M.V. Graham, J.A. Purdy, and B. Emami. Clinical dose-volume histogram analysis for pneumonitis after 3d treatment for non-small cell lung cancer (nsclc). *Int J Radiat Oncol Biol Phys*, 45:323–329, 1999.

[36] M.K. Martel, R.K. Ten Haken, and M.B. Hazuka. Dose-volume histogram and 3-d treatment planning evaluation of patients with pneumonitis. *Int J Radiat Oncol Biol Phys*, 28:575–581, 1994.

[37] M. K. Martel, R. K. Ten Haken, M. B. Hazuka, M. L. Kessler, M. Strawderman, A. T. Turrisi, T. S. Lawrence, B. A. Fraass, and A. S. Lichter. Estimation of tumor control probability model parameters from 3-d dose distributions of non-small cell lung cancer patients. *Lung Cancer*, 24(1):31–37, 1999.

[38] G. Gagliardi, J. Bjohle, and I. Lax. Radiation pneumonitis after breast cancer irradiation: Analysis of the complication probability using the relative seriality model. *Int J Radiat Oncol Biol Phys*, 46:373–381, 2000.

[39] Y. Seppenwoolde and J.V. Lebesque. Partical irradiation of the lung. *Semin Radiat Oncol*, 11:247–258, 2001.

[40] K. De Jaeger, M.S. Hoogeman, M. Engelsman, Y. Seppenwoolde, and E.M.F. Damen. Incorporating an improved dose-calculation algorithm in

conformal radiotherapy of lung cancer: Re-evaluation of dose in normal lung tissue. *Radiat Oncol*, 69:1–10, 2003.

[41] Y. Seppenwoolde, J.V. Lebesque, K. De Jaeger, J.S.A. Belderbos, L.J. Boersma, C.Schilstra, G.T. Henning, J.A. Hayman, M.K. Martel, and R.K. Ten Haken. Comparing different ntcp models that predict the incidence of radiation pneumonitis. *Int J Radiat Oncol Biol Phys*, 55:724–735, 2003.

[42] A.E. Nahum, J. Uzan, P. Jain, Z.I. Malik, J.D. Fenwick, and C.R. Baker. Quantitative tumour control predictions for the radiotherapy of non-small cell lung tumours. In *Poster at the joint AAPM/COMP meeting: Vancouver, BC, 31 July -4 Aug*, 2011.

[43] H.D. Suit, S. Stake, A. Taghian, P. Okunieff, and J.T. Efird. Clinical implications of heterogeneity of tumour response to radiation therapy. *Radiat Oncol*, 25:251–260, 1992.

[44] S.M. Bentzen. Radiobiological considerations in the design of clinical trials. *Radiat Oncol*, 32:1–11, 1994.

[45] P. Okunieff, D. Morgan, A. Niemierko, and H.D. Suit. Radiation dose-response of human tumours. *Int J Radiat Oncol Biol Phys*, 32:1227–1237, 1995.

[46] A.A. Khalil, S.M. Bentzen, and J. Overgaard. Steepness of the dose-response curve as a function of volume in an experimental tumour irradiated under ambient or hypoxic conditions. *Int J Radiat Oncol Biol Phys*, 39:797–802, 1997.

[47] S.M. Bentzen and S.L. Tucker. Quantifying the position and steepness of radiation dose-response curves. *Int J Radiat Oncol Biol Phys*, 71:531–542, 1997.

[48] B. Sanchez-Nieto and A.E. Nahum. The delta-tcp concept: A clinically useful measure of tumour control probabitliy. *Int J Radiat Oncol Biol Phys*, 44:369–380, 1999.

[49] M.S. Bhandare, A. Jackson, A. Eisbruch, C.C. Pan, J.C. Flickinger, P. Antonelli, and W.M. Mendenhall. Radiation therapy and hearing loss. *Int J Radiat Oncol Biol Phys*, 76 (Suppl.):S50–S57, 2010.

[50] A.N. Viswanathan, E.D. Yorke, L.B. Marks, P.J. Eifel, and W.U. Shipley. Radiation dose-volume effects of the urinary bladder. *Int J Radiat Oncol Biol Phys*, 76 (Suppl.):S116–S122, 2010.

[51] B.D. Kavanagh, C.C. Pan, L.A. Dawson, S.K. Das, X. Allen Li, R.K. Ten Haken, and M. Miften. Radiation dose-volume effects in the stomach and small bowel. *Int J Radiat Oncol Biol Phys*, 76 (Suppl.):S101–S107, 2010.

[52] J.P. Kirkpatrick, A.J. van der Kogel, and T.E. Schultheiss. Radiation dose-volume effects in the spinal cord. *Int J Radiat Oncol Biol Phys*, 76 (Suppl.):S42–S49, 2010.

[53] J.O. Deasy, V. Moiseenko, L. Marks, K.S. Clifford Chao, J. Nam, and A. Eisbruch. Radiotherapy dose-volume effects on salaivary gland function. *Int J Radiat Oncol Biol Phys*, 76 (Suppl.):S25–S63, 2010.

[54] J.M. Michalski, H. Gay, A. Jackson, S.L. Tucker, and J.O. Deasy. Radiation dose-volume effects in radation-induced rectal injury. *Int J Radiat Oncol Biol Phys*, 76 (Suppl.):S123–S129, 2010.

[55] M. Roach, J. Nam G. Gagliardi, I.E. Naqa, J.O. Deasy, and L.B. Marks. Radiation dose-volume effects and the penile bulb. *Int J Radiat Oncol Biol Phys*, 76 (Suppl.):S130–S134, 2010.

[56] C. Mayo, M.K. Martel, L.B. Marks, J. Flickinger, J. Nam, and J. Kirkpatrick. Radiation dose-volume effects of optic nerves and chiasm. *Int J Radiat Oncol Biol Phys*, 76 (Suppl.):S28–S35, 2010.

[57] L.B. Marks, S.M. Benzen, J.O. Deasy, F-M. Spring Kong, J.D. Bradley, I.S. Vogelius, I.E. Naqa, J.L. Hubbs, J.V. Lebesque, R.D. Timmerman M.K. Martel, and A. Jackson. Radiation dose-volume effects in the lung. *Int J Radiat Oncol Biol Phys*, 76 (Suppl.):S70–S76, 2010.

[58] T. Rancati, M. Schwarz, A.M. Allen, F. Feng, A. Popovtzer, B. Mittal, and A. Eisbruch. Radiation dose-volume effects in the larynx and pharynx. *Int J Radiat Oncol Biol Phys*, 76 (Suppl.):S64–S69, 2010.

[59] G. Gagliardi, L.S. Constine, V. Moiseenko, C. Correa, L.J. Pierce, A.M. Allen, and L.B. Marks. Radiation dose-volume effects in the heart. *Int J Radiat Oncol Biol Phys*, 76 (Suppl.):S77–S85, 2010.

[60] M. Werner-Waisk, E. Yorke, J.O. Deasy, J. Nam, and L.B. Marks. Radiation dose-volume effects in the esophagus. *Int J Radiat Oncol Biol Phys*, 76 (Suppl.):S86–S93, 2010.

[61] Y.R. Lawrence, X. Allen Li, I.E. Naqa, C.A. Hahn, L.B. Marks, T.E. Merchent, and A.P. Dicker. Radiation dose-volume effects in the brain. *Int J Radiat Oncol Biol Phys*, 76 (Suppl.):S20–S27, 2010.

[62] C.C. Pan, B.D. Kavanagh, L.A. Dawson, X. Allen Li, S.K. Das, M. Miften, and R.K. Ten Haken. Radiation associated liver injury. *Int J Radiat Oncol Biol Phys*, 76 (Suppl.):S94–S100, 2010.

[63] L.A. Dawson, B.D. Kavanagh, A.C. Paulino, S.K. Das, M. Miften, X. Allen Li, C. Pan, R.K. Ten Haken, and T.E. Schultheiss. Radiation associated kidney injury. *Int J Radiat Oncol Biol Phys*, 76 (Suppl.):S108–S115, 2010.

[64] C. Mayo, E. Yorke, and T.E. Merchent. Radiation associated brainstem injury. *Int J Radiat Oncol Biol Phys*, 76 (Suppl.):S36–S41), 2010.

[65] C.G. Orton, P.M. Mondalek, J.T. Spicka, D.S. Herron, and L.I. Andres. Lung corrections in photon beam treatment planning: are we ready? *Int J Radiat Oncol Biol Phys*, 10:2191–2199, 1984.

[66] J.E. O'Connor. The density scaling theorem applied to lateral electronic equilibrium. *Med Phys*, 11:678–680, 1984.

[67] M.A. Hunt, G.E. Desobry, B. Fowble, and L.R. Coia. Effect of low-density lateral interfaces on soft-tissue doses. *Int J Radiat Oncol Biol Phys*, 37:475–482, 1997.

[68] N. Papanikolaou, J.J. Battista, A.L. Boyer, C. Kappas, E. Klein, T.R. Mackie, M. Sharpe, and J. van Dyk. Aapm report no. 85: Tissue inhomogeneity corrections for megavoltage photon beams. Technical report, American Association of Physicists in Medicine, 2004.

[69] L.R. Aarup, A.E. Nahum, C. Zacharatou, T. Juhler-Nøttrup, T. Knöös, H. Nyström, L. Specht, E. Wieslander, and S.S. Korreman. The effect of different lung densities on the accuracy of various radiotherapy dose calculation methods: implications for tumour coverage. *Radiother Oncol*, 91:405–414, 2009.

[70] J.C.L. Chow, M.K.K. Leung, and J. Van Dyk. Variations of lung density and geometry on inhomogeneity correction algorithms: a monte carlo dosimetric evaluation. *Med Phys*, 36:3619–3630, 2009.

[71] B. Disher, G. Hajdok, S. Gaede, and J.J. Battista. An in-depth monte carlo study of lateral electron disequilibrium for small fields in ultra-low density lung: implications for modern radiotherapy. *Phys Med Biol*, 57:1543–1559, 2012.

[72] K.C. Tsien. The application of automatic computing machines to radiation treatment planning. *Br J Radiol*, 28:432–439, 1955.

[73] R. E. Bentley. Digital computers in radiation treatment planning. *B Jr Radiol*, 37:748–755, 1964.

[74] A. Ahnesjö and A. Trepp. Acquisition of the effective lateral electron energy fluence distribution for photon beam dose calculations by convolution methods. *Phys Med Biol*, 36:973–985, 1991.

[75] A. Ahnesjö, M. Saxner, and A. Trepp. A pencil beam model for photon dose calculation. *Med Phys*, 19(2):263–273, 1992.

[76] P. R. M. Storchi and E. Woudstra. Calculation models for determining the absorbed dose in water phantoms in off-axis planes of rectangular fields of open and wedged photon beams. *Phys Med Biol*, 40:511–527, 1995.

[77] P. R. M. Storchi and E. Woudstra. Calculation of the absorbed dose distribution due to irregularly shaped photon beams using pencil beam kernels derived from basic beam data. *Phys Med Biol*, 41:637–656, 1996.

[78] P. R. M. Storchi, L. J. van Battum, and E. Woudstra. Calculation of a pencil beam kernel from measured photon beam data. *Phys Med Biol*, 44:2917–2928, 1999.

[79] B.H. Shahine, M.S.A.L. Al-Ghazi, and E. El-Khatib. Experimental evaluation of interface doses in the presence of air cavities compared with treatment planning algorithms. *Med Phys*, 26:350–355, 1999.

[80] F.C.P. du Plessis, C.A. Willemse, M.G. Lotter, and L. Goedhals. Comparison of the batho, etar and monte carlo dose calculation methods in ct based patient models. *Med Phys*, 28:582–589, 2001.

[81] A. Ahnesjö. Collapsed cone convolution of radiant energy for photon dose calculation in heterogeneous media. *Med Phys*, 16(4):577–592, 1989.

[82] N. Papanikolaou, T. R. Mackie, and M Gehring C. Meger-Wells. Investigation of the convolution method for polyenergetic spectra. *Med Phys*, 20:1327–1336, 1993.

[83] W. Ulmer and W. Kaissl. The inverse problem of a gaussian convolution and its application to the finite size of the measurement chambers/detectors in photon and proton dosimetry. *Phys Med Biol*, 48:707–727, 2003.

[84] W. Ulmer, J. Pyyry, and W. Kaissl. A 3d photon superposition/convolution algorithm and its foundation on results of monte carlo simulations. *Phys Med Biol*, 50:1767–1790, 2005.

[85] A. Fogliata, E. Vanetti, D. Albers, C. Brink, A. Clivio, T. Knöös, G. Nicolini, and L. Cozzi. On the dosimetric behaviour of photon dose calculation algorithms in the presence of simple geometric heterogeneities: comparison with monte carlo calculations. *Phys Med Biol*, 52:1363–1385, 2007.

[86] A. Fogliata, G. Nicolini, E. Vanetti, A. Clivio, P. Winkler, and L. Cozzi. The impact of photon dose calculation algorithms on expected dose distributions

in lungs under different respiratory phases. *Phys Med Biol*, 53:2375–2390, 2008.

[87] T. Knöös, E. Wieslander, L. Cozzi, C. Brink, A. Fogliata, D. Albers, H. Nyström, and S. Lassen. Comparison of dose calculation algorithms for treatment planning in external photon beam therapy for clinical situations. *Phys Med Biol*, 51(22):5785–5807, 2006.

[88] James C L Chow, Eugene Wong, Jeff Z Chen, and Jake Van Dyk. Comparison of dose calculation algorithms with monte carlo methods for photon arcs. *Med Phys*, 30(10):2686–2694, Oct 2003.

[89] P. Carrasco, N. Jornet, M. A. Duch, L. Weber, M. Ginjaume, T. Eudaldo, D. Jurado, A. Ruiz, and M. Ribas. Comparison of dose calculation algorithms in phantoms with lung equivalent heterogeneities under conditions of lateral electronic disequilibrium. *Med Phys*, 31(10):2899–2911, Oct 2004.

[90] P. Carrasco, N. Jornet, M. A. Duch, V. Panettieri, L. Weber, T. Eudaldo, M. Ginjaume, and M. Ribas. Comparison of dose calculation algorithms in slab phantoms with cortical bone equivalent heterogeneities. *Med Phys*, 34(8):3323–3333, Aug 2007.

[91] V. Panettieri, Z.I. Malik, C.V. Eswar, D.B. Landau, J.M. Thornton, A.E. Nahum, W.P. Mayles, and J.D. Fenwick. Influence of dose calculation algorithms on isotoxic dose-escalation of non-small cell lung cancer radiotherapy. *Radiather Oncol*, 97:418–424, 2010.

[92] A. Carver, M. Gilmore, S. Riley, J. Uzan, and W.P. Mayles. An analytical approach to acceptance criteria for quality assurance of intensity modulated radiotherapy. *Radiother Oncol*, 100:453–455, 2011.

[93] I.A. Popescu, C.P. Shaw, S.F. Zavgorodni, and W.A. Beckham. Absolute dose calculations for monte carlo simulations of radiotherapy beams. *Phys Med Biol*, 50(14):3375–3392, Jul 2005.

[94] R. Mohan, C. Chui, and L. Lidofsky. Differential pencil beam dose computation model for photons. *Med Phys*, 13:64–73, 1986.

[95] J. Milan and R.E. Bentley. The storage and manipulation of radiation dose data in a small digital computer. *Br J Radiol*, 47:115–121, 1974.

[96] *Eclipse v.10 algorithms reference guide, Varian Medical Systems, Palo Alto, USA*.

[97] *Oncentra v.4.0 Physics and Algorithms, Nucletron, Veenendaal, The Netherlands*.

[98] H. Batho. Lung corrections in cobalt-60 beam therapy. *J Can Assoc Radiol*, 15:79–83, 1964.

[99] E. El-Khatib and J. J. Battista. Improved lung dose calculation using tissue-maximum ratios in the batho correction. *Med Phys*, 11:279–286, 1984.

[100] S. Webb and R. A. Fox. Verification by monte carlo methods of a power law tissue-air ratio algorithm for inhomogeneity corrections in photon beam dose calculations. *Phys Med Biol*, 25:225–240, 1980.

[101] M.E. Young and J.D. Gaylord. Experimental tests of corrections for tissue inhomogeneities in radiotherapy. *Br J Radiol*, 43:349–355, 1970.

[102] S.J. Thomas. A modified power-law formula for inhomogeneity corrections in beams of high-energy x rays. *Med Phys*, 18:719–723, 1991.

[103] M.R. Sontag and J.R. Cunningham. Clinical application of a ct based treatment planning system. *Comput Tomogr*, 2:117–130, 1978.

[104] M.R. Sontag and J.R. Cunningham. The equivalent tissue-air ratio method for making absorbed dose calculations in a heterogeneous medium. *Radiology*, 129:787–794, 1978b.

[105] W. Ulmer and D. Harder. A triple gaussian pencil beam model for photon beam treatment planning. *Med Phys*, 5:25–30, 1995.

[106] W. Ulmer and D. Harder. Applications of a triple gaussian pencil beam model for photon beam treatment planning. *Med Phys*, 6:68–74, 1996.

[107] L. Tillikainen, S. Siljamaki, H. Helminen, J. Alakuijala, and J. Pyyry. Determination of parameters for a multiple-source model of megavoltage photon beams using optimization methods. *Phys Med Biol*, 52:1441–1467, 2007.

[108] L. Tillikainen, H. Helminen, T. Torsti, S. Siljamaki, J. Alakuijala, J. Pyyry, and W. Ulmer. A 3d pencil-beam-based superposition algorithm for photon dose calculation in heterogeneous media. *Phys Med Biol*, 53:3821–3839, 2008.

[109] A. Van Esch, L. Tillikainen, J. Pyykkonen, M. Tenhunen, H. Helminen, S. Siljamaki, J. Alakuijala, M. Paiusco, M. Iori, and D.P. Huyskens. Testing of the analytical anisotropic algorithm for photon dose calculation. *Med Phys*, 33:4130–4148, 2006.

[110] D. W. O. Rogers, B. A. Faddegon, G. X. Ding, C. M. Ma, J. We, and T. R Mackie . BEAM: a Monte Carlo code to simulate radiotherapy treatment units. *Med Phys*, 22(5):503–524, May 1995.

[111] T.R. Mackie, A.F. Bielajew, D.W.O. Rogers, and J.J. Battista. Generation of photon energy deposition kernels using the egs monte carlo code. *Phys Med Biol*, 33:1–20, 1988.

[112] *Pinnacle3 Physics reference guide, Philips Medical Systems, Fitchburg, USA*.

[113] G. Starkschall, R.E.Jr. Steadham, R.A. Popple, S. Ahmad, and I. Rosen. Beam-commissioning methodology for a three-dimensional convolution/superposition photon dose algorithm. *J Appl Clin Med Phys*, 1:8–27, 2000.

[114] M.M. Aspradakis, R.H. Morrison, N.D. Richmond, and A. Steele. Experimental verificationof convolution/superposition photon dose calculations for radiotherapy treatment planning. *Phys Med Biol*, 48:2873–2893, 2003.

[115] A. Nisbet, I. Beange, H.S. Vollmar, C. Irvine, A. Morgan, and D.I. Thwaites. Dosimetric verification of a commercial collapsed cone algorithm in simulated clinical situations. *Radiat Oncol*, 73:79–88, 2004.

[116] L. Paelinck, N. Reynaert, H. Thierens, W. De Neve, and C. De Wagter. Experimental verification of lung dose with radiochromic film: comparison with monte carlo simulations and commercially available treatment planning systems. *Phys Med Biol*, 50:2055–2069, 2005.

[117] A. Ahnesjö, P. Andreo, and A. Brahme. Calculation and application of point spread functions for treatment planning with high energy photon beams. *Acta Oncol*, 26(1):49–56, 1987.

[118] Y. Zhu and A. Boyer. X-ray dose computations in heterogeneous media using 3-dimensional FFT convolution. *Phys Med Biol*, 35:315, 1990.

[119] P. Andreo. Monte Carlo techniques in medical radiation physics. *Phys Med Biol*, 36:861–920, 1991.

[120] J. Seco, E. Adams, M. Bidmead, M. Partridge, and F. Verhaegen. Head-and-neck IMRT treatments assessed with a Monte Carlo dose calculation engine. *Phys Med Biol*, 50:817–830, 2005.

[121] D.E. Raeside. An introduction to monte carlo methods. *American J Phys*, 42:20–26, 1974.

[122] D.E. Raeside. Monte carlo principles and applications. *Phys Med Biol*, 21:181–197, 1976.

[123] O. Klein and Y. Nishina. Uber die streuung von strahlung durch freie electronen nach der neuren relativistischen quantendynamik von dirac. *Z Physik*, 52:853–868, 1929.

[124] M.J. Berger. Monte carlo calculation of the penetration and diffusion of fast charged particles. *Methods Comput Phys*, 1:135–215, 1963.

[125] H.A. Bethe. Scattering of electrons. *Z fur Physik*, 76:293, 1932.

[126] H.A. Bethe. Moliere theory of multiple scattering. *Phys Rev*, 89:1256–1266, 1953.

[127] E.J. Hall, editor. *Radiobiology for the Radiologist*. Lippincott, Wiliams and Wilkins, Philadelphia, 5th edition.

[128] F. Ellis. Nominal standard dose and the ret. *Br J Radiol*, 44:101–108, 1971.

[129] J. Fowler. The linear-quadratic formula and progress in fractionated radiotherapy. *Br J Radiol*, 62:679–694, 1989.

[130] A.E. Nahum, J. Uzan, P. Jain, Z. Malik, J. Fenwick, and C. Baker. Quantitative tumour control predictions for the radiotherapy of non-small-cell lung tumours. In *AAPM 2011, Vancouver, Canada*, 2011.

[131] Saunders M, Dische S, Barrett A, Harvey A, Griffths G, and Parmar M. Continuous, hyperfractionated, accelerated radiotherapy (chart) versus conventional radiotherapy in non-small cell lung cancer: mature data from the randomised multicentre trial. *Radiat Oncol*, 52:137–148, 1999.

[132] R. Timmerman, R. Paulus, J. Galvin, J. Michalski, W. Straube, and *et al.* Bradley, J. Sterotactic body radiation therapy for inoperable early stage lung cancer. *J Am Cancer Associat*, 17:1070–1076, 2010.

[133] M. Guerrero and X. Allen Li. Extending the linear-quadratic model for large fraction doses pertinent to stereotactic radiotherapy. *Phys Med Biol*, 49:4825–4835, 2004.

[134] M. Carlone, D. Wilkins, and P. Raaphorst. The modified linear-quadratic model of guerrero and li can be derived from a mechanistic basis and exhibits linear-quadratic-linear behaviour. *Phys Med Biol*, 50:L9–L15, 2005.

[135] J.F. Fowler. 21 years of biologically effective dose. *Br J Radiol*, 83:554–568, 2010.

[136] J. Selvaraj, J. Uzan, and A.E. Nahum. TCP loss due to setup errors as a function of dose-response slope and number of fractions. *Radiother Oncol*, 99:S36, 2011.

[137] G.G. Steel, editor. *Basic clinical radiobiology for radiation oncologists*. Arnold, London, 1993.

[138] H.R. Withers and J.M. Taylor. Critical volume model. *Int J Radiat Oncol Biol Phys*, 34:923–930, 1993.

[139] J. T. Lyman. Complication probability as assessed from dose-volume histograms. *Radiat Res Suppl*, 8:S13–S19, 1985.

[140] Niclas Pettersson, Jan Nyman, and Karl-Axel Johansson. Radiation-induced rib fractures after hypofractionated stereotactic body radiation

therapy of non-small cell lung cancer: a dose- and volume-response analysis. *Radiother Oncol*, 91(3):360–368, Jun 2009.

[141] V.A. Semenenko and X.A. Li. Lyman-Kutcher-Burman NTCP model parameters for radiation pneumonitis and xerostomia based on combined analysis of published clinical data. *Phys Med Biol*, 53:737–755, 2008.

[142] F.M. Buffa and A E Nahum. Monte carlo dose calculations and radiobiological modelling: analysis of the effect of the statistical noise of the dose distribution on the probability of tumour control. *Phys Med Biol*, 45:3009–3023, 2000.

[143] P J Keall, J V Siebers, R Jeraj, and R Mohan. The effect of dose calculation uncertainty on the evaluation of radiotherapy plans. *Med Phys*, 3:478–484, 2000.

[144] I Kawrakow. The effect of monte carlo statistical uncertainties on the evaluation of dose distributions in radiation treatment planning. *Phys Med Biol*, 49:1549–1556, 2004.

[145] S. B. Jiang, T. Pawlicki, and C. M. Ma. Removing the effect of statistical uncertainty on dose-volume histograms from monte carlo dose calculations. *Phys Med Biol*, 45(8):2151–2161, Aug 2000.

[146] C-M. Ma, J. S. Li, S. B. Jiang, T. Pawlicki, W. Xiong, L. H. Qin, and J. Yang. Effect of statistical uncertainties on monte carlo treatment planning. *Phys Med Biol*, 50(5):891–907, Mar 2005.

[147] http://irs.inms.nrc.ca/.

[148] J.A. Halbleib. *Monte Carlo Transport of Electrons and Photons*. Pleneum, Newyork, 1988.

[149] M. Berger and S. Seltzer. ETRAN Monte Carlo code system for electron and photon transport through extended media. Technical report, Radiation Shielding Information Center (RICC) Report CCC-107, Oak Ridge National Laboratory, Oak Ridge, TN, 1973.

[150] R.L. Ford and W.R. Nelson. The EGS code system-Version 3, report SLAC-210. Technical report, Standford Linear Accelerator, CA, 1978.

[151] W.R. Nelson, H. Hirayama, and Rogers D.W.O. The EGS4 code system, Report SLAC-265. Technical report, Stanford Linear Accelerator, Stanford, CA, 1985.

[152] I. Kawrakow, E. Mainegra-Hing, Rogers D.W.O., F. Tessier, and B. R. B. Walters. EGSnrc code system: Monte Carlo simulation of electron and photon transport, PIRS-701. Technical report, National Research Council of Canada, Ottawa, Ontorio, 2011.

[153] D.W.O. Rogers, B. Walters, and I. Kawrakow. *BEAMnrc Users manual, NRCC Report PIRS-0509(A)revL.* National Research Council, Canada, 2011.

[154] B. R. B. Walters, I Kawrakow, and Rogers D.W.O. DOSXYZnrc Users Manual, NRCC Report PIRS-794revB. Technical report, National Research Council of Canada, Ottawa, 2011.

[155] F.B Brown. MCNP-A general purpose Monte Carlo-particle transport code, version 5. Technical report, Los Alamos National Laboratory, Los Alamos, NM, 2003.

[156] S. Agostinelli. GEANT4-A simulation toolkit. *Nucl Instrum Methods Phys Res A*, 506:250–303, 2003.

[157] J. Baro, J. Sempau, J.M. Fernández-Varea, and F Salvat. PENELOPE-An algorithm for Monte-Carlo simulation of the penetration and energy-loss of electrons and positrons in matter. *Nucl Instrum Methods Phys Res A*, 100:31–46, 1995.

[158] I Kawrakow, M. Fippel, and K. Friedrich. 3D electron dose calculation using a voxel based Monte Carlo algorithm(VMC). *Med Phys*, 23:445–457, 1996.

[159] M. Fippel. Fast Monte Carlo calculation for photon beams on the VMC electron algorithm. *Med Phys*, 26:1466–1475, 1999.

[160] F. Verhaegen and J. Seuntjens. Monte Carlo modelling of external radiotherapy photon beams. *Phys Med Biol*, 48:R107–R164, 2003.

[161] I. Kawrakow and B. R. B. Walters. Efficient photon beam dose calculations using dosxyznrc with beamnrc. *Med Phys*, 33:3046–56, 2006.

[162] Indrin J Chetty, Bruce Curran, Joanna E Cygler, John J DeMarco, Gary Ezzell, Bruce A Faddegon, Iwan Kawrakow, Paul J Keall, Helen Liu, C. M Charlie Ma, D. W O Rogers, Jan Seuntjens, Daryoush Sheikh-Bagheri, and Jeffrey V Siebers. Report of the aapm task group no. 105: Issues associated with clinical implementation of monte carlo-based photon and electron external beam treatment planning. *Med Phys*, 34(12):4818–4853, Dec 2007.

[163] I. Kawrakow, D. W. O. Rogers, and B. R. B. Walters. Large efficiency improvements in beamnrc using directional bremsstrahlung splitting. *Med Phys*, 31:2883–98, 2004.

[164] B. R. B. Walters and I. Kawrakow. Technical note: Overprediction of dose with default PRESTA-I boundary crossing in DOSXYZnrc and BEAMnrc. *Med Phys*, 34:647–650, 2007.

[165] B. R. B. Walters and I Kawrakow. A"HOWFARLESS" option to increase efficiency of homogeneous phantom calculations with DOSXYZnrc. *Med Phys*, 34:3794–3807, 2007.

[166] E. Heath and J. Seuntjens. Development and validation of a beamnrc component module for accurate monte carlo modelling of the varian dynamic millennium multileaf collimator. *Phys Med Biol*, 48:4045–4063, 2003.

[167] Varian Medical Systems, Palo Alto, US. *Enhanced dynamic wedge implementation guide*, 1996.

[168] Liu H. H. Verhaegen, F. Incorporating dynamic collimator motion in monte carlo simulations: an application in modelling a dynamic wedge. *Phys Med Biol*, 46(2):287–296, Feb 2001.

[169] Das I. J. Verhaegen, F. Monte carlo modelling of a virtual wedge. *Phys Med Biol*, 44(12):N251–N259, Dec 1999.

[170] C. Duzenli, McClean, and C. B. Field. Backscatter into the beam monitor chamber: implications for dosimetry of asymmetric collimators. *Med Phys*, 20:363–367, 1993.

[171] M. K. Yu and Mansour F. Sloboda, R. S. Measurement of photon beam backscatter from collimators to the beam monitor chamber using target-current-pulse-counting and telescopic techniques. *Phys Med Biol*, 41:1107–1117, 1996.

[172] Muthuswamy M. S. Ten Haken R. K. Lam, K. L. Measurement of backscatter to the monitor chamber of medical accelerators using target charge. *Med Phys*, 25:334–338, 1998.

[173] Mackie T. R. McCullough E. C. Liu, H. H. Modeling photon output caused by backscattered radiation into the monitor chamber from collimator jaws using a monte carlo technique. *Med Phys*, 27(4):737–744, Apr 2000.

[174] Symonds-Tayler R. Liu H. H. Nahum A. E. Verhaegen, F. Backscatter towards the monitor ion chamber in high-energy photon and electron beams: charge integration versus monte carlo simulation. *Phys Med Biol*, 45(11):3159–3170, Nov 2000.

[175] J. Sempau, S.J. Wilderman, and A.F. Bielajew. DPM, a fast, accurate Monte Carlo code optimized for photon and electron radiotherapy treatment planning dose calculations. *Phys Med Biol*, 45:2263–2291, 2000.

[176] J. Sempau, A. Sánchez-Reyes, F. Salvat, H. Oulad ben Tahar, S.B. Jiang, and J.M. Fernández. Monte Carlo simulation of electron beams from an accelerator head using PENELOPE. *Phys Med Biol*, 46:1163–1186, 2001.

[177] Burns D. T. Hohfeld K. Huq M. S Kanai T. Laitano F. Smyth V. G. Vynckier S. Andreo, P. Absorbed dose determination in external beam radiotherapy: An international code of practice for dosimetry based on standards of absorbed dose to water. *IAEA Technical Report Series 398*, 2000.

[178] Biggs P. J. Coursey B. M. Hanson W. F. Huq M. S. Nath R. Rogers D. W. O. Almond, P. R. Aapm task group 51: Protocol for clinical reference

dosimetry of high-energy photon and electron beams. *Med Phys*, 26:1847–70, 1999.

[179] J.V. Siebers, P.J. Keall, A.E. Nahum, and R. Mohan. Converting absorbed dose to medium to absorbed dose to water for Monte Carlo based photon beam dose calculations. *Phys Med Biol*, 45:983–995, 2000.

[180] J.M. Fernández, P. Carrasco, V. Panettieri, and L. Brualla. Monte Carlo based water/medium stopping-power ratios for various ICRP and ICRU tissues. *Phys Med Biol*, 52:6475–6483, 2007.

[181] Rogers D.W.O. Sheikh-Bagheri, D. Sensitivity of megavoltage photon beam monte carlo simulations to electron beam and other parameters. *Med Phys*, 29:379–390, 2002.

[182] Damilakis J. E. Mazonakis M. Stratakis J. Varveris H. Gourtsoyiannis N. Tzedakis, A. Influence of initial electron beam parameters on monte carlo calculated absorbed dose distributions for radiotherapy photon beams. *Med Phys*, 31:907–913, 2004.

[183] Chen Y. Lu W. Mackie T. R. Olivera G. H. Vynckier S. Sterpin, E. On the relationships between electron spot size, focul spot size, and virtual source position in monte carlo simulations. *Med Phys*, 38:1579–1586, 2011.

[184] S. Chiu-Tsao, Y. Ho, R. Shankar, L. Wang, and L.B. Harrison. Energy dependence of response of new high sensitivity radiochromic films for megavoltage and kilovoltage radiation energies. *Med Phys*, 32:2245–2253, 2005.

[185] A. Rink, I.A. Vitkin, and D.A. Jaffray. Characterisation and real-time optical measurements of the ionising radiation dose response for a new radiochromic medium. *Med Phys*, 32:2510–2516, 2005.

[186] M. Fuss, E. Sturtewagon, C. De Wagter, and D. Georg. Dosimetric characterization of gafchromic EBT film and its implication on film dosimetry quality assurance. *Phys Med Biol*, 52:4211–4225, 2007.

[187] Slobodan Devic. Radiochromic film dosimetry: Past, present, and future. *Physica Medica*, 27:122–134, 2011.

[188] Gafchromic EBT2 - Self developing film for radiotherapy dosimetry. Technical report, International Specialty products, New Jersey, USA, 2010.

[189] M. Martišíková, B. Ackermann, and O. Jäkel. Analysis of uncertainties in Gafchromic EBT film dosimetry of photon beams. *Phys Med Biol*, 53:7013–7027, 2008.

[190] A. Micke, D.F. Lewis, and X. Yu. Multichannel film dosimetry with nonuniformity correction. *Med Phy*, 38:2523–2534, 2011.

[191] C. Huet, S. Dagois, S. Derreumaux, F. Trompier, C. Chenaf, and I. Robbes. Characterization and optimization of ebt2 radiochromic films dosimetry system for precise measurements of output factors in small fields used in radiotherapy. *Radiat Meas*, 47:40–49, 2012.

[192] B. Hartmann, M. Martisiková, and O. Jäkel. Homogeneity of Gafchromic EBT2 film. *Med Phys*, 37:1753–1756, 2010.

[193] J. Menegotti, A. Delana, and A. Martignano. Radiochromic film dosimetry with flatbed scanners: A fast and accurate method for dose calibration and uniformity correction with single film exposure. *Med Phys*, 35:3078–3085, 2008.

[194] M.V. Willaims, N.D. James, E.T. Summers, A. Barrett, and D.V. Ash. National survey of radiotherapy fractionation practice in 2003. *Clin Oncol*, 18:3–14, 2006.

[195] U. Haedinger, T. Krieger, M. Flentje, and J. Wulf. Influence of calculation model on dose distribution in stereotactic radiotherapy for pulmonary targets. *Int J Radiat Oncol Biol Phys*, 61:239–249, 2005.

[196] I. Lax, V. Panettieri, B. Wennberg, M.A. Duch, I. Näslund, P. Baumann, and G. Gagliardi. Dose distributions in sbrt of lung tumors: Comparison between two different treatment planning algorithms and monte-carlo simulation including breathing motions. *Acta Oncol*, 45:978–988, 2006.

[197] V. Panettieri, B. Wennberg, G. Gagliardi, M. A. Duch, M. Ginjaume, and I. Lax. SBRT of lung tumours: Monte Carlo simulation with PENELOPE

of dose distributions including respiratory motion and comparison with different treatment planning systems. *Phys Med Biol*, 52:4265–4281, 2007.

[198] F. Hasenbalg, H. Neuenschwander, R. Mini, and E.J. Born. Collapsed cone convolution and analytical anisotropic algorithm dose calculations compared to VMC++ monte carlo simulations in clinical cases. *Phys Med Biol*, 52:3679–3691, 2007.

[199] J. Uzan and A.E. Nahum. Biosuite, software for radiobiologically guided optimization of prescription dose and fractionation scheme in radiotherapy. *Br J Radiol*, 85:1279–1286, 2012.

[200] B. Fraass, K. Doppke, M. Hunt, G. Kutcher, G. Starkschall, and R. Stern J. Van Dyke. American association of physicists in medicine radiation therapy committee task group 53: Quality assurance for clinical radiotherapy treatment planning. *Med Phys*, 25:1773–1829, 1998.

[201] T.B. Nielsen, E. Wieslander, A. Fogliata, M. Nielsen, O. Hansen, and C. Brink. Influence of dose calculation algorithms on the predicted dose distributions and ntcp values for nsclc patients. *Med Phys*, 38:2412–2418, 2011.

[202] M.R. Arnfield, C.H. Sianter, J. Siebers, P. Garmon, L. Cox., and R. Mohan. The impact of electron transport on the accuracy of computed dose. *Med Phys*, 27:1265–1274, 2000.

[203] E. Sterpin, M. Tomsej, B. De Smedt, N. Reynaert, and S. Vynckier. Monte carlo evaluation of the AAA treatment planning algorithm in a heterogeneous multilayer phantom and imrt clinical treatments for an elekta SL25 linear accelerator. *Med Phys*, 34:1665–1677, 2007.

[204] T. Bortfeld, K. Jokiavarsi, M. Goitein, and Jiang S.B. Kung, J. Effects of intra-fraction motion on imrt dose delivery: statistical analysis and simulation. *Phys Med Biol*, 47:2203–2220, 2002.

[205] C.S. Chui, E. Yorke, and L. Hong. The effects of intra-fraction organ motion on the delivery of intensity-modulated field with a multileaf collimator. *Med Phys*, 30:1736–1746, 2003.

[206] I. Fotina, P. Winkler, T. Künzler, Simmat I. Rieterer, J, and D. Georg. Advanced kernel methods vs. Monte Carlo-based dose calculation for high energy photon beams. *Radiother Oncol*, 93:645–653, 2009.

[207] E.D. Yorke, A. Jackson, E.R. Kenneth, S.A. Merrick, D. Gabrys, E.S. Venkatraman, and et al. Dose-volume factors contributing to the incidence of radiation pneumonitis in non-small-cell lung cancer patients treated with three-dimensional conformal radiation therapy. *Int J Radiat Oncol Biol Phys*, 54:329–339, 2002.

[208] D.T. Chang, K.R. Oliver, C.G. Morris, C. Liu, J.F. Dempsey, R.K. Benda, and et al. The impact of heterogeneity correction on dosimetric parameters that predict for radiation pneumonitis. *Int J Radiat Oncol Biol Phys*, 65:125–131, 2006.

[209] J.A. Langendijk, C.R. Leemans, J. Buter, J. Berghof, and B.J. Slotman. The additional value of chemotherapy to radiotherapy in locally advanced nasopharyngeal carcinoma: A meta-analysis of the published literature. *J Clin Oncol*, 22:4604–4612, 2004.

[210] J. Cheng, K. Chao, and D. Low. Comparison of intensity modulation radiation therapy (IMRT) treatment techniques for nasopharyngeal carcinoma. *Int J Cancer*, 96:126–131, 2001.

[211] M.A. Hunt, M.J. Zelefsky, S. Wolden, C.S. Chui, T. LoSasso, and K. et al. Rosenzweig. Treatment planning and delivery of intensity-modulated radiation therapy for primary nasopharynx cancer. *Int J Radiat Oncol Biol Phys*, 49:623–632, 2001.

[212] M.K. Kam, R.M. Chau, J. Suen, P.H. Choi, and P.M. Teo. Intensity-modulated radiotherapy in nasopharyngeal carcinoma: dosimetric advantage over conventional plans and feasibility of dose escalation. *Int J Radiat Oncol Biol Phys*, 56:145–157, 2002.

[213] E.E. Klein, L.M. Chin, R.K. Rice, and B.J. Mijnheer. The influence of air cavities on interface doses for photon beams. *Int J Radiat Oncol Biol Phys*, 27:419–427, 1993.

[214] P.M. Ostwald, T. Kron, and C.S. Hamilton. Assessment of mucosal underdosing in larynx irradiation. *Int J Radiat Oncol Biol Phys*, 36:181–187, 1996.

[215] W.K. Kan, P.M Wu, H.T. Leung, T.C. Lo, C.W. Chung, and D.L.W. et al. Kwong. The effect of nasopharyngeal air cavity on x-ray interface doses. *Phys Med Biol*, 43:529–537, 1998.

[216] C. Martens, N. Reynaert, C. De Wagter, P. Nilsson, H. Coghe, and H. et al. Palmans. Underdosage of the upper-airway mucosa for small fields as used in intensity-modulated radiation therapy: A comparison between radiochromic film measurements, Monte Carlo simulations, and collapsed cone convolution calculations. *Med Phys*, 29:1528–1535, 2002.

[217] P. Francescon, S. Cora, and P. Chovati. Dose verification of an IMRT treatment planning system with the BEAM EGS4-based Monte Carlo code. *Med Phys*, 30:144–157, 2003.

[218] M.W.K. Kan, J.Y.C. Cheung, L.H.T. Leung, B.M.F. Lau, and P.K.N Yu. The accuracy of dose calculations by anisotropic analytical algorithms for stereotactic radiotherapy in nasopharyngeal carcinoma. *Phys Med Biol*, 56:397–413, 2011.

[219] J.V. Siebers, P.J. Keall, J.O. Kim, and R. Mohan. A method for photon beam Monte Carlo multileaf collimator particle transport. *Phys Med Biol*, 47:3225–3249, 2002.

[220] R.J. Amdur, C. Liu, J. Li, W. Mendenhall, and R. Hinerman. Matching intensity-modulated radiation therapy to an anterior low neck field. *Int J Radiat Oncol Biol Phys*, 69(2 Suppl):S46–S48, 2007.

[221] J. Deng, T. Pawlicki, Y. Chen, J. Li, S.B. Jiang, and C-M. Ma. The MLC tongue-and-groove effect on IMRT dose distributions. *Phys Med Biol*, 46:1039–1060, 2001.

[222] A. Jackson, G.J. Kutcher, and E.D. Yorke. Probability of radation-induced complications for normal tissues with parallel architechture subject to nonuniform irradiation. *Med Phys*, 20:613–625, 1993.

[223] A. Niemierko and M. Goitein. Modeling of normal tissue response to radiation: the critical volume model. *Int J Radiat Oncol Biol Phys*, 25:135–145, 1993.

[224] P. Stavrev, N. Stavreva, A. Niemierko, and M. Goitein. Generalization of model of tissue reponse to radiation based on the idea of functional subunits and binomial statistics. *Phys Med Biol*, 46:1501–1518, 2001.

[225] E. Rutkowska, C.R. Baker, and A.E. Nahum. Mechanistic simulation of normal-tissue damage in radiotherapy - implications for dose-volume analyses. *Phys Med Biol*, 55:2121–2136, 2010.

[226] H. Nikjoo, S. Uehara, W.E. Wison, M. Hoshi, and D.T. Goodhead. Track structure in radiation biology: theory and applications. *Int J Radiat Oncol Biol Phys*, 73:355–364, 1998.

[227] H. Nikjoo, S. Uehara, I.G. Khvostunov, F.A. Cucinotta, W.E. Wilson, and D.T. Goodhead. Monte carlo track structure for radiation biology and space applications. *Physica Medica*, 17:38–44, 2001.

[228] R. Morrison. The results of treatment of cancer of the bladder - a clinical contribution to radiobiology. *Clin Radiol*, 26:67–75, 1975.

[229] J.V. Moore, J.H. Hendry, and R.D. Hunter. Dose incidence curves for tumour control and normal tissue injury in relation to the response of clonogenic cells. *Radiat Oncol*, 1:143–157, 1983.

[230] G. Hanks, K.L. Martz, and J.J. Diamond. The effect of dose on local control of prostate cancer. *Int J Radiat Oncol Biol Phys*, 15:1299–1305, 1988.